A NEW SPIN ON PRIMORDIAL HYDROGEN RECOMBINATION

and

A REFINED MODEL FOR SPINNING DUST RADIATION

Thesis by

Yacine Ali-Haïmoud

In Partial Fulfillment of the Requirements

for the Degree of

Doctor of Philosophy

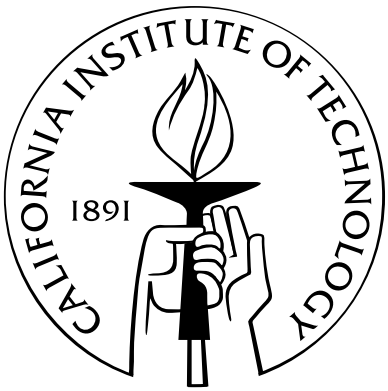

California Institute of Technology

Pasadena, California

2011

(Defended May 9, 2011)

A Djeddi, pour m'avoir tiré les oreilles en me disant "il faut bien travailler".

A Papi, pour m'avoir montré les plaisirs simples de la vie.

A Mané et Mami pour leur douceur.

Acknowledgements

Despite the seriousness of the topics addressed in this thesis, most of the "work" that I have been doing during these years was actually a lot of fun. I would therefore like to start by thanking my fellow taxpayers for giving me the opportunity to have a hobby as my job.

It is a rare privilege to be able to see beauty in an equation or an idea, and this taste could only be acquired and educated with the help of many patient teachers, more than I could list here. In particular, Professors Castaing and Mercier, if you ever read these lines, I thank you for your communicative passion and dedication to teaching.

I was extremely lucky during my stay at Caltech to be advised by Prof. Christopher Hirata, who has set an example for me in many ways. The vastness of Chris' knowledge is only equaled by his great humility and the patience with which he would share his wisdom with anyone who needs an explanation. Ever since his first description of the Fokker-Planck equation at the Red Door Café, Chris' regular impromptu blackboard derivations have enlightened my years of graduate school. He has assigned me interesting and important problems to work on, and has guided me through their solutions. Above all, I would like to thank him for being always available, supportive and kind. I am honored and proud to be Chris' first official graduate student.

Other professors have been very helpful during these few years. I thank Prof. Clive Dickinson for patiently mentoring me during my first year of graduate school and Prof. Anthony Readhead for giving me the opportunity to spend a few weeks at the Cosmic Background Imager in Chile. I also thank Prof. Marc Kamionkowski for initiating me to "quick and dirty" theoretical astrophysics and giving me advice when I needed it, as well as warm encouragements. I recently had the pleasure to work with Prof. Yanbei Chen, who has introduced me to the interesting field of gravity theory.

I started by mentioning the fun of being a graduate student. Often, the fun part comes after long and not-so-fun weeks or months of hard work. Luckily, my office has always been a welcoming place. My long-term officemates and now friends, Nate, Dan and Anthony, have created a warm and relaxed atmosphere — they even laughed at my jokes, sometimes — while still scientifically stimulating.

My well being and balance has been greatly helped by my friends and family. Being far away from home for such a long time is not always easy (and not only because of the lack of good cheese).

Several people have come across my path, that brought me solace, or even just an attentive ear and kind words when needed. You who recognize yourselves, I thank you for being kind to me.

My final words will be for my parents. You have always given me unconditional love and support and taught me things that no book nor school can teach. Thanks to you, my childhood dreams have become a reality. Maman, Papa, my debt to you is far beyond what I could ever give back. All I can hope for is to make you proud.

Standard acknowledgements

This thesis has been funded in part by the U.S. Department of Energy (Contract No. DE-FG03-92-ER40701) and the National Science Foundation (Contracts No. AST-0607857 and AST-0807337). I have also benefitted from a fellowship of the Carnot Foundation.

Remerciements

Malgré le sérieux des sujets traités dans cette thèse, la plupart du "travail" que j'ai fait pendant ces années m'a procuré beaucoup de plaisir. J'aimerais donc commencer par remercier les contribuables qui m'ont donné l'opportunité d'avoir un hobby en guise d'emploi.

C'est un privilège rare que de pouvoir voir de la beauté dans une équation ou une idée. Je n'aurais pu acquérir et éduquer ce goût sans l'aide de nombreux enseignants dévoués, dont la liste est trop longue pour être détaillée ici. J'aimerais tout particulièrement remercier Messieurs Castaing et Mercier pour leur passion communicative et leur dévouement pour l'enseignement.

J'ai eu la grande chance d'avoir effectué ma thèse sous la direction de Professeur Christopher Hirata, dont je suis honoré et fier d'être officiellement le premier étudiant. L'étendue des connaissances de Chris n'a d'égale que sa grande humilité et la patience sans fin avec laquelle il partage son savoir. Depuis notre première discussion au Red Door Café, les leçons improvisées de Chris au tableau ont rythmé et illuminé mes années de thèse. Chris m'a donné des problèmes intéressants et importants sur lesquels travailler, et m'a guidé avec sagesse pour les résoudre. Par dessus tout, j'aimerais le remercier d'avoir toujours été disponible et compréhensif, et pour sa grande gentillesse.

D'autres professeurs ont été d'une grande aide pendant ces années à Caltech. Je remercie Professeur Clive Dickinson d'avoir été un mentor patient pendant ma première année, et Professeur Anthony Readhead de m'avoir donné l'opportunité de passer quelques semaines au Cosmic Background Imager au Chili. J'aimerais aussi remercier Professeur Marc Kamionkowski de m'avoir initié à l'astrophysique théorique "quick and dirty", m'avoir donné de bons conseils lorsque j'en avais besoin, et de m'avoir encouragé et montré son appréciation. J'ai récemment eu le plaisir de collaborer avec Professeur Yanbei Chen, qui m'a introduit au sujet passionant de la théorie de la

gravité.

J'ai commencé par évoquer le plaisir d'être un thésard. Souvent, le plaisir et la satisfaction ne viennent qu'après de longues semaines voire longs mois de travail pénible et frustrant. Heureusement, mon bureau a toujours été un endroit accueillant. Mes collègues de bureau de longue date, et à présent amis, Nate, Dan et Anthony, ont su créer une atmosphère chaleureuse et détendue — ils ont même ri à mes jeux de mots douteux, parfois — tout en restant stimulante scientifiquement.

Mon bien-être et équilibre a été beaucoup aidé par mes amis et proches. Être loin de chez soi pour si longtemps n'est pas toujours facile (et pas seulement à cause du manque de bon fromage). Vous, qui vous reconnaîtrez, je vous remercie de m'avoir apporté du réconfort, ou tout simplement une oreille attentive quand j'ai avais besoin.

Mes dernières pensées iront à mes parents. Vous m'avez toujours donné un amour et un soutien inconditionnels et enseigné des choses que l'on ne trouve pas dans les livres. Grâce à vous, mes rêves d'enfant sont devenus réalité. Maman, Papa, je vous dois bien plus que je ne pourrai jamais vous rendre. Tout ce que je peux espérer, c'est de vous rendre fiers.

Abstract

This thesis describes theoretical calculations in two subjects: the primordial recombination of the electron-proton plasma about 400,000 years after the Big Bang and electric dipole radiation from spinning dust grains in the present-day interstellar medium.

Primordial hydrogen recombination has recently been the subject of a renewed attention because of the impact of its theoretical uncertainties on predicted cosmic microwave background (CMB) anisotropy power spectra. The physics of the primordial recombination problem can be divided into two qualitatively different aspects. On the one hand, a detailed treatment of the non-thermal radiation field in the optically thick Lyman lines is required for an accurate recombination history near the peak of the visibility function. On the other hand, stimulated recombinations and out-of equilibrium effects are important at late times and a multilevel calculation is required to correctly compute the low-redshift end of the ionization history. Another facet of the problem is the requirement of computational efficiency, as a large number of recombination histories must be evaluated in Markov chains when analyzing CMB data. In this thesis, an effective multilevel atom method is presented, that speeds up multilevel atom computations by more than 5 orders of magnitude. The impact of previously ignored radiative transfer effects is quantified, and explicitly shown to be negligible. Finally, the numerical implementation of a fast and highly accurate primordial recombination code partly written by the author is described.

The second part of this thesis is devoted to one of the potential galactic foregrounds for CMB experiments: the rotational emission from small dust grains. The rotational state of dust grains is described, first classically, and assuming that grains are rotating about their axis of greatest inertia. This assumption is then lifted, and a quantum-mechanical calculation is presented for disk-like grains with a randomized nutation state. In both cases, the probability distribution for the total grain angular momentum is computed with a Fokker-Planck equation, and the resulting emissivity is evaluated, as a function of environmental parameters. These computations are implemented in a public code written by the author.

Contents

Acknowledgements **iv**

Abstract **vii**

List of Figures **xiv**

List of Tables **xvi**

1 General introduction and summary **1**

I Primordial hydrogen recombination **4**

2 Introduction **5**

2.1 Motivations: an improved prediction for CMB anisotropy 5

2.2 Hydrogen recombination: overview 9

2.2.1 The effective three-level atom model 9

2.2.2 Hydrogen recombination phenomenology 14

2.2.3 Validity of the assumptions made 15

2.3 Outline of Part I 18

3 Effective multilevel atom method for primordial hydrogen recombination **19**

3.1 Introduction 19

3.2 Network of bound-bound and bound-free transitions 21

3.2.1 Recombination to and photoionization from the excited states 21

3.2.2 Transitions between excited states 22

3.2.3 Transitions to the ground state 22

3.3 The standard multilevel atom method 23

3.4 New method of solution: the effective multilevel atom 24

3.4.1 Motivations and general formulation 25

3.4.2 Equivalence with the standard MLA method 28

3.4.3 Choice of interface states . . . 31
3.4.4 Further simplification: the effective four-level atom . . . 32
3.5 Implementation and results . . . 36
3.5.1 Computation of the effective rates . . . 36
3.5.2 Ultrafast EMLA code . . . 38
3.5.3 Results and code comparison . . . 38
3.6 Conclusions and future directions . . . 40
3.A Appendix: Proofs of relations involving effective rates . . . 42
3.A.1 Preliminaries . . . 42
3.A.2 Invertibility of the system defining the P_K^i, P_K^e . . . 42
3.A.3 Proof of the complementarity relation $\sum_i P_K^i + P_K^e = 1$ . . . 43
3.A.4 Detailed balance relations . . . 44
3.A.5 Proof of Eq. (3.51) . . . 45
3.A.6 Expression of X_K in terms of x_i, x_e . . . 45
3.B Appendix: Computation of the effective rates . . . 46
3.B.1 Sparse matrix technique for the evaluation of the P_K^i . . . 46
3.B.2 Extrapolation of the effective rates to $n_{\max} = \infty$ . . . 47

4 Radiative transfer effects in primordial hydrogen recombination 48
4.1 Introduction . . . 48
4.2 Radiative transfer in the Lyman lines . . . 49
4.2.1 Basic notation . . . 49
4.2.2 Line processes . . . 50
4.2.2.1 True absorption and emission . . . 51
4.2.2.2 Coherent scattering . . . 53
4.2.2.3 The radiative transfer equation . . . 54
4.2.3 Net decay rate in the Lyman-n line . . . 57
4.2.4 The Sobolev approximation . . . 58
4.3 The Lyman alpha line . . . 59
4.3.1 Thomson scattering in Lyman-α . . . 60
4.3.2 Interaction with the Deuterium Lyman-α line . . . 63
4.3.2.1 Motivations . . . 63
4.3.2.2 Spectral distortions caused by deuterium . . . 64
4.3.2.3 Analytic estimate for the number of spectral distortion photons . . . 65
4.4 Higher-order, non-overlapping Lyman lines ($2 \leq n \lesssim 23$) . . . 69
4.4.1 List of efficient Lyman transitions . . . 69

4.4.2 Resonant scattering in the low-lying Lyman lines . . . 70
4.5 Overlap of the high-lying Lyman lines ($n \gtrsim 24$) . . . 71
4.5.1 Motivations . . . 71
4.5.2 Photoionization and recombination from and to the ground state . . . 73
4.5.3 The radiative transfer equation in the presence of multiple overlapping lines, and photoionization and recombination from and to the ground state . . . 74
4.5.4 Generalized escape probability formalism . . . 76
4.5.4.1 Preliminaries . . . 76
4.5.4.2 Interline transition probabilities . . . 77
4.5.4.3 Net decay rate in the Ly-i transition . . . 78
4.5.4.4 Net rate of recombinations to the ground state . . . 79
4.5.4.5 Rate of change of the ground state population . . . 80
4.5.5 Evaluation of the overlap-induced transition rates . . . 81
4.5.6 Results . . . 83
4.6 Population inversion . . . 84
4.7 Conclusions . . . 84
4.A Appendix: Notation used in this chapter . . . 86
4.B Appendix: Resonant scattering in a Doppler core dominated line . . . 88
4.B.1 The radiative transfer equation in the presence of partial frequency redistribution 88
4.B.2 Escape probability . . . 90
4.B.3 Hermite polynomial expansion of the scattering kernel . . . 91
4.B.4 Solution of the steady-state radiative transfer equation with scattering . . . 93

5 A fast and highly accurate primordial hydrogen recombination code 97
5.1 Introduction . . . 97
5.2 Two-photon processes: formal description . . . 98
5.2.1 Overview . . . 98
5.2.2 Two-photon decays and Raman scattering . . . 99
5.2.3 Resonant scattering in Lyman-α . . . 100
5.2.4 The radiative transfer equation . . . 102
5.2.5 Inclusion in the effective multilevel atom rate equations . . . 102
5.2.5.1 Formal two-photon decay rates . . . 102
5.2.5.2 Decomposition into "1+1" transitions and non-resonant contributions 102
5.2.5.3 "1+1" Resonant contribution . . . 103
5.2.5.4 "Pure two-photon" non-resonant contribution . . . 105
5.3 Numerical solution of the radiative transfer equation . . . 105

5.3.1 Discretization of the radiative transfer equation . . . 105
5.3.2 Solution of the discretized radiative transfer equation . . . 107
5.3.3 Populations of the excited states . . . 109
5.3.4 Evolution of the coupled system of level populations and radiation field . . . 110
5.3.5 Implementation, convergence tests and results . . . 111
5.4 Conclusions . . . 113
5.A Appendix: Numerical integration of the recombination ODE . . . 116
5.A.1 Post-Saha expansion at early phases of hydrogen recombination . . . 116
5.A.2 Explicit numerical integration at later times . . . 116
5.B Appendix: Stable numerical radiative transfer equations . . . 117

6 Prospects for detection of heavy elements present at the epoch of primordial recombination 118
6.1 Introduction . . . 118
6.2 Effect of neutral metals on the Lyman-α decay rate . . . 120
6.2.1 Continuum opacity in Lyα due to photoionization of neutral metals . . . 120
6.2.2 Ionization state of metals and results . . . 122
6.3 The Bowen resonance-fluorescence mechanism for oxygen . . . 123
6.4 Additional free electrons due to ionized metals . . . 126
6.5 Conclusions . . . 126

II Spinning dust radiation 128

7 Introduction 129
7.1 Motivations . . . 129
7.2 Outline of Part II . . . 130

8 A refined model for spinning dust radiation 132
8.1 Introduction . . . 132
8.2 Electric dipole radiation . . . 133
8.3 Dust grain properties . . . 134
8.3.1 Grain shapes . . . 134
8.3.2 Size distribution . . . 134
8.3.3 Dipole moments . . . 136
8.3.4 Grain charge . . . 137
8.4 The Fokker-Planck equation . . . 137
8.4.1 Form of the equation in spherical polar coordinates . . . 137

8.4.2 Normalized damping and excitation coefficients . . . 140
8.5 Collisional damping and excitation . . . 141
8.5.1 General considerations: spherical grain . . . 142
8.5.1.1 Computation of P_{esc} . . . 143
8.5.1.2 Computation of $K(\theta)$ . . . 143
8.5.1.3 Damping and excitation rates . . . 144
8.5.1.4 Evaporation temperature T_{ev} . . . 145
8.5.2 Collision with neutral H atoms: neutral grain, general grain shape . . . 148
8.5.3 Collisions with neutral atoms: charged grains . . . 149
8.5.4 Collisions with ions: charged grains . . . 150
8.5.5 Collisions with ions, neutral grain . . . 153
8.6 Plasma drag . . . 156
8.6.1 Charged grain . . . 156
8.6.2 Neutral grain . . . 160
8.7 Infrared emission . . . 163
8.8 Photoelectric emission . . . 166
8.9 Random H_2 formation . . . 167
8.10 Resulting emissivity and effect of various parameters . . . 168
8.10.1 General shape of the rotational distribution function . . . 168
8.10.2 Emissivity . . . 170
8.10.3 Effect of the intrinsic dipole moment . . . 171
8.10.4 Effect of number density . . . 173
8.10.5 Effect of the gas temperature . . . 175
8.10.6 Effect of the radiation field intensity . . . 176
8.10.7 Effect of the ionization fraction . . . 177
8.10.8 Concluding remarks . . . 178
8.11 Conclusion . . . 178
8.A Appendix: numerical evaluation of $\mathcal{I}(\frac{\omega b}{v}, e, Z_g)$ . . . 183
8.A.1 Positively charged grains . . . 183
8.A.2 Negatively charged grains . . . 183

9 Spinning and wobbling dust: Quantum-mechanical treatment 185

9.1 Introduction . . . 185
9.2 Rotation of a disk-like grain . . . 185
9.2.1 General description . . . 186
9.2.2 Rotational configuration . . . 186

9.2.3 Angular momentum distribution . . . 188
9.2.4 Form of the principle of detailed balance . . . 188
9.3 Quantum mechanical expressions for spontaneous transition rates . . . 190
9.3.1 Transition frequencies . . . 190
9.3.2 Decay rates . . . 190
9.4 Electric dipole emission and radiative damping . . . 192
9.4.1 Spontaneous decay rates . . . 193
9.4.2 Radiated power . . . 193
9.4.3 Radiation-reaction torque with a nonzero CMB temperature . . . 195
9.5 Plasma excitation and drag . . . 199
9.6 Infrared excitation and damping . . . 203
9.7 Collisions . . . 206
9.8 Results . . . 206
9.8.1 Angular momentum distribution . . . 206
9.8.2 Change in emissivity . . . 209
9.8.3 Sensitivity to dipole moment orientation . . . 209
9.9 Discussion . . . 211
9.A Appendix: Evaluation of the plasma excitation and drag coefficients . . . 215

Bibliography **216**

List of Figures

2.1 Rates of Lyman-α decays and two-photon decays as a function of redshift 13
2.2 Peebles C-factor and population of the first excited state during hydrogen recombination 14

3.1 Schematic representation of the effective multilevel atom method 26
3.2 Schematic representation of the simplified effective multilevel atom method 35
3.3 "Exact fudge factor", $\mathcal{A}_{\rm B}(T_{\rm m}, T_{\rm r})/\alpha_{\rm B}(T_{\rm m})$ as a function of redshift 37
3.4 Fraction of effective recombinations that lead to the $2s$ state 37
3.5 Recombination histories for several maximum number of shells $n_{\rm max}$, up $n_{\rm max} = 500$. 39
3.6 A comparison of our ultrafast code to RecSparse 40
3.7 Effect of accounting for high-n transitions on the recombination history 41

4.1 Characteristic widths $\mathcal{W}$ and $\mathcal{S}$ for the Lyman-α line as a function of redshift 57
4.2 Characteristic strength and region of influence of Thomson scattering in Lyman-α . . 61
4.3 Changes to the recombination history due to Thomson scattering. Figure provided by Christopher Hirata. 63
4.4 Schematic representation of the deuterium problem 69
4.5 Number of distortion photons per deuterium atom 70
4.6 Effect of feedback between Lyman lines on the recombination history 70
4.7 Differential optical depth in the overlapping high-lying Lyman lines 81
4.8 Decrease in the escape probability due to partial frequency redistribution 95
4.9 Normalized photon occupation number as a function of frequency 96

5.1 Sparsity pattern of the matrix equations solved by HyRec 110
5.2 Changes in the recombination history due to two-photon decays and Raman scattering 113
5.3 Changes in the recombination history due to frequency diffusion in Lyman-α 114
5.4 Comparison of HyRec to other recombination codes with radiative transfer 114

6.1 Neutral fraction of beryllium, boron and silicon as a function of redshift 124
6.2 Minimum abundance of metals required to affect radiative transfer in Lyman-α 124

8.1 Effect of assumptions on grain shape on the spinning dust spectrum 135
8.2 Evaporation temperature as a function of grain size 146
8.3 Effect of the evaporation temperature model on the spinning dust spectrum 147
8.4 Normalized damping and excitation rates for collisions of a neutral grain with ions . . 155
8.5 Contour levels of the function $\mathcal{I}(\frac{\omega b}{v}, e, Z_g)$ used in the plasma drag calculation 161
8.6 Normalized rotational excitation rate due to interactions with the plasma 163
8.7 Infrared emission damping and excitation coefficients in CNM conditions 166
8.8 Rotational distribution function for a grain radius $a = 7$ Å, in CNM conditions 169
8.9 Characteristic rotation rate as a function of grain radius for CNM conditions 171
8.10 Power radiated by one grain of radius $a = 3.5$ Å in CNM conditions 172
8.11 Spinning dust emissivity for CNM environment 172
8.12 Effect of the intrinsic electric dipole moment on spinning dust spectrum 174
8.13 Effect of various environmental parameters on the spinning dust spectrum 179
8.14 Spinning dust spectra for several environmental conditions 180

9.1 Power radiated per unit frequency by a disklike dust grain, for a given $\Omega = \hbar J/I_3$ . . 196
9.2 Dimensionless plasma excitation and drag coefficients, for $N_{\rm C} = 54$ in the WIM 203
9.3 Probability distribution function for the parameter $\Omega = L/I_3$ for a 5 Å grain 207
9.4 Power radiated by a grain of radius $a = 5$ Å in WIM conditions 208
9.5 Spinning dust emissivity in WIM environment. 208
9.6 Spinning dust spectra for several environments, accounting for grain wobbling 210
9.7 Effect of the ratio of in-plane to total dipole moment on the peak frequency 212
9.8 Effect of the ratio of in-plane to total dipole moment on the total power 213

List of Tables

4.1 Notation used in Chapter 4 86

9.1 Characteristic timescales for UV photons absorption and rotational damping for idealized interstellar phases 187

Chapter 1

General introduction and summary

This thesis treats two seemingly very different topics: the recombination of the primordial plasma when the Universe was about 400,000 years old and composed almost exclusively of hydrogen and helium, and the physics of rotation of dust grains (or complex molecules) in the interstellar medium (ISM) today, 13.6 billion years after the Big Bang. These two subjects, however, share several common points, besides being interesting physics problems.

First, from a cosmologist point of view, both studies are motivated by improving our predictions and measurements of the cosmic microwave background (CMB) anisotropy. After its serendipitous discovery by Penzias and Wilson in 1965 [1, 2], the CMB became one of the cornerstones of the hot Big Bang model. The measurement of its tiny anisotropies to greater and greater accuracy, starting with COBE[1] and culminating with the WMAP mission[2], propelled cosmology into the era of high-precision. A standard cosmological model is now firmly established, and its free parameters are measured to an excellent accuracy: the Universe is filled with a black-body radiation with temperature $T_0 = 2.73$ K [3], it is nearly spatially flat, and its energy content is shared between the rest-mass of standard "baryonic" matter (about 5%), a dark matter component (about 23%) that only interacts gravitationally, and a mysterious "dark energy" component (about 72%) that has a negative pressure and causes today's acceleration of the universal expansion [4]. Moreover, the Universe is believed to have undergone a period of inflation soon after the Big Bang, during which density perturbations were seeded with a nearly scale-invariant power spectrum, the imprint of which is visible in the CMB anisotropy power spectrum.

So what would we gain from measuring the parameters of the standard model to yet another decimal place? Part of the answer lies in the very denomination of the majority of the components of the present Universe, which remain dark areas of our knowledge. Whereas a few particle candidates for dark matter have been suggested, our understanding of dark energy remains rudimentary. This component remains best described by a simple — maybe too simple — cosmological constant, the

[1] http://lambda.gsfc.nasa.gov/product/cobe/
[2] http://lambda.gsfc.nasa.gov/product/map/current/

value of which is uncomfortably low compared to what can be obtained from a naive dimensional analysis estimate. Inflation is another mostly unknown part of the Universe's history, and a plethora of models exist that do fit the current data, strengthening the case for their general features, but allowing for a large variety of possible scenarios. More accurate CMB data will help measure *qualitative* features that cannot be currently detected, or, in other words, measure additional parameters of an extended standard cosmological model, such as an evolving equation of state for dark energy, or a running spectral index for the primordial power spectrum. Such measurements will help theorists to better understand the fundamental physical processes that underlie dark energy and inflation.

With these motivations, ESA's *Planck* mission[3] has started measuring the CMB anisotropy to an unprecedented accuracy. In fact, *Planck*'s sensitivity is so high that theoretical predictions need to be made more accurate so that their errors do not lead to a biased interpretation of the data [5]. This theoretical accuracy requirement is what motivates the first part of this thesis, concerned with improving the computation of the primordial recombination history, on which the predicted CMB anisotropy depends critically. The drawback of a higher accuracy is in general an increased computational burden. An important contribution of this thesis is to introduce a method that greatly simplifies the most computationally expensive aspect of the recombination problem, without any approximation. The final product of this work is a highly accurate and fast primordial recombination code, HyRec[4], co-written by the author and C. Hirata, which will hopefully be used for future CMB data analysis.

Whereas the first part of this thesis deals, to some extent, with the cosmological *signal*, the second part is concerned with one of the potential *noise* sources that may hinder its detection. Electric dipole radiation from spinning dust grains (most likely, Polycyclic Aromatic Hydrocarbons or PAHs) is a possible mechanism for the "anomalous microwave emission" (AME) that seems omnipresent in our Galaxy (a statement which has recently been strengthened by *Planck*'s early results [6]). Some foreground removal methods require the knowledge of the spectral characteristics of Galactic foregrounds, and it is therefore important to understand them as precisely as possible. The second part of this thesis revisits the theory of spinning dust radiation, first introduced by Draine & Lazarian [7, 8] as a candidate for the AME. Here also, the final product is a public code, SpDust[5], that has very recently been used by the *Planck* team to test the spinning dust hypothesis with the first data release.

In addition to their motivations form a cosmologist point of view, the two subjects treated in the remainder of this thesis share very similar characteristics and make use of a common set of physics tools. First, in both cases, we are dealing with similar physical environments: partially ionized gases with densities of a few tenths to a few thousands particles per cubic centimeter and temperatures of a

[3] http://www.esa.int/SPECIALS/Planck/index.html
[4] HyRec is available for download at http://www.tapir.caltech.edu/∼yacine/hyrec/hyrec.html
[5] SpDust is available for download at http://www.tapir.caltech.edu/∼yacine/spdust/spdust.html

few tens to a few thousands of Kelvins. Both the primordial plasma and the ISM are mostly composed of hydrogen and helium. However, the metal-enriched ISM allows for more complex physics (with the drawback that one can compute fewer things from first principles), in particular the physics of dust grains. Both environments, due to their extremely low densities, are out of equilibrium, which leads to non-thermal distributions — whether it is for the population of excited states in hydrogen atoms or dust grains, or the radiation field generated by hydrogen recombination or dust grain transitions. A very important physicist's tool, the fluctuation-dissipation theorem, or the principle of detailed balance (both arise from the same microscopic physics), is used repeatedly throughout this work. In both studies, we will come across some basic radiative transfer calculations, in homogeneous and isotropic media, as well as elementary quantum mechanical problems. We believe that the topics treated in this thesis are not only interesting for their cosmological implications, but also for the richness of the physical processes involved, which however remain simple enough that relatively robust predictions can be made from first principle calculations.

The remainder of this thesis is organized as follows. Part I studies the recombination of the primordial electron-proton plasma. We first motivate the study and review the the basics of cosmological recombination in Chapter 2. Chapter 3 describes the effective multilevel atom method that alleviates the computational burden associated with the highly excited states of hydrogen. Chapter 4 considers radiative transfer effects in primordial hydrogen recombination. Two-photon processes and the numerical method of solution for the radiative transfer equation used in HyRec are presented in Chapter 5. Finally, Chapter 6 assesses whether the high-sensitivity of *Planck* to the recombination history can be used to constrain the abundance of heavy elements at the surface of last scatter. Part II is devoted to improving Draine & Lazarian's model for spinning dust radiation. In Chapter 8, we revisit their classical computations for a grain rotating around its axis of greatest inertia. Finally, Chapter 9 contains the largest portion of unpublished work. There, we treat the rotation of dust grains quantum-mechanically, and study the effect of rotation around a non-principal axis of inertia.

Part I

Primordial hydrogen recombination

Chapter 2

Introduction

2.1 Motivations: an improved prediction for CMB anisotropy

The first measurements of the cosmic microwave background (CMB) spectrum [9] and temperature anisotropies [10] changed cosmology from a qualitative to a robust and predictive science. Since then our picture of the Universe has become more and more accurate. Observations of high-redshift type Ia supernovae [11, 12] have made it clear that nearly three fourths of the energy budget of our Universe is a non-clustering "dark energy" fluid with a negative pressure. In the last decade, the measurements of the temperature and polarization anisotropies in the CMB by the Wilkinson Microwave Anisotropy Probe (WMAP) [4] have confirmed this picture and propelled cosmology into the era of high precision. Combined with other CMB measurements (for example, BOOMERANG [13], CBI [14], ACBAR [15], QUaD [16]) and large-scale structure surveys (2dF [17], SDSS [18]), WMAP results have firmly established the ΛCDM model as the standard picture of our Universe.

What has also emerged from this high-precision data is our ignorance of the large majority of the constituents of the Universe. Only $\sim 5\%$ of our Universe is in the form of known matter (most of which is not luminous), the rest is in the form of an unknown clustering "dark matter" ($\sim 23\%$) or the even more disconcerting "dark energy" ($\sim 72\%$). In addition, it is now widely believed that the Universe underwent an *inflationary* phase early on that sourced the nearly scale-invariant primordial density perturbations, which led to the large-scale structure we observe today. Inflation requires non-standard physics, and at present there is no consensus on the mechanism that made the Universe inflate, and only few constraints on the numerous inflationary models are available from observations.

The *Planck* satellite, launched in May 2009, will measure the power spectrum of temperature anisotropies in the CMB, $C_\ell^{\rm TT}$, with a sub-percent accuracy, up to multipole moments $\ell \sim 2500$ [19, 20]. It will also measure the power spectrum of E-mode polarization anisotropies up to $\ell \sim 1500$. With this unprecedented ultra-high-precision data, cosmologists will be in a position to infer cosmological parameters accurate to the sub-percent level. The high resolution of *Planck* observations

will provide a lever arm to precisely measure the spectral index of scalar density perturbations $n_{\rm S}$ and their running $\alpha_{\rm S}$, therefore usefully constraining models of inflation. The polarization data will help break degeneracies of cosmological parameters with the optical depth to the surface of last scattering τ, giving us a better handle on the epoch of reionization. This wealth of upcoming high-precision data from *Planck*, as well as that from ongoing experiments (ACT [21], SPT [22]) or possible future space-based polarization missions (CMBPol [23]), can be fully exploited only if our theoretical predictions of CMB anisotropies are at least as accurate as the data.

The physics of CMB anisotropy generation is now well understood, and public Boltzmann codes are available (CMBFast [24], CAMB [25], CMBEasy [26]), which evolve the linear equations of matter and radiation perturbations and output highly accurate CMB temperature and polarization angular power spectra, for a given ionization history [27]. The dominant source of systematic uncertainty in the predicted C_ℓs is the recombination history [5]. Not only the peak and width of the visibility function are important, but the precise shape of its tails is also critical at the sub-percent level of accuracy, in particular for the Silk damping tail [28] of the anisotropy power spectrum (for a quick overview of these concepts, see Box 1 below). This has motivated Seager et al. [29, 30] to revise the seminal work of Peebles [31] and Zeldovich et al. [32] and extend their effective three-level atom model to a multilevel atom (MLA) calculation. Their recombination code, RecFast, is accurate to the percent level, and is a part of the Boltzmann codes routinely used for current day CMB data analysis. While sufficiently accurate for WMAP data, RecFast does not satisfy the level of accuracy required by *Planck* [33, 34].

In the last few years, significant work has been devoted to further understanding the rich physics of cosmological hydrogen recombination. On the one hand, accurate recombination histories need to account for as large a number as possible of excited states of hydrogen. This is particularly important at late times, $z \lesssim 800$–900, when the free electron abundance becomes very low and the slow recombinations to the excited states become the "bottleneck" of the recombination process. In these conditions, it is important to precisely account for all possible recombination pathways by including a large number of excited states in MLA calculations. Since the recombination rates strongly depend on the angular momentum quantum number l, an accurate code must resolve the angular momentum substates [35, 36] and lift the statistical equilibrium assumption previously made. The standard MLA approach requires solving for the population of all the excited states accounted for, which is computationally expensive and has limited recent high-n computations [37, 38] to only a few points in parameter space. Recently, we have introduced a new effective MLA (EMLA) method [39], which makes it possible to account for virtually infinitely many excited states, while preserving the computational efficiency of a simple few-level atom model. The EMLA approach consists in factoring the effect of the "interior" excited states (states which are not connected to the ground state) into effective recombination and photoionization coefficients and bound bound transition rates

for the small number of "interface" states radiatively connected to the ground state, i.e., $2s, 2p$ and the low-lying p states.

Another important aspect of the recombination problem is that of radiative transfer in the vicinity of the Lyman lines, in particular Lyman-α. In its early stages, hydrogen recombination is mostly controlled by the slow escape (via redshifting) of photons from the Lyman-α line and the rate of two-photon decays from the $2s$ state. Accurate values for these rates require treatments of the radiation field that go beyond the simple Sobolev approximation [29, 40]. Important corrections include feedback from higher-order lines [41, 42], time-dependent effects in Ly-α [43], and frequency diffusion due to resonant scattering [44, 45, 46]. An accurate $2s-1s$ two-photon decay rate also requires following the radiation field to account for stimulated decays [47] and absorption of non-thermal photons [48, 49]. Dubrovich & Grachev [50] suggested that two-photon transitions from higher levels may have a significant effect on the recombination history. Later computations confirmed this idea [51], and provided an accurate treatment of radiative transfer in the presence of two-photon transitions, as well as a solution for the double-counting problem (which arises for resonant two-photon transitions, already included in the one-photon treatment as "1+1" transitions) [49, 52].

The accuracy requirement is less stringent for primordial helium recombination, as it is completed by $z \sim 1700$, much earlier than the peak of the visibility function. Corrections at the percent level are still important, and several works have been devoted to the problem [53, 54, 5, 29, 50, 55, 56, 57, 58, 59, 60]. The most important effect is continuum opacity in the He I $2^1P^o - 1^1S$ line due to photoionization of neutral hydrogen, which requires a detailed radiative transfer analysis [55, 56, 59]. The inclusion of the intercombination line He I] $2^3P^o - 1^1S$ is also significant.

Several other processes have been investigated and shown not to be significant for CMB anisotropies, for example the effects of the isotopes D and ^{3}He [58, 42, 40], lithium recombination [61], quadrupole transitions [37], high-order Lyman line overlap [40], and Thomson scattering [46, 40]. Collisional processes are negligible for helium recombination [58]; for hydrogen recombination, collisional corrections appear to be small [38], but whether they are truly negligible is still under investigation.

After a decade of being placed under scrutiny, primordial recombination now seems to be understood to a sufficient level of accuracy for *Planck* data analysis (with the possible exception of the effect of collisional transitions). The final goal of all these studies, and one of the main thrusts of this thesis, is to provide a recombination model including all the important physics, and implement it in a complete and fast recombination code. In the first part of this thesis, we present our contributions to the detailed recombination theory that has emerged from this series of works and describe the computational methods used in the implementation of HyRec, a fast and highly accurate primordial hydrogen and helium recombination code. We will only discuss the physics of hydrogen recombination and refer the reader to Refs. [56, 62] and references therein for an account of helium recombination physics.

Box 1: The visibility function and Silk damping

Changes in the recombination history $x_e(z)$ affect the CMB anisotropy in two ways: through the visibility function and Silk damping. We only give a brief explanation of these concepts here, and refer the interested reader to standard cosmology textbooks for a more complete treatment, for example Ref. [63].

• The visibility function

The optical depth for Thomson scattering (cross-section $\sigma_{\rm T}$) between the time t and today (time t_0) is

$$\tau = \int_t^{t_0} n_e(t') c\sigma_{\rm T} {\rm d}t' = \int_0^z \frac{n_e(z')c\sigma_{\rm T}}{H(z')} \frac{{\rm d}z'}{1+z'}. \tag{2.1}$$

The probability for a photon to be scattered while traveling through an infinitesimal optical depth ${\rm d}\tau$ is just ${\rm d}\tau$. And the probability of survival (i.e., non-scattering) of a photon while traveling through a finite optical depth τ is ${\rm e}^{-\tau}$. Therefore, the probability that a photon was *last scattered* in the interval $[\tau, \tau + {\rm d}\tau]$ is ${\rm e}^{-\tau}{\rm d}\tau$. The *visibility function* is the probability distribution for last scattering of photons in redshift domain:

$$g(z) \equiv {\rm e}^{-\tau(z)} \frac{{\rm d}\tau}{{\rm d}z} = \frac{n_e(z)c\sigma_{\rm T}}{(1+z)H(z)} {\rm e}^{-\tau(z)}. \tag{2.2}$$

We plot the visibility function in the left panel below. It peaks at $z \approx 1080$ and has a long low-redshift "tail", which is also important for high-precision CMB measurements. As an example, a correct MLA treatment (Chapter 3) lowers $g(z)$ at low-z in comparison to Peebles' model (Section 2.2.1). This leads to an enhanced predicted CMB anisotropy as photons are less rescattered at low redshifts.

• Silk damping

Prior to their last scattering at redshift $z_{\rm rec} \approx 1080$, photons go through a random walk as they scatter off free electrons. At redshift $z > z_{\rm rec}$, their mean free path is (in physical length)

$$L_{\rm mfp}(z) \approx \frac{1}{n_e(z)\sigma_{\rm T}}. \tag{2.3}$$

The variance of the *comoving* length travelled prior to last scattering is then

$$\lambda_{\rm D}^2 \equiv \langle \Delta x^2 \rangle \approx \int_0^{t_{\rm rec}} \left(\frac{L_{\rm mfp}(z)}{a} \right)^2 \frac{c{\rm d}t}{L_{\rm mfp}(z)} = \int_{z_{\rm rec}}^{\infty} \frac{c(1+z){\rm d}z}{H(z) n_e(z) \sigma_{\rm T}}. \tag{2.4}$$

Any perturbation with wavelength $\lambda \lesssim \lambda_{\rm D}$ is therefore damped (photons from hot spots and cool spots can efficiently mix before last scattering). For the standard cosmology, we find $\lambda_{\rm D} \sim 20$ Mpc with the simple estimate (2.4). A more accurate treatment would give a ~ 3 times larger length, which subtends an angle of $\sim 10'$. We can see on the plot below (right panel; adapted from Fig. 2.8 of Ref. [19]) that anisotropies are indeed exponentially damped for multipole moments $\ell \gtrsim \ell_{\rm D} \sim 1000$.

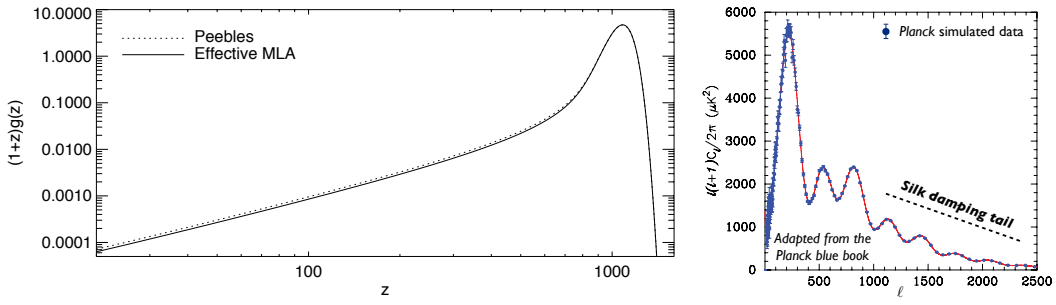

2.2 Hydrogen recombination: overview

2.2.1 The effective three-level atom model

The main quantity of interest in the first part of this thesis is the free electron fraction as a function of redshift, $x_e(z) \equiv n_e/n_{\rm H}$, where n_e and $n_{\rm H}$ are the number densities of free electrons and hydrogen (neutral and ionized), respectively. One might naively expect that recombination proceeds in Saha equilibrium, $x_e = x_e^{\rm S}(n_{\rm H}, T_{\rm r})$, where the Saha equilibrium free electron fraction is the solution of

$$\frac{(x_e^{\rm S})^2}{1-x_e^{\rm S}} = \frac{(2\pi\mu_e T_{\rm r})^{3/2}}{h^3 n_{\rm H}} \exp\left(-E_I/T_{\rm r}\right) = g_e \exp\left(-E_I/T_{\rm r}\right), \tag{2.5}$$

where $E_I = 13.6$ eV is the binding energy of atomic hydrogen, μ_e is the reduced mass of the electron-proton system and $T_{\rm r}(z)$ is the radiation temperature. In Eq. (2.5) we have defined the coefficient g_e, to be used repeatedly, as:

$$g_e \equiv \frac{(2\pi\mu_e T_{\rm r})^{3/2}}{h^3 n_{\rm H}}. \tag{2.6}$$

This coefficient can be seen as the degeneracy factor of thermally moving free electrons.

The Saha equilibrium solution, however, implicitly relies on two assumptions: (*i*) the rate of recombinations and photoionizations must be much faster than the rate of cosmological expansion, given by the Hubble factor $H(z)$, and (*ii*) all bound-bound and bound-free transitions must be mediated by blackbody photons. Both assumptions are in fact broken during primordial hydrogen recombination, and recombination proceeds much slower than in Saha equilibrium. As pointed out in Ref. [64], the recombination process is first slowed down by the reabsorption of non-thermal Lyman-α photons, and then by the slow rate of recombinations in the very dilute primordial plasma.

The first detailed calculation of the primordial recombination history was carried out in the seminal papers by Peebles [31] and Zeldovich et al. [32], who established the simple yet insightful theory that we describe below.

Recombination and photoionization processes

We first show that direct recombinations to the ground state are highly inefficient, as they produce photons that can immediately ionize another hydrogen atom. The mean free path of a photon with energy just above the ionization threshold E_I is given by [65]

$$L_{\rm mfp} = \frac{1}{n_{1s}\sigma_{\rm pi}} = \frac{1}{n_{\rm H} x_{1s} \sigma_{\rm pi}}, \tag{2.7}$$

where n_{1s} is the abundance of ground state hydrogen, $x_{1s} \equiv n_{1s}/n_{\rm H}$ and $\sigma_{\rm pi} \approx 6 \times 10^{-18}$ cm^2 is the photoionization cross-section at threshold. The total number density of hydrogen is given by

$$n_{\rm H}(z) = 250 \text{ cm}^{-3} \left(\frac{1+z}{1100}\right)^3 \frac{\Omega_b h^2}{0.022} \frac{1 - Y_{\rm He}}{0.76}, \tag{2.8}$$

where we have normalized the baryon abundance $\Omega_b h^2$ and the helium mass fraction $Y_{\rm He}$ to their current best estimates [4, 66]. Photons just above the ionization threshold are therefore absorbed by neutral hydrogen atoms in a characteristic time

$$t_{\rm abs} = \frac{L_{\rm mfp}}{c} \approx \frac{2 \times 10^4}{x_{1s}} \text{ sec} \left(\frac{1+\text{z}}{1100}\right)^{-3}. \tag{2.9}$$

Therefore, as soon as a tiny fraction of hydrogen has recombined ($x_{1s} \gtrsim 10^{-9}$), ionizing photons are absorbed, or re-absorbed, in a time much shorter than the characteristic expansion time $t_{\rm exp} \sim 300,000$ years, i.e., nearly instantaneously.

Electrons and protons can therefore recombine efficiently only to the excited states of hydrogen. This situation is familiar in the study of the interstellar medium: it is referred to as "case-B" recombination (see e.g. Ref. [67]). Once they have recombined to one of the excited states of hydrogen, electrons "cascade down" to the $n = 2$ shell, on a much shorter timescale than the overall recombination timescale. Recombinations to the excited states nl (with coefficient α_{nl}) can therefore *effectively* be accounted for as recombinations to the $n = 2$ shell with the case-B recombination coefficient,

$$\alpha_{\rm B} \equiv \sum_{n \geq 2} \alpha_{nl}. \tag{2.10}$$

The effective rate of recombinations is then

$$\dot{x}_e\big|_{\rm rec} = -\dot{x}_2\big|_{\rm rec} = -n_{\rm H} x_e^2 \alpha_{\rm B}(T_{\rm m}), \tag{2.11}$$

where $x_2 \equiv n_{{\rm H}(n=2)}/n_{\rm H}$ is the fractional abundance of hydrogen in the first excited state and $T_{\rm m}$ is the matter temperature, locked to the radiation temperature $T_{\rm r}$ by Thomson scattering at most times during recombination. The reverse process, photoionizations from the excited states, must also be accounted for, and has a rate

$$\dot{x}_e\big|_{\rm ion} = \sum_{n \geq 2} x_{nl} \beta_{nl}(T_{\rm r}), \tag{2.12}$$

where x_{nl} is the fractional abundance of hydrogen in the state nl and β_{nl} is the photoionization rate from that state. It depends on the radiation temperature as photoionizations are caused by

blackbody photons, and is related to the corresponding recombination coefficient by detailed balance:

$$\beta_{nl}(T_{\rm r}) = \frac{g_e}{g_l} {\rm e}^{E_n/T_{\rm r}} n_{\rm H} \alpha_{nl}(T_{\rm m} = T_{\rm r}), \tag{2.13}$$

where g_e was defined in Eq. (2.6), $E_n \equiv -E_I/n^2$ is the energy of the n-th shell, and $g_l \equiv 2l+1$ is the degeneracy of the state nl. We can now simplify Eq. (2.12) with the additional assumption that excited states are in Boltzmann equilibrium with the first excited state, i.e.,

$$x_{nl} = x_2 \frac{g_l}{4} \exp\left(\frac{E_2 - E_n}{T_{\rm r}}\right). \tag{2.14}$$

Inserting Eqs. (2.13) and (2.14) into Eq. (2.12), we can rewrite the rate of photoionizations from the excited states (which can effectively be seen as photoionizations from the $n = 2$ state) as

$$\dot{x}_e\big|_{\rm ion} = -\dot{x}_2\big|_{\rm ion} = x_2 \beta_{\rm B}(T_{\rm r}), \tag{2.15}$$

where the effective photoionization rate is related to the case-B recombination coefficient by

$$\beta_{\rm B}(T_{\rm r}) = \frac{g_e}{4} {\rm e}^{E_2/T_{\rm r}} n_{\rm H} \alpha_{\rm B}(T_{\rm m} = T_{\rm r}). \tag{2.16}$$

Transitions to the ground state

Once they have reached the $n = 2$ shell, electrons can reach the ground state by emitting a Lyman-α photon from the $2p$ state. Due to the very high optical depth of the Lyman-α transition, emitted photons will however almost certainly be reabsorbed by another atom. This is similar to the case of ionizing photons which are immediately reabsorbed, but atoms in the $2p$ state have no other option to decay to the ground state, unlike free electrons that can be captured in an excited state, so computing the very small net decay rate is important.

The way out of this Lyman-α "bottleneck" is for photons to redshift below the Lyα resonant frequency due to cosmological expansion. We denote f_ν the photon occupation number at frequency ν [for a blackbody at temperature T, we would have $f_\nu = \left({\rm e}^{h\nu/kT} - 1\right)^{-1}$]. Simple phase-space considerations give us the number of photons per frequency interval per hydrogen atom, $\mathcal{N}_\nu = \frac{8\pi\nu^2}{c^3 n_{\rm H}} f_\nu$. The rate at which photons redshift across a frequency ν due to cosmological expansion, per hydrogen atom, is then given by $H\nu\mathcal{N}_\nu$. The *net* decay rate in the Lyman-α line, per hydrogen atom, is then given by the difference between the rate at which photons produced in the line redshift out of the line and the rate at which photons from the blue side redshift into the line. On the blue side of the line, the photon occupation number can be approximated by a blackbody. Since the

energy of Lyα photons is ~ 40 times larger than $T_{\rm r}$, we have

$$f^{+}_{\nu_{\rm Ly\alpha}} \approx {\rm e}^{-E_{21}/T_{\rm r}}, \tag{2.17}$$

where $E_{21} = E_2 - E_1 = \frac{3}{4}E_I$ is the energy of Lyα photons. The line being optically thick, the photon occupation number equilibrates with the $2p$ to $1s$ ratio, and, just redward of the line, we have

$$f^{-}_{\nu_{\rm Ly\alpha}} = \frac{x_{2p}}{3x_{1s}} = \frac{x_2}{4x_{1s}}, \tag{2.18}$$

where in statistical equilibrium $x_{2p} = \frac{3}{4}x_2$. The net rate of Lyman-α decays is then given by

$$\dot{x}_{1s}\big|_{\rm Ly\alpha} = -\dot{x}_2\big|_{\rm Ly\alpha} = H\nu_{\rm Ly\alpha}\left(\mathcal{N}^{-}_{\nu_{\rm Ly\alpha}} - \mathcal{N}^{+}_{\nu_{\rm Ly\alpha}}\right) = R_{\rm Ly\alpha}\left(\frac{3}{4}x_2 - 3x_{1s}{\rm e}^{-E_{21}/T_{\rm r}}\right), \tag{2.19}$$

where we have defined the rate of escape of Lyα photons per atom in the $2p$ state,

$$R_{\rm Ly\alpha} \equiv \frac{8\pi H}{3n_{\rm H}x_{1s}\lambda^3_{\rm Ly\alpha}}. \tag{2.20}$$

Eqs. (2.19–2.20) can also be derived in the Sobolev approximation, in the limit of large Sobolev optical depth; we will do so in Chapter 4. We show the rate $R_{\rm Ly\alpha}$ as a function of redshift in Fig. 2.1. We see that at all relevant times during primordial recombination, $3R_{\rm Ly\alpha}$ is of the order of a few to a few tens of net decays per second. This extremely slow net Lyman-α decay rate is comparable to the rate of two-photon decays from the $2s$ state, $\Lambda_{2s,1s} \approx 8.22$ s^{-1} [68, 69]. The latter therefore significantly contribute to the recombination dynamics, and should be accounted for as a transition channel from the first excited state to the ground state [31, 32] (in fact, in the late sixties, it was believed that $\Omega_b = 1$ and $R_{\rm Ly\alpha}$ was thought to be even lower; Refs. [31, 32] had therefore concluded that the large majority of decays to the ground state proceeded through two-photon decays; using modern estimates for cosmological parameters, Ref. [70] find that $\sim 57\%$ of ground state hydrogen is formed following a two-photon decay). The net rate of two-photon decays from the $2s$ state is:

$$\dot{x}_{1s}\big|_{2\gamma} = -\dot{x}_2\big|_{2\gamma} = \Lambda_{2s,1s}\left(x_{2s} - x_{1s}{\rm e}^{-E_{21}/T_{\rm r}}\right) = \Lambda_{2s,1s}\left(\frac{x_2}{4} - x_{1s}{\rm e}^{-E_{21}/T_{\rm r}}\right), \tag{2.21}$$

where the second term accounts for two-photon absorptions and can be obtained by a detailed balance argument.

Population of the excited state and recombination rate

We now have all the relevant rates to solve for the free-electron fraction. The last simplification is to realize that the atomic rates, even for the slow $2s \to 1s$ decays or the slow escape out of the

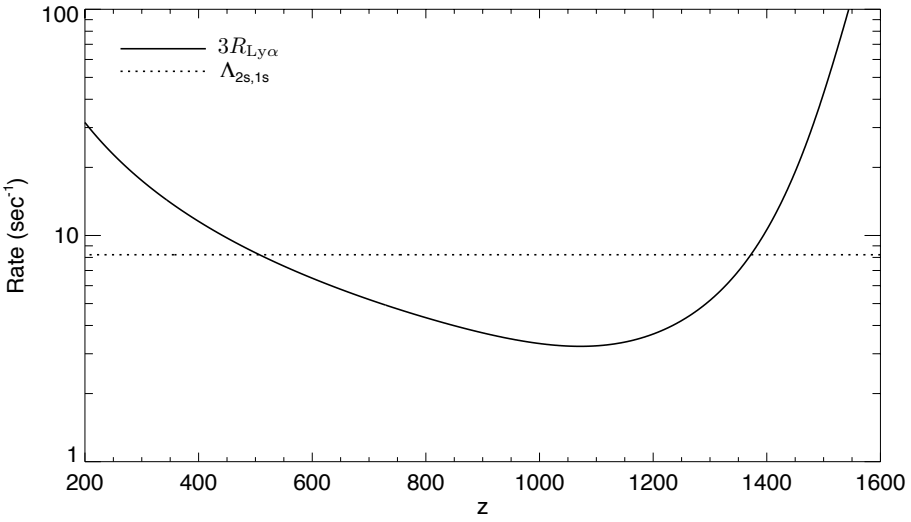

Figure 2.1: Rate of Lyman-α escape per atom in the $2s$ state, $3R_{\rm Ly\alpha}$, where $R_{\rm Ly\alpha}$ is given by Eq. (2.20) (evaluated with the modern value of $\Omega_b h^2$), compared to the spontaneous two-photon decay rate from $2s$, $\Lambda_{2s,1s}$, as a function of redshift, for a standard recombination history.

Lyα resonance, are many orders of magnitude larger than the overall recombination rate, which is of the order of (10 times) the Hubble expansion rate, that is $\sim 10^{-13} - 10^{-12}$ s^{-1}. The population of the $n = 2$ shell can therefore be obtained to high accuracy in the steady-state approximation, i.e., assuming that the net rate of recombinations to the $n = 2$ shell equals the net rate of transitions to the ground state:

$$\dot{x}_2 = \dot{x}_2\big|_{\rm rec} + \dot{x}_2\big|_{\rm ion} + \dot{x}_2\big|_{\rm Ly\alpha} + \dot{x}_2\big|_{2\gamma} \approx 0. \tag{2.22}$$

We can therefore solve for x_2 and obtain:

$$x_2 = 4\frac{n_{\rm H} x_e^2 \alpha_{\rm B} + (3R_{\rm Ly\alpha} + \Lambda_{2s,1s})\, x_{1s} {\rm e}^{-E_{21}/T_{\rm r}}}{4\beta_{\rm B} + 3R_{\rm Ly\alpha} + \Lambda_{2s,1s}}. \tag{2.23}$$

From Eqs. (2.11) and (2.15) we then obtain the rate of change of the free electron fraction:

$$\dot{x}_e = \dot{x}_e\big|_{\rm rec} + \dot{x}_e\big|_{\rm ion} = -C\left(n_{\rm H} x_e^2 \alpha_{\rm B} - 4x_{1s}\beta_{\rm B} {\rm e}^{-E_{21}/T_{\rm r}}\right), \tag{2.24}$$

where the Peebles C-factor is given by

$$C \equiv \frac{3R_{\rm Ly\alpha} + \Lambda_{2s,1s}}{4\beta_{\rm B} + 3R_{\rm Ly\alpha} + \Lambda_{2s,1s}}. \tag{2.25}$$

As noted by Peebles, this factor represents the probability that an atom initially the $n = 2$ shell reaches the ground state before being photoionized. Note that we could have obtained the same equation starting from $\dot{x}_e = -\dot{x}_{1s} = -(\dot{x}_{1s}|_{2p} + \dot{x}_{1s}|_{2s})$ (this is because we have set $\dot{x}_2 = 0$).

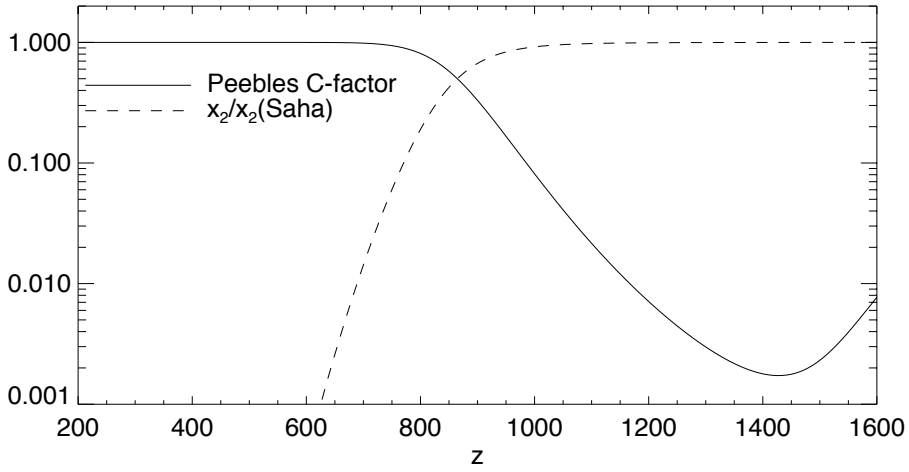

Figure 2.2: Peebles C-factor [Eq. (2.25)] and ratio of the population of the $n = 2$ shell to its value in Saha equilibrium with the continuum, as a function of redshift.

At all relevant times during the epoch of hydrogen recombination, $x_2 \ll 1$, and therefore $x_{1s} = 1 - x_e$. If matter and radiation temperatures are set to be equal, Eq. (2.24) is therefore a simple ordinary differential equation for x_e, that can be easily integrated. A simple improvement is to also explicitly follow the matter temperature evolution, which is determined by the Compton evolution equation:

$$\dot{T}_{\rm m} = -2HT_{\rm m} + \frac{8\sigma_{\rm T} a_{\rm r} T_{\rm r}^4 x_e (T_{\rm r} - T_{\rm m})}{3(1 + f_{\rm He} + x_e) m_e c}, \tag{2.26}$$

where $\sigma_{\rm T}$ is the Thomson cross section, $a_{\rm r}$ is the radiation constant, m_e is the electron mass and $f_{\rm He}$ is the He:H ratio by number of nuclei.

2.2.2 Hydrogen recombination phenomenology

We show in Fig. 2.2 the evolution of the Peebles C-factor and the population of the $n = 2$ shell relative to its value in Saha equilibrium with the continuum, $x_2|_{\rm Saha} \equiv \frac{4}{g_e} {\rm e}^{-E_2/T} x_e^2$. We can see that there are two distinct regimes.

Early times

At early times ($z \gtrsim 900$), electrons in the $n = 2$ shell have a high probability of being photoionized, and the C-factor is much smaller than unity, $C \ll 1$. As a consequence, the population of the $n = 2$ shell is very close to Saha equilibrium with the continuum, as can be seen by rewriting Eq. (2.23) in the form

$$x_2 = (1 - C) \frac{4}{g_e} {\rm e}^{-E_2/T} x_e^2 + C \; 4 x_{1s} {\rm e}^{-E_{21}/T}, \tag{2.27}$$

where we have assumed $T_{\rm r} = T_{\rm m} = T$ and used Eqs. (2.16) and (2.25). During that period, the recombination rate is therefore virtually independent of the exact value of the recombination coefficient, and is entirely determined by the small net decay rate from the $n = 2$ shell to the ground state:

$$\dot{x}_e(z \gtrsim 900) = -\dot{x}_{1s} \approx (3R_{\rm Ly\alpha} + \Lambda_{2s,1s}) \left[\frac{x_2|_{\rm Saha}}{4} - x_{1s}{\rm e}^{-E_{21}/T}\right]. \tag{2.28}$$

The recombination rate is of order $\sim C n_{\rm H} x_e^2 \alpha_{\rm B} \sim 10^{-13}$ sec^{-1} (using Eq. (2.8), $\alpha_{\rm B} \sim 10^{-13}$ cm^{-3} and $C \sim 10^{-2}$), which is of the same order as the Hubble expansion rate. Saha equilibrium with the ground state can therefore not be maintained and the free electron fraction quickly becomes orders of magnitude larger than the Saha equilibrium prediction. Since $x_2 \approx x_2({\rm Saha})$, this means that the excited states becomes over-populated with respect to Boltzmann equilibrium with the ground state. This situation is usually referred to as the "$n = 2$ bottleneck".

Late times

At late times ($z \lesssim 800$), $C \approx 1$, and the $n = 2$ shell is no longer in Saha equilibrium with the continuum (note that it is *not* in Boltzmann equilibrium with the ground state either, as the rate of recombinations to the $n = 2$ shell dominates over the net rate of two-photon or Ly-α absorptions from the ground state). The free electron fraction is now many orders of magnitude above the value it would have in Saha equilibrium. In that case, the second term in Eq. (2.24) is negligible and the evolution of the free electron fraction becomes:

$$\dot{x}_e(z \lesssim 800) \approx -n_{\rm H} x_e^2 \alpha_{\rm B}. \tag{2.29}$$

As we can see, the evolution of the free electron fraction is then virtually independent of the rate of decays to the ground state from the $n = 2$ shell, but is highly sensitive to the exact value of the effective recombination coefficient.

2.2.3 Validity of the assumptions made

The simple yet insightful effective three-level atom model presented in Section 2.2.1 provides a good approximation for the recombination problem and remained essentially unaltered for several decades. However, this simple theory relies on many simplifying assumptions, the validity of which we assess now.

Steady-state approximation for the excited states ✓

The formal way to assess the validity of the steady-state approximation is to compute the eigenvalues of the transition matrix in a multilevel calculation (to be described soon). This was done in Ref. [37],

where it was found that the minimum eigenvalue of the rate matrix is ~ 1 sec^{-1}. This could be expected as the rate of Ly-α decays per atom in the $2p$ state is $R_{\rm Ly\alpha}$, which has a minimum of ~ 1 sec^{-1} at $z \approx 1100$ (see Fig. 2.1). This minimum rate is ~ 12 orders of magnitude larger than the recombination rate. The steady-state approximation was also checked explicitly in Ref. [38] where the solution of the time-dependent problem was computed (i.e., solving coupled ordinary differential equations for x_e and the populations of the excited states). There again, it was found to be very accurate. Note that this approximation also underlies the use of the case-B recombination coefficient, as electrons captured in excited states are assumed to "cascade down" instantaneously to the first excited shell.

Case-B recombination ✓

In the model presented above, we have simply neglected altogether recombinations to the ground state. In reality, there is a small net rate of recombinations to the ground state due to redshifting of photons below the Lyman-continuum threshold, similar to what we described for the Lyman-α line:

$$\dot{x}_e|_{1s,\rm direct} = -\frac{8\pi H}{n_{\rm H}\lambda_{\rm c}^3 x_{1s}}\left[\frac{x_e^2}{g_e} - x_{1s}{\rm e}^{-E_I/T}\right] = \frac{(4/3)^3}{C}\frac{3R_{\rm Ly\alpha}}{4\beta_{\rm B}}{\rm e}^{E_2/T}\dot{x}_e, \tag{2.30}$$

where $\lambda_{\rm c} = \frac{4}{3}\lambda_{\rm Ly\alpha}$ is the wavelength of Lyman-continuum photons at the ionization threshold and we have used Eq. (2.24) for $\dot{x}_e$ on the right-hand-side. We can see already that escape of Lyman-continuum photons is a small correction, due to the term ${\rm e}^{E_2/T} \approx \exp\left[-13\left(\frac{1100}{1+z}\right)\right]$. We checked that adding the rate (2.30) to the recombination rate leads to an acceleration of recombination by a very small amount $|\Delta x_e/x_e| < 7\times 10^{-6}$, in agreement with the results of Ref. [41]. Primordial hydrogen recombination is therefore indeed a case-B recombination, to the level of accuracy required.

Case-B recombination *coefficient* ×

For the first 20 years or so after the first works on primordial recombination, the main improvement that was made (besides using more up-to-date cosmological parameters) was using a more accurate case-B recombination coefficient (see Refs. [71, 5] and references therein). The most accurate fitting formula is given in Ref. [72]. However, the case-B coefficient as defined in Eq. (2.10) does not account for two important aspects:

(i) The bath of blackbody photons cause *stimulated recombinations* [73], which are not accounted for in Eq. (2.10). Stimulated recombinations will speed-up recombination. One cannot simply replace each coefficient $\alpha_{nl}(T_{\rm m})$ by the spontaneous + stimulated recombination coefficient $\alpha_{nl}(T_{\rm m}, T_{\rm r})$ because the sum would be divergent, as the photon occupation number diverges at zero energies (see for example Fig. 4 of Ref. [38]).

(ii) The blackbody photons also *alter the "cascading down"* of captured electrons: an excited

atom may be photoionized before decaying to the first excited state. The sum in Eq. (2.10) should therefore be weighted by the probabilities to actually reach the first excited state.

(*iii*) At late times, when the intensity of the blackbody radiation field decreases, excited states *cannot be maintained in Boltzmann equilibrium* with each other. This is especially true for $2s$ and $2p$, and one should split the case-B recombination coefficient appropriately between the two states.

From the discussion in Section 2.2.2, we can anticipate that these considerations may be important at late times.

Lyman-α escape rate $\times$

The treatment of the Lyman-α presented in Section 2.2.1 is very simplistic: the radiation field is just assumed to be a step function. Since $\sim 43\%$ of recombinations proceed through a Lyman-α decay [70], a more sophisticated radiative transfer calculation is required. Moreover, higher-order Lyman lines also need to be considered. We can anticipate that more accurate calculations of the Ly-α decay rate and decays in the higher-order Lyman lines will affect the peak of the visibility function (see Section 2.2.2).

Two-photon decay rate $\times$

The majority of decays to the ground state proceed through the two-photon channel. The simple expression for decay rate given in Eq. (2.21) does not account for two processes:

(*i*) *Stimulated two-photon decays*, particularly important when one of the two photons has energy of the order of or less than $T_{\rm r}$ [47].

(*ii*) *Absorption of non-thermal photons* emitted in the Lyman-α line [48].

In addition, two-photon decays from higher-order excited states are also important [50]. Since the bulk of these decays are near resonance with a Lyman line (i.e., the higher-energy photon is close to a Lyman frequency), this also requires a radiative transfer treatment. Again, we expect such corrections to be mostly important at early times $z \gtrsim 900$ and affect the peak of the visibility function.

From the above discussion, we see that corrections to the recombination model can be subdivided into two distinct categories:

(*i*) Radiative transfer calculations, mainly in the Lyman-α line, and also in higher-order lines. These calculations must also properly account for two-photon decays from $2s$ and the higher-order states. Corrections to the simple decay rates Eqs. (2.19) and (2.21) are expected to mostly affect the early time recombination history $z \gtrsim 900$. Since the visibility function peaks at $z \approx 1100$, small corrections to the net decay rates may have important consequences on the C_ℓ's and even *a priori* small effects should be considered.

(*ii*) Multilevel atom calculations, that properly account for all transitions between excited states of hydrogen and generalize the effective three-level atom model. Such modifications will mostly affect the low redshift tail of the visibility function, and the accuracy requirement is somewhat lower than for (*i*).

2.3 Outline of Part I

In the remainder of this part, we describe our work on both the radiative transfer and the multilevel aspects of primordial hydrogen recombination. We first consider the late-time corrections due to the multilevel structure of hydrogen. Chapter 3 is devoted to the description of the network of transitions in hydrogen, and to the exposition of the effective multilevel atom method, suggested in Y. Ali-Haïmoud & C. M. Hirata, Phys. Rev. D **82**, 063521 (2010). This method leads to a considerable speedup of multilevel atom recombination computations. Chapter 4 is adapted from Y. Ali-Haïmoud, D. Grin & C. M. Hirata, Phys. Rev. D **82**, 123502 (2010). In this work, we quantify the impact of several previously neglected radiative transfer effects on the recombination history. Chapter 5 describes the implementation of HyRec, a fast and highly accurate recombination code that the author developed with C. Hirata. This chapter is adapted from the first part of Y. Ali-Haïmoud & C. M. Hirata, Phys. Rev. D **83**, 043513 (2011). It does not include C. Hirata's contribution on helium recombination, but the reader is encouraged to read the paper for a description of this equally interesting problem. Finally, Chapter 6 is a reproduction of Y. Ali-Haïmoud, C. M. Hirata & M. Kamionkowski, Phys. Rev. D **83**, 083508 (2011). In this chapter, slightly different from the main line of research developed in the remainder of this part, we consider whether the high sensitivity of future CMB experiments on the recombination history can be used to detect eventual heavy elements present at the epoch of last scatter. All the mentioned published papers are fully or partially reproduced here with permission, copyright (2010, 2011) by the American Physical Society.

Acknowledgements

I would like to thank Christopher Hirata for directing me to work on such an interesting topic, and for his contributions to the research described here. I also thank Marc Kamionkowski for suggesting the study of the effect of heavy elements at the surface of last scatter and his contributions to this work. I have enjoyed discussing and collaborating with Daniel Grin on various aspects of the recombination problem. Finally, I thank the participants of the July 2009 Paris Workshop on Cosmological Recombination, in particular Jens Chluba, for many conversations on primordial hydrogen recombination. Jens Chluba and I are currently running a detailed code comparison of our respective recombination codes, CosmoRec and HyRec, which has unfortunately not yet been completed at the time of submission of this thesis.

Chapter 3

Effective multilevel atom method for primordial hydrogen recombination[1]

3.1 Introduction

We saw in Section 2.2.2 that the effective three-level atom (TLA) model [31, 32] cannot fully capture the effect of the bath of blackbody photons on the recombination process: *stimulated* recombinations must also be accounted for, as well as bound-bound transitions among excited states and photoionizations events that impede some of the "cascading" electrons to reach the first excited states. Such processes will essentially affect the low-redshift tail of the ionization history, but are still important given the sensitivity of upcoming CMB experiments.

One way to account exactly for these processes is to solve simultaneously for the free electron fraction and the populations of all (or at least, a large number of) excited states. This method of solution, which we refer to as the standard multilevel atom (MLA) method, is commonly used in the study of emission lines in the interstellar medium. In fact, it was first used in the context of primordial recombination to compute the spectrum of emitted lines [74, 75]. After it was understood that non-equilibrium of excited states and stimulated recombinations may have an effect on the recombination history itself [5], the first detailed MLA calculations were carried by Seager et al. [29, 30]. In practice, one cannot account for an infinite number of excited states and must impose a cutoff in MLA computations, i.e., discard states with principal quantum number higher than a given $n_{\max}$. Refs. [29, 30] computed recombination histories including up to $n_{\max} = 300$ excited states, assuming that angular momentum substates within a given energy shell are in statistical equilibrium. They

[1] The material in this chapter was mostly adapted from the paper *Ultrafast effective multilevel atom method for primordial hydrogen recombination*, Y. Ali-Haïmoud & C. M. Hirata, Phys. Rev. D **82**, 063521 (2010), with the exception of Section 3.4.4, which is an exerpt from the paper *HyRec: A fast and highly accurate primordial hydrogen recombination code*, Y. Ali-Haïmoud & C. M. Hirata, Phys. Rev. D **83**, 043513 (2011). Reproduced here with permission, copyright (2010, 2011) by the American Physical Society.

found that the residual ionization fraction at low redshift is decreased by approximately 10% with respect to the TLA prediction. It was later shown that the desired sub-percent accuracy can only be reached when explicitly resolving the out-of-equilibrium angular momentum substates [35, 36], which requires the MLA codes to follow $N_{\rm level} = n_{\rm max}(n_{\rm max}+1)/2$ individual states. Moreover, the ordinary differential equations (ODEs) describing the level populations are stiff, requiring the solution of large $N_{\rm level} \times N_{\rm level}$ systems of equations at each integration time step. This problem has been solved by several authors [36, 37, 38]; however, these standard MLA codes take hours to days to compute a single recombination history.

Eventually, it is necessary to be able to produce not only accurate but also *fast* recombination histories, to be included in Markov Chain Monte Carlo (MCMC) codes for cosmological parameter estimation. The MCMC requires CMB power spectra (and hence recombination histories) to be generated at each proposed point in cosmological parameter space, with a typical chain sampling $\mathcal{O}(10^5)$ points [76]. Furthermore, dozens of MCMCs are often run with different combinations of observational constraints and different parameter spaces. This makes it impractical to include recombination codes that run for more than a few seconds in the MCMC. One solution is to precompute recombination histories $x_e(z|H_0, T_{\rm CMB}, \Omega_m h^2, \Omega_b h^2, Y_{\rm He}, N_\nu)$ on a grid of cosmological parameters, and then use elaborate interpolation algorithms to evaluate the recombination history for any cosmology [77], or to construct fitting functions [30, 78]. However, such procedures need to be re-trained every time additional parameters are added, and are rather unsatisfying regarding their physical significance.

In this chapter, we present a new[2], *effective* multilevel atom method (hereafter EMLA), that is a simple generalization of Peebles' TLA model presented in Section 2.2.1, but accounts *exactly* for the multilevel structure of hydrogen, and allows for the inclusion of virtually infinitely many excited states of hydrogen and all relevant bound-bound and bound-free transitions. The improved recombination equations are exactly equivalent to the standard MLA equations, but have the same computational cost as the TLA model (for an equal treatment of radiative transfer), while being much more accurate. The basic idea is that the vast majority of the excited hydrogen levels are populated and depopulated only by *optically thin* radiative transitions (bound-bound and bound-free) in a bath of thermal photons; we show that their effect can be "integrated out" leaving only a few functions of the matter and radiation temperatures $T_{\rm m}$ and $T_{\rm r}$ (this list would include the free electron density n_e if we incorporated collisions), which can be pre-tabulated. These functions are just the generalization of the case-B recombination coefficient. In an actual call to the recombination code from an MCMC, it is then only necessary to solve an *effective* MLA with a smaller number of levels, which eliminates the computationally difficult $N_{\rm level} \times N_{\rm level}$ system solution in the traditional MLA. [The idea is similar in spirit to the line-of-sight integral method for the computation of the

[2]It has recently been brought to my attention that this method was independently suggested by M. S. Burgin [79, 80]. Due to translation delays, this work only became known in the Western world several months after the publication of our paper.

CMB power spectrum [24], which eliminated a large number of independent variables from the cosmological perturbation theory system of ODEs (the high-order moments of the radiation field, Θ_ℓ for $\ell \gg 1$) in favor of pretabulated spherical Bessel functions.] Our method achieves a speed-up of the recombination calculation by 5 to 6 orders of magnitude.

This chapter is organized as follows. In Section 3.2 we review the general picture of hydrogen recombination, and the bound-bound and bound-free transition rates involved in the calculation. In Section 3.3 we describe the standard MLA method. We present our new EMLA method in Section 3.4 and demonstrate its equivalence with the standard MLA formulation. We describe our numerical implementation and results in Section 3.5, and conclude in Section 3.6. Appendix 3.A gives mathematical proofs for various relations satisfied by the effective rates. Appendix 3.B gives the details of our numerical evaluation of the effective rates.

3.2 Network of bound-bound and bound-free transitions

Here we give explicit expressions for the bound-bound and bound-free rates discussed above. Subscripts nl refer to the bound state of principal quantum number n and angular momentum quantum number l. We denote $\alpha_{\rm fs}$ the fine structure constant, $\mu_e \equiv m_e m_p/(m_e + m_p)$ the reduced mass of the electron-proton system, E_I the ionization energy of hydrogen, and $E_n \equiv -E_I n^{-2}$ the energy of the $n^{\rm th}$ shell. Finally, we denote by $f_{\rm BB}(E, T_{\rm r}) \equiv (\mathrm{e}^{E/T_{\rm r}} - 1)^{-1}$ the photon occupation number at energy E in the blackbody radiation field at temperature $T_{\rm r}$.

3.2.1 Recombination to and photoionization from the excited states

We have justified in Section 2.2.3 that direct recombinations to the ground state can be neglected, and we only need to consider recombinations to the excited states. The recombination coefficient to the excited state nl, including stimulated recombinations, is denoted $\alpha_{nl}(T_{\rm m}, T_{\rm r})$ (it has units of cm^3 s^{-1}). The photoionization rate per atom in the state nl is denoted $\beta_{nl}(T_{\rm r})$. Both can be expressed in terms of the bound-free radial matrix elements $g(n, l, \kappa, l')$ [81]. Defining

$$\gamma_{nl}(\kappa) \equiv \frac{2}{3n^2}\alpha_{\rm fs}^3 \frac{E_I}{h}(1 + n^2\kappa^2)^3 \times \sum_{l'=l\pm1} \max(l, l') g(n, l, \kappa, l')^2, \tag{3.1}$$

where κ denotes the momentum of the outgoing electron in units of $\hbar/a_0$ (where a_0 is the reduced-mass Bohr radius), the recombination coefficient is given by [81]:

$$\alpha_{nl}(T_{\rm m}, T_{\rm r}) = \frac{h^3}{(2\pi\mu_e T_m)^{3/2}} \times \int_0^{+\infty} \mathrm{e}^{-E_I\kappa^2/T_{\rm m}} \gamma_{nl}(\kappa) \times \left[1 + f_{\rm BB}\left(E_{\kappa n}, T_{\rm r}\right)\right] \mathrm{d}(\kappa^2), \tag{3.2}$$

where $E_{\kappa n} \equiv E_I(\kappa^2 + n^{-2})$. The photoionization rate only depends on the radiation temperature and can be obtained by detailed balance considerations from the recombination coefficient:

$$\beta_{nl}(T_{\rm r}) = \frac{(2\pi\mu_e T_r)^{3/2}}{(2l+1)h^3} {\rm e}^{E_n/T_{\rm r}} \alpha_{nl}(T_{\rm m} = T_{\rm r}, T_{\rm r}). \tag{3.3}$$

3.2.2 Transitions between excited states

We denote $R_{nl,n'l'}$ the transition rate from the excited state nl to the excited state $n'l'$. It has units of sec^{-1} per atom in the initial state. Transitions among excited states can be either radiative or collisional:

$$R_{nl,n'l'} = R^{\rm rad}_{nl,n'l'}(T_{\rm r}) + R^{\rm coll}_{nl,n'l'}(T_{\rm m}, n_e), \tag{3.4}$$

where $n_e = n_p$ is the abundance of free electrons or free protons. In this work, we follow exclusively the radiative rates. These are given by

$$R^{\rm rad}_{nl,n'l'} = \begin{cases} A_{nl,n'l'} \left[1 + f_{\rm BB}(E_{nn'}, T_{\rm r})\right] & \text{if } E_n > E_{n'} \\ \frac{g_{l'}}{g_l} {\rm e}^{-E_{n'n}/T_{\rm r}} R^{\rm rad}_{n'l',nl} & \text{if } E_n < E_{n'}, \end{cases} \tag{3.5}$$

where $E_{nn'} \equiv E_n - E_{n'}$ is the energy difference between the excited levels, $g_l \equiv 2l + 1$ is the degeneracy of the state nl, and $A_{nl,n'l'}$ is the Einstein A-coefficient for the $nl, n'l'$ transition, which may be obtained from the radial matrix element $R^{nl}_{n'l'}$[82]:

$$A_{nl,n'l'} = \frac{2\pi}{3} \alpha^3_{\rm fs} \frac{E_I}{h} \left(\frac{1}{n'^2} - \frac{1}{n^2}\right)^3 \frac{\max(l, l')}{2l+1} |R^{nl}_{n'l'}|^2. \tag{3.6}$$

An important underlying assumption of Eq. (3.5) is that transitions between excited states are *optically thin*. The maximum Sobolev optical depth (to be defined in Chapter 4) in these transitions is indeed at most 5.5×10^{-4} [49]. The consequence is that bound-bound transitions between excited states only depend on the radiation temperature.

3.2.3 Transitions to the ground state

Transitions to the ground state require a more subtle treatment than optically thin transitions between excited states. Their rates have in general complicated dependences, not only on the radiation temperature but also on cosmology. To remain general, we denote the *net* $i \to 1s$ decay rate in the form

$$\dot{x}_{1s}\big|_i = -\dot{x}_i\big|_{1s} = x_i \tilde{R}_{i,1s} - x_{1s} \tilde{R}_{1s,i}, \tag{3.7}$$

where the notation $\tilde{R}$ is meant to emphasize the complicated (not necessarily analytical) functional form. The equations presented in this chapter are general and can accommodate any particular form

for the $\tilde{R}_{i,1s}$ and $\tilde{R}_{1s,i}$.

In this chapter, we will concentrate on the multilevel aspect and simply consider Lyman transitions (Ly-α and higher-order transitions), and two-photon transitions from $2s$, with the basic treatment given in Section 2.2.1. The generalization of Eq. (2.19) to any optically thick Lyman transition is

$$\dot{x}_{1s}\big|_{np} = -\dot{x}_{np}\big|_{1s} = \frac{8\pi H}{3\lambda_n^3 n_{\rm H} x_{1s}} \left(x_{np} - 3x_{1s} f_{np}^{+}\right), \tag{3.8}$$

where $\lambda_n \equiv hc/E_{n1}$ is the transition wavelength, and f_{np}^{+} is the photon occupation number at the blue side of the corresponding Ly-n line. The simplest assumption is to take $f_{np}^{+} = f_{\rm BB}(E_{n1}, T_{\rm r})$, i.e., assume the incoming radiation on the blue side of the line has a blackbody spectrum. This assumption is actually violated due to feedback from higher-frequency Lyman lines (e.g., radiation escaping from Lyβ can redshift into Lyα) [41, 56, 42]. If no radiative processes affect the radiation field between neighboring Lyman lines, then

$$f_{np}^{+}(z) = f_{n+1,p}^{-}(z'), \tag{3.9}$$

where the earlier redshift z' is given by

$$z' = \frac{\lambda_{{\rm Ly}n}}{\lambda_{{\rm Ly}(n+1)}}(1+z) - 1. \tag{3.10}$$

In the optically thick limit which is valid here, the photon occupation number redward of the Ly-n line is given by $f_{np}^{-} = x_{np}/(3x_{1s})$. We recall that two-photon decays from the $2s$ state are crucial to the recombination dynamics. In this chapter we use the simplest expression for the net $2s \to 1s$ two-photon decay rate, Eq. (2.21), which we recall here:

$$\dot{x}_{1s}\big|_{2s} = -\dot{x}_{2s}\big|_{1s} = \Lambda_{2s1s}\left(x_{2s} - x_{1s}{\rm e}^{-E_2/T_{\rm r}}\right), \tag{3.11}$$

where $\Lambda_{2s1s} \approx 8.22\ {\rm s}^{-1}$ is the total $2s \to 1s$ two-photon decay rate [83].

3.3 The standard multilevel atom method

Although the standard MLA formulation does not make this distinction, we cast the excited states of hydrogen into two categories. On the one hand, most excited states are not directly radiatively connected to the ground state. We call these states "interior" states and denote X_K the fractional abundance of hydrogen in the interior state $K \in \{3s, 3d, 4s, 4d, 4f, 5s, ...\}$. On the other hand, the $2s$ and np states ($n \geq 2$) are directly radiatively connected with the ground state. We call these states "interface" states and denote x_i the fractional abundance of hydrogen in the interface state $i \in \{2s, 2p, 3p, ...\}$.

In the standard MLA formulation, the free electron fraction $x_e(z)$ is evolved by solving the hierarchy of coupled differential equations: for the interior states,

$$\dot{X}_K = x_e^2 n_{\rm H} \alpha_K + \sum_L X_L R_{L,K} + \sum_j x_j R_{j,K} - X_K \Big(\beta_K + \sum_L R_{K,L} + \sum_j R_{K,j} \Big); \tag{3.12}$$

for the interface states,

$$\dot{x}_i = x_e^2 n_{\rm H} \alpha_i + \sum_L X_L R_{L,i} + \sum_j x_j R_{j,i} + x_{1s} \tilde{R}_{1s,i} - x_i \Big(\beta_i + \sum_L R_{i,L} + \sum_j R_{i,j} + \tilde{R}_{i,1s} \Big); \tag{3.13}$$

and for the free electrons and ground state,

$$\dot{x}_e = -\dot{x}_{1s} = x_{1s} \sum_i \tilde{R}_{1s,i} - \sum_i x_i \tilde{R}_{i,1s}. \tag{3.14}$$

The radiative rates between excited states are many orders of magnitude larger than the rate at which recombination proceeds, which is of the order of the Hubble rate. Even the relatively small net rates out of the interface states ($\Lambda_{2s,1s}$ and $R_{{\rm Ly}\alpha}$) are still more than 12 orders of magnitude larger than the Hubble rate. The populations of the excited states can therefore be obtained to high accuracy in the steady-state approximation (this approximation is ubiquitous in many problems and has long been used in the context of cosmological recombination [31, 49, 37], where its accuracy has been tested explicitly [38]). Setting $\dot{X}_K$ and $\dot{x}_i$ to zero in Eqs. (3.12) and (3.13), we see that the problem amounts to first solving a system of linear algebraic equations for the X_K, x_i, with an inhomogeneous term depending on x_e, and then using the populations x_i in Eq. (3.14) to evolve the free electron fraction. The solution of the system of equations (3.12), (3.13) needs to be done at *every time step*, since the inhomogeneous term of the equation depends on the ionization history, which explicitly depends on time as well as on the cosmological parameters. Recent work [37, 38] has shown that to compute sufficiently accurate recombination histories, one needs to account for excited states up to a principal quantum number $n_{\rm max} \sim 100$, resolving the angular momentum substates. This requires solving an $\mathcal{O}\left(10^4 \times 10^4\right)$ system of equations at each time step, which, even with modern computers, is extremely time consuming.

3.4 New method of solution: the effective multilevel atom

We now give a computationally efficient method of solution for the primordial recombination problem. We factor the effect of the numerous transitions involving interior states in terms of effective transitions into and out of the much smaller number of interface states. Once the rates of these effective transitions are tabulated, the cosmological evolution of the free electron fraction can be

obtained from a simple effective few-level atom calculation. We describe the method in Section 3.4.1 and give the proof of its exact equivalence to the standard MLA method in Section 3.4.2. In the subsequent Section 3.4.3, we consider which states should be treated as interface states. Finally, Section 3.4.4 provides a further simplification of the problem, which is reduced to an effective four-level atom calculation.

3.4.1 Motivations and general formulation

We first note that the only quantity of importance for CMB power spectrum calculations is the free electron fraction as a function of redshift, $x_e(z)$. The populations of the excited states are calculated only as an intermediate step — if they are desired (for example, to calculate Hα scattering features [84] or the recombination spectrum [74, 75, 35]), the populations of the excited states can be obtained by solving Eqs. (3.12, 3.13) once the free electron fraction is known. Furthermore, only the "interface" states $2s$ and np (and ns, nd when accounting for two-photon processes from higher-order states) are directly connected to the ground state and directly appear in the evolution equation for the free electron fraction Eq. (3.14). All other ("interior") excited states are only connected with other excited states or with the continuum, through optically thin radiative transitions (and to a lesser extent through collisions [36]). Interior states are only transitional states: an electron in the "interior" rapidly transitions through spontaneous and stimulated decays or absorptions caused by the blackbody radiation field (or collisions with free electrons and protons), until it is either photoionized, or reaches an interface state. There can be a very large number of transitions before any of these outcomes occurs, but the passage through the "interior" is always very short compared to the overall recombination timescale, and can be considered as instantaneous (for the same reason that the steady-state approximation is valid in the standard MLA formulation).

Instead of computing the fraction of hydrogen in each interior state K, one can rather evaluate the probabilities that an atom initially in the interior state K ultimately reaches one of the interface states or gets photoionized. Of course, after reaching an interface state, the atom may perfectly transition back to an interior state, or get photoionized. However, we consider the probability of *first* reaching a given interface state before any other one, which is uniquely defined. For an atom in the interior state K, we denote by P_K^i the probability of ultimately reaching the interface state i, and P_K^e the probability of ultimately being photoionized. An excited atom initially in the interior state K has a probability $R_{K,i}/\Gamma_K$ to *directly* decay to the interface state i, where Γ_K is the total width (or inverse lifetime) of the state K:

$$\Gamma_K \equiv \sum_{L \neq K} R_{K,L} + \sum_j R_{K,j} + \beta_K. \tag{3.15}$$

The atom may also first decay or get excited to *another* interior state $L \neq K$, with a probabil-

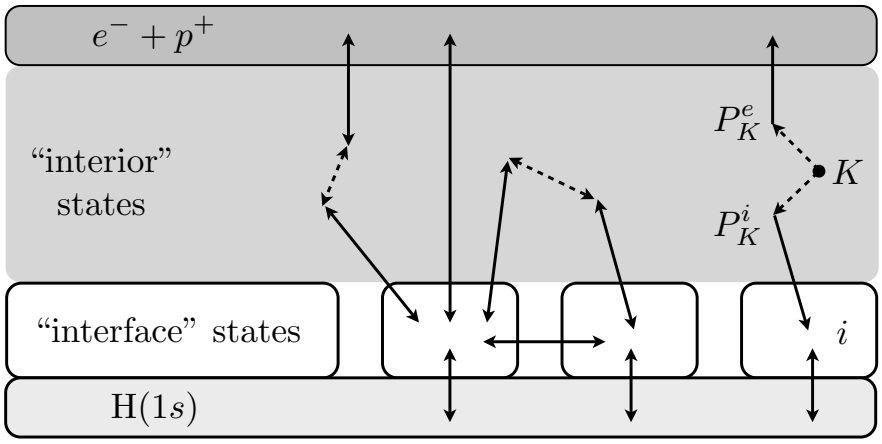

Figure 3.1: Schematic representation of the formulation of the recombination problem adopted in this work. Dotted arrows represent possibly numerous fast transitions within the "interior".

ity $R_{K,L}/\Gamma_K$, from which it may then eventually reach the interface state i with probability P_L^i. Mathematically, these various paths translate into the following system of linear equations for the probabilities P_K^i:

$$P_K^i = \sum_{L \neq K} \frac{R_{K,L}}{\Gamma_K} P_L^i + \frac{R_{K,i}}{\Gamma_K}. \tag{3.16}$$

Similarly, the P_K^e must satisfy the self-consistency relations:

$$P_K^e = \sum_{L \neq K} \frac{R_{K,L}}{\Gamma_K} P_L^e + \frac{\beta_K}{\Gamma_K}, \tag{3.17}$$

We show in Appendix 3.A.2 that these linear systems are invertible and therefore uniquely determine P_K^i and P_K^e. In Appendix 3.A.3 we prove the complementarity relation,

$$\sum_i P_K^i + P_K^e = 1, \tag{3.18}$$

which has the simple physical interpretation that an atom in the Kth interior state eventually reaches an interface state or is photoionized with unit probability.

Once these probabilities are known, it is possible to describe the large number of transitions between all the states in a simplified manner, in terms of effective rates into and out of the interface states. To clarify the explanation, we illustrate in Figure 3.1 the processes described below.

An electron and a proton can effectively recombine to the interface state i either through a direct recombination (with coefficient α_i), or following a recombination to an interior state K (with coefficient α_K), from which a sequence of interior transitions may ultimately lead to the interface state

i with probability P_K^i. The effective recombination coefficient to the interface state i is therefore:

$$\mathcal{A}_i \equiv \alpha_i + \sum_K \alpha_K P_K^i. \tag{3.19}$$

Conversely, an atom in the interface state i may effectively be ionized either through a direct photoionization (with rate β_i), or after being first excited to an interior state K (with rate $R_{i,K}$), from which the atom may ultimately be photoionized after a series of interior transitions with probability P_K^e. The effective photoionization rate from the interface state i is therefore:

$$\mathcal{B}_i \equiv \beta_i + \sum_K R_{i,K} P_K^e. \tag{3.20}$$

Finally, atoms can effectively transition from an interface state i to another interface state j, either through a direct transition if it is allowed, or after first transitioning through the interior. The effective transfer rate between the ith and jth interface states is therefore:

$$\mathcal{R}_{i,j} \equiv R_{i,j} + \sum_K R_{i,K} P_K^j \quad (j \neq i). \tag{3.21}$$

The rate of change of the population of the interface state i is therefore:

$$\dot{x}_i = x_e^2 n_{\rm H} \mathcal{A}_i + \sum_{j \neq i} x_j \mathcal{R}_{j,i} + x_{1s} \tilde{R}_{1s,i} - x_i \Big(\mathcal{B}_i + \sum_{j \neq i} \mathcal{R}_{i,j} + \tilde{R}_{i,1s} \Big), \tag{3.22}$$

where we have included the effective transitions described above, as well as transitions from and to the ground state.

The system of equations (3.16–3.22) is exactly equivalent to the standard MLA formulation, as we shall show in Section 3.4.2 below. Moreover, we will show that the rate of change of the free electron fraction, Eq. (3.14), can also be written in the equivalent form

$$\dot{x}_e = -\sum_i \left(n_{\rm H} x_e^2 \mathcal{A}_i - x_i \mathcal{B}_i \right). \tag{3.23}$$

Let us now consider the dependences of the effective rates. In the purely radiative case, the probabilities P_K^i and P_K^e only depend on the radiation temperature $T_{\rm r}$, since transitions between excited states and photoionizations only depend on the locally thermal radiation field. As a consequence, the effective recombination rates $\mathcal{A}_i\left(T_{\rm m}, T_{\rm r}\right)$ are only functions of matter and radiation temperatures and the effective photoionization and bound-bound rates $\mathcal{B}_i\left(T_{\rm r}\right)$ and $\mathcal{R}_{i,j}\left(T_{\rm r}\right)$ are functions of the radiation temperature only. When including collisional transitions, all effective rates become functions of the three variables $T_{\rm r}, T_{\rm m}$ and n_e. In all cases, effective rates can be easily tabulated *once and for all* and interpolated when needed for a recombination calculation.

Intuitively, we would expect that $\mathcal{A}_i$, $\mathcal{B}_i$, and $\mathcal{R}_{i,j}$ satisfy the detailed balance relations,

$$g_i \mathrm{e}^{-E_i/T_\mathrm{r}} \mathcal{R}_{i,j}(T_\mathrm{r}) = g_j \mathrm{e}^{-E_j/T_\mathrm{r}} \mathcal{R}_{j,i}(T_\mathrm{r}) \tag{3.24}$$

and

$$g_i \mathrm{e}^{-E_i/T_\mathrm{r}} \mathcal{B}_i(T_\mathrm{r}) = \frac{(2\pi\mu_e T_\mathrm{r})^{3/2}}{h^3} \mathcal{A}_i(T_\mathrm{m} = T_\mathrm{r}, T_\mathrm{r}). \tag{3.25}$$

We show in Appendix 3.A.4 that these equations are indeed valid. This means that we only need to tabulate half of the $\mathcal{R}_{i,j}$ [the other half can be obtained from Eq. (3.24)] and all the $\mathcal{A}_i$ [the $\mathcal{B}_i$ can be obtained from Eq. (3.25); in particular, we do not need to solve for the P^e_K].

We note that the probabilities P^i_K, P^e_K are a generalization of the cascade matrix technique introduced by Seaton [85]. Seaton's calculation assumed a vanishing ambient radiation field, so that electrons can only "cascade down" to lower energy states. In the context of the recombination of the primeval plasma, one cannot ignore the strong thermal radiation field, and electrons rather "cascade up and down," following spontaneous and stimulated decays or photon absorption events. The spirit of our method is however identical to Seaton's cascade-capture equations [85], where the "cascading" process is decoupled from the particular process populating the excited states, or from the depopulation of the interface states.

We emphasize that the method presented here is a simple generalization of the effective TLA model, with the case-B recombination coefficient being replaced by the effective recombination coefficients, which are computed individually for each interface state $2s$, $2p, 3p, ...$

3.4.2 Equivalence with the standard MLA method

This section is dedicated to proving the equivalence of the EMLA equations, Eqs. (3.16–3.22), with the standard MLA equations, Eqs. (3.12, 3.13), in the steady-state limit for the interior states (i.e., where we set $\dot{X}_K \approx 0$). The steady-state approximation does not need to be made for the interface states to demonstrate the equivalence of the two formulations (but we do use it for practical computations since it is valid to very high accuracy).

We denote by N the number of interior states and n_* the number of interface states (we will address in Section 3.4.3 the issue of which states need to be considered as interface states).

We begin by defining the $N \times N$ rate matrix $\mathbf{M}$ with elements

$$M_{KL} \equiv \delta_{KL}\Gamma_K - (1 - \delta_{KL})\, R_{K,L}. \tag{3.26}$$

We also define the $n_* + 1$ length-N vectors $\mathbf{P}^i, \mathbf{P}^e$, the components of which are the probabilities

P_K^i and P_K^e, respectively, and the $n_* + 1$ length-N vectors $\mathbf{R}^i, \mathbf{R}^e$ of components

$$R_K^i \equiv R_{K,i}, \tag{3.27}$$

$$R_K^e \equiv \beta_K. \tag{3.28}$$

The defining equations for the probabilities, Eqs. (3.16, 3.17), can be written in matrix form $\mathbf{MP}^i = \mathbf{R}^i$ and $\mathbf{MP^e} = \mathbf{R^e}$ respectively (after multiplication by Γ_K). We show in Appendix 3.A.2 that the matrix $\mathbf{M}(T_\mathrm{r})$ is invertible, for any temperature $T_\mathrm{r} \geq 0$. The formal solutions for the probabilities are therefore

$$\mathbf{P}^i = \mathbf{M}^{-1}\mathbf{R}^i, \tag{3.29}$$

$$\mathbf{P}^e = \mathbf{M}^{-1}\mathbf{R}^e. \tag{3.30}$$

We also define the length-N vector $\mathbf{X}$ which contains the populations of the interior states X_K, and the length-N vector $\mathbf{S}$ of components

$$S_K \equiv x_e^2 n_\mathrm{H} \alpha_K + \sum_j x_j R_{j,K}. \tag{3.31}$$

A careful look at Eq. (3.12) in the steady-state approximation ($\dot{X}_K = 0$) shows that it is the matrix equation $\mathbf{M}^\mathrm{T}\mathbf{X} = \mathbf{S}$, which has the solution:

$$\mathbf{X} = \left(\mathbf{M}^\mathrm{T}\right)^{-1}\mathbf{S} = \left(\mathbf{M}^{-1}\right)^\mathrm{T}\mathbf{S}. \tag{3.32}$$

Both Eqs. (3.13) and (3.22) can be cast in the form

$$\dot{x}_i = x_e^2 n_\mathrm{H}\alpha_i + \sum_{j\neq i} x_i R_{j,i} + x_{1s}\tilde{R}_{1s,i} - x_i\Big(\beta_i + \sum_{j\neq i} R_{i,j} + \tilde{R}_{i,1s}\Big) + \dot{x}_i|_\mathrm{interior}. \tag{3.33}$$

The only a different term, *a priori*, is the net transition rate from the interior to the state i, $\dot{x}_i|_\mathrm{interior}$. In the standard MLA formulation, Eq. (3.13), this term is

$$\dot{x}_i|_\mathrm{interior}^\mathrm{(MLA)} = \sum_K \left(X_K R_K^i - x_i R_{i,K}\right) = \mathbf{X}^\mathrm{T}\mathbf{R}^i - x_i \sum_K R_{i,K}. \tag{3.34}$$

With our new formulation, Eq. (3.22), using the definitions of the effective rates Eqs. (3.19–3.21), the net transition rate from the interior to the state i is:

$$\dot{x}_i|_\mathrm{interior}^\mathrm{(EMLA)} = \sum_K \left[x_e^2 n_\mathrm{H}\alpha_K P_K^i + \sum_{j\neq i} x_j R_{j,K} P_K^i - x_i R_{i,K}(P_K^e + \sum_{j\neq i} P_K^j)\right]. \tag{3.35}$$

Using the complementarity relation Eq. (3.18), we rewrite $P_K^e + \sum_{j\neq i} P_K^j = 1 - P_K^i$. We then recognize that the common factor of P_K^i is just the K-th component of the vector $\mathbf{S}$, Eq. (3.31), so we can rewrite Eq. (3.35) as

$$\dot{x}_i|_{\text{interior}}^{(\text{EMLA})} = \mathbf{S}^{\mathrm{T}}\mathbf{P}^i - x_i \sum_K R_{i,K}. \tag{3.36}$$

From the formal solution for the populations of the interior states Eq. (3.32), we have

$$\mathbf{X}^{\mathrm{T}}\mathbf{R}^i = \mathbf{S}^{\mathrm{T}}\mathbf{M}^{-1}\mathbf{R}^i = \mathbf{S}^{\mathrm{T}}\mathbf{P}^i, \tag{3.37}$$

where the second equality is obtained from the formal solution for the probabilities P_K^i, Eq. (3.29). We therefore see from Eqs. (3.34) and (3.36) that

$$\dot{x}_i|_{\text{interior}}^{(\text{MLA})} = \dot{x}_i|_{\text{interior}}^{(\text{EMLA})}, \tag{3.38}$$

and hence the two formulations are *exactly* equivalent. They only differ by the order in which the bilinear product $\mathbf{S}^{\mathrm{T}}\mathbf{M}^{-1}\mathbf{R}^i$ is evaluated.

Finally, we show that Eq. (3.23) correctly gives the rate of change of the free electron fraction. In the standard MLA formulation, the rate of change of the free electron fraction can be written as:

$$\dot{x}_e = -\sum_K \left[n_{\mathrm{H}} x_e^2 \alpha_K - X_K \beta_K\right] - \sum_i \left[n_{\mathrm{H}} x_e^2 \alpha_i - x_i \beta_i\right]. \tag{3.39}$$

This formula is never used in standard MLA codes, as it requires a summation over a large number of nearly canceling terms, and MLA codes use instead $\dot{x}_e = -\dot{x}_{1s}$ to compute the rate of change of the free electron fraction. Eq. (3.39) remains however formally correct. Using Eqs. (3.32) and (3.30), we rewrite:

$$\begin{aligned}
\sum_K X_K \beta_K &= \sum_{K,L} \beta_K \left(\mathbf{M}^{-1}\right)_{LK} \left[n_{\mathrm{H}} x_e^2 \alpha_L + \sum_i x_i R_{i,L}\right] = \sum_L P_L^e \left[n_{\mathrm{H}} x_e^2 \alpha_L + \sum_i x_i R_{i,L}\right] \\
&= \sum_L n_{\mathrm{H}} x_e^2 \alpha_L - n_{\mathrm{H}} x_e^2 \sum_i \sum_L \alpha_L P_L^i + \sum_i x_i \sum_L R_{i,L} P_L^e,
\end{aligned} \tag{3.40}$$

where in the last equality we have used the complementarity relation $\sum_i P_K^i + P_K^e = 1$. Inserting this result into Eq. (3.39), and using the definitions of the effective recombination coefficients and photoionization rates Eqs. (3.19) and (3.20), we immediately recover Eq. (3.23).

3.4.3 Choice of interface states

If one naively includes all np states up to $n = n_{\rm max} = \mathcal{O}(100)$ in the list of interface states, the interpolation of effective rates can become somewhat cumbersome as it involves $\mathcal{O}\left(10^4\right)$ functions of one to three variables. However, only the lowest few of these states actually have significant transition rates to the ground state; indeed, most of the decays to the ground state proceed through either $2s$ (two-photon decay) or $2p$ (Lyα escape), as anticipated in the earliest studies [31, 32].

The rate of Lyman line escape is dominated by the lowest few lines. For example, if the relative populations of the excited states were given by the Boltzmann ratios (which is a good approximation until late times) then the net decay rate in the $np \rightarrow 1s$ transition (not accounting for feedback from the next line) would be proportional to

$$\dot{x}_{np\rightarrow 1s} \propto (1 - n^{-2})^3 e^{-E_n/T_{\rm r}}. \tag{3.41}$$

This relation would imply that the Lyβ escape rate is $< 1\%$ of the Lyα escape rate, and the higher-order Lyman lines contribute even less. Previous computations of the escape rates (e.g., Ref. [49]) agree with this expectation. These considerations imply that for $n \geq 3$, $\dot{x}_{1s}|_{np} \ll \dot{x}_{1s}|_{2p}$ in Eq. (3.14). Moreover, an atom in the np state with $n \geq 3$ is much more likely to spontaneously decay to $n's$ or $n'd$, with $2 \leq n' < n$, than to emit a Lyman-n photon that successfully escapes the line. This implies that $\left|\dot{x}_{np}|_{1s}\right| \ll \left|\dot{x}_{np}\right|$ in Eq. (3.13).

In addition to a very low net decay rate out of the np states for $n \geq 3$, feedback between neighboring lines further suppresses their efficiency as interface states. The few photons that escape the Ly$(n+1)$ line will be reabsorbed almost certainly in the next lower line, after a redshift interval

$$\Delta z = z_{\rm em} - z_{\rm ab} = (1 + z_{\rm ab}) \left(\frac{E_{n+1,1}}{E_{n1}} - 1 \right). \tag{3.42}$$

Feedback between the lowest-lying lines is not instantaneous: $\Delta z/(1 + z_{\rm ab}) = 0.185$ for Lyβ $\rightarrow$Lyα feedback, 0.055 for Lyγ $\rightarrow$Lyβ, and 0.024 for Lyδ $\rightarrow$Lyγ. However, for higher-order lines, feedback rapidly becomes nearly instantaneous as $\Delta z/(1 + z_{\rm ab}) \sim 2/n^3$. Thus the effect of the higher Lyman lines is even weaker than Eq. (3.41) would suggest. Recent work [42] has shown that including lines above Lyβ results in a fractional error $|\Delta x_e|/x_e$ of at most $\approx 3 \times 10^{-4}$.

We therefore conclude that very accurate recombination histories can be obtained by only including $2s$ and the low-lying p-states as interface states and neglecting higher-order Lyman transitions altogether (we will show below that accounting for Lyα Lyβ and Lyγ and feedback between them is sufficient). In addition, when considering two-photon transitions from higher levels, one should in principle add the ns and nd states as "interface" states. However, only two-photon transitions from $2s$, $3s$ and $3d$, are important (and $4s$, $4d$ at the level of a few 10^{-4}), see Chapter 5 and Refs. [49, 52].

The number of efficient "interface" states, which we denote n_*, is therefore small ($n_* = 8$ is sufficient from the above discussion).

We can now see that our formulation in terms of effective transition rates and interface states is much better adapted for a fast recombination calculation that the standard MLA formulation. To compute accurate recombination histories, explicitly accounting for high-n shells of hydrogen, one first needs to tabulate a *few functions* $\{\mathcal{A}_i\}$ and $\{\mathcal{R}_{i,j}\}$ on temperature grids. The computation of the effective rates is the time-consuming part of the calculation; however, since they are independent of the cosmological parameters, this can be done once, and not repeated for each cosmology. When considering n_* interface states, the free electron fraction can then be computed very quickly for any given cosmology by solving the $n_* + 1$ equations (3.22) and (3.14) or (3.23), interpolating the effective rates from the pre-computed tables. Note that Eq. (3.22) is a simple $n_* \times n_*$ system of linear algebraic equations in the steady-state approximation. In the following section we show that we can simplify the the problem even further by reducing it to an effective four-level atom model.

3.4.4 Further simplification: the effective four-level atom

If we wish to follow n_* "interface" states, then the system of equations (3.22), in the steady-state approximation, is an $n_* \times n_*$ system. Moreover, one needs to interpolate n_* functions of 2 variables (the effective recombination coefficients — the effective photoionization rates are obtained by detailed balance), and $n_*(n_* - 1)/2$ functions of 1 variable (half of the effective bound-bound rates, the other half being obtained by detailed balance). Here we show how this system can be further reduced to a 2×2 system involving only $2s$ and $2p$, requiring only 2 functions of 2 variables and 1 function of 1 variable, with virtually no loss of accuracy.

For now on we use the general index K for all states with principal quantum number $n \geq 3$. Even if some of the states with $n \geq 3$ are radiatively connected to the ground state, one can still formally define the effective transition rates Eqs. (3.19), (3.20) and (3.21) for the $2s$ and $2p$ states because of the near-instantaneity of transitions out of the excited states. However, these coefficients do not have a simple temperature dependence anymore, and are therefore not well suited for fast interpolation. Indeed, the probabilities P_K^i and P_K^e, where $i = 2s, 2p$, are still defined by Eqs. (3.16) and (3.17), but the inverse lifetime of the state K, Eq. (3.15), should now account for the net downward transition rate to the ground state, and one should make the replacement:

$$\Gamma_K \rightarrow \tilde{\Gamma}_K \equiv \Gamma_K(T_\mathrm{r}) + \tilde{R}_{K,1s}, \tag{3.43}$$

where we define $\Gamma_K(T_\mathrm{r})$ as the inverse lifetime of the K-th interface state when transitions to the ground state are not included. In addition, we need to define additional effective transition rates

with the ground state. For $i = 2s, 2p$, we define:

$$\tilde{\mathcal{R}}_{i,1s} \equiv \tilde{R}_{i,1s} + \sum_K R_{i,K} \tilde{P}_K^{1s} \tag{3.44}$$

and

$$\tilde{\mathcal{R}}_{1s,i} \equiv \tilde{R}_{1s,i} + \sum_K \tilde{R}_{1s,K} P_K^i, \tag{3.45}$$

where the probabilities $\tilde{P}_K^{1s}$ must satisfy the self-consistency relations:

$$\tilde{P}_K^{1s} = \sum_{L \neq K} \frac{R_{K,L}}{\tilde{\Gamma}_K} \tilde{P}_L^{1s} + \frac{\tilde{R}_{K,1s}}{\tilde{\Gamma}_K}. \tag{3.46}$$

The standard MLA equations, in the steady-state approximation for the excited states with $n \geq 3$, can then be shown to be exactly equivalent to the following set of equations: for the net rate of production of $2s$,

$$\dot{x}_{2s} = x_e^2 n_{\rm H} \mathcal{A}_{2s} + x_{2p} \mathcal{R}_{2p,2s} + x_{1s} \tilde{\mathcal{R}}_{1s,2s} - x_{2s} \left(\mathcal{B}_{2s} + \mathcal{R}_{2s,2p} + \tilde{\mathcal{R}}_{2s,1s} \right); \tag{3.47}$$

for the net rate of production of $2p$,

$$\dot{x}_{2p} = x_e^2 n_{\rm H} \mathcal{A}_{2p} + x_{2s} \mathcal{R}_{2s,2p} + x_{1s} \tilde{\mathcal{R}}_{1s,2p} - x_{2p} \left(\mathcal{B}_{2p} + \mathcal{R}_{2p,2s} + \tilde{\mathcal{R}}_{2p,1s} \right); \tag{3.48}$$

and for either the net recombination rate or the net rate of generation of H(1s),

$$\dot{x}_e = \sum_{i=2s,2p} \left[x_i \mathcal{B}_i - x_e^2 n_{\rm H} \mathcal{A}_i \right] \tag{3.49}$$

$$= \sum_{i=2s,2p} \left[x_{1s} \tilde{\mathcal{R}}_{1s,i} - x_i \tilde{\mathcal{R}}_{i,1s} \right]. \tag{3.50}$$

The proof of equivalence is exactly the same as that of Section 3.4.2 and we do not reproduce it here. Note that we use the same notation for the effective rates independently of the number of "interface" states considered, but they obviously have a different meaning that should be clear from the context.

The coefficients in the above system are in principle not simple functions of temperature anymore if one wishes to account for the transitions to the ground state from excited states with $n \geq 3$. We can nevertheless simplify their expressions with some minimal approximations. We start by noticing that for excited states nl with $n \geq 3$, the rate of spontaneous decays to the $n', l \pm 1$ states with $1 < n' < n$ is much larger than the net decay rate to the ground state. For the $3p$ state for example, we find that in the Sobolev approximation for Lyβ decays, $\tilde{R}_{3p,1s}/A_{3p,2s} < 8 \times 10^{-6}$ for $200 < z < 1600$, where

$A_{3p,2s}$ is the Einstein A-coefficient of the $3p \to 2s$ transition. Therefore, to an excellent accuracy (with relative errors of order $\tilde{R}_{K,1s}/\Gamma_K$), one can neglect $\tilde{R}_{K,1s}$ in Eq. (3.43), and simply use $\Gamma_K(T_\mathrm{r})$ instead of $\tilde{\Gamma}_K$ wherever the latter appears. With this approximation, the rate coefficients $\mathcal{A}_{2s/2p}$, $\mathcal{B}_{2s/2p}$ and $\mathcal{R}_{2s,2p}$ are simply the usual effective rates computed in the case that only $2s$ and $2p$ are considered as interface states, and depend only on matter and radiation temperatures. We explain in Appendix 3.B.2 how we obtain effective rates extrapolated to $n_\mathrm{max} = \infty$.

We show in Appendix 3.A.5 that using $\tilde{\Gamma}_K \approx \Gamma_K(T_\mathrm{r})$ in Eq. (3.46), we can rewrite Eq. (3.44) as:

$$\tilde{\mathcal{R}}_{i,1s} = \tilde{R}_{i,1s} + \sum_K \tilde{R}_{K,1s} \frac{g_K}{g_i} \mathrm{e}^{-E_{K2}/T_\mathrm{r}} P_K^i(T_\mathrm{r}), \tag{3.51}$$

where g_K, g_i are the statistical weights of the states K, i and $E_{K2} \equiv E_K - E_2$ is the energy difference between the state K and the $n = 2$ shell.

In addition, the populations of the "weak" interface states X_K are sometimes required — for example the photon occupation number depends on the populations of the s and d states, see Section 5.3.2. We show in Appendix 3.A.6 that the following relation is verified for $T_\mathrm{m} = T_\mathrm{r}$:

$$X_K\big|_{T_\mathrm{m}=T_\mathrm{r}} = \frac{g_K}{g_e} \mathrm{e}^{-E_K/T_\mathrm{r}} P_K^e(T_\mathrm{r}) x_e^2 + \sum_{i=2s,2p} \frac{g_K}{g_i} \mathrm{e}^{-E_{K2}/T_\mathrm{r}} P_K^i(T_\mathrm{r}) x_i. \tag{3.52}$$

In fact, $T_\mathrm{m} < T_\mathrm{r}$ and the coefficient of x_e^2 in the above equation should be slightly higher. In practice though, $|T_\mathrm{m}/T_\mathrm{r} - 1| < 1\%$ for $z \gtrsim 500$, and for lower redshifts $P_K^e \ll 1$ and transitions to the ground state are unimportant anyway, so the above equation is very accurate at all times.

We therefore only need to tabulate the additional $2(n_* - 2)$ functions $P_K^{2s}(T_\mathrm{r})$ and $P_K^{2p}(T_\mathrm{r})$ to account for $n_* - 2$ "weak" interface states in addition to $2s$ and $2p$ (note that $P_K^e = 1 - P_K^{2s} - P_K^{2p}$).

In practice, we can further reduce the computational load by simply using $P_{ns}^{2s} = P_{nd}^{2s} = P_{np}^{2p} = 0$, $P_{ns}^{2p} = P_{nd}^{2p} = P_{np}^{2s} = 1$. This amounts to assuming that for $n \geq 3$, ns and nd states are in Boltzmann equilibrium with $2p$, whereas np states are in Boltzmann equilibrium with $2s$ — see Eq. (3.52), and rewriting transitions from $n \geq 3$ states as transitions from the $n = 2$ state to which they are tightly coupled. This is extremely accurate at all times when accurate transition rates to the ground state are required. The validity of this statement is somewhat weaker for the $n = 4$ states, which are somewhat in between equilibrium with the $2s$ state and the $2p$ state (because allowed transitions connect them to both states). However, as decays from $4p$, $4s$ and $4d$ only marginally affect recombination anyway (at the level of a few 10^{-4}), and $2s$ and $2p$ are very close to equilibrium at the relevant times, this approximation is still very accurate. We explicitly checked that using the approximate values for the P_K^i instead of their exact values in Eqs. (3.45), (3.51) and (3.52) leads to maximum errors on the recombination history $|\Delta x_e|/x_e < 3 \times 10^{-5}$.

We illustrate the simplification to an effective four-level atom in Fig. 3.2.

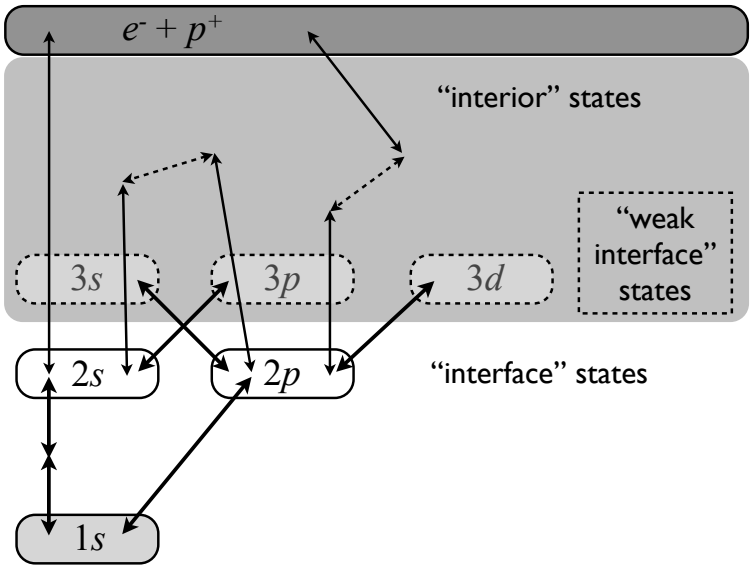

Figure 3.2: Schematic representation of the hydrogen atom, with the nomenclature used in this work. Slow transitions from the "weak interface" states to the ground state are counted as transitions from the $n = 2$ state with which they are in equilibrium. The problem reduces to an effective four-level atom calculation.

The system of equations (3.47), (3.48) and (3.49) is just the extension of Peebles effective three-level atom to an effective four-level atom, properly accounting for the nonzero radiation field, the nearly instantaneous multiple transitions between excited states, the fact that $2s$ and $2p$ are out of Boltzmann equilibrium, and possibly additional radiative transfer effects and decays from higher shells through the appropriate coefficients $\tilde{\mathcal{R}}$. Making the usual steady-state assumption for the excited states, we can first solve for x_{2s} and x_{2p} and then evolve x_e. When using the simple $2p \leftrightarrow 1s$ and $2s \leftrightarrow 1s$ transition rates of Section 2.2.1, the system is simple enough that we may write the function $\dot{x}_e$ explicitly as an illustration:

$$\dot{x}_e = -C_{2s}\left(n_{\rm H}x_e^2\mathcal{A}_{2s} - x_{1s}\mathcal{B}_{2s}\mathrm{e}^{-E_{21}/T_{\rm r}}\right) - C_{2p}\left(n_{\rm H}x_e^2\mathcal{A}_{2p} - 3x_{1s}\mathcal{B}_{2p}\mathrm{e}^{-E_{21}/T_{\rm r}}\right), \tag{3.53}$$

where the C-factors are given by

$$C_{2s} \equiv \frac{\Lambda_{2s,1s} + \mathcal{R}_{2s,2p}\frac{R_{\rm Ly\alpha}}{\Gamma_{2p}}}{\Gamma_{2s} - \mathcal{R}_{2s,2p}\frac{\mathcal{R}_{2p,2s}}{\Gamma_{2p}}}, \tag{3.54}$$

and

$$C_{2p} \equiv \frac{R_{\rm Ly\alpha} + \mathcal{R}_{2p,2s}\frac{\Lambda_{2s,1s}}{\Gamma_{2s}}}{\Gamma_{2p} - \mathcal{R}_{2p,2s}\frac{\mathcal{R}_{2s,2p}}{\Gamma_{2s}}}, \tag{3.55}$$

where $R_{\mathrm{Ly}\alpha}$ was defined in Eq. (2.20) and we have used the effective inverse lifetimes:

$$\begin{aligned} \Gamma_{2s} &\equiv \mathcal{B}_{2s} + \mathcal{R}_{2s,2p} + \Lambda_{2s,1s} \quad \text{and} \\ \Gamma_{2p} &\equiv \mathcal{B}_{2p} + \mathcal{R}_{2p,2s} + R_{\mathrm{Ly}\alpha}. \end{aligned} \tag{3.56}$$

The variation of the factors C_{2s} and C_{2p} as a function of redshift is very similarly to that of the Peebles C-factor, see Fig. 2.2.

3.5 Implementation and results

Here we give some details on the implementation of our EMLA code. Section 3.5.1 describes the computation of the effective rates (the computationally expensive part of the calculation, which needs to be done only once). Section 3.5.2 describes the implementation of the ultrafast effective few-level atom calculation. We show our recombination histories and compare our results with the existing standard MLA code RecSparse [37] in Section 3.5.3.

3.5.1 Computation of the effective rates

We have implemented the calculation of the effective rates in the purely radiative case. Bound-free rates were computed by numerically integrating Eq. (3.2) using an 11-point Newton-Cotes method, where the radial matrix elements $g(n, l, \kappa, l')$ were obtained using the recursion relation given by Burgess [81]. Einstein A-coefficients were computed by using the recursion relations obtained by Hey [86] for the radial matrix elements $R^{nl}_{n'l'}$. Finally, we obtained the probabilities P^i_K using a sparse matrix technique similar to that of Ref. [37] when solving Eq. (3.16) (see Appendix 3.B.1 for details). We accounted explicitly for all excited states up to a principal quantum number n_{max}, resolving angular momentum substates. We tabulated the effective rates $\mathcal{A}_i(T_{\mathrm{m}}, T_{\mathrm{r}})$ on a grid of 100 log-spaced points in T_{r} from 0.004 to 0.4 eV and 40 linearly spaced points in $T_{\mathrm{m}}/T_{\mathrm{r}}$ from 0.1 to 1.0, and $\mathcal{R}_{i,j}(T_{\mathrm{r}})$ on the grid of points in T_{r}. We tabulated the effective rates for several values of n_{max}, up to $n_{\mathrm{max}} = 600$, and extrapolated them to $n_{\mathrm{max}} = \infty$ (see details in Appendix 3.B.2).

Figure 3.3 shows the total effective recombination coefficient $\mathcal{A}_{\mathrm{B}}(T_{\mathrm{m}}, T_{\mathrm{r}}) \equiv \mathcal{A}_{2s}(T_{\mathrm{m}}, T_{\mathrm{r}}) + \mathcal{A}_{2p}(T_{\mathrm{m}}, T_{\mathrm{r}})$, normalized to the case-B recombination coefficient $\alpha_{\mathrm{B}}(T_{\mathrm{m}})$. Note that $\alpha_{\mathrm{B}}(T_{\mathrm{m}})$ is just $\mathcal{A}_{\mathrm{B}}(T_{\mathrm{m}}, T_{\mathrm{r}} = 0)$ with our notation; indeed, for $T_{\mathrm{r}} = 0$, $\beta_K = 0$ and therefore $P^e_K = 0$ for all K so $\sum_i P^i_K = 1$ and hence $\sum_i \mathcal{A}_i = \sum_i \alpha_i + \sum_K \alpha_K = \sum_{nl} \alpha_{nl}$, where the last sum is over all excited states.

In Fig. 3.4, we show the ratio $\mathcal{A}_{2s}(T_{\mathrm{m}}, T_{\mathrm{r}})/\mathcal{A}_{\mathrm{B}}(T_{\mathrm{m}}, T_{\mathrm{r}})$, which is the fraction of recombinations to the $n = 2$ shell that are to the $2s$ level. This fraction is in general different from the intuitive value of 1/4, and its exact value depends on temperature.

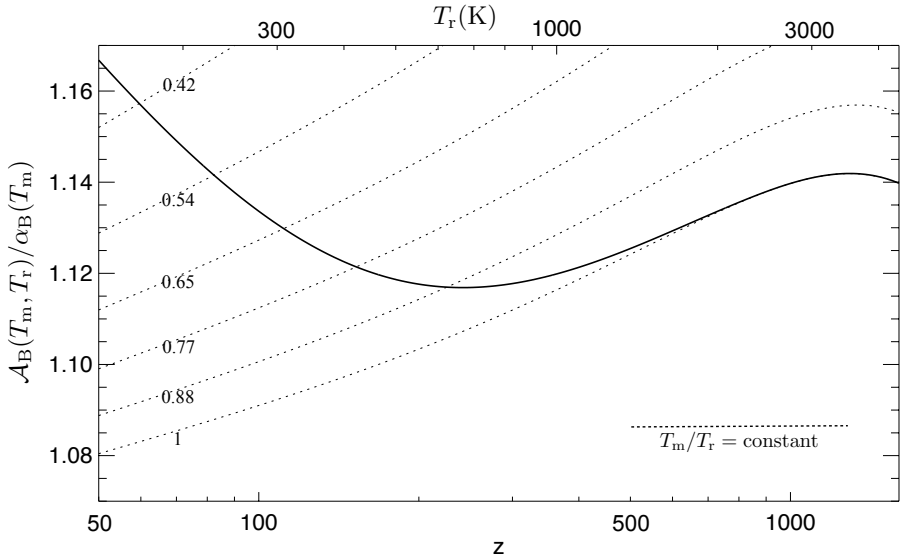

Figure 3.3: "Exact fudge factor" $\mathcal{A}_{\rm B}(T_{\rm m},T_{\rm r})/\alpha_{\rm B}(T_{\rm m})$, where we use the fit of Ref. [72] for the case-B recombination coefficient $\alpha_{\rm B}(T_{\rm m})$. The solid thick line shows the evolution of this quantity as a function of redshift, for $T_{\rm m}(z)$ computed by our recombination code (see text for details). We have overlaid contours of constant $T_{\rm m}/T_{\rm r}$ as dotted lines, as a function of $T_{\rm r}$ (the value of $T_{\rm m}/T_{\rm r}$ is indicated below each line). For comparison, the code RECFAST uses a constant fudge factor $F = 1.14$ to mimic the effect of high-n states.

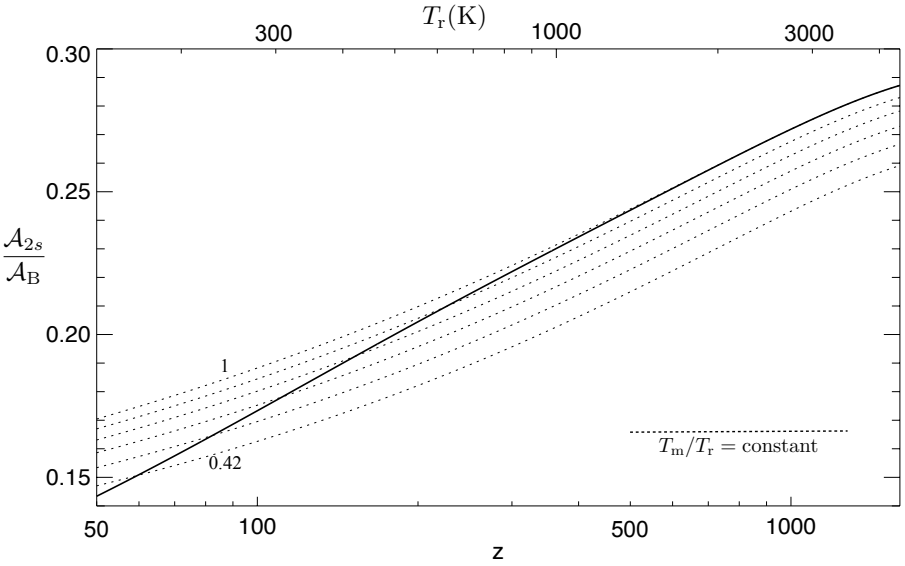

Figure 3.4: Fraction of the effective recombinations to the $n = 2$ shell that lead to atomic hydrogen in the $2s$ state (as opposed to the $2p$ state). This fraction differs from the naive expectation of 1/4 and depends on temperature. The solid thick line shows the evolution of this quanity as a function of redshift, for $T_{\rm m}(z)$ computed by our recombination code (see text for details). We have overlaid contours of constant $T_{\rm m}/T_{\rm r}$ as dotted lines, as a function of $T_{\rm r}$ (same values as in Fig. 3.3, but notice that here the upper curve corresponds to $T_{\rm m}/T_{\rm r} = 1$).

3.5.2 Ultrafast EMLA code

In order to actually compute the recombination history, we require an evolution equation for the free electron fraction, $\dot{x}_e(x_e, n_{\rm H}, H, T_{\rm m}, T_{\rm r})$ and a similar equation for $\dot{T}_{\rm m}$ (or a prescription for $T_{\rm m}$). For comparison with the standard MLA code RecSparse [37], we have implemented the case of 3 interface states $i \in \{2s, 2p, 3p\}$ ($n_* = 3$), and have used the non-extrapolated tables of effective rates for several values of $n_{\rm max}$.

To compute $\dot{x}_e$, we first obtain the downward $\mathcal{R}_{i,j}(T_{\rm r})$ from our table via cubic polynomial (4-point) interpolation and $\mathcal{A}_i(T_{\rm m}, T_{\rm r})$ via bicubic interpolation (2-dimensional in $\ln T_{\rm r}$ and $T_{\rm m}/T_{\rm r}$ using 4×4 points). The upward $\mathcal{R}_{j,i}(T_{\rm r})$ are obtained using Eq. (3.24) and the effective photoionization rates $\mathcal{B}_i(T_{\rm r})$ are obtained using Eq. (3.25). We then solve for the $\{x_i\}$ using Eq. (3.22), and finally obtain $\dot{x}_e$ using Eq. (3.14).

The matter temperature is determined by the Compton evolution equation, Eq. (2.26). At high redshift, one may use the steady-state solution (see Appendix A of Ref. [49]),

$$T_{\rm m} \approx T_{\rm m,ss} \equiv T_{\rm r} \left[1 + \frac{3(1 + f_{\rm He} + x_e) m_e c H}{8 \sigma_{\rm T} a_{\rm r} T_{\rm r}^4 x_e} \right]^{-1} . \tag{3.57}$$

At the highest redshifts, the ODE describing hydrogen recombination is stiff; therefore for $z > 1570$ we follow the recombination history using perturbation theory around the Saha approximation. At $500 < z < 1570$ we use Eq. (3.57) to set the matter temperature, and a fourth-order Runge-Kutta integration algorithm (RK4) to follow the single ODE for $x_e(z)$; and at $z < 500$ we use RK4 to follow the two ODEs for $x_e(z)$ and $T_{\rm m}(z)$ simultaneously. The integration step size is $\Delta z = -1.0$ (negative since we go from high to low redshifts)[3].

3.5.3 Results and code comparison

The recurring computation time of our ultrafast EMLA code is 0.08 seconds on a MacBook laptop computer with a 2.1 GHz processor, independently of $n_{\rm max}$. Our recombination histories are shown in Figure 3.5. We compared our results with the existing standard MLA code RecSparse for $n_{\rm max} = 16$, 32, 64, 128 and 250. As can be seen in Figure 3.6, the two codes agree to better than 8×10^{-5} across the range $200 < z < 1600$, despite having different methods for accounting for the excited states, and independent implementations for matrix elements and ODE integration.

In Fig. 3.7 we show the changes to the recombination history resulting from an accurate effective multilevel computation, as compared to the effective three-level atom computation, using in both cases the simple decay rates to the ground state described in Sec 2.2.1. For comparison, we also show the resulting changes when using an effective three-level atom model with a fudge factor $F = 1.14$

[3]These parameters were changed in the final version of the code, see Chapter 5, but the ones described here were used for code comparison.

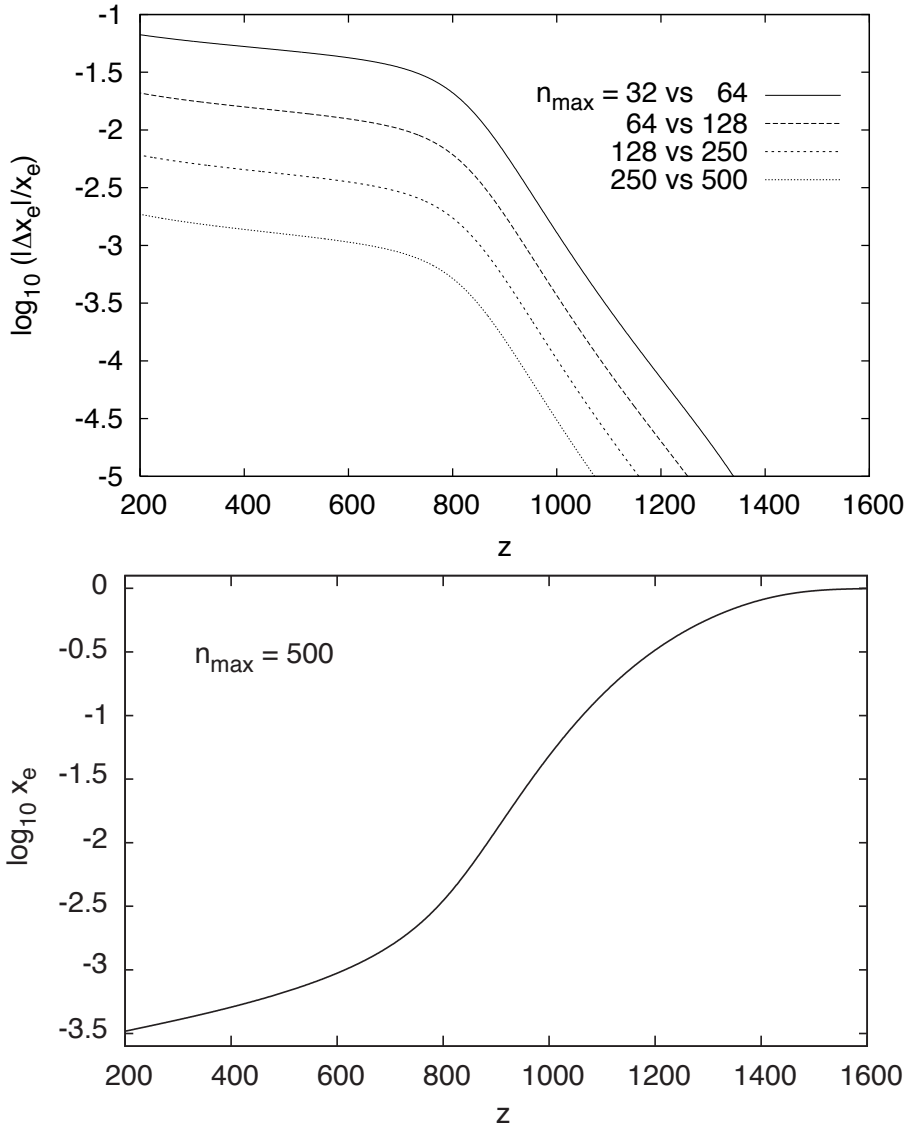

Figure 3.5: *Top panel*: Relative differences between recombination histories computed with successively more accurate effective rates. *Bottom panel*: Recombination history for effective rates computed with $n_{\max} = 500$, i.e., accounting explicitly for 125,250 states of the hydrogen atom. Figures provided by Christopher Hirata.

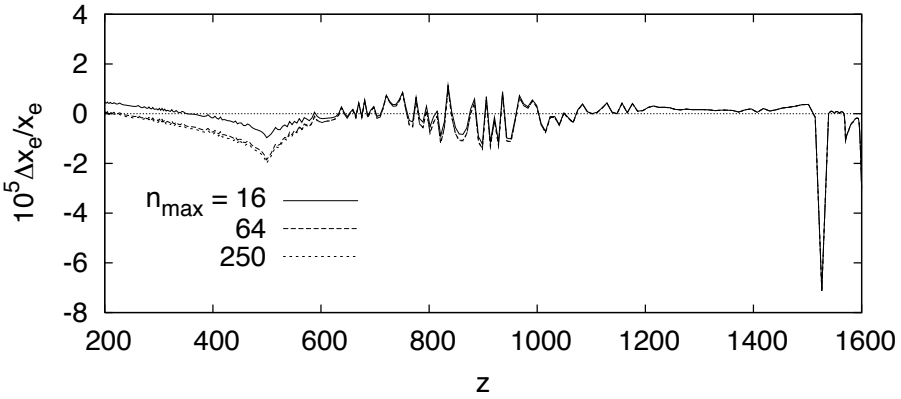

Figure 3.6: A comparison of our ultrafast code to RecSparse [37], for different values of $n_{\max}$. The vertical axis is the fractional difference in free electron abundance rescaled by 10^5 (positive indicating that RecSparse gives a larger x_e). We see that the maximum fractional deviation is $< 8 \times 10^{-5}$. The feature around $z = 1540$ is due to a time-step change in RecSparse. Figure provided by Christopher Hirata and data from RecSparse computations provided by Daniel Grin.

as in the code RecFast [30]. We checked that it is not possible to reproduce the correct effective MLA computation with a constant fudge factor in an effective three-level atom. We find that the best fitting fudge factor would be $F = 1.126$, with relative errors reaching 0.2 %. In any case, the effective MLA computation is so simple and computationally efficient that the need for non-physical fudge factors does not arise.

3.6 Conclusions and future directions

We have shown that the computation of primordial hydrogen recombination can be factored into two independent calculations. On the one hand, most excited states are not directly radiatively connected to the ground state, and undergo transitions caused by the thermal bath of blackbody photons at the relevant frequencies, as well as the thermal electrons and protons. One can account for these numerous transitions with effective transition rates into and out of the "interface" states which are connected to the ground state. The computationally intensive aspect of a recombination calculation in fact resides in the evaluation of these effective rates, which are functions of matter and radiation temperature only, and are a generalization of the case-B recombination coefficient. This calculation being independent of cosmological parameters, it can be done prior to any recombination calculation, once and for all. A simple effective few-level atom can then be evolved for any set of cosmological parameters, without any need for "fudge factors" or approximations.

Collisional transitions were not included in our computations. They may be particularly important for the high-n states. The effective rates computed here are therefore only approximating the correct rates in the limit of zero density. Our formalism is general and collisions can be included as

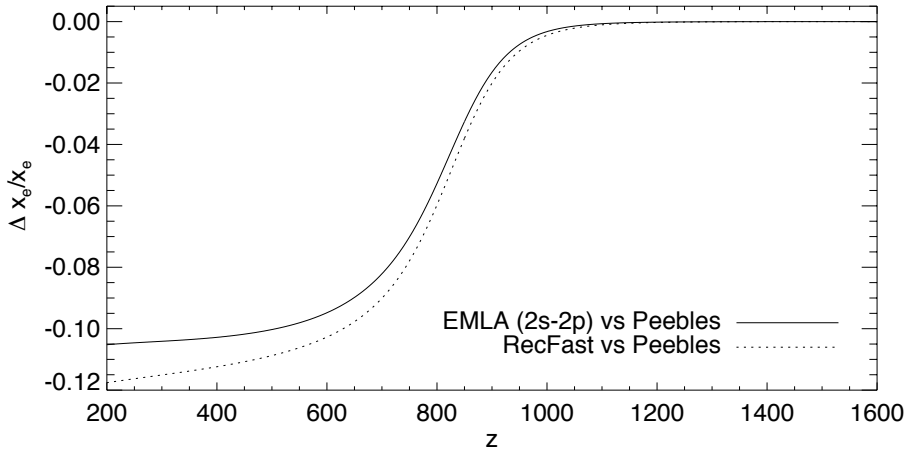

Figure 3.7: Fractional changes in the ionization history relative to the effective three-level atom model. The "RecFast" model is an effective three-level atom with the case-B recombination coefficient multiplied by a fudge factor F = 1.14. The same prescription for the evolution of the matter temperature is used in all cases, see Section 5.3.5.

soon as accurate rates are available (the main change would be that the interpolation tables would require $\ln n_e$ as an additional independent variable).

The formalism developed in this chapter is general and can accommodate any form of the transition rates to the ground state. In the subsequent chapters, we shall dwell on the radiative transfer effects, which are constitute a conceptually more challenging aspect of primordial recombination.

3.A Appendix: Proofs of relations involving effective rates

3.A.1 Preliminaries

The purpose of this appendix is to prove some relations involving effective rates and give some details regarding their numerical evaluation.

We recall that in our notation, capital indices K, L refer to "interior" excited states, and lowercase indices i, j refer to "interface" excited states. We have previously defined the rate matrix $\mathbf{M}(T_\mathrm{r})$ with coefficients:

$$M_{KL} = \delta_{KL}\Gamma_K - (1-\delta_{KL})R_{K,L}, \tag{3.58}$$

where $R_{K,L}(T_\mathrm{r})$ is the rate of $K \to L$ transitions and $\Gamma_K(T_\mathrm{r})$ is the inverse lifetime of the interior state K. In Section 3.4.2, we have shown that the populations of the interface states are given by:

$$X_K = \sum_L \left(\mathbf{M}^{-1}\right)_{LK} \left[n_\mathrm{H} x_e^2 \alpha_L + \sum_i x_i R_{i,L} \right]. \tag{3.59}$$

We also showed that the probabilities P_K^i and P_K^e are given by

$$P_K^i = \sum_L \left(\mathbf{M}^{-1}\right)_{KL} R_{L,i}, \tag{3.60}$$

and

$$P_K^e = \sum_L \left(\mathbf{M}^{-1}\right)_{KL} \beta_L. \tag{3.61}$$

3.A.2 Invertibility of the system defining the P_K^i, P_K^e

In this section we show that the matrix $\mathbf{M}(T_\mathrm{r})$ defined in Eq. (3.58) is non-singular, for any value of the radiation temperature $T_\mathrm{r} \geq 0$.

Let us consider the eigenvalue equation $\mathbf{Mb} = \mathbf{0}$ and select a particular K_1 such that $|b_{K_1}| \geq |b_L|$ for all L. The eigenvalue equation implies

$$\begin{aligned} 0 &= \left| M_{K_1K_1} b_{K_1} + \sum_{L \neq K} M_{K_1 L} b_L \right| \\ &\geq M_{K_1K_1} \left| b_{K_1} \right| - \sum_{L \neq K_1} \left| M_{K_1 L} \right| \left| b_L \right|, \end{aligned} \tag{3.62}$$

where we have used the inverse triangle inequality. The matrix $\mathbf{M}$ is diagonally dominant, i.e.,

$$\forall K, \quad M_{KK} = \Gamma_K \geq \sum_{L \neq K} R_{K,L} = \sum_{L \neq K} |M_{KL}|. \tag{3.63}$$

Using the inequality (3.63) for $K = K_1$ in Eq. (3.62), we obtain

$$0 \geq \sum_{L \neq K_1} \left|M_{K_1 L}\right| \left(|b_{K_1}| - |b_L|\right). \tag{3.64}$$

For any interior state K_1, there always exists a sequence of transitions that ultimately leads to some interface state i, $K_1 \to K_2 \to ... \to K_n \to i$, for any temperature $T_\mathrm{r} \geq 0$. (i.e., there are no "dead end" interior states). In particular, $\left|M_{K_1 K_2}\right| = R_{K_1,K_2} > 0$. For Eq. (3.64) to hold, it is therefore necessary that $|b_{K_1}| = |b_{K_2}|$. Repeating the above reasoning recursively leads to $|b_{K_1}| = |b_{K_2}| = ... = |b_{K_n}|$.

For the last interior state of this sequence, K_n, the inequality (3.63) is strict since $R_{K_n,i} > 0$. The eigenvalue equation projected on K_n leads to Eq. (3.62) for K_n:

$$0 \geq M_{K_n K_n}|b_{K_n}| - \sum_{L \neq K_n} \left|M_{K_n L}\right||b_L|. \tag{3.65}$$

If $\mathbf{b} \neq \mathbf{0}$, then $|b_{K_n}| > 0$ and the strict inequality (3.63) for $K = K_n$ used in Eq. (3.65) implies the contradictory result

$$0 > \sum_{L \neq K_n} \left|M_{K_n L}\right| \left(|b_{K_n}| - |b_L|\right) \geq 0. \tag{3.66}$$

As a consequence, $\mathbf{Mb} = \mathbf{0}$ implies that $\mathbf{b} = \mathbf{0}$ necessarily. This proves that $\mathbf{M}(T_\mathrm{r})$ is nonsingular, for any $T_\mathrm{r} \geq 0$.

3.A.3 Proof of the complementarity relation $\sum_i \boldsymbol{P_K^i + P_K^e = 1}$

We define the length-N vector $\mathbf{V} \equiv (1, 1, ..., 1)^\mathrm{T}$, and note that

$$(\mathbf{MV})_K = \sum_L M_{KL} = \sum_j R_{K,j} + \beta_K \tag{3.67}$$

(the $R_{K,L}$ terms cancel). In matrix form, this reads:

$$\mathbf{MV} = \sum_j \mathbf{R}^j + \mathbf{R}^e = \mathbf{M} \left[\sum_j \mathbf{P}^j + \mathbf{P}^e\right]. \tag{3.68}$$

The matrix $\mathbf{M}$ being invertible, this implies $\sum_j \mathbf{P}^j + \mathbf{P}^e = \mathbf{V}$, which once projected on each component K is just the complementarity relation Eq. (3.18).

3.A.4 Detailed balance relations

This appendix is dedicated to proving the detailed balance relations for $\mathcal{R}_{i,j}$ and $\mathcal{B}_i$. We denote g_K the statistical weight of state K. Defining the contributions of individual states to the partition function,

$$Q_K \equiv g_K e^{-E_K/T_\mathrm{r}} \tag{3.69}$$

and similarly for Q_i, we make use of the standard principle of detailed balance for rates connecting individual states,

$$Q_K R_{K,L} = Q_L R_{L,K}, \tag{3.70}$$

and similarly $Q_K R_{K,i} = Q_i R_{i,K}$.

We begin by defining the $N \times N$ nonsingular diagonal matrix $\mathbf{F}$ that is proportional to the equilibrium abundances,

$$F_{KL} \equiv Q_K \delta_{KL}. \tag{3.71}$$

Then Eq. (3.70) combined with the definition Eq. (3.26) implies that $\mathbf{FM}$ is *symmetric*. It therefore follows that its matrix inverse $\mathbf{M}^{-1}\mathbf{F}^{-1}$ is symmetric, and hence that

$$\frac{(\mathbf{M}^{-1})_{KL}}{Q_L} = \frac{(\mathbf{M}^{-1})_{LK}}{Q_K}. \tag{3.72}$$

The transition rate, Eq. (3.21), can be expanded using Eq. (3.29) as

$$\mathcal{R}_{i,j} = R_{i,j} + \sum_{K,L} (\mathbf{M}^{-1})_{KL} R_{i,K} R_{L,j}. \tag{3.73}$$

We then see that:

$$\begin{aligned} Q_i \mathcal{R}_{i,j} &= Q_i R_{i,j} + \sum_{K,L} Q_i (\mathbf{M}^{-1})_{KL} R_{i,K} R_{L,j} = Q_i R_{i,j} + \sum_{K,L} Q_K (\mathbf{M}^{-1})_{KL} R_{K,i} R_{L,j} \\ &= Q_j R_{j,i} + \sum_{K,L} Q_L (\mathbf{M}^{-1})_{LK} R_{K,i} R_{L,j} = Q_j R_{j,i} + \sum_{K,L} Q_j (\mathbf{M}^{-1})_{LK} R_{K,i} R_{j,L} \\ &= Q_j \mathcal{R}_{j,i}, \end{aligned} \tag{3.74}$$

where we have used Eq. (3.70) twice and in the third equality used Eq. (3.72). This proves Eq. (3.24).

We may also relate the effective recombination and photoionization rates. To do so, we consider the case of $T_\mathrm{m} = T_\mathrm{r}$ and define

$$q \equiv \left(\frac{2\pi \mu_e T_\mathrm{r}}{h^2} \right)^{3/2}. \tag{3.75}$$

Then Eq. (3.3) can be written as $Q_{nl}\beta_{nl} = q\alpha_{nl}$. Using Eq. (3.30), we see that

$$\begin{aligned} Q_i\mathcal{B}_i &= Q_i\beta_i + \sum_{K,L} Q_i R_{i,K}(\mathbf{M}^{-1})_{KL}\beta_L = q\alpha_i + \sum_{K,L} Q_K R_{K,i}(\mathbf{M}^{-1})_{KL}\beta_L \\ &= q\alpha_i + \sum_{K,L} Q_L R_{K,i}(\mathbf{M}^{-1})_{LK}\beta_L = q\alpha_i + \sum_{K,L} qR_{K,i}(\mathbf{M}^{-1})_{LK}\alpha_L = q\mathcal{A}_i, \end{aligned} \tag{3.76}$$

where in the last equality we have used Eq. (3.19) with the P_K^i determined by Eq. (3.29). This proves Eq. (3.25).

3.A.5 Proof of Eq. (3.51)

Consider Eq. (3.46) with $\tilde{\Gamma}_K \approx \Gamma_K(T_\mathrm{r})$. The formal solution for the $\tilde{P}_K^{1s}$ is given by:

$$\tilde{P}_K^{1s} = \sum_L \left(\mathbf{M}^{-1}\right)_{KL} \tilde{R}_{L,1s}. \tag{3.77}$$

Therefore one may rewrite Eq. (3.44), for $i = 2s, 2p$:

$$\tilde{\mathcal{R}}_{i,1s} = \tilde{R}_{i,1s} + \sum_K \lambda_{i,K}(T_\mathrm{r})\tilde{R}_{K,1s}, \tag{3.78}$$

where we have defined

$$\begin{aligned} \lambda_{i,K}(T_\mathrm{r}) &\equiv \sum_L R_{i,L}\left(\mathbf{M}^{-1}\right)_{LK} = \sum_L R_{i,L}\frac{Q_K}{Q_L}\left(\mathbf{M}^{-1}\right)_{KL} = \sum_L R_{L,i}\frac{Q_K}{Q_i}\left(\mathbf{M}^{-1}\right)_{KL} \\ &= \frac{g_K}{g_i}\mathrm{e}^{-E_{Ki}/T_\mathrm{r}} P_K^i(T_\mathrm{r}), \end{aligned} \tag{3.79}$$

where in the second equality we used Eq. (3.72), in the third equality we used the detailed balance relation verified by $R_{i,L}$ and $R_{L,i}$, and in the last line we used the formal solution for P_K^i, Eq. (3.60). We therefore obtain Eq. (3.51).

3.A.6 Expression of X_K in terms of x_i, x_e

Taking $T_\mathrm{m} = T_\mathrm{r}$ and using the detailed balance relation $q\alpha_L = Q_L\beta_L$, we rewrite Eq. (3.59) as follows:

$$\begin{aligned} X_K &= q^{-1}n_\mathrm{H}x_e^2\sum_L Q_L\left(\mathbf{M}^{-1}\right)_{LK}\beta_L + \sum_i x_i\sum_L\left(\mathbf{M}^{-1}\right)_{LK}\frac{Q_L}{Q_i}R_{L,i} \\ &= q^{-1}n_\mathrm{H}x_e^2 Q_K\sum_L\left(\mathbf{M}^{-1}\right)_{KL}\beta_L + \sum_i x_i\frac{Q_K}{Q_i}\sum_L\left(\mathbf{M}^{-1}\right)_{KL}R_{L,i}, \end{aligned} \tag{3.80}$$

where in the last equality we have used Eq. (3.72). Using the formal solutions for the probabilities Eqs. (3.60), (3.61), we see that we recover Eq. (3.52).

3.B Appendix: Computation of the effective rates

3.B.1 Sparse matrix technique[4] for the evaluation of the P_K^i

In order to compute the probabilities P_K^i, one needs to solve the linear large linear system given in Eq. (3.16), truncated to only account for states with principal quantum number $n \leq n_{\max}$. Because of selection rules, the system is very sparse and we can solve it efficiently using a sparse matrix approach similar to that of Grin & Hirata [37].

We separate the interior states in groups of identical angular momentum l. For each interface state i, we define the $n_{\max}+1$ vectors $\vec{P}_l^i$, with $0 \leq l \leq l_{\max} \equiv n_{\max}-1$, such that $\vec{P}_l^i$ has $n_{\max}-l$ non-vanishing elements $P_l^i[n] \equiv P_{nl}^i$ for $n \geq l+1$. We also define the matrices $\mathbf{M}_{l,l\pm1}$ of elements given by:

$$M_{l,l\pm1}[n][n'] = \frac{R_{n,l,n',l\pm1}}{\Gamma_{nl}}, \tag{3.81}$$

and the source vectors $\vec{s}_l^{\,i}$ of elements

$$s_l^i[n] = \frac{R_{nl,i}}{\Gamma_{nl}}. \tag{3.82}$$

The system to be solved, Eq. (3.16), can be rewritten in the form:

$$\begin{aligned}
\vec{P}_0^i - \mathbf{M}_{0,1}\vec{P}_1^i &= \vec{s}_0^{\,i} && (3.83)\\
-\mathbf{M}_{l,l-1}\vec{P}_{l-1}^i + \vec{P}_l^i - \mathbf{M}_{l,l+1}\vec{P}_{l+1}^i &= \vec{s}_l^{\,i} \qquad \text{for } 1 \leq l < l_{\max}, && (3.84)\\
-\mathbf{M}_{l_{\max},l_{\max}-1}\vec{P}_{l_{\max}-1}^i + \vec{P}_{l_{\max}}^i &= \vec{s}_{l_{\max}}^{\,i}. && (3.85)
\end{aligned}$$

Note that a simplification from the case of Ref. [37] is that the only non-vanishing source vectors (for interface states $2s$ and np) are $\vec{s}_0^{\,np}$, $\vec{s}_1^{\,2s}$ and $\vec{s}_2^{\,np}$. We now define the matrices $\mathbf{G}_l$ by the recursion relation:

$$\begin{aligned}
\mathbf{G}_{l_{\max}} &\equiv \mathbf{M}_{l_{\max},l_{\max}-1} && (3.86)\\
(\mathbf{1} - \mathbf{M}_{l,l+1}\mathbf{G}_{l+1})\mathbf{G}_l &\equiv \mathbf{M}_{l,l-1} \qquad \text{for } 1 \leq l < l_{\max} && (3.87)
\end{aligned}$$

and the vectors $\vec{S}_2^i, \vec{S}_1^i$ such that:

$$\begin{aligned}
(\mathbf{1} - \mathbf{M}_{2,3}\mathbf{G}_3)\vec{S}_2^i &\equiv \vec{s}_2^{\,i} && (3.88)\\
(\mathbf{1} - \mathbf{M}_{1,2}\mathbf{G}_2)\vec{S}_1^i &\equiv \vec{s}_1^{\,i} + \mathbf{M}_{1,2}\vec{S}_2^i. && (3.89)
\end{aligned}$$

[4] The material presented in this section is unpublished.

Once all these matrix equations have been solved, the solution to the system is obtained as follows:

$$(\mathbf{1} - \mathbf{M}_{0,1}\mathbf{G}_1)\vec{P}_0^i = \vec{s}_0^i + \mathbf{M}_{0,1}\vec{S}_1^i \tag{3.90}$$

$$\vec{P}_1^i = \mathbf{G}_1\vec{P}_0^i + \vec{S}_1^i \tag{3.91}$$

$$\vec{P}_2^i = \mathbf{G}_2\vec{P}_1^i + \vec{S}_2^i \tag{3.92}$$

$$\vec{P}_l^i = \mathbf{G}_l\vec{P}_{l-1}^i, \quad 3 \leq l \leq l_{\max}. \tag{3.93}$$

3.B.2 Extrapolation of the effective rates to $n_{\max} = \infty$

We have tabulated the effective rates $\mathcal{A}_{2s}(T_\mathrm{m}, T_\mathrm{r})$, $\mathcal{A}_{2p}(T_\mathrm{m}, T_\mathrm{r})$ and $\mathcal{R}_{2s,2p}(T_\mathrm{r})$, including all excited states up to the principal quantum number $n_{\max}$, for several values of $n_{\max}$ up to 600, over the temperature range 0.004 eV $\leq T_\mathrm{r} \leq$ 0.4 eV, $0.1 \leq T_\mathrm{m}/T_\mathrm{r} \leq 1$. This range of temperatures corresponds to $20 < z < 1650$ for a wide range of cosmologies. For every pair $(T_\mathrm{m}, T_\mathrm{r})$, we have fitted the effective rates by the following functional form:

$$\mathcal{A}_i(T_\mathrm{m}, T_\mathrm{r}; n_{\max}) = \mathcal{A}_i(T_\mathrm{m}, T_\mathrm{r}; \infty)\left(1 - \frac{\kappa}{(n_{\max})^\gamma}\right), \tag{3.94}$$

and similarly for $\mathcal{R}_{2s,2p}$, where κ and γ depend on T_m and T_r as well as on the coefficient being fitted. This allows us to extrapolate the effective rates to $n_{\max} \to \infty$. Of course, this is only a formal extrapolation, as for n larger than a few thousands, the excited states of hydrogen are no more well defined (see Ref. [87] for a discussion). The extrapolated rates are still more accurate than those computed with a a finite number of states. The residuals of the fit have a maximum relative amplitude of 5×10^{-4} over the whole range of temperature considered, for $200 \leq n_{\max} \leq 600$, and more than an order of magnitude smaller on the restricted range $T_\mathrm{r} \geq 0.04$ eV, $T_\mathrm{m}/T_\mathrm{r} \geq 0.8$ which corresponds to $z \gtrsim 200$ (note that neglecting the overlap of the high-lying Lyman lines leads to errors in the effective rates of similar amplitude [40]). For reference, the maximum relative difference between the effective rates computed with $n_{\max} = 600$ and their extrapolation at $n_{\max} = \infty$ is 0.05 over the whole range of temperature considered, and 0.002 over the restricted range corresponding to $z \gtrsim 200$. We checked that our method recovers the correct case-B recombination coefficient $\alpha_B(T_\mathrm{m}) \equiv \sum_{i=2s,2p} \mathcal{A}_i(T_\mathrm{m}, T_\mathrm{r} = 0; \infty)$. Our extrapolated α_B agrees with the fit of Ref. [72] to better than 0.2 % for $T_\mathrm{m} > 40$ K, which is the accuracy claimed by the authors of Ref. [72].

Chapter 4

Radiative transfer effects in primordial hydrogen recombination[1]

4.1 Introduction

In the previous chapter we have considered one of the two aspects of the recombination problem, the multilevel atom and the "high-n" problem. The second facet of the problem is to properly model the transitions from the "interface" states to the ground state, of particular importance at early times when the overall recombination rate is controlled by the so called "$n = 2$ bottleneck". Hydrogen atoms in the $n = 2$ shell can reach the ground state either through emissions of single photons from the $2p$ state, which slowly escape the optically thick Lyman-α transition through cosmological redshifting, or from the $2s$ state, through forbidden two-photon decays. Previous studies have examined a series of effects that may affect these transition rates, including but not limited to stimulated $2s \rightarrow 1s$ two-photon decays and non-thermal $1s \rightarrow 2s$ two-photon absorptions [47, 48, 49], feedback between neighboring lines of the optically thick Lyman series [41, 42], time-dependent effects in the Lyman-α line [43, 49], two-photon decays from higher excited states [50, 51, 49, 52], and diffusion in the Lyman-α line [44, 46, 45].

The purpose of this chapter is mainly to assess the importance of several radiative transfer effects in the Lyman lines, that have not been investigated yet, or not in sufficient detail (we defer a detailed discussion of radiative transfer in the presence of two-photon decays to Chapter 5). In Section 4.2, we review the theory of radiative transfer in the vicinity of a resonant line in an expanding Universe. We then turn to the Lyman-α line, for which we study the effect of Thomson scattering (Section 4.3.1) and the interaction with the Lyα line of deuterium (Section 4.3.2). In Section 4.4, we quantify

[1]The material in this chapter was adapted from the paper *Radiative transfer effects in primordial hydrogen recombination*, Y. Ali-Haïmoud, D. Grin & C. M. Hirata, Phys. Rev. D **82**, 123502 (2010). Reproduced here with permission, copyright (2010) by the American Physical Society.

the importance of the high-lying, non-overlapping Lyman transitions. Section 4.5 is devoted to the overlapping high-lying Lyman lines. We also explore the possibility of a cosmological recombination maser in Section 4.6. We summarize and discuss our results in Section 4.7. Appendix 4.A summarizes the notation used in this chapter and Appendix 4.B describes the computation of the modified escape probability in a Doppler-dominated line with partial frequency redistribution.

4.2 Radiative transfer in the Lyman lines

4.2.1 Basic notation

In this section, we present the basic quantities and notation used throughout this chapter. We summarize our notation in Table 4.1.

The photon occupation number at frequency ν is denoted f_ν. In the case of a black body spectrum with temperature T, $f_\nu = \left(\mathrm{e}^{h\nu/kT} - 1\right)^{-1}$. We will also make use of the number of photons per hydrogen atom per unit frequency,

$$\mathcal{N}_\nu \equiv \frac{8\pi\nu^2}{c^3 N_{\rm H}} f_\nu, \tag{4.1}$$

where $N_{\rm H}$ is the number density of hydrogen atoms. The population of a species X relative to the total abundance of hydrogen is denoted $x_{\rm X} \equiv N_{\rm X}/N_{\rm H}$. The fractional abundance of hydrogen in the state $[n, l]$ is denoted x_{nl}. For the low l states, we use the spectroscopic notation $s, p, d, ...$, so the ground state is denoted $1s$ and the $[n, l = 1]$ states are denoted np.

This work will be concerned primarily with the $np \rightarrow 1s$ transitions, which will be referred to as the Lyman-n (or Ly-n) transitions. The Ly-2 transition therefore designates, in that convention, the Lyman-α (Lyα) transition. We denote the resonant Ly-n transition frequency

$$\nu_n \equiv \frac{4}{3}\left(1 - \frac{1}{n^2}\right)\nu_{\rm Ly\alpha} = \left(1 - \frac{1}{n^2}\right)\nu_c, \tag{4.2}$$

where $\nu_{\rm Ly\alpha} \approx 2.47 \times 10^{15}$ Hz is the Lyman α frequency, and $\nu_c = \frac{4}{3}\nu_{\rm Ly\alpha}$ is the Lyman-limit frequency. The spontaneous emission rate (Einstein A-coefficient) in the Ly-n transition is [82]:

$$A_{np,1s} = \frac{2^{13}\pi^3}{3^2 n^3} \frac{\left(1 - \frac{1}{n}\right)^{2n-5}}{\left(1 + \frac{1}{n}\right)^{2n+5}} \frac{\nu_n^3}{c^2} \alpha a_0^2 \tag{4.3}$$

$$\underset{n \gg 1}{\sim} \frac{2^{13}\pi^3}{3^2 \exp(4)} \frac{1}{n^3} \frac{\nu_c^3}{c^2} \alpha a_0^2, \tag{4.4}$$

where α is the fine-structure constant and a_0 is the Bohr radius.

We define the ratio

$$f_{\rm eq}^n \equiv \frac{x_{np}}{3x_{1s}}, \tag{4.5}$$

which is the equilibrium value of the photon occupation number at the Ly-n transition frequency.

The Sobolev optical depth for the hydrogen Ly-n transition is [75, 29]:

$$\tau_n = \frac{3c^3 N_{\rm H} x_{1s}}{8\pi H \nu_n^3} A_{np,1s} \left(1 - \frac{x_{np}}{3x_{1s}}\right), \tag{4.6}$$

where $H(z)$ is the Hubble expansion rate. In all that follows, we will neglect stimulated emission in the Lyman lines, as the photon occupation number near Ly-n is of order $f_{\rm eq}^n \ll 1$ (the largest value is for $n = 2$ and is less than 10^{-11} for $z < 1600$). In particular, we can neglect the last term[2] in the expression for the Sobolev optical depth Eq. (4.6).

Finally, we will refer to the matter temperature as $T_{\rm m}$ and the radiation temperature as $T_{\rm r}$. In practice, the matter temperature is locked to the radiation temperature through Thomson scattering, and the relative difference between the two is below a percent until redshift $z \approx 500$ [29, 56].

4.2.2 Line processes

Consider an excited hydrogen atom in the np state; it has two mutually exclusive fates.

The first possibility is that it reaches another excited state $n's$ or $n'd$, with $n' \neq 1$, either through a spontaneous or stimulated decay if $n' < n$ or following the absorption of a CMB photon if $n' > n$. It can also be photoionized by a CMB photon.

The second possibility is that the atom spontaneously decays to the ground state, emitting a Ly-n photon. In principle, this decay can also be stimulated. However, even when accounting for non-thermal distortions to the radiation field, the photon occupation number at Lyman frequencies is extremely small, and stimulated emission in the Lyman lines can be neglected.

The probabilities of these two complementary fates are denoted $p_{\rm ab}^n$ and $p_{\rm sc}^n$, respectively (the justification of the notation will become clearer in the next paragraph). Given the width (or inverse lifetime) Γ_{np} of the np state (the sum of the rates of all transitions depopulating this state), they are given by:

$$p_{\rm sc}^n = \frac{A_{np,1s}}{\Gamma_{np}} = 1 - p_{\rm ab}^n. \tag{4.7}$$

If we now assume that the considered atom was initially in the ground state and reached the np state after the absorption of a resonant Ly-n photon, the two fates mentioned above can be described in a two-photon picture.

First, if the atom reaches another excited state $n' < n$, the overall reaction $\mathrm{H}(1s) + \gamma(\text{Ly-}n) \rightarrow$

[2]When dealing with the possibility of cosmological masers in Section 4.6, we will of course explicitly account for this term and use the appropriate expression for the Sobolev optical depth in a general (not necessarily Lyman) transition.

$\mathrm{H}(n'l) + \gamma'$ is a (possibly stimulated) Raman scattering event. If the atom absorbs a CMB photon and reaches a higher excited state $n' > n$ (or gets photoionized), the overall reaction $\mathrm{H}(1s) + \gamma(\text{Ly-}n) + \gamma' \rightarrow \mathrm{H}(n'l)$ (or $\rightarrow e^- + p^+$) is a two-photon absorption (or two-photon photoionization) event. In these cases we will refer to the absorption of the Ly-n photon as a true absorption event, in the sense that the photon is destroyed in the process. The emission of a Ly-n photon following the inverse reaction chain will be referred to as a true emission event.

Secondly, if the atom decays back to the ground state, the overall reaction $\mathrm{H}(1s) + \gamma(\text{Ly-}n) \rightarrow \mathrm{H}(1s) + \gamma(\text{Ly-}n)$ is a Rayleigh scattering event (which in what follows we will refer to as a scattering event for short). In that case the incoming and outgoing photons have the same frequency in the atom's rest frame. Their frequencies in the comoving frame (frame in which the CMB appears isotropic) are Doppler-shifted with respect to the atom's rest frame frequencies. Since the Doppler shift depends on the relative orientation of the photon propagation direction and the atom's velocity, the frequencies of the incoming and outgoing photons in the comoving frame are in general different. They are however statistically correlated, as will be described in Section 4.2.2.2.

4.2.2.1 True absorption and emission

The rate of true emission of resonant Ly-n photons at frequency ν, per H atom, per frequency interval, is given by [56, 45]:

$$\dot{\mathcal{N}}_\nu\big|_{\mathrm{em}} = \left(\sum_{(n'\neq 1),l} x_{n'l} R_{n'l\rightarrow np} + x_e x_p N_{\mathrm{H}} \alpha_{np} \right) \times p_{\mathrm{sc}}^n \; \varphi_n(\nu). \tag{4.8}$$

In the above equation, $R_{n'l\rightarrow np}$ is the radiative transition rate per hydrogen atom from the $n'l$ state to the np state, including stimulated transitions, α_{np} is the direct recombination coefficient to the np state, including stimulated recombinations, and $\varphi_n(\nu)$ is the line profile, which has the Voigt shape[3]:

$$\varphi_n(\nu) = \frac{1}{\nu_n \Delta_{\mathrm{H}}} \phi_{\mathrm{V}} \left(\frac{\nu - \nu_n}{\nu_n \Delta_{\mathrm{H}}}; a_n \right), \tag{4.9}$$

where

$$\phi_{\mathrm{V}}(x; a) \equiv \frac{a}{\pi^{3/2}} \int_{-\infty}^{+\infty} \frac{\mathrm{e}^{-t^2}}{a^2 + (x-t)^2} \mathrm{d}t, \tag{4.10}$$

is the dimensionless Voigt profile,

$$\Delta_{\mathrm{H}} \equiv \sqrt{\frac{2kT_{\mathrm{m}}}{m_{\mathrm{H}} c^2}} \approx 2.35 \times 10^{-5} \left(\frac{1+z}{1100} \frac{T_{\mathrm{m}}}{T_{\mathrm{r}}} \right)^{-1/2} \tag{4.11}$$

[3]The Voigt profile can be derived quantum-mechanically, in the two-photon picture, when one neglects the variation of multiplicative factors ν/ν_n across the line and uses the resonance approximation. See e.g. Ref. [45] for fits to the correct profile in the case of the Lyman α line. We will consider the correct two-photon profiles in Chapter 5.

is the dimensionless Doppler width and

$$a_n = \frac{\Gamma_{np}}{4\pi\nu_n\Delta_{\rm H}} = \frac{1}{p^n_{\rm sc}}\frac{A_{np,1s}}{4\pi\nu_n\Delta_{\rm H}} \tag{4.12}$$

is the dimensionless Voigt parameter of the line.

For small Voigt parameters $a \ll 1$, which is the case in all Lyman lines at the epoch of recombination, the Voigt profile has the well known asymptotic behaviors in the line center and in the damping wings:

$$\phi_{\rm V}(x;a) \approx \begin{cases} \frac{1}{\sqrt{\pi}}{\rm e}^{-x^2} & \text{if } x \lesssim x_a, \\ \frac{a}{\pi x^2} & \text{if } x \gtrsim x_a, \end{cases} \tag{4.13}$$

where the transition scale x_a is the solution of [88]:

$$x_a^2{\rm e}^{-x_a^2} = \frac{a}{\sqrt{\pi}}. \tag{4.14}$$

In general, for $a \ll 1$, $x_a \sim 3$.

Following Ref. [56], we define

$$f^n_{\rm (em)} \equiv \frac{\sum_{(n'\neq 1),l} x_{n'l}R_{n'l\rightarrow np} + x_e x_p N_{\rm H}\alpha_{np}}{3x_{1s}\Gamma_{np}p^n_{\rm ab}}, \tag{4.15}$$

so that the true emission rate per H atom per frequency interval can be rewritten as:

$$\dot{\mathcal{N}}_\nu\big|_{\rm em} = p^n_{\rm ab}\ 3x_{1s}A_{np,1s}\varphi_n(\nu)f^n_{\rm (em)}. \tag{4.16}$$

The rate of true absorption of resonant photons is simply the total rate of absorption times the true absorption probability. The absorption profile differs from the emission profile by a factor ${\rm e}^{h(\nu-\nu_n)/(kT)}$, where $T = T_{\rm r}$ in the wings (because the low-energy photon of the two-photon process comes from a black-body distribution and the excited states of hydrogen are near Boltzmann equilibrium with each other at temperature $T_{\rm r}$ [49, 45]), and $T = T_{\rm m}$ in the Doppler core, where atomic recoil tends to equilibrate the radiation field with the atoms' thermal velocity distribution. The rate of true absorption of resonant Ly-n photons at frequency ν, per H atom, per frequency interval, is therefore given by:

$$\dot{\mathcal{N}}_\nu\big|_{\rm ab} = -p^n_{\rm ab}3x_{1s}A_{np,1s}\varphi_n(\nu){\rm e}^{\frac{h(\nu-\nu_n)}{kT}}f_\nu. \tag{4.17}$$

The net (uncompensated) rate of true emission of resonant Ly-n photons at frequency ν, per H atom, is therefore:

$$\dot{\mathcal{N}}_\nu\big|_{\rm em,ab} = p^n_{\rm ab}\ 3x_{1s}A_{np,1s}\varphi_n(\nu) \times \left[f^n_{\rm (em)} - {\rm e}^{\frac{h(\nu-\nu_n)}{kT}}f_\nu\right]. \tag{4.18}$$

It will be useful in what follows to cast this expression into a different but equivalent form, which can be done with the following considerations.

The rate of change in the population of the np state is:

$$\begin{aligned}\dot{x}_{np} &= \sum_{n',l} x_{n'l} R_{n'l\rightarrow np} + x_e x_p N_{\rm H} \alpha_{np} - x_{np}\Gamma_{np} \\ &= 3x_{1s}\Gamma_{np} p_{\rm ab}^n f_{\rm (em)}^n + x_{1s} R_{1s\rightarrow np} - x_{np}\Gamma_{np}. \end{aligned} \tag{4.19}$$

The radiative rates (of order $\sim 10^8$ s^{-1}) are many orders of magnitude larger than the overall recombination rate, which is of order the Hubble rate $H \sim 10^{-13}$ s^{-1}. The population of the excited states can therefore be obtained to an excellent accuracy by using the steady-state approximation and setting $\dot{x}_{np} = 0$ in the above equation. Setting the left-hand side of Eq. (4.19) to zero, we can solve for $f_{\rm (em)}^n$:

$$f_{\rm (em)}^n = \frac{1}{3x_{1s}\Gamma_{np} p_{\rm ab}^n} \left[x_{np}\Gamma_{np} - x_{1s} R_{1s\rightarrow np} \right]. \tag{4.20}$$

The total (including both true absorptions and absorptions leading to a scattering) $1s \rightarrow np$ (forward only) excitation rate per H atom is given by:

$$x_{1s} R_{1s\rightarrow np} = 3x_{1s} A_{np,1s} \int \varphi_n(\nu) {\rm e}^{\frac{h(\nu-\nu_n)}{kT}} f_\nu {\rm d}\nu. \tag{4.21}$$

This finally gives us the following relation for $f_{\rm (em)}^n$ [43]:

$$p_{\rm ab}^n f_{\rm (em)}^n = f_{\rm eq}^n - p_{\rm sc}^n \int \varphi_n(\nu) {\rm e}^{\frac{h(\nu-\nu_n)}{kT}} f_\nu {\rm d}\nu. \tag{4.22}$$

We can now rewrite the net rate of true emission of resonant Ly-n photons at frequency ν, per H atom, in a form exactly equivalent to Eq. (4.18):

$$\dot{\mathcal{N}}_\nu\big|_{\rm em,ab} = 3x_{1s} A_{np,1s} \varphi_n(\nu) \left\{ f_{\rm eq}^n - {\rm e}^{\frac{h(\nu-\nu_n)}{kT}} f_\nu + p_{\rm sc}^n \left[{\rm e}^{\frac{h(\nu-\nu_n)}{kT}} f_\nu - \int \varphi_n(\nu') {\rm e}^{\frac{h(\nu'-\nu_n)}{kT}} f_{\nu'} {\rm d}\nu' \right] \right\}. \tag{4.23}$$

4.2.2.2 Coherent scattering

The rate at which resonant scattering removes photons from the line, at frequency ν, (in photons per second per H atom per frequency interval) is the total absorption rate times the scattering probability:

$$\dot{\mathcal{N}}_\nu\big|_{\rm sc,-} = -p_{\rm sc}^n 3x_{1s} A_{np,1s} \varphi_n(\nu) {\rm e}^{\frac{h(\nu-\nu_n)}{kT}} f_\nu. \tag{4.24}$$

The rate at which resonant scattering injects photons in the line, at frequency ν, depends on the absorption at all other frequencies, since incoming and outgoing photon frequencies are correlated:

$$\dot{\mathcal{N}}_\nu\big|_{\mathrm{sc},+} = p_{\mathrm{sc}}^n 3x_{1s}A_{np,1s} \times \int p_n(\nu|\nu')\varphi_n(\nu')\mathrm{e}^{\frac{h(\nu'-\nu_n)}{kT}} f_{\nu'}\mathrm{d}\nu', \tag{4.25}$$

where $p_n(\nu|\nu')$ is the probability that the outgoing photon has frequency ν in the comoving frame given that the incoming photon had frequency ν'. It accounts for the random thermal motions of the scattering atoms (at temperature T_{m}) and depends on the angular probability distribution of a scattering event. It is normalized:

$$\text{for all } \nu', \ \int p_n(\nu|\nu')\mathrm{d}\nu = 1, \tag{4.26}$$

and to respect detailed balance, must satisfy

$$p_n(\nu|\nu')\varphi_n(\nu') = p_n(\nu'|\nu)\varphi_n(\nu). \tag{4.27}$$

The scattering redistribution kernel

$$R_n(\nu,\nu') \equiv p_n(\nu|\nu')\varphi_n(\nu')\mathrm{e}^{\frac{h(\nu'-\nu_n)}{kT}} \tag{4.28}$$

is calculated in Ref. [89] (in which, however, atomic recoil during a scattering event is not accounted for).

The most general form for the rate of change of the photon field through resonant scattering is given by Eqs. (4.24) and (4.25). However, in the case where the radiation field is smooth on the scale of a characteristic frequency shift in a scattering $\langle\Delta\nu^2\rangle^{1/2} = \nu_n\Delta_{\mathrm{H}}$, one can approximate the integral operator by a second-order differential operator. The rate of change of $\mathcal{N}_\nu$ due to scattering is then given by a Fokker-Planck equation [90, 91, 92, 44, 45, 46], accounting for scattering as a diffusive process in frequency space, with a systematic shift (or drift) due to recoil and Doppler boosting:

$$\dot{\mathcal{N}}_\nu\big|_{\mathrm{sc}}^{\mathrm{FP}} = p_{\mathrm{sc}}^n 3x_{1s}A_{np,1s}\frac{\partial}{\partial\nu}\left\{\frac{\nu^2\Delta_{\mathrm{H}}^2}{2}\varphi_n(\nu)\left[\frac{\partial f_\nu}{\partial\nu} + \frac{h}{kT_{\mathrm{m}}}f_\nu\right]\right\}. \tag{4.29}$$

4.2.2.3 The radiative transfer equation

In the vicinity of the Ly-n line, the photon occupation number evolves under the influence of the resonant processes described above, as well as eventual non resonant processes that may act in the vicinity of the line. The time-dependent radiative transfer equation (the Boltzmann equation for

the photon fluid) can be written in the general form:

$$\frac{\mathrm{d}f_\nu}{\mathrm{d}t} \equiv \frac{\partial f_\nu}{\partial t} - H\nu\frac{\partial f_\nu}{\partial \nu} = \dot{f}_\nu\big|_{\mathrm{em,ab,sc}} + \dot{f}_\nu\big|_{\mathrm{nr}}, \tag{4.30}$$

where $\mathrm{d}/\mathrm{d}t$ is the derivative along a photon trajectory, and $\dot{f}_\nu|_{\mathrm{nr}}$ groups all processes that are not resonant with the considered line (these could include absorption and emission from neighboring lines for example). The contribution of resonant processes is obtained with the conversion:

$$\dot{f}_\nu\big|_{\mathrm{em,ab,sc}} = \frac{c^3 N_{\mathrm{H}}}{8\pi\nu^2}\dot{\mathcal{N}}_\nu\big|_{\mathrm{em,ab,sc}}. \tag{4.31}$$

Neglecting the variation of multiplicative factors ν/ν_n across the line, and using the definition of τ_n, Eq. (4.6), as well as Eq. (4.23), the most general expression for the resonant term can be written:

$$\begin{aligned} -\frac{1}{H\nu}\dot{f}_\nu\big|_{\mathrm{em,ab,sc}} &= \tau_n\varphi_n(\nu)\left[\mathrm{e}^{\frac{h(\nu-\nu_n)}{kT}}f_\nu - f^n_{\mathrm{eq}}\right] \\ &+ p^n_{\mathrm{sc}}\tau_n\int\left[\varphi_n(\nu)\varphi_n(\nu')\mathrm{e}^{\frac{h(\nu'-\nu_n)}{kT}} - R_n(\nu,\nu')\right]f_{\nu'}\mathrm{d}\nu'. \end{aligned} \tag{4.32}$$

The radiative transfer equation, Eq. (4.30), with $\dot{f}_\nu|_{\mathrm{em,ab,sc}}$ given by Eq. (4.32), is therefore, in the general case, a time-dependent, partial integro-differential equation. As a result, it is computationally expensive to solve without further approximations.

If the radiation field varies on a frequency scale large compared to a Doppler width, then we can use the Fokker-Planck operator for the scattering term, and the above term can be approximated by:

$$-\frac{1}{H\nu}\dot{f}_\nu\big|_{\mathrm{em,ab,sc}} \approx p^n_{\mathrm{ab}}\tau_n\varphi_n(\nu)\left[\mathrm{e}^{\frac{h(\nu-\nu_n)}{kT}}f_\nu - f^n_{(\mathrm{em})}\right] - p^n_{\mathrm{sc}}\tau_n\frac{\partial}{\partial\nu}\left\{\frac{\nu^2\Delta^2_{\mathrm{H}}}{2}\varphi_n(\nu)\left[\frac{\partial f_\nu}{\partial\nu} + \frac{h}{kT_{\mathrm{m}}}f_\nu\right]\right\}. \tag{4.33}$$

More insight can be gained by considering some characteristic scales of the problem. Using the asymptotic expansion for the wings of the Voigt profile, Eq. (4.13), we obtain the total optical depth for true absorption in each damping wing:

$$\tau_n^{\mathrm{ab,wing}} = p^n_{\mathrm{ab}}\tau_n\frac{a_n}{\pi x_{a_n}}. \tag{4.34}$$

If $\tau_n^{\mathrm{ab,wing}} \ll 1$, the damping wings are optically thin to true absorption, and one can use the Doppler core approximation to the Voigt profile in the radiative transfer equation. If $\tau_n^{\mathrm{ab,wing}} \gg 1$, then the wings are optically thick for true absorption up to a detuning from the line center:

$$\mathcal{W}_n \equiv p^n_{\mathrm{ab}}\tau_n\frac{a_n}{\pi}\nu_n\Delta_{\mathrm{H}} \gg \nu_n\Delta_{\mathrm{H}}. \tag{4.35}$$

In that case, the radiation field is near its equilibrium value $f_\nu \approx f^n_{(\mathrm{em})} \mathrm{e}^{-h(\nu-\nu_n)/kT}$ within a detuning from the line center $|\nu - \nu_n| \lesssim \mathcal{W}_n$.

One can similarly define the optical depth for resonant scattering in each damping wing, $\tau_n^{\mathrm{sc,wing}}$. If $\tau_n^{\mathrm{sc,wing}} \gg 1$, we can see using dimensional analysis that resonant scattering, when described with a Fokker-Planck operator, is effective up to a characteristic detuning from the line center

$$\mathcal{S}_n \equiv \left(p^n_{\mathrm{sc}} \tau_n \frac{a_n}{2\pi}\right)^{1/3} \nu_n \Delta_{\mathrm{H}}. \tag{4.36}$$

The physical meaning of this quantity can be understood as follows. A photon with initial frequency ν can diffuse (in frequency space) to the line center in a characteristic time

$$\Delta t_{\mathrm{diff}} \sim \frac{(\nu - \nu_n)^2}{(\nu_n \Delta_{\mathrm{H}})^2} \frac{1}{c x_{1s} N_{\mathrm{H}} \sigma_n(\nu)}, \tag{4.37}$$

where $\sigma_n(\nu)$ is the cross section for resonant scattering:

$$\sigma_n(\nu) \equiv p^n_{\mathrm{sc}} \frac{3}{8\pi} \frac{c^2}{\nu_n^2} A_{np,1s} \varphi_n(\nu). \tag{4.38}$$

The time it takes for the photon to redshift from ν to ν_n (if $\nu > \nu_n$, or from ν_n to ν in the opposite case) is

$$\Delta t_{\mathrm{redshift}} = \frac{|\nu - \nu_n|}{\nu_n H}. \tag{4.39}$$

Using the damping wings approximation for $\varphi_n(\nu)$ Eq. (4.13), the definition of the Sobolev optical depth Eq. (4.6), and Eq. (4.36), we obtain:

$$\frac{\Delta t_{\mathrm{diff}}}{\Delta t_{\mathrm{redshift}}} \sim \left(\frac{|\nu - \nu_n|}{\mathcal{S}_n}\right)^3. \tag{4.40}$$

Therefore the radiation field will reach the equilibrium spectrum $f_\nu \propto \mathrm{e}^{-h\nu/kT_{\mathrm{m}}}$ within a detuning from the line center $|\nu - \nu_n| \lesssim \mathcal{S}_n$, due to the very fast redistribution of photon frequencies through resonant scattering.

As an illustration, we show in Fig. 4.1 the parameters $\mathcal{W}_2, \mathcal{S}_2$ for the Lyman-α line, extracted from the MLA code described in Ref. [49]. We see that for $z \gtrsim 800$, $\mathcal{S}_2 \geq \mathcal{W}_2 > \nu_{\mathrm{Ly}\alpha} \Delta_{\mathrm{H}}$ and at all relevant times $\mathcal{S}_2 \gg \nu_{\mathrm{Ly}\alpha} \Delta_{\mathrm{H}}$. According to the above discussion, the radiation field in the vicinity of Lyα is therefore smooth on a frequency scale $\Delta\nu \sim \mathcal{S}_2$ around line center, and the use of the Fokker-Planck operator for resonant scattering is well justified.

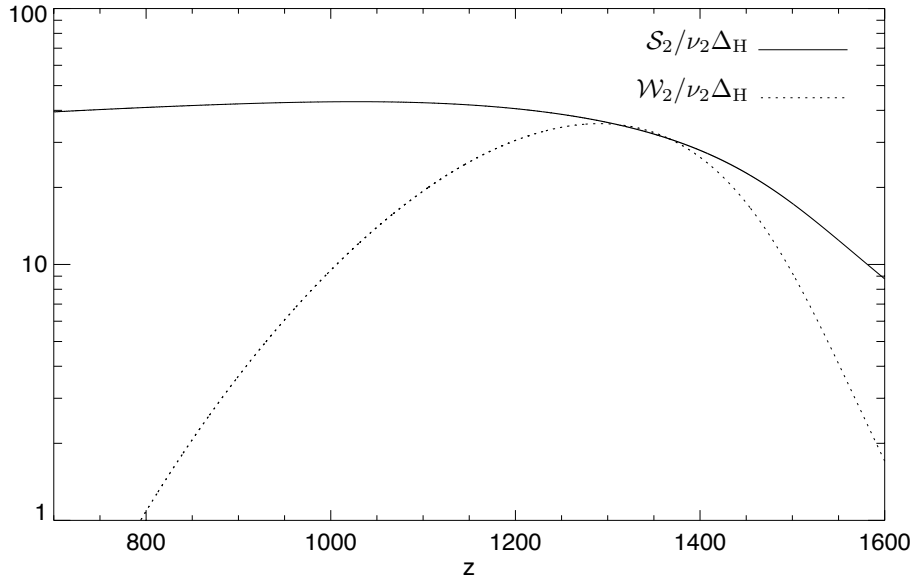

Figure 4.1: Characteristic widths $\mathcal{W}, \mathcal{S}$ for the Lyman-α line, in units of Doppler widths, as a function of redshift for a standard recombination history.

4.2.3 Net decay rate in the Lyman-n line

The exact shape of the radiation field in the vicinity of resonant lines is by itself of interest when predicting potentially observable spectral distortions to the black body spectrum of the CMB [35]. In the context of cosmological recombination, the quantities of interest are the net (uncompensated) bound-bound and bound-free rates, which are required to evolve the atomic level populations and the free electron fraction in a MLA code. In particular, the net rate of $np \rightarrow 1s$ decays is given by:

$$\dot{x}_{np\rightarrow 1s} = \dot{x}_{1s}\big|_{np} = -\dot{x}_{np}\big|_{1s} = \frac{\mathrm{d}}{\mathrm{d}t}\int \mathcal{N}_\nu \mathrm{d}\nu = \int \dot{\mathcal{N}}_\nu\big|_{\rm em,ab}\mathrm{d}\nu. \tag{4.41}$$

Using Eq. (4.23), we see that this can be written:

$$\dot{x}_{np\rightarrow 1s} = 3x_{1s}A_{np,1s}\int \left[f^n_{\rm eq} - \mathrm{e}^{\frac{h(\nu-\nu_n)}{kT}} f_\nu\right]\varphi_n(\nu)\mathrm{d}\nu, \tag{4.42}$$

where we used the fact that the term proportional to $p^n_{\rm sc}$ in Eq. (4.23) integrates to zero.

As can be seen in Eq. (4.42), the net decay rate in the Ly-n transition depends on the radiation field. The latter in turns depends on the atomic level populations through $\tau_n, p^n_{\rm sc}$ and $f^n_{\rm eq}$, as well on eventual non-resonant processes acting in the vicinity of the line, as can be seen from the radiative transfer equation [Eqs. (4.30), (4.32) or (4.33)].

4.2.4 The Sobolev approximation

Equations (4.30) and (4.32) give the most general form[4] of the radiative transfer equation, in a homogeneous expanding Universe. It has no analytic solution, because of its complexity and since it requires the values of the level populations, which in turn depend on the radiation field. It can however be simplified and decoupled under some approximations, for which an analytic solution exists. The Sobolev approximation [75, 29] relies on the following assumptions:

(i) *No non-resonant processes* act in the vicinity of the line ($\dot{f}_\nu|_{\rm nr} = 0$ in Eq. (4.30)).

(ii) *Steady-state*: the time it takes a photon to redshift across the line is of order $w/H\nu_n$, where w is the characteristic line width. If the line is very narrow, $w \ll \nu_n$, then this time is much smaller than the Hubble time, therefore physical quantities, such as $n_{\rm H}, T_{\rm r}, T_{\rm m}, H, x_e, x_{nl}$ vary very little during the time it takes a photon to redshift through the line. As a consequence, one can neglect the time dependence in Eq. (4.30).

(iii) *Equal absorption and emission profile.* This assumption also derives from the assumption of an infinitesimally thin line, in which case one can take the exponential factors to be unity in Eq. (4.17).

(iv) *Complete redistribution* of emitted photons. Mathematically, this means that $p_n(\nu|\nu')$ is independent of ν' in Eq. (4.25). Because of assumption (iii), it is also assumed that $p_n(\nu|\nu') = \varphi_n(\nu)$, i.e., the scattered photons are completely redistributed over the line profile. This implies that $R_n(\nu,\nu') = \varphi_n(\nu)\varphi_n(\nu')$, and therefore the integral in Eq. (4.32) vanishes (taking the exponential to be unity).

The radiative transfer equation, under these assumptions, becomes the much simpler ordinary differential equation:

$$\frac{{\rm d}f_\nu}{{\rm d}\nu} = \tau_n \varphi_n(\nu)\left(f_\nu - f^n_{\rm eq}\right). \tag{4.43}$$

It has the analytic solution

$$f_\nu = f^n_{\rm eq} + (f^n_+ - f^n_{\rm eq}) \exp\left[-\tau_n \int_\nu^{+\infty} \varphi_n(\nu'){\rm d}\nu'\right], \tag{4.44}$$

where f^n_+ is the photon occupation number at the blue side of the line. The photon occupation number at the red side of the line is therefore

$$f^n_- = f^n_{\rm eq} + (f^n_+ - f^n_{\rm eq}){\rm e}^{-\tau_n}. \tag{4.45}$$

[4]We neglected the variation of phase-space factors ν/ν_n across the line, as well as stimulated emission and stimulated scatterings.

Integrating Eq. (4.43) from $-\infty$ to $+\infty$ gives

$$f_+^n - f_-^n = \tau_n \int \left[f_\nu - f_{\rm eq}^n\right] \varphi_n(\nu) \mathrm{d}\nu. \tag{4.46}$$

This, combined with Eqs. (4.42) and (4.45) finally gives us the standard Sobolev expression for the net decay rate in the line:

$$\dot{x}_{np\rightarrow 1s} = 3 x_{1s} A_{np,1s} P_{\rm S,}{}_n \left[f_{\rm eq}^n - f_+^n\right], \tag{4.47}$$

where

$$P_{{\rm S},n} \equiv \frac{1 - \mathrm{e}^{-\tau_n}}{\tau_n} \tag{4.48}$$

is the Sobolev escape probability. In the case of Lyman transitions, $\tau_n \gg 1$, and $P_{{\rm S},n} \approx 1/\tau_n$. The net decay rate becomes, using Eq. (4.6):

$$\dot{x}_{np\rightarrow 1s} = \frac{8\pi H \nu_n^3}{c^3 N_{\rm H}} \left[f_{\rm eq}^n - f_+^n\right], \tag{4.49}$$

which is simply the rate at which distortion photons redshift across the line, which we derived heuristically in Section 2.2.1.

The Sobolev approximation provides relatively accurate net decay rates, despite the multiple assumptions that it relies on, and recombination histories currently used for CMB analysis [29, 30], which use this approximation, are accurate at the percent level. The level of precision required by upcoming CMB experiments has motivated recent work to obtain more accurate solutions to the radiative transfer equation and net bound-bound rates in the optically thick Lyman lines. In this work we investigate previously ignored radiative transfer effects, and quantify as much as possible the errors made by the inevitable approximations that still need to be made.

4.3 The Lyman alpha line

The Lyman-α transition is one of the bottlenecks of hydrogen recombination. Electrons recombine to the excited states of hydrogen, from which they eventually cascade down to the $n = 2$ state. They can then reach the ground state either by a two-photon decay from the $2s$ state, with rate $\Lambda_{2s1s} \approx 8.22\ \mathrm{s}^{-1}$, or from the $2p$ state, by redshifting out of the Lyman-α resonance, with rate $A_{2p1s} P_{\rm esc}$, where $P_{\rm esc}$ is the escape probability. Due to its substantial impact on the recombination history (see for example Fig. 11 in Ref. [43]), the net decay rate, or equivalently the escape probability in Lyα has been studied extensively, including time-dependent effects [90, 43], two-photon processes [49, 52], resonant scattering [93, 94, 44, 46, 45], and Thomson scattering [46]. In this section we consider two additional effects: the non-local aspect of Thomson scattering (Section 4.3.1), and a quantitative estimate of the effect of deuterium on hydrogen recombination (Section 4.3.2).

To simplify the notation we drop the subscripts and superscripts "2" in this section, and all the quantities previously defined implicitly refer to Lyα.

4.3.1 Thomson scattering in Lyman-α

Thomson scattering in the vicinity of resonant lines was investigated in the context of helium recombination [58] with a Monte Carlo method and found to lead to negligible changes to the recombination history. Its effect on the hydrogen Lyα line was investigated recently [46] and found to lead to negligible corrections to the escape probability and the recombination history. In Ref. [46] however, electron scattering was described with the Kompaneets equation, which is not valid in the context of cosmological hydrogen recombination, as we argue below. Here we provide a more rigorous treatment of Thomson scattering, using the full redistribution kernel, which we incorporate in the Lyman-α radiative transfer code described in Ref. [45].

The strength of Thomson scattering is characterized by its differential optical depth, flat in frequency in the non relativistic limit [58]:

$$\eta_e \equiv \frac{N_{\rm H} x_{\rm e} \sigma_{\rm T} c}{H \nu_{\rm Ly\alpha}}, \tag{4.50}$$

where $\sigma_{\rm T} \approx 6.65 \times 10^{-25}$ cm^2 is the Thomson cross section.

Thomson scatterings can affect the recombination history if they take place within the characteristic width $\mathcal{W}$ over which the Lyman-α line is optically thick for true absorption. We show in Fig. 4.2 the mean number of Thomson scattering events within a detuning $\mathcal{W}$ of line center, $\eta_e \mathcal{W}$. We see that it peaks at ~ 0.08 for $z \sim 1375$, and remains above 0.001 for $z \gtrsim 1000$, which suggests that Thomson scattering is potentially important at the sub-percent level and should be carefully accounted for.

The rate of change of the number of photons per unit frequency per hydrogen atom due to Thomson scattering, neglecting stimulated scatterings, is:

$$\dot{\mathcal{N}}_\nu\big|_{\rm T} = N_{\rm H} x_{\rm e} \sigma_{\rm T} c \left[-\mathcal{N}_\nu + \int \mathcal{N}_{\nu'} R_{\rm T}(\nu' \rightarrow \nu) {\rm d}\nu' \right], \tag{4.51}$$

where $R_{\rm T}(\nu' \rightarrow \nu)$ is the electron scattering kernel.

If the radiation field is smooth on the scale of a characteristic frequency shift during a scattering $\Delta\nu_{\rm e} \equiv \nu_{\rm Ly\alpha} \sqrt{2kT_{\rm m}/m_e c^2}$, then the integral operator for electron scattering can be approximated by a Fokker-Planck operator, accounting for diffusion and drift in frequency space with rates [95]:

$$\frac{{\rm d}\langle \Delta\nu^2 \rangle}{{\rm d}t} = N_{\rm H} x_{\rm e} \sigma_{\rm T} c \, \nu^2 \frac{2kT_{\rm m}}{m_{\rm e} c^2} \tag{4.52}$$

$$\frac{{\rm d}\langle \Delta\nu \rangle}{{\rm d}t} = N_{\rm H} x_{\rm e} \sigma_{\rm T} c \, \nu \frac{4kT_{\rm m} - h\nu}{m_{\rm e} c^2}. \tag{4.53}$$

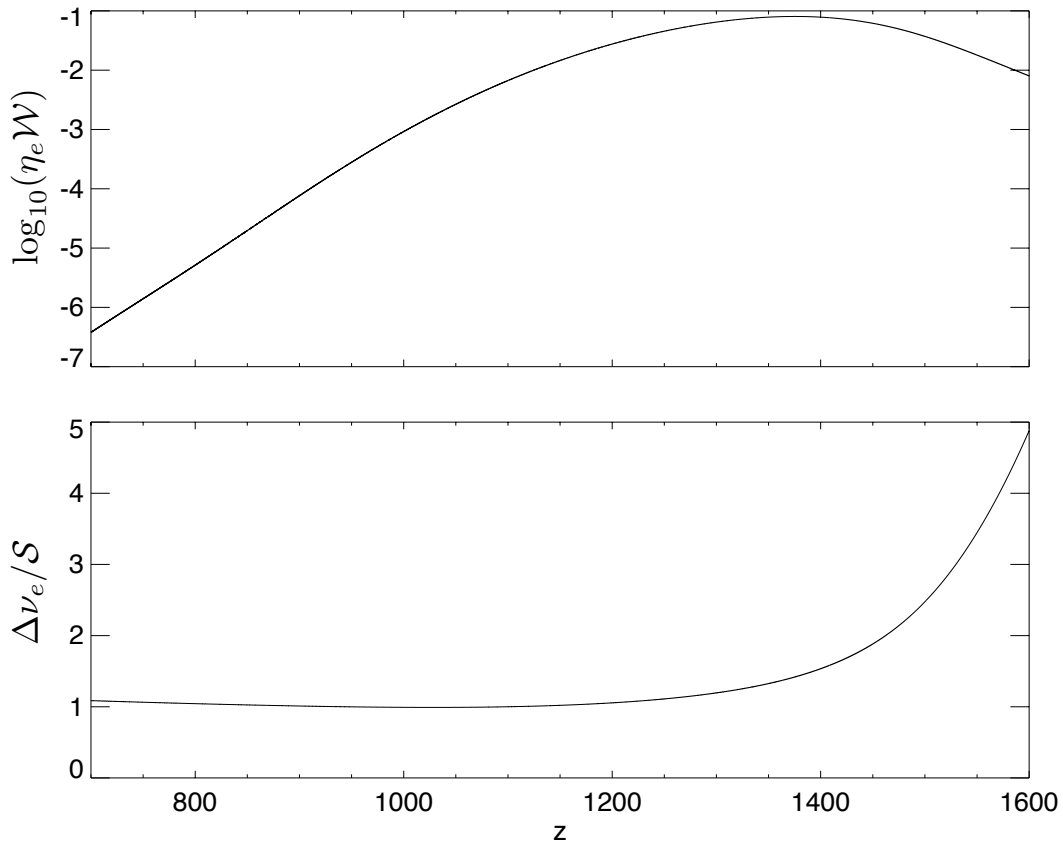

Figure 4.2: *Top panel*: characteristic number of electron scatterings within the region where the Lyα line is optically thick for true absorption. *Bottom panel*: ratio of the characteristic frequency shift during a Thomson scattering event to the characteristic width over which the Lyα line is smoothed out by frequent resonant scatterings.

The corresponding Fokker-Planck equation is known as the Kompaneets equation:

$$\dot{\mathcal{N}}_\nu\big|_{\rm T}^{\rm FP} = N_{\rm H} x_{\rm e} \sigma_{\rm T} c \frac{k T_{\rm m}}{m_{\rm e} c^2} \frac{\partial}{\partial \nu} \left\{ \nu^4 \left[\frac{\partial}{\partial \nu} \left(\frac{\mathcal{N}_\nu}{\nu^2} \right) + \frac{h}{k T_{\rm m}} \frac{\mathcal{N}_\nu}{\nu^2} \right] \right\}. \tag{4.54}$$

This is the approximation that was made in Ref. [46]. However, due to the small mass of the electron, the characteristic frequency shift during an electron scattering event $\Delta\nu_{\rm e}$ can be larger than the characteristic width over which the radiation field changes in the vicinity of the line. This characteristic width is of order $\mathcal{S}$ (which is $\gtrsim \mathcal{W}$ at all times, see Fig. 4.1), set by frequency diffusion due to resonant scattering near line center (see end of Section 4.2.2.3). We see from Fig. 4.2 that $\Delta\nu_e \geq \mathcal{S}$ at all times, and therefore electron scattering cannot be considered as a diffusive process and the Kompaneets equation is not valid in this context.

We have implemented the correct integral scattering kernel given by Eq. (4.51) in the Lyman-α transfer code developed in Ref. [45]. Accurate approximate expressions of the electron scattering

kernel $R_{\rm T}(\nu' \to \nu)$ are given in Ref. [95]. For the purpose of our calculation, we only need the kernel calculated in the non-relativistic limit adequate here, for a dipolar angular distribution [96]. We set

$$R_{\rm T}(\nu' \to \nu) + R_{\rm T}(\nu \to \nu') = \frac{2}{\Delta\nu_e}\mathcal{R}\left(\frac{\nu - \nu'}{\Delta\nu_e}\right), \tag{4.55}$$

where the dimensionless kernel $\mathcal{R}$ is given by[5] [96, 95]:

$$\mathcal{R}(\beta) = \frac{1}{10\sqrt{\pi}}\left[11 + 4\beta^2 + \frac{1}{2}\beta^4\right]\exp\left(-\frac{\beta^2}{4}\right) - \frac{1}{4}\left[3 + \beta^2 + \frac{1}{10}\beta^4\right]|\beta|\ \mathrm{erfc}\left(\frac{|\beta|}{2}\right). \tag{4.56}$$

We moreover require that detailed balance is satisfied, i.e., that the Planck spectrum $\mathcal{N}_\nu \propto \nu^2 \mathrm{e}^{-h\nu/(kT_{\rm m})}$ (in the limit $h\nu \gg kT_{\rm m}$ valid here) is preserved by imposing:

$$\frac{R_{\rm T}(\nu \to \nu')}{R_{\rm T}(\nu' \to \nu)} = \frac{\nu'^2}{\nu^2}\exp\left[\frac{h(\nu - \nu')}{kT_{\rm m}}\right]. \tag{4.57}$$

When evolving the number of photons per H nucleus per frequency bin in the $i^{\rm th}$ frequency bin, $N_i = \mathcal{N}_{\nu_i}\nu_i\Delta\ln\nu$, the radiative transfer code uses a backward Euler method which requires inverting the matrix equation:

$$M_{ij}(t + \Delta t)N_j(t + \Delta t) = N_i(t). \tag{4.58}$$

The matrix to be inverted, $\mathbf{M}$, is tridiagonal in the case where only absorption, emission, and resonant scattering (described by a Fokker-Planck operator) are present. Thomson scattering breaks this tridiagonality, which renders the system prohibitively time-consuming to invert ($\mathbf{M}$ is a 801×801 matrix in our lowest resolution run). However, we can use the fact that Thomson scattering is only a perturbation to the radiative transfer equation. Therefore, $\mathbf{M} = \mathbf{M}_0 + \delta\mathbf{M}$, where $\mathbf{M}_0$ is an easily invertible tridiagonal matrix, and the perturbation $\delta\mathbf{M}$ due to Thomson scattering is such that its eigenvalues are always small compared to those of $\mathbf{M}_0$. We can therefore invert the perturbed matrix using the expansion:

$$(\mathbf{M}_0 + \delta\mathbf{M})^{-1} = \mathbf{M}_0^{-1} - \mathbf{M}_0^{-1}(\delta\mathbf{M})\mathbf{M}_0^{-1} + \mathbf{M}_0^{-1}(\delta\mathbf{M})\mathbf{M}_0^{-1}(\delta\mathbf{M})\mathbf{M}_0^{-1} - \cdots. \tag{4.59}$$

We find that the second order of the expansion is usually sufficient, with a maximum change of the net decay rate in the line of 1.5×10^{-5} between the first and second order.

We show the resulting changes in the free electron fraction in Fig. 4.3. We can see that at early times, $z \gtrsim 1350$, Thomson scattering *delays* recombination. Indeed, the relatively large frequency changes during electron scatterings allow photons to be moved from the red side of the line to the blue side of the line, and vice versa. Because of the large jump in photon occupation number across the line, the net photon flux is from the red side to the blue side. As a consequence, some escaping

[5] There is a typo in Ref. [96]: erf should be erfc.

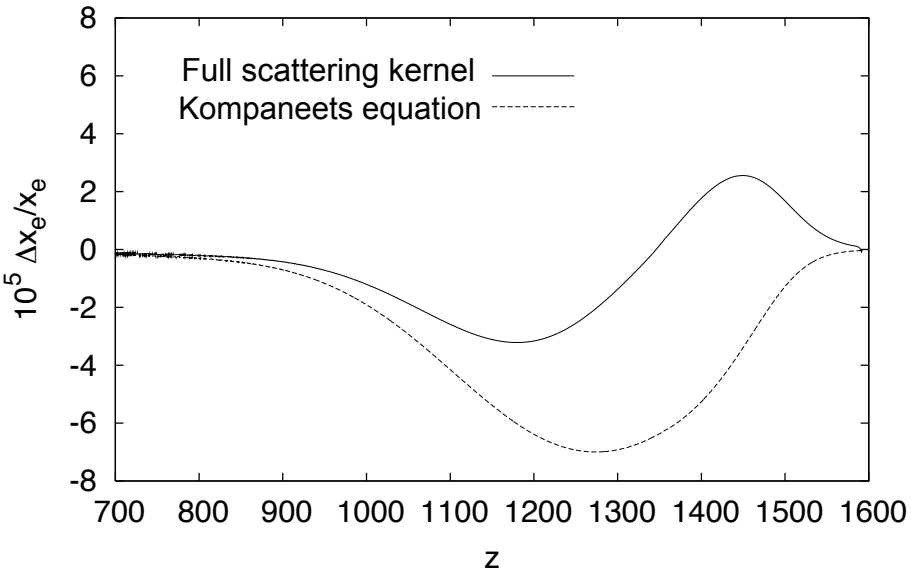

Figure 4.3: Changes to the recombination history due to Thomson scattering. Figure provided by Christopher Hirata.

photons are re-injected into the line, where they can be absorbed, which decreases the escape rate and delays recombination. At later times, this effect is not so important as the radiation profile becomes smoother ($\Delta\nu_e \sim \mathcal{S}$, see Fig. 4.2). The systematic frequency loss during scattering events due to electron recoil starts to dominate, and Thomson scattering helps photons escaping out of the line and speeds up recombination.

For comparison, we have also implemented the Kompaneets equation (4.54), in a similar fashion as resonant scattering (see Ref. [45] for details on the implementation). We can see that using the Kompaneets equation does not represent accurately the physics of Thomson scattering, as it cannot capture the large frequency shifts at early times. The error in the correction is of order the correction itself, and it has the wrong sign at early times. However, the basic conclusion reached in Ref. [46] remains valid: Thomson scattering can indeed be safely ignored during cosmic hydrogen recombination, since it leads to corrections to the ionization fraction of at most $\Delta x_e/x_e \sim \pm 3\times 10^{-5}$.

4.3.2 Interaction with the Deuterium Lyman-α line

4.3.2.1 Motivations

A second radiative transfer effect associated with the Lyman-α transition is the interaction of the hydrogen and deuterium lines. Due to the slightly larger reduced mass of deuterium, the Lyman-α frequency in deuterium $\nu_{\rm D} \equiv \nu_{{\rm Ly}\alpha}({\rm D})$ is shifted to a higher frequency than that of hydrogen,

$\nu_{\rm H} \equiv \nu_{{\rm Ly}\alpha}({\rm H})$. The relative shift, to first order in $m_{\rm e}/m_{\rm p}$, and with $m_{\rm D^+} \approx 2m_{\rm p}$, is:

$$\frac{\nu_{\rm D} - \nu_{\rm H}}{\nu_{\rm H}} \approx \frac{m_{\rm e}}{2m_{\rm p}} \approx 2.7 \times 10^{-4}. \tag{4.60}$$

This separation is ~ 10 times the Doppler width of the hydrogen line so the D Ly-α line center lies in the blue damping wing of the H Ly-α line. Despite the tiny fractional abundance of primordial deuterium $x_{\rm D} = 2.87^{+0.22}_{-0.21} \times 10^{-5}$ [97], the D Ly-α line is still optically thick during cosmological hydrogen recombination, $\tau_{\rm D,Ly\alpha} \approx x_{\rm D}\tau_{\rm H,Ly\alpha} \sim 10^2 - 10^4$. This has motivated the authors of Ref. [42] to consider the possible screening of radiation incoming into the H Lyα line by the optically thick, bluer D Lyα line. Ref. [42] pointed out that the deuterium line lies in the optically thick part of the H Lyα wings ($|\nu_{\rm D} - \nu_{\rm H}| \lesssim \mathcal{W}, \mathcal{S}$, see Fig. 4.1) and concluded, without further justification, that the screening was absent. Here we explain in detail how the two lines interact and explicitly compute the effect of deuterium on the recombination history. We show that the effect is completely negligible, independently of the fact that $|\nu_{\rm D} - \nu_{\rm H}| \lesssim \mathcal{W}, \mathcal{S}$ (which does, however, indeed lead to an additional suppression).

4.3.2.2 Spectral distortions caused by deuterium

Our first step is to understand the physical mechanism of deuterium recombination. The rates of D and H recombination are tied together via the charge-exchange reaction

$$\mathrm{D^+ + H}(1s) \leftrightarrow \mathrm{D}(1s) + \mathrm{H^+}, \tag{4.61}$$

which has a forward rate coefficient of order $\sim 10^{-9}\,\mathrm{cm^3\,s^{-1}}$ [98]; at recombination-era densities of $\sim 500\,\mathrm{cm^{-3}}$ this implies an equilibrium timescale of $\sim 2 \times 10^6\,\mathrm{s}$, i.e., six orders of magnitude shorter than the recombination timescale itself. Thus to a very good approximation, the deuterium ionization fraction tracks that of hydrogen:

$$\frac{x_{\rm D^+}}{x_{\rm D(1s)}} \approx \frac{x_{\rm H^+}}{x_{\rm H(1s)}} \mathrm{e}^{-\frac{\Delta E_{\rm I}}{kT_{\rm m}}} \approx \frac{x_e}{1 - x_e} \mathrm{e}^{-\frac{\Delta E_{\rm I}}{kT_{\rm m}}} \approx \frac{x_e}{1 - x_e}, \tag{4.62}$$

where the difference in ionization energies of deuterium and hydrogen, $\Delta E_{\rm I}/k \approx 41$ K, is small compared to the matter temperature during recombination. Using the last approximation, we obtain

$$x_{\rm D^+} \approx x_{\rm D} x_e, \tag{4.63}$$

$$x_{\rm D(1s)} \approx x_{\rm D} x_{\rm H(1s)}. \tag{4.64}$$

Note, however, that the populations of the excited states *do not*, satisfy such a relation, i.e.,, *a priori*, $x_{\rm D(2p)} \neq x_{\rm D} x_{\rm H(2p)}$.

Like hydrogen, deuterium may recombine radiatively and reach the ground state either via $2s \to 1s$ two-photon decay or Lyα escape; the *net* rate of recombinations (H+D) is simply the sum of the two rates, and charge exchange [Eq. (4.61)] distributes the bound electrons between H and D. It is clear that the absolute rate of transitions to the ground state via the optically thin $2s \to 1s$ transition will be much smaller for D than H because of its lower abundance; however for the Lyα channel in principle the rates could be comparable because the Lyα(D) optical depth is smaller than the Lyα(H) optical depth by a factor of $\sim x_{\rm D}$, and hence the escape probability is enhanced by a factor of $x_{\rm D}^{-1}$. However, since Lyα(D) is located blueward of Lyα(H), all photons emitted in Lyα(D) will be re-absorbed in Lyα(H); and all photons absorbed in the Lyα(D) transition would have been absorbed anyway had the deuterium not been present. Thus the *net* (integrated over time) number of recombinations that proceed via Lyα(D) escape is zero. However, the re-absorption of the D photons is not instantaneous, so at any given time the presence of deuterium causes an additional distortion to the radiation field (on top of the distortion to the blackbody spectrum due to H$(2p) \to$ H$(1s)$ decays in the blue wing of H Lyα). The number of additional distortion photons per hydrogen atom is

$$U = \int \frac{8\pi\nu^2}{c^3 N_{\rm H}} [f_\nu^{(\rm H+D)} - f_\nu^{(\rm H)}] \, {\rm d}\nu, \tag{4.65}$$

where $f_\nu^{(\rm H)}$ is the photon occupation number when only hydrogen is present, and $f_\nu^{(\rm H+D)}$ is its value when the presence of deuterium is accounted for.

Note that $U(t) \to 0$ at both early times (because the radiation field is thermal independently of the presence of deuterium) and late times (since after recombination is over, there are no more Lyα photons produced).

The correction to the rate of formation of ground-state atoms through the (H+D) $2p \to 1s$ channel is then equal to the rate of creation of distortion photons:

$$\Delta\dot{x}_{1s}|_{\rm Ly\alpha(D)} = -\Delta\dot{x}_e|_{\rm Ly\alpha(D)} = \dot{U}. \tag{4.66}$$

4.3.2.3 Analytic estimate for the number of spectral distortion photons[6]

We now compute the number of spectral distortion photons. We will treat the deuterium line in the Sobolev approximation, i.e., assuming that its profile is a delta-function. This approximation is well justified since the deuterium line is dominated by its Doppler core: the damping wings are only marginally optically thick, and the differential optical depth in the deuterium wings is always much smaller than that of hydrogen anyway (see for example Fig. 7 of Ref. [42]). In this case complete redistribution is a good approximation since both partial and complete redistribution have a similar

[6]This section is not part of the published paper [40], where the interested reader will find a more elaborate treatment that accounts for frequency diffusion. Here I have opted for a simpler and less complete, but hopefully more enlightening calculation.

characteristic frequency width, the Doppler width of the line (see Appendix 4.B). For the hydrogen line, we only consider true absorption and emission and neglect frequency diffusion due to resonant scattering. We will discuss the validity of this approximation at the end of the section. Finally, since $\nu_{\rm D} - \nu_{\rm H} \sim 10^{-4}\nu_{\rm H}$, we can work in the steady-state approximation in the vicinity of the Lyα lines.

In the blue damping wing of the hydrogen Lyα line, and for $\nu \neq \nu_{\rm D}$, the steady-state radiative transfer equation for the distortion $\Delta f_\nu \equiv f_\nu - {\rm e}^{-h\nu/(kT_{\rm r})}$ can be written

$$\frac{\partial \Delta f_\nu}{\partial \nu} = \frac{\mathcal{W}}{(\nu - \nu_{\rm H})^2}\left(\Delta f_\nu - \Delta f_{\rm eq}^{\rm H}\right), \tag{4.67}$$

where $\Delta f_{\rm eq}^{\rm H} \equiv x_{{\rm H}(2p)}/(3x_{{\rm H}(1s)}) - {\rm e}^{-h\nu_{\rm H}/(kT_{\rm r})}$. To arrive at Eq. (4.67), we have used Eq. (4.18) and (4.31) in the damping wing approximation, used Eq. (4.22) to approximate $f_{\rm (em)}^{\rm H} \approx f_{\rm eq}^{\rm H}$, and the definition of $\mathcal{W}$, Eq. (4.35). We have also assumed equal absorption and emission profiles, which is a good approximation since $h(\nu_{\rm D} - \nu_{\rm H})/(kT_{\rm r}) \ll 1$.

The optical depth in the H Lyα damping wing blueward of the deuterium line is

$$\tau \equiv \frac{\mathcal{W}}{\nu_{\rm D} - \nu_{\rm H}}. \tag{4.68}$$

We find that $0.02 \lesssim \tau \lesssim 3$ for $700 < z < 1600$, with a maximum of $\tau \approx 3.2$ at $z \approx 1300$. The photon occupation number incoming on the blue side of the deuterium line is therefore

$$\Delta f_+^{\rm D} = \Delta f_{\rm eq}^{\rm H}\left(1 - {\rm e}^{-\tau}\right), \tag{4.69}$$

where we assumed that the photon occupation number at $\nu \to \infty$ is a blackbody (i.e., we neglect feedback from Ly β).

In the Sobolev approximation, $\Delta f_-^{\rm D} = \Delta f_{\rm eq}^{\rm D} \equiv x_{{\rm D}(2p)}/(3x_{{\rm D}(1s)}) - {\rm e}^{-h\nu_{\rm D}/(kT_{\rm r})}$ since the deuterium line is optically thick. The radiation field between the two lines is therefore

$$\Delta f_\nu^{\rm (H+D)} = \Delta f_{\rm eq}^{\rm H} + \left(\Delta f_{\rm eq}^{\rm D} - \Delta f_{\rm eq}^{\rm H}\right)\exp\left[\frac{\mathcal{W}}{\nu_{\rm D} - \nu_{\rm H}} - \frac{\mathcal{W}}{\nu - \nu_{\rm H}}\right], \quad \nu_{\rm H} < \nu < \nu_{\rm D}, \tag{4.70}$$

whereas in the absence of the deuterium line, it would be

$$\Delta f_\nu^{\rm (H)} = \Delta f_{\rm eq}^{\rm H}\left(1 - \exp\left[-\frac{\mathcal{W}}{\nu - \nu_{\rm H}}\right]\right). \tag{4.71}$$

The number of distortion photons [Eq. (4.65)] is therefore

$$U = \frac{8\pi\nu_{{\rm Ly}\alpha}^2}{c^3 N_{\rm H}}(\nu_{\rm D} - \nu_{\rm H})\left[\left(\Delta f_{\rm eq}^{\rm D} - \Delta f_{\rm eq}^{\rm H}\right) + \Delta f_{\rm eq}^{\rm H}{\rm e}^{-\tau}\right]\mathcal{I}(\tau), \tag{4.72}$$

where we have defined

$$\mathcal{I}(\tau) \equiv \tau \mathrm{e}^{\tau} \int_{\tau}^{\infty} \mathrm{e}^{-u} \frac{\mathrm{d}u}{u^2}. \tag{4.73}$$

We find that the function $\mathcal{I}(\tau)$ is fit to better than 2% accuracy over the range of interest $0.02 < \tau < 3.3$ by the simple formula

$$\mathcal{I}(\tau) \approx \frac{1}{1 + 1.5\ \tau^{0.8}}. \tag{4.74}$$

Using Eq. (4.69) and the definition of $R_{\mathrm{Ly}\alpha}$ (the rate of Lyα escape per atom in the $2p$ state), Eq. (2.20), we can rewrite Eq. (4.72) in the form

$$U = H^{-1}\ \frac{\nu_{\mathrm{D}} - \nu_{\mathrm{H}}}{\nu_{\mathrm{H}}}\ \mathcal{I}(\tau) R_{\mathrm{Ly}\alpha} 3 x_{\mathrm{H}(1s)} \left[\Delta f_{\mathrm{eq}}^{\mathrm{D}} - \Delta f_{+}^{\mathrm{D}}\right]. \tag{4.75}$$

We now need to estimate the population of the excited state in deuterium in order to obtain the difference $\Delta f_{\mathrm{eq}}^{\mathrm{D}} - \Delta f_{+}^{\mathrm{D}}$. The population of the $n = 2$ shell of deuterium is controlled by net recombinations to the excited states and Lyman-α decays (as mentioned earlier, decays to the ground state through the Lyman-α channel are dominant over two-photon decays from the $2s$ state because of the relatively low optical depth of the D Lyα line). We can obtain the contribution of the former with a Peebles-like estimate [31]:

$$\dot{x}_{\mathrm{D}(2p)}\big|_{\mathrm{rec}} = \frac{3}{4}\alpha_{\mathrm{B}} N_{\mathrm{H}} x_{\mathrm{e}} x_{\mathrm{D}^+} - \beta_{\mathrm{B}} x_{\mathrm{D}(2p)} = \frac{3}{4}\alpha_{\mathrm{B}} N_{\mathrm{H}} x_{\mathrm{D}} x_{\mathrm{e}}^2 - \beta_{\mathrm{B}} x_{\mathrm{D}(2p)}, \tag{4.76}$$

where $\alpha_{\mathrm{B}}(T_{\mathrm{m}})$ is the case-B recombination coefficient, and we have used $x_{\mathrm{D}^+} \approx x_{\mathrm{D}} x_e$ in the second equality. The net rate of Lyα decays in the deuterium line is, in the Sobolev approximation:

$$\dot{x}_{\mathrm{D}(2p)}\big|_{\mathrm{Ly}\alpha} = \frac{8\pi H \nu_{\mathrm{Ly}\alpha}^3}{c^3 N_{\mathrm{H}}} \left(\Delta f_{+}^{\mathrm{D}} - \Delta f_{\mathrm{eq}}^{\mathrm{D}}\right) = 3 R_{\mathrm{Ly}\alpha} x_{\mathrm{H}(1s)} \left(\Delta f_{+}^{\mathrm{D}} - \Delta f_{\mathrm{eq}}^{\mathrm{D}}\right), \tag{4.77}$$

where $R_{\mathrm{Ly}\alpha}$ is the rate of escape of Lyα photons per atom in the $2p$ state and was defined in Eq. (2.20). We can now solve for the the population of the excited state, in the steady-state approximation:

$$\dot{x}_{\mathrm{D}(2p)}\big|_{\mathrm{rec}} + \dot{x}_{\mathrm{D}(2p)}\big|_{\mathrm{Ly}\alpha} \approx 0, \tag{4.78}$$

from which we obtain [recalling that $\Delta f_{\mathrm{eq}}^{\mathrm{D}} \equiv x_{\mathrm{D}(2p)}/(3 x_{\mathrm{D}(1s)}) - \mathrm{e}^{-h\nu_{\mathrm{D}}/(kT_{\mathrm{r}})}$]

$$\Delta f_{\mathrm{eq}}^{\mathrm{D}} - \Delta f_{+}^{\mathrm{D}} = \frac{\frac{1}{4}\alpha_{\mathrm{B}} N_{\mathrm{H}} x_e^2 - \beta_{\mathrm{B}} x_{\mathrm{H}(1s)} \mathrm{e}^{-h\nu_{\mathrm{H}}/(kT_{\mathrm{r}})} - \beta_{\mathrm{B}} x_{\mathrm{H}(1s)} \Delta f_{+}^{\mathrm{D}}}{x_{\mathrm{H}(1s)} \left(\beta_{\mathrm{B}} + \frac{R_{\mathrm{Ly}\alpha}}{x_{\mathrm{D}}}\right)}. \tag{4.79}$$

We can simplify Eq. (4.79) with the following considerations. First, we can simplify the denominator since $R_{\mathrm{Ly}\alpha} \gtrsim 10^{-3}\beta_{\mathrm{B}} \gg x_{\mathrm{D}}\beta_{\mathrm{B}}$ (i.e., the rate of Lyα escape is much larger than the rate of photoionizations from the excited state in deuterium). Secondly, using Eq. (4.69) we can simplify the

numerator. Thirdly, assuming Boltzmann equilibrium between excited states of hydrogen (which is a good approximation whenever radiative transfer effects are important), we arrive at

$$\Delta f^{\rm D}_{\rm eq} - \Delta f^{\rm D}_{+} = \frac{1}{4}\frac{x_{\rm D}}{R_{{\rm Ly}\alpha} x_{{\rm H}(1s)}}\left[\alpha_{\rm B} N_{\rm H} x_e^2 - \beta_{\rm B} x_{{\rm H}(n=2)} + {\rm e}^{-\tau}\beta_{\rm B}\left(x_{{\rm H}(n=2)} - 4 x_{{\rm H}(1s)} {\rm e}^{-h\nu_{\rm H}/(kT_{\rm r})}\right)\right]. \tag{4.80}$$

Finally, using again a simple Peebles' estimate for hydrogen (see Section 2.2.1), we arrive at

$$\Delta f^{\rm D}_{\rm eq} - \Delta f^{\rm D}_{+} = x_{\rm D}\frac{3R_{{\rm Ly}\alpha} + \Lambda_{2s,1s}}{4R_{{\rm Ly}\alpha}}\left[1 + {\rm e}^{-\tau}\frac{4\beta_{\rm B}}{3R_{{\rm Ly}\alpha} + \Lambda_{2s,1s}}\right]\Delta f^{\rm H}_{\rm eq}, \tag{4.81}$$

or, equivalently,

$$\Delta f^{\rm D}_{\rm eq} - \Delta f^{\rm D}_{+} = -\frac{1}{4}\frac{x_{\rm D}}{R_{{\rm Ly}\alpha} x_{{\rm H}(1s)}}\left[1 + {\rm e}^{-\tau}\frac{4\beta_{\rm B}}{3R_{{\rm Ly}\alpha} + \Lambda_{2s,1s}}\right]\dot{x}_e, \tag{4.82}$$

and our final estimate for the number of distortion photons is

$$U = \frac{3}{4}H^{-1} x_{\rm D}\frac{\nu_{\rm D} - \nu_{\rm H}}{\nu_{\rm H}}\mathcal{I}(\tau)\left[1 + {\rm e}^{-\tau}\frac{4\beta_{\rm B}}{3R_{{\rm Ly}\alpha} + \Lambda_{2s,1s}}\right]|\dot{x}_e|. \tag{4.83}$$

We show the number of distortion photons per deuterium atom, $U/x_{\rm D}$, as a function of redshift, in Fig. 4.5. We see that this number is already relatively small at all times, and since $x_{\rm D} \sim 10^{-5}$, we conclude that the effect of deuterium on the recombination history is completely negligible (for comparison, two-photon decays and Raman scattering events, which represent a $\sim 1\%$ correction to the recombination history, lead to a distortion $U_{2\gamma} \sim 0.01$, see Fig. 9 of Ref. [49]).

To summarize the essential points, the distortion is very small because

(*i*) the separation between the lines is very small $(\nu_{\rm D} - \nu_{\rm H})/\nu_{\rm H} \ll 1$ and there is just not much space (in the frequency domain) that can be filled with distortion photons, see Eq. (4.75) or Fig. 4.4,

(*ii*) the optical depth in the deuterium Lyα line is low enough (although still $\gg 1$) that Lyα escape dominates over photoionizations from the excited states and therefore the excited state population equilibrates such that $\Delta f^{\rm D}_{\rm eq} - \Delta f^{\rm D}_{+} \sim x_{\rm D}\Delta f^{\rm H}_{\rm eq}$, see Eq. (4.81), and

(*iii*) even if (*i*) and (*ii*) are already sufficient to largely suppress any distortion, the fact that the damping wing of hydrogen is marginally optically thick ($\tau \gtrsim 1$) adds an additional suppression (see Fig. 4.5), through $\mathcal{I}(\tau) < 1$ and the exponential factor ${\rm e}^{-\tau}$ in Eq. (4.81), because the the radiation field is already nearly in equilibrium with the H Lyα line at the D Lyα frequency.

Finally, we have not considered the effect of frequency diffusion here. We treat this case in Ref. [40], where we find that frequency diffusion suppresses the distortion even more, essentially by enhancing effect (*iii*). The reason is that the deuterium line lies with the diffusion-dominated region, $(\nu_{\rm D} - \nu_{\rm H})^3 \ll \mathcal{S}^3$.

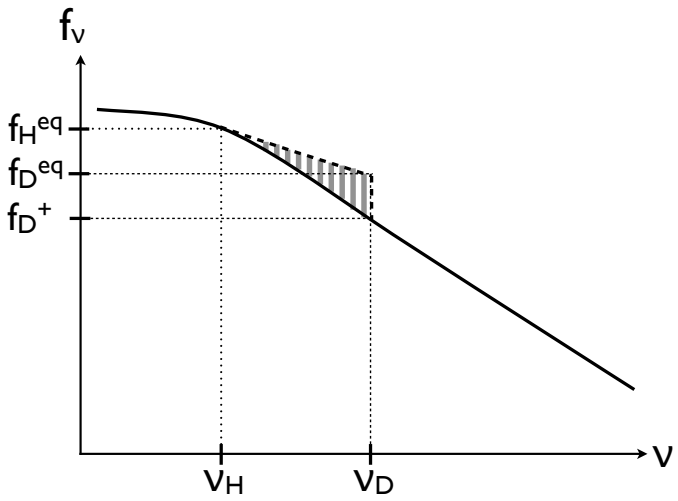

Figure 4.4: Schematic representation of the deuterium problem: the distortion induced by the presence of the deuterium line is shown as the hatched area.

4.4 Higher-order, non-overlapping Lyman lines ($2 \leq n \lesssim 23$)

4.4.1 List of efficient Lyman transitions

One of the strengths of the EMLA formulation is that it only requires the computations of effective transition rates for a small set of "interface" states. These "interface" states should in principle be $2s, 2p$, and all the higher lying p states. However, as we saw in Section 3.4.3, only the lowest few Lyman transitions significantly contribute to the overall recombination rate, and one can neglect higher-order Lyman transitions without loss of accuracy. The aim of this section is to verify this statement quantitatively.

In Fig. 4.6 we show the effect of adding higher-order Lyman transitions and feedback between them. This initially speeds up recombination by adding more decay paths to the ground state, then slows it down due to delayed reabsorptions of Lyβ photons in the Lyα line. Our results are similar to those of Ref. [42]. We checked that it is sufficient to include Lyman transitions up to Lyγ, and that including higher-order Lyman transitions leads to relative changes to the recombination history of at most 10^{-5}. This statement was also confirmed with the MLA code RecSparse [37].

4.4.2 Resonant scattering in the low-lying Lyman lines

The Lyman-α line has a particularly high resonant scattering probability, as atoms in the $2p$ state can leave the state only through spontaneous Ly-α decay, or through absorption of a CMB photon (typically, $p_{\rm ab} \sim 10^{-4}$ at $z = 1100$, see Fig. 1 of Ref. [52]). There is no lower energy state to spontaneously decay to other than the ground state. For higher-order Lyman transitions, though,

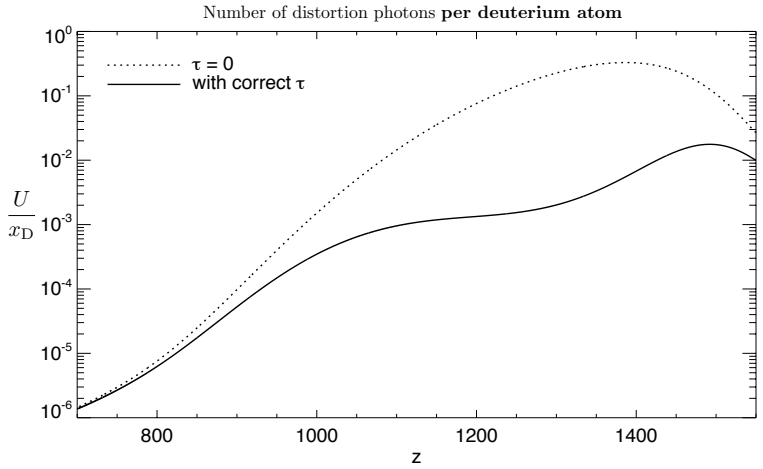

Figure 4.5: Number of distortion photons **per deuterium atom** (in the limit $R_{\rm Ly\alpha} \gg x_{\rm D}\beta_{\rm B}$). The dotted line shows the corresponding distortion if we set $\tau = 0$, i.e., treat the H Lyα line as a delta-function. Multiplying by $x_{\rm D} \sim 3 \times 10^{-5}$, we see that the number of distortion photons per hydrogen atom is minuscule.

there are multiple allowed channels out of the np state, $np \rightarrow n'l$, with $1 < n' < n$ and $l = 0, 2$. Therefore the scattering probability defined in Eq. (4.7) becomes comparable to the absorption probability, $p_{\rm sc}^n \sim p_{\rm ab}^n$ (in vacuum, $p_{\rm ab}^{{\rm Ly}\beta} \approx 0.12$ and $p_{\rm ab}^{{\rm Ly}\gamma} \approx 0.16$). From Eqs. (4.35) and (4.36), we can see that in that case

$$\left(\frac{\mathcal{S}_n}{\nu_n \Delta_{\rm H}}\right)^3 \sim \frac{\mathcal{W}_n}{\nu_n \Delta_{\rm H}}. \tag{4.84}$$

The wings of the Lyβ and Lyγ lines are optically thick for true absorption (this is the case for all Ly-n lines with $n \lesssim 13$). This implies (see Eq. (4.35) and corresponding discussion):

$$1 \ll \frac{\mathcal{W}_n}{\nu_n \Delta_{\rm H}} \ll \left(\frac{\mathcal{W}_n}{\nu_n \Delta_{\rm H}}\right)^3, \tag{4.85}$$

where the the second inequality is a consequence of the first one. From Eq. (4.84), we therefore obtain that for the low-lying Lyman lines above Lyα, $(\mathcal{S}_n/\mathcal{W}_n)^3 \ll 1$. This means that frequency diffusion is efficient only on a small fraction of the width over which the line is optically thick to true absorption.

There is not a simple relationship between the ratio $(\mathcal{S}_n/\mathcal{W}_n)^3$ and the impact of frequency diffusion on the Ly-n decay rate. However, the effect of frequency diffusion clearly increases with this ratio. Radiative transfer computations including frequency diffusion were carried out for the Lyman-α line, which showed that frequency diffusion leads to corrections of a few percents to the net decay rate in Lyα [45, 46]. As shown in Fig. 4.1, $(\mathcal{S}_2/\mathcal{W}_2)^3 \gg 1$ at most times for the Lyα line, in contrast with what we just showed for the higher-order lines. Therefore, we can expect that frequency diffusion would lead to corrections of much less than a percent to the net decay rate in

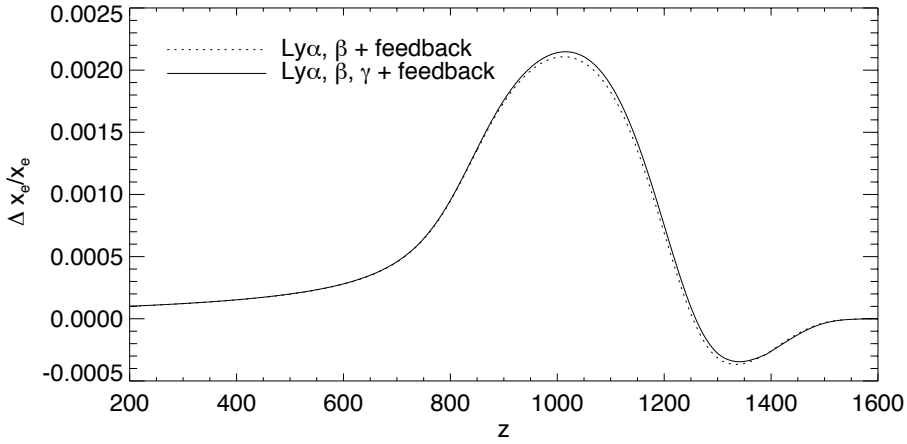

Figure 4.6: Fractional changes in the ionization history when including higher-order Lyman transitions and feedback between them, compared to the effective multilevel atom model with $2s$ and $2p$ only. Adding lines above Lyγ has a negligible effect.

the Lyβ and Lyγ lines. Since Lyβ decays themselves contribute of the order of a percent only to the overall recombination rate, sub-percent corrections to their rate can therefore be safely neglected at the level of accuracy required.

As a conclusion, resonant scattering in Lyβ and higher-order Lyman lines does not affect the recombination dynamics to any significant level.

4.5 Overlap of the high-lying Lyman lines ($n \gtrsim 24$)

4.5.1 Motivations

In the previous section we have shown that Lyman transitions above Lyγ do not affect the recombination history to a significant level and can be ignored. However, this relied on using the Sobolev approximation for the net decay rate out of the optically thick Lyman lines. As we show below, high-lying Lyman lines overlap with each other, or even with the continuum, which breaks assumption (i) of the Sobolev approximation that each line is isolated. In this section we address the consequences of this feature.

For $n \gtrsim 13$, the Lyman lines are dominated by their Doppler core (the damping wings become optically thin). The condition for the two neighboring Ly-(n+1) and Ly-n lines to overlap is therefore that their separation $\nu_{n+1} - \nu_n \sim 2\nu_c/n^3$ becomes of order the Doppler width of an individual line, $\nu_n \Delta_{\rm H} \sim \nu_c \Delta_{\rm H}$. Overlap therefore occurs for

$$n \gtrsim n_{\rm ov} \equiv \left(\frac{2}{\Delta_{\rm H}}\right)^{1/3} \approx 44 \left(\frac{T_{\rm m}}{3000\ {\rm K}}\right)^{-1/6}. \tag{4.86}$$

For even higher-order lines, the separation with the continuum $\nu_c - \nu_n = \nu_c/n^2$ becomes of the order of a Doppler width. This occurs for

$$n \gtrsim n_{\rm ov,c} \equiv \Delta_{\rm H}^{-1/2} \approx 206 \left(\frac{T_{\rm m}}{3000K}\right)^{-1/4}. \tag{4.87}$$

Intuitively, one can expect that line overlap amounts to adding new transitions $R^{(\rm ov)}_{np\rightarrow n'p}$ between high-lying p states, as photons emitted in the $np \rightarrow 1s$ transition can be re-absorbed immediately in a neighboring $1s \rightarrow n'p$ transition. More importantly, overlap with the continuum provides an additional recombination pathway. Direct recombinations to the ground state are usually considered as highly inefficient as the resulting emitted photons can immediately ionize neutral hydrogen atoms in their ground state. We have considered the possibility of continuum escape (similar to Lyman-α escape) in Section 2.2.3, where we showed that it leads to negligible corrections to the ionization history $\Delta x_e/x_e \sim 10^{-6}$ (see also Ref. [41]). If overlap of the highest Lyman lines with the continuum is accounted for, it becomes possible for free electrons and protons to successfully recombine to the ground state of hydrogen, if the emitted photon subsequently excites another atom to a high-lying p state rather that ionizing it. The recombination event $e^- + p \rightarrow 1s + \gamma$ immediately followed by the absorption event $1s + \gamma \rightarrow np$ thus corresponds to an additional, indirect recombination event to the np state, to which a coefficient $\alpha^{(\rm ov)}_{np}$ can be associated. The reverse process corresponds to an additional photoionization rate, $\beta^{(\rm ov)}_{np}$.

Modern recombination codes account for the excited states of hydrogen up to extremely high principal quantum number $n_{\rm max} \gtrsim 200$ [37, 38], and recently up to $n_{\rm max} = 500$ [39]. It is therefore important to quantify the impact of line overlap on the recombination history. In what follows we develop a formalism that generalizes the Sobolev escape probability method, and accounts for the overlap of the high-lying Lyman lines.

We start by evaluating the effect of photoionization and recombinations from and to the ground state on the radiation field and providing the relevant equations.

4.5.2 Photoionization and recombination from and to the ground state

The frequency-dependent photoionization cross section from the ground state is, in the atom's rest frame:

$$\sigma(\nu) = \sigma_0 \; g\left(\frac{\nu}{\nu_{\rm c}}\right), \tag{4.88}$$

where

$$\sigma_0 \equiv \frac{2^9\pi^2}{3\exp(4)}\alpha a_0^2 \approx 6.3 \times 10^{-18}\ {\rm cm}^2 \tag{4.89}$$

is the photoionization cross section at threshold and the function $g(\kappa)$ is such that $g(\kappa < 1) = 0$, $g(1) = 1$, and varies on a scale $\Delta\kappa \sim 1$ for $\kappa > 1$ [82]. The Doppler-averaged cross section is

therefore:

$$\overline{\sigma}(\nu;T_{\rm m}) = \int_{-\infty}^{+\infty} \sigma(\nu[1-u\Delta_{\rm H}])\frac{{\rm e}^{-u^2}}{\sqrt{\pi}}{\rm d}u = \sigma_0 \int_{-\infty}^{\frac{\nu-\nu_{\rm c}}{\nu\Delta_{\rm H}}} g\left(\frac{\nu}{\nu_{\rm c}}[1-u\Delta_{\rm H}]\right)\frac{{\rm e}^{-u^2}}{\sqrt{\pi}}{\rm d}u. \tag{4.90}$$

In what follows we use the distance to the Lyman limit in Doppler width units:

$$x \equiv \frac{\nu-\nu_{\rm c}}{\nu_{\rm c}\Delta_{\rm H}}. \tag{4.91}$$

The Doppler-averaged cross section can be rewritten as

$$\overline{\sigma}(\nu;T_{\rm m}) = \int_{-\infty}^{\frac{x}{1+x\Delta_{\rm H}}} g\left([1+x\Delta_{\rm H}][1-u\Delta_{\rm H}]\right)\frac{{\rm e}^{-u^2}}{\sqrt{\pi}}{\rm d}u. \tag{4.92}$$

For frequencies within a few Doppler widths from the Lyman limit ($|x| \sim$ a few), the argument of g in the integral is $1+\mathcal{O}(\Delta_{\rm H})$. Since g varies very little on a scale $\Delta_{\rm H}$, we can set it to its threshold value in the integral, $g \approx 1$. We therefore obtain the Doppler-averaged photoionization cross section, for frequencies within a few Doppler widths of the ionization threshold:

$$\overline{\sigma}(\nu;T_{\rm m}) \approx \sigma_0\left[1-\frac{1}{2}{\rm erfc}(x)\right] \equiv \sigma_0\phi_{\rm c}(x), \tag{4.93}$$

where the last equality defines the dimensionless profile $\phi_c(x)$.

The rate of photoionizations from the ground state per hydrogen atom per frequency interval (for the photoionizing photon) is then:

$$\dot{\mathcal{N}_\nu}\big|_{\rm phot} = -c\overline{\sigma}(\nu;T_{\rm m})N_{\rm H}x_{1s}\mathcal{N}_\nu. \tag{4.94}$$

Detailed balance considerations show that the differential recombination coefficient to the ground state, per frequency interval for the outgoing photon (in units of ${\rm cm^3 s^{-1} Hz^{-1}}$) is given by:

$$\frac{{\rm d}\alpha_{1s}}{{\rm d}\nu} = \frac{8\pi\nu^2}{c^2}\overline{\sigma}(\nu;T_{\rm m}){\rm e}^{-\frac{h(\nu-\nu_c)}{kT_{\rm m}}}\left(\frac{2\pi\hbar^2}{m_e kT_{\rm m}}\right)^{3/2}. \tag{4.95}$$

The rate of recombinations to the ground state per hydrogen atom per frequency interval (for the emitted photon) is then

$$\dot{\mathcal{N}_\nu}\big|_{\rm rec} = N_{\rm H}x_e^2\frac{{\rm d}\alpha_{1s}}{{\rm d}\nu}. \tag{4.96}$$

We define the continuum equilibrium occupation number:

$$f_{\rm eq}^c \equiv \frac{N_{\rm H}x_e^2}{x_{1s}}\left(\frac{2\pi\hbar^2}{m_e kT_{\rm m}}\right)^{3/2}. \tag{4.97}$$

The rate of change of the photon occupation number due to photoionizations and recombinations from and to the ground state, neglecting stimulated recombinations, can then be written as:

$$\dot{f}_\nu\big|_{\rm c} = -c\overline{\sigma}(\nu;T_{\rm m})N_{\rm H}x_{1s}\left[f_\nu - {\rm e}^{-\frac{h(\nu-\nu_{\rm c})}{kT_{\rm m}}}f_{\rm eq}^{c}\right]. \tag{4.98}$$

4.5.3 The radiative transfer equation in the presence of multiple overlapping lines, and photoionization and recombination from and to the ground state

The time-dependent radiative transfer equation for the photon occupation number f_ν, Eqs. (4.30) and (4.32), in the presence of multiple lines, is (if one line is considered as the fiducial line, then the other lines and continuum absorption and emission constitute the "non-resonant" processes in that equation):

$$\begin{aligned} -\frac{1}{H\nu}\frac{\partial f_\nu}{\partial t} + \frac{\partial f_\nu}{\partial \nu} &= \sum_n \tau_n \varphi_n(\nu)\left[{\rm e}^{\frac{h(\nu-\nu_n)}{kT_{\rm m}}}f_\nu - f_{\rm eq}^{n}\right] + \frac{c\overline{\sigma}(\nu)N_{\rm H}x_{1s}}{H\nu}\left[f_\nu - {\rm e}^{-\frac{h(\nu-\nu_{\rm c})}{kT_{\rm m}}}f_{\rm eq}^{c}\right] \\ &+ \sum_n p_{\rm sc}^{n}\tau_n \int\left[\varphi_n(\nu)\varphi_n(\nu'){\rm e}^{\frac{h(\nu'-\nu_n)}{kT_{\rm m}}} - R_n(\nu,\nu')\right]f_{\nu'}{\rm d}\nu'. \end{aligned} \tag{4.99}$$

Since line overlap is expected to be a small correction to the recombination history, we can neglect "corrections to the correction" and make some approximations to simplify the calculations. As the potentially important effect is the violation of assumption (i) of the Sobolev approximation, we will lift this assumption, but keep the other three assumptions on which it relies, as we justify below.

First, as we are considering the radiation field over a characteristic frequency width a few Doppler widths, which corresponds to changes in the scale factor $\Delta a/a \sim 10^{-4}$, we can make the usual steady-state approximation by neglecting the time derivative. We also approximate the exponentials by unity since their exponents are of order $\sim \Delta_{\rm H}\frac{h\nu_{\rm c}}{kT_{\rm m}} \sim 10^{-3}$. In addition, we approximate the Doppler width of the Ly-n line $\nu_n\Delta_{\rm H} \approx \nu_{\rm c}\Delta_{\rm H}$, neglecting corrections of order $\mathcal{O}(n^{-2})$. Finally, we will assume complete redistribution for resonant scattering. The validity of the latter approximation is more difficult to precisely quantify, but it can be justified with the following arguments. Firstly, the resonant scattering probability $p_{\rm sc}^{n}$ rapidly decreases as n increases due to the abundance of low-energy photons that can easily photoionize atoms in the np state or cause transitions to neighboring excited states. We find, for $T_{\rm m} = 3000$ K, $p_{\rm sc}^{25} = 0.44$, $p_{\rm sc}^{50} = 0.28$, $p_{\rm sc}^{100} = 0.17$ and $p_{\rm sc}^{200} = 0.09$. Secondly, for a Doppler-dominated line, partial redistribution is close to complete redistribution, in the sense that both distributions have a similar characteristic width, of the order of a Doppler width. We explicitly compute the change in escape probability in a single Doppler-dominated line with partial frequency redistribution in Appendix 4.B. There we show that the escape probability is changed by at most a few percent with respect to the complete redistribution case. This contrasts

with the Lyα line, where complete redistribution can change photon frequencies by many Doppler widths due to the optical thickness of the Damping wings, and the distinction between the two types of redistribution is important.

We work with the dimensionless frequency x defined in Eq. (4.91). We define the optical depth for continuum absorption, per unit Doppler width:

$$\Phi_c(x) \equiv \tau_c \phi_c(x), \tag{4.100}$$

where

$$\tau_c \equiv \Delta_{\rm H} \frac{c\sigma_0 N_{\rm H} x_{1s}}{H}. \tag{4.101}$$

We further define:

$$x_n \equiv \frac{\nu_n - \nu_{\rm c}}{\nu_{\rm c}\Delta_{\rm H}} = -\frac{1}{n^2 \Delta_{\rm H}} \tag{4.102}$$

$$\Phi_n(x) \equiv \tau_n \phi_n(x) \equiv \tau_n \frac{1}{\sqrt{\pi}} {\rm e}^{-(x-x_n)^2} \tag{4.103}$$

$$\Phi(x) \equiv \sum_n \Phi_n(x) + \Phi_{\rm c}(x). \tag{4.104}$$

The steady-state radiative transfer equation for $f(x)$ becomes, with the approximations justified above:

$$\frac{{\rm d}f}{{\rm d}x} = \sum_n \Phi_n(x) \left[f(x) - f_{\rm eq}^n\right] + \Phi_{\rm c}(x) \left[f(x) - f_{\rm eq}^c\right] \tag{4.105}$$

Since the continuum is optically thick, we set the boundary condition to $f(+\infty) = f_{\rm eq}^c$. Note that our treatment does not allow for any continuum escape in the absence of high-lying Lyman lines (the total optical depth for continuum absorption is infinite in our approximation). However, this has been shown to be negligible and lead to corrections to the ionization history $\Delta x_e/x_e \sim 10^{-6}$ [41].

4.5.4 Generalized escape probability formalism

4.5.4.1 Preliminaries

Let us consider the probability distribution Π_ν of photons injected with a total rate $\Gamma_{\rm inj}$ and a profile $\varphi_{\rm inj}(\nu)$ (normalized to unity), that then undergo line and continuum absorption. The evolution of the probability distribution is given by an equation similar to the radiative transfer equation Eq. (4.99) (assuming complete redistribution and taking the exponential terms to unity):

$$\frac{{\rm d}\Pi_\nu}{{\rm d}t} = \frac{\partial \Pi_\nu}{\partial t} - H\nu \frac{\partial \Pi_\nu}{\partial \nu} = \Gamma_{\rm inj}\varphi_{\rm inj}(\nu) - H\nu \sum_n \tau_n \varphi_n(\nu) \Pi_\nu - c\overline{\sigma}(\nu) N_{\rm H} x_{1s} \Pi_\nu. \tag{4.106}$$

The rate at which these photons are absorbed in the Ly-n transition is then $H\nu\tau_n \int \varphi_n(\nu)\Pi_\nu \mathrm{d}\nu$, and the rate at which they are absorbed by the continuum is $\int c\overline{\sigma}(\nu)N_{\mathrm{H}}x_{1s}\Pi_\nu \mathrm{d}\nu$. Finally, these photons may also escape the set of overlapping lines by redshifting below their resonant frequencies. If we only consider lines above a given frequency ν_{low} (below which lines can be considered as isolated), then the escape rate is $H\nu_{\mathrm{low}}\Pi_{\nu_{\mathrm{low}}}$. In practice, ν_{low} is many Doppler widths below ν_c (so $x_{\mathrm{low}} \ll -1$), but still close enough to ν_c that we can approximate the escape rate by $H\nu_c\Pi_\nu(x \rightarrow -\infty)$.

Now in steady state, the sum of all these rates must equal the injection rate (there are no other possible fates than those described above for the injected photons). This can be checked explicitly by integrating Eq. (4.106) from ν_{low} to $+\infty$ in the steady-state limit (with boundary condition $\Pi(+\infty) = 0$ since no photons are injected at infinity). Therefore, the steady-state *probability* that injected photons are absorbed in the Ly-n line is

$$P(\mathrm{inj} \rightarrow n) = \frac{H\nu_c}{\Gamma_{\mathrm{inj}}}\tau_n \int \varphi_n(\nu)\Pi_\nu \mathrm{d}\nu, \tag{4.107}$$

the probability that they cause a photoionization is

$$P(\mathrm{inj} \rightarrow c) = \frac{1}{\Gamma_{\mathrm{inj}}} \int c\overline{\sigma}(\nu)N_{\mathrm{H}}x_{1s}\Pi_\nu \mathrm{d}\nu, \tag{4.108}$$

and the probability that they escape without being absorbed is

$$P(\mathrm{inj} \rightarrow \mathrm{esc}) = \frac{H\nu_c}{\Gamma_{\mathrm{inj}}}\Pi_\nu(x \rightarrow -\infty). \tag{4.109}$$

In what follows, we apply this idea to develop a formalism for interline transition probabilities.

4.5.4.2 Interline transition probabilities

Taking advantage of the linearity of Eq. (4.105), we can decompose $f(x)$ on a set of basis functions:

$$f(x) = \sum_j f^j_{\mathrm{eq}}\tau_j v_j(x) + f^c_{\mathrm{eq}} \int_{-\infty}^{+\infty} \Phi_c(y)G(x,y)\mathrm{d}y, \tag{4.110}$$

where the functions $v_j(x)$ satisfy the linear inhomogeneous differential equations:

$$\frac{\mathrm{d}v_j}{\mathrm{d}x} = \Phi(x)v_j(x) - \phi_j(x), \tag{4.111}$$

with boundary conditions $v_j(+\infty) = 0$, and the Green's function $G(x,y)$ satisfy a similar equation:

$$\frac{\mathrm{d}G}{\mathrm{d}x} = \Phi(x)G(x,y) - \delta(x-y), \tag{4.112}$$

with boundary condition $G(+\infty, y) = 0$. The asymptotic behavior of $G(x, y)$ at $x \gg 1$ is:

$$G(x,y) \underset{x\gg 1}{\approx} \begin{cases} 0 & \text{if } x > y, \\ \mathrm{e}^{\tau_c(x-y)} & \text{if } x < y, \end{cases} \tag{4.113}$$

where we used $\Phi(+\infty) = \Phi_c(+\infty) = \tau_c$. We therefore recover the appropriate boundary condition for $f(x)$ at $+\infty$:

$$f(x \gg 1) \approx f_{\rm eq}^c \int_x^{+\infty} \tau_c \mathrm{e}^{\tau_c(x-y)} \mathrm{d}y = f_{\rm eq}^c. \tag{4.114}$$

We can now use the results from the previous section. Using $\Pi_\nu = v_j(x)/(\nu_c \Delta_{\rm H})$, $\varphi_{\rm inj}(\nu) = \phi_j(x)/(\nu_c \Delta_{\rm H})$, and $\Gamma_{\rm inj} = H/\Delta_{\rm H}$, we see that Eq. (4.111) is the steady-state version of Eq. (4.106). Therefore the steady-state probabilities that a photon emitted in the Ly-j line is later absorbed in a Ly-i transition, or subsequently photo-ionizes an atom in its ground state are, respectively:

$$P(j \to i) = \int \Phi_i(x) v_j(x) \mathrm{d}x, \tag{4.115}$$

$$P(j \to c) = \int \Phi_c(x) v_j(x) \mathrm{d}x. \tag{4.116}$$

The probability that a photon emitted in the Ly-j line escapes at $x = -\infty$ without being reabsorbed in any line or causing a photoionization is given by

$$P(j \to \mathrm{esc}) = v_j(-\infty). \tag{4.117}$$

Clearly, the probability of escape from the whole set of overlapping lines is vanishingly small, except possibly for photons emitted from the lowest lying line considered as "overlapping". The region of line overlap blends smoothly into the region of quasi-instantaneous feedback between neighboring Lyman lines, for $n \lesssim 20$–30. Therefore, even for photons emitted from the lowest line considered as "overlapping" with the next higher line, there is still a near-unity probability of being reabsorbed quasi instantaneously in the next lower transition. Therefore, in practice, we have $P(j \to \mathrm{esc}) = 0$ for all lines considered as overlapping, or simply close enough that feedback is quasi-instantaneous.

Integrating Eq. (4.111) from $-\infty$ to $+\infty$, we can see that these probabilities are complementary, as they should:

$$\sum_i P(j \to i) + P(j \to c) = 1. \tag{4.118}$$

The Green's function $G(x, y)$ can similarly be interpreted as the steady-state number distribution for continuum photons initially injected at the frequency y. The probabilities that a photon emitted at frequency y is absorbed in the Ly-i transition, absorbed by the continuum, or escapes at $-\infty$ are,

respectively:

$$P(y \to i) = \int \Phi_i(x) G(x,y) \mathrm{d}x \tag{4.119}$$

$$P(y \to c) = \int \Phi_c(x) G(x,y) \mathrm{d}x \tag{4.120}$$

$$P(y \to \mathrm{esc}) = G(-\infty, y). \tag{4.121}$$

Again, the probability for photons emitted in the continuum to escape the whole set of high-lying overlapping lines is vanishingly small, which means that in practice we have $P(y \to \mathrm{esc}) = 0$.

Finally, one can check that these probabilities are indeed complementary by integrating Eq. (4.112) between $-\infty$ and $+\infty$:

$$\sum_i P(y \to i) + P(y \to c) = 1. \tag{4.122}$$

4.5.4.3 Net decay rate in the Ly-i transition

From Eq. (4.42), the net decay rate in the Ly$-i$ line is

$$\dot{x}_{ip \to 1s} = 3 x_{1s} A_{ip,1s} \int \left[f^i_{\mathrm{eq}} - f(x) \right] \phi_i(x) \mathrm{d}x = A_{ip,1s} x_i - 3 x_{1s} \frac{A_{ip,1s}}{\tau_i} \int f(x) \Phi_i(x) \mathrm{d}x. \tag{4.123}$$

Using the expansion (4.110) for $f(x)$ and the definitions for the interline transition probabilities, we rewrite

$$\dot{x}_{ip \to 1s} = A_{ip,1s} x_{ip} - \frac{A_{ip,1s}}{\tau_i} \sum_j \tau_j x_{jp} P(j \to i) - 3 x_{1s} \frac{A_{ip,1s}}{\tau_i} f^c_{\mathrm{eq}} \int_{-\infty}^{+\infty} \Phi_c(y) P(y \to i) \mathrm{d}y. \tag{4.124}$$

We notice that $A_{ip,1s}/\tau_i \times \tau_j = A_{jp,1s}$ (approximating $\nu_i \approx \nu_j \approx \nu_c$). Also, using Eqs. (4.6), (4.95) and (4.101), we obtain that

$$3 x_{1s} \frac{A_{ip,1s}}{\tau_i} f^c_{\mathrm{eq}} \Phi_c(y) = N_{\mathrm{H}} x_e^2 \frac{\mathrm{d}\alpha_{1s}}{\mathrm{d}y}, \tag{4.125}$$

where $\frac{\mathrm{d}\alpha_{1s}}{\mathrm{d}x} \equiv \nu_c \Delta_{\mathrm{H}} \frac{\mathrm{d}\alpha_{1s}}{\mathrm{d}\nu}$ is the differential recombination coefficient to the ground state per unit Doppler width. Using the complementarity relation (4.118), we can now rewrite the net decay rate in the Ly-i transition as:

$$\dot{x}_{ip \to 1s} = x_{ip} \left(\sum_{j \neq i} R^{(\mathrm{ov})}_{ip \to jp} + \beta^{(\mathrm{ov})}_{ip} \right) - \sum_{j \neq i} x_{jp} R^{(\mathrm{ov})}_{jp \to ip} - N_{\mathrm{H}} x_e^2 \alpha^{(\mathrm{ov})}_{ip}, \tag{4.126}$$

where we have defined the overlap-induced transition rates

$$R^{(\mathrm{ov})}_{ip \to jp} \equiv A_{ip,1s} P(i \to j), \tag{4.127}$$

and the overlap-induced recombination coefficients and photoionization rates:

$$\alpha_{ip}^{(\mathrm{ov})} \equiv \int \frac{\mathrm{d}\alpha_{1s}}{\mathrm{d}y} P(y \to i)\mathrm{d}y, \tag{4.128}$$

$$\beta_{ip}^{(\mathrm{ov})} \equiv A_{ip,1s} P(i \to c). \tag{4.129}$$

4.5.4.4 Net rate of recombinations to the ground state

The net rate of recombinations to the ground state, per hydrogen atom, is

$$\begin{aligned} \dot{x}_{c\to 1s} &= \frac{8\pi\nu_{\mathrm{c}}^2}{c^2} x_{1s} \int \overline{\sigma}(\nu) \left[\mathrm{e}^{-\frac{h(\nu-\nu_{\mathrm{c}})}{kT_{\mathrm{m}}}} f_{\mathrm{eq}}^{c} - f_{\nu}\right] \mathrm{d}\nu \\ &\approx \frac{8\pi\nu_{\mathrm{c}}^2}{c^2} x_{1s} \nu_{\mathrm{c}} \Delta_{\mathrm{H}} \sigma_0 \int \phi_c(x) \left[f_{\mathrm{eq}}^{c} - f(x)\right] \mathrm{d}x, \end{aligned} \tag{4.130}$$

where in the second line we took $\mathrm{e}^{-\frac{h(\nu-\nu_{\mathrm{c}})}{kT_{\mathrm{m}}}} \approx 1$ in the vicinity of the Lyman limit. Using again the decomposition (4.110) and the definitions of the interline transition probabilities, we get:

$$\dot{x}_{c\to 1s} = \frac{8\pi\nu_{\mathrm{c}}^2}{c^2} x_{1s} \nu_{\mathrm{c}} \Delta_{\mathrm{H}} \sigma_0 f_{\mathrm{eq}}^{c} \times \Gamma_c - \frac{8\pi\nu_{\mathrm{c}}^3}{3c^2} \Delta_{\mathrm{H}} \sigma_0 \sum_j x_{jp} \frac{\tau_j}{\tau_c} P(j \to c), \tag{4.131}$$

where we have defined

$$\begin{aligned} \Gamma_c &\equiv \int \phi_c(x) \left[1 - \int \Phi_c(y) G(x,y) \mathrm{d}y\right] \mathrm{d}x \\ &= \int \mathrm{d}x\ \phi_c(x) \int \mathrm{d}y \left[\delta(y-x) - \int \Phi_c(y) G(x,y)\right] \\ &= \int \mathrm{d}y \int \mathrm{d}x\ \phi_c(x) \left[\delta(y-x) - \int \Phi_c(y) G(x,y)\right] \\ &= \int \phi_c(y) \left[1 - P(y \to c)\right] \mathrm{d}y = \int \phi_c(y) \sum_j P(y \to j), \end{aligned} \tag{4.132}$$

where we have used the definition (4.120) of $P(y \to c)$ in the fourth equality, and in the last equality we have used the complementarity relation (4.122).

After some algebraic manipulations, we can cast the net rate of recombinations to the ground state in the following form:

$$\dot{x}_{c\to 1s} = \sum_j \left[N_{\mathrm{H}} x_e^2 \alpha_{jp}^{(\mathrm{ov})} - x_{jp} \beta_{jp}^{(\mathrm{ov})}\right], \tag{4.133}$$

where the overlap-induced recombination coefficients and photoionization rates have been defined in Eqs. (4.128) and (4.129).

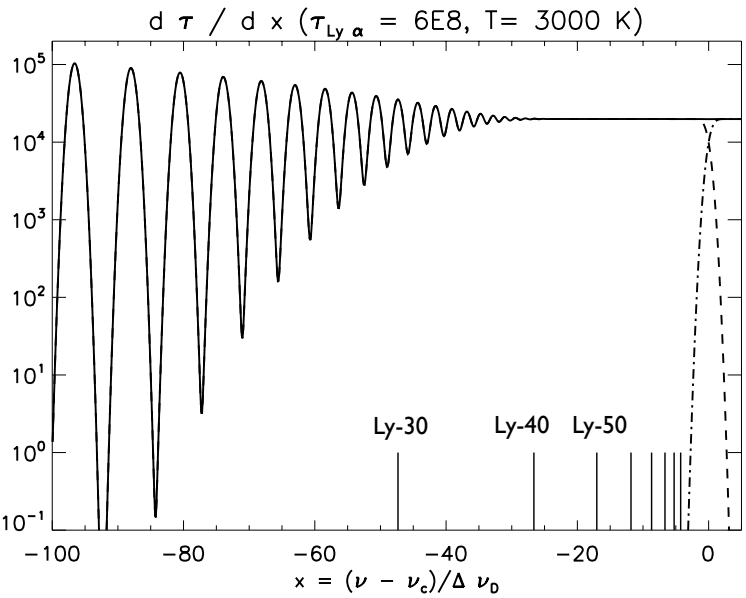

Figure 4.7: Differential optical depth per unit Doppler width, $\Phi(x)$, for fiducial values $\tau_{\rm Ly\alpha} = 6\times10^8$ and $T_{\rm m} = 3000$ K. The dashed line is the contribution from Lyman lines, the dot-dashed line is the contribution from photoionization from the ground state, and the solid line is their sum. The position of the Lyman-30 to 100 resonant frequencies (spaced by $\Delta n = 10$) is shown.

4.5.4.5 Rate of change of the ground state population

Adding Eqs. (4.126) and (4.133), we see that the net rate of change for the ground state population due to decays from the overlapping lines and recombination to the ground state is zero:

$$\dot{x}_{1s}^{(\rm ov)} = -\dot{x}_{e}^{(\rm ov)} = \sum_{j,\ \rm ov} \dot{x}_{jp\rightarrow 1s} + \dot{x}_{c\rightarrow 1s} = 0. \tag{4.134}$$

This can be understood intuitively since any photon emitted from one of the overlapping lines is bound to be reabsorbed in a neighboring line or photoionize an atom from the ground state; similarly, a photon emitted after a recombination to the ground state will almost certainly be reabsorbed in a high-lying Lyman line, or cause a subsequent photoionization. In other words, no escape is possible from the series of high-lying lines, and the net decay rate to the ground state therefore vanishes. Line overlap can therefore only influence the recombination history indirectly, through changing the populations of the excited states.

We now turn to the numerical evaluation of the overlap-induced transition rates.

4.5.5 Evaluation of the overlap-induced transition rates

We show in Fig. 4.7 the optical depth per unit Doppler width, $\Phi(x)$. It can be seen that for $x \gtrsim x_{n_{\rm ov}}$, $\Phi(x)$ is nearly constant. This can be explicitly derived as follows. From Eqs. (4.3), (4.6), (4.89) and

(4.101), we can show that

$$\tau_n \underset{n\gg 1}{\sim} \frac{2}{\Delta_{\rm H} n^3}\tau_c. \tag{4.135}$$

Moreover, the separation between two neighboring high-lying lines has the asymptotic expression

$$x_{n+1} - x_n \sim \frac{2}{\Delta_{\rm H} n^3}. \tag{4.136}$$

For $x \gtrsim x_{n_{\rm ov}}$ (such that the separation between neighboring lines becomes small compared to unity), we can approximate the sum of optical depths due to Lyman transitions as a Riemann integral:

$$\begin{aligned}\sum_n \tau_n \phi_n(x) &\approx \tau_c \sum_n (x_{n+1} - x_n)\, \frac{1}{\sqrt{\pi}} {\rm e}^{-(x-x_n)^2} \\ &\approx \tau_c \frac{1}{\sqrt{\pi}} \int_{-\infty}^{0} {\rm e}^{-(x-u)^2} {\rm d}u = \frac{\tau_c}{2}{\rm erfc}(x) = \tau_c - \tau_c \phi_c(x).\end{aligned} \tag{4.137}$$

Thus, we obtain, using the definition (4.104):

$$\Phi(x \gtrsim x_{n_{\rm ov}}) \approx \tau_c. \tag{4.138}$$

Equation (4.111) therefore has an analytic solution:

$$v_j(x) = \frac{1}{2}{\rm e}^{-(x-x_j)^2}{\rm erfc}\left(x - x_j + \frac{\tau_c}{2}\right){\rm e}^{\left(x-x_j+\frac{\tau_c}{2}\right)^2} \approx \frac{1}{\tau_c}\frac{{\rm e}^{-(x-x_j)^2}}{\sqrt{\pi}}, \tag{4.139}$$

where in the second line we used $\tau_c \gg 1$ ($\tau_c \gtrsim 10^2$ at all times). We therefore obtain:

$$P(j \to i) \approx \frac{\tau_i}{\tau_c}\frac{1}{\sqrt{2\pi}}{\rm e}^{-\frac{1}{2}(x_i-x_j)^2} \approx \frac{2}{\Delta_{\rm H} i^3}\frac{1}{\sqrt{2\pi}}{\rm e}^{-\frac{1}{2}(x_i-x_j)^2} \tag{4.140}$$

$$P(j \to c) \approx 1 - \frac{1}{2\sqrt{\pi}}\int_{-\infty}^{+\infty}{\rm erfc}(x){\rm e}^{-(x-x_i)^2}{\rm d}x = 1 - \frac{1}{2}{\rm erfc}\left(\frac{x_j}{\sqrt{2}}\right), \tag{4.141}$$

where the integral can be evaluated after differentiating with respect to x_i. The overlap-induced transition rates $R^{\rm (ov)}_{ip\to jp}$ and photoionization rates $\beta^{\rm (ov)}_{jp}$ can then be obtained from Eqs. (4.127) and (4.129).

Similarly, the function $v_c(x) \equiv \int \phi_c(y)G(x,y){\rm d}y$ satisfies the following differential equation:

$$\frac{{\rm d}v_c}{{\rm d}x} = \Phi(x)v_c(x) - \phi_c(x), \tag{4.142}$$

which has the solution, valid to lowest order in $1/\tau_c$:

$$v_c(x) \approx \frac{1}{\tau_c}\left[1 - \frac{1}{2}{\rm erfc}(x)\right]. \tag{4.143}$$

The overlap-induced recombination coefficient can then be written as:

$$\alpha_{ip}^{(\mathrm{ov})} = \frac{8\pi\nu_c^3\Delta_{\mathrm{H}}}{c^2}\sigma_0\left(\frac{2\pi\hbar^2}{m_e k T_{\mathrm{m}}}\right)^{3/2}\int \Phi_i(x)v_c(x)\mathrm{d}x, \tag{4.144}$$

where we used Eqs. (4.119), (4.125) and (4.128).

After some manipulations, we can show that the overlap-induced recombination coefficients can be simply expressed in terms of the overlap-induced photoionization rates:

$$\alpha_{ip}^{(\mathrm{ov})} \approx 3\left(\frac{2\pi\hbar^2}{m_e k T_{\mathrm{m}}}\right)^{3/2}\beta_{ip}. \tag{4.145}$$

From the asymptotic expression of $A_{jp,1s} \propto j^{-3}$, we can also show that

$$R_{jp\rightarrow ip} \approx R_{ip\rightarrow jp}. \tag{4.146}$$

Equations (4.145) and (4.146) are simply the usual detailed balance relations, in the limit $\nu_i \approx \nu_j \approx \nu_c$.

The expressions provided in this section are valid for $n \gtrsim n_{\mathrm{ov}}$, when Lyman lines are within less than a Doppler width of each other. We therefore expect the expressions for $\beta_{np}^{(\mathrm{ov})}$ and $\alpha_{np}^{(\mathrm{ov})}$ to be accurate in the regime where they are significant, for $n \gtrsim n_{\mathrm{ov,c}} \gg n_{\mathrm{ov}}$. On the other hand, the interline transition probabilities $P(i \rightarrow j)$ should smoothly transition from the asymptotic expression (4.140) for $i, j \gtrsim n_{\mathrm{ov}}$ to the Sobolev values for nearly instantaneous feedback for $i, j \lesssim n_{\mathrm{ov}}$, that is

$$P(i \rightarrow j) = \tau_i^{-1}\delta_{j,i-1} + \left(1 - \tau_i^{-1}\right)\delta_{ij} \approx \delta_{ij}. \tag{4.147}$$

We checked that this is indeed the case by integrating numerically Eqs. (4.111) and (4.115). We therefore set $P(i \rightarrow j) = \delta_{i,j}$ for $\min(i, j) < n_{\mathrm{ov}}$, and use Eq. (4.140) otherwise. Since, as we shall see below, line overlap appears to lead to negligible changes to the recombination history, the exact value of the interline transition probabilities near n_{ov} is not critical.

4.5.6 Results

As we showed in Section 4.5.4.5, the net rate of change of the ground state population through the high-lying Lyman transitions vanishes. Since any $np \rightarrow 1s$ transition is systematically followed by the absorption of the emitted photon, the high-lying np states are virtually radiatively connected to one another (and to the continuum), rather than being radiatively connected to the ground state. In the language of Ref. [39], the high-lying p states are *interior* states. The EMLA formalism developed in Ref. [39] can then easily be extended to include the overlap-induced transitions, which only depend on the matter temperature.

We added the overlap-induced $\mathrm{H}(np) \leftrightarrow \mathrm{H}(n'p)$ and $\mathrm{H}(np) \leftrightarrow e^- + p$ transitions to our effective rates code. We computed the change in the effective recombination coefficients $\mathcal{A}_{2s}$, $\mathcal{A}_{2p}$ and effective $2p \to 2s$ transition rate $\mathcal{R}_{2p\to 2s}$ when the states $2s,\ 2p$ are considered as the only interface states (i.e., cutting off the Lyβ transition and above for simplicity; the effect of overlap is independent of that simplification). We find that the relative changes in each of the effective coefficients are at most a few times 10^{-5}. As a comparison, the change in total effective recombination coefficient between $n_{\max} = 100$ and $n_{\max} = 200$ is of order 0.3 to 2% over the temperature range considered; from $n_{\max} = 200$ to $n_{\max} = 400$, this change is of order 0.08 to 0.6%. Therefore, the effect of overlap is a few orders of magnitude smaller than the mere error due to the necessary truncation of the high energy shells when computing the effective rates. Since previous work [37, 38] have shown that MLA computations with $n_{\max} \sim 100$ already reach the desired level of accuracy, we conclude that line overlap can be safely ignored.

4.6 Population inversion[7]

The populations of the $2p$ and $2s$ states are strongly out of equilibrium towards the end of the epoch of primordial recombination, with the ratio $x_{2p}/3x_{2s}$ reaching values as large as ~ 3 for z $\sim 500-600$. Although we do not track the populations of the $2p_{3/2}$ and $2p_{1/2}$ states separately, the overlap of the $1s_{1/2} - 2p_{1/2}$ and $1s_{1/2} - 2p_{3/2}$ Lyα doublet ensures that they are in statistical equilibrium, so $x_{2p_{3/2}}/2x_{2s_{1/2}} = x_{2p}/3x_{2s}$. It is therefore *a priori* possible for the 11 GHz $2p_{3/2} \to 2s_{1/2}$ transition to be amplified. We checked however that the largest negative optical depth in this transition is $\tau \sim -10^{-7}$ for $z \sim 1100$, and therefore the population inversion does not lead to any significant amplification.

4.7 Conclusions

In this chapter, we have evaluated the impact of several radiative transfer effects on cosmological hydrogen recombination:

• *Thomson scattering in the Ly-α line* was shown to be negligible, with corrections to the recombination history $|\Delta x_e/x_e| \lesssim 3 \times 10^{-5}$. We showed that at early times, $z \gtrsim 1300$, the dominant effect was a *delay* of recombination, due to the reinjection of photons from the red side of the line back into the blue side of the line during large angle scattering events. That effect can only be properly accounted for with a full kernel approach, since scattered photons are redistributed on frequency scales larger than the characteristic scale over which the radiation field changes. At lower

[7] I have removed the part of this section addressing population inversion in the high-n states, which is Daniel Grin's work and can be found in the published paper [40], as well as in Daniel Grin's thesis [87].

redshifts, recoil becomes dominant and Thomson scattering accelerates recombination by helping photons escape from the Lyα line.

• *Distortions from the deuterium Ly-α line* were shown to be negligible. Indeed, the very fast D($2p$) $\rightarrow$ D($1s$) transition rate, due to the relatively small optical depth in the deuterium line, brings the deuterium $2p$ to $1s$ ratio close to equilibrium with the incoming radiation field on the D Lyα line. Moreover, any distortions are further washed out due to the very large frequency diffusion rate caused by resonant scattering by neutral hydrogen. Accounting for deuterium therefore leads to changes of at most $\mathcal{O}(10^{-5})$ to the recombination history due to the small change in the expansion history and the ambiguity in defining x_e.

• *The high-lying, non-overlapping Lyman transitions* above Lyγ (strictly) can be artificially cut off without loss of accuracy. Only the $2s, 2p, 3p$ and $4p$ states therefore need to be considered as "interface" states in an EMLA computation [39]. Diffusion in Lyβ and higher lines can be neglected.

• *Overlap of the high-lying Lyman lines*, as well as overlap of the extremely high-lying lines with the continuum, was shown to lead to $\mathcal{O}(10^{-5})$ changes to the effective transition rates. This change is a few orders of magnitude smaller than the mere truncation error in the effective transition rates computed with $n_{\rm max} \sim 100$ energy shells. The effect of line overlap is therefore negligible.

• *Cosmological hydrogen masers* are shown not to arise in this purely radiative treatment.

The goal of the ongoing work in the field is to develop a complete theory for hydrogen recombination, with a well understood error budget. In this chapter, we have evaluated the impact of some radiative transfer effects that had not been previously addressed. While it is possible that some effects have not been considered yet, we believe that most of the radiative transfer effects relevant in primordial hydrogen recombination are now well understood. The picture is less clear for the effect of collisional processes [38], for which the rates are relatively poorly known. Ultimately, we need a recombination code that is not only accurate, but also fast, in order to be included in Markov chains for cosmological parameter estimation; this will be the subject of the next chapter.

4.A Appendix: Notation used in this chapter

Table 4.1: Notation used in this chapter. Units of "1" means the quantity is dimensionless.

Symbol	Units	Description	Equation
$A_{np,1s}$	s^{-1}	Einstein A-coefficient for the spontaneous decay $np \to 1s$	Eq. (4.3)
a_n	1	dimensionless Voigt parameter for the Ly-n transition	$a_n = \Gamma_{np}/(4\pi\nu_n\Delta_\mathrm{H})$
f_ν	1	photon occupation number at frequency ν	
f^n_eq	1	equilibrium value of f_ν near Ly-n	$f^n_\mathrm{eq} = x_{np}/(3x_{1s})$
$f^n_\mathrm{(em)}$	1	equilibrium value of f_ν near Ly-n, with true absorption and emission only	Eq. (4.15)
H	s^{-1}	Hubble expansion rate	
N_H	cm^{-3}	total number density of hydrogen nuclei	
N_X	cm^{-3}	number density of species X	
$\mathcal{N}_\nu$	Hz^{-1}	number of photons per hydrogen atom per unit frequency	$\mathcal{N}_\nu = \frac{8\pi\nu^2}{c^3 N_\mathrm{H}} f_\nu$
p^n_sc	1	fraction of photon absorptions in Ly-n resulting in a scattering	$p^n_\mathrm{sc} = A_{np,1s}/\Gamma_{np}$
p^n_ab	1	fraction of true photon absorptions in Ly-n	$p^n_\mathrm{ab} = 1 - p^n_\mathrm{sc}$
$R_{n'l\to np}$	s^{-1}	radiative transition rate $n'l \to np$ per hydrogen atom in the $[n', l]$ state	
$R_n(\nu, \nu')$	Hz^{-2}	resonant scattering redistribution kernel in Ly-n	Eq.(4.28)
$R_\mathrm{T}(\nu \to \nu')$	Hz^{-1}	Thomson scattering kernel	Eq. (4.51)
$\mathcal{R}(\delta)$	1	dimensionless Thomson scattering kernel	Eq. (4.56)
$\mathcal{S}_n$	Hz	width over which resonant scattering is effective in Ly-n	Eq. (4.36)
$\mathcal{S}$	Hz	width over which resonant scattering is effective in Lyα	$\mathcal{S} = \mathcal{S}_2$
S	1	dimensionless width over which resonant scattering is effective in Lyα	$S = (h\mathcal{S}/(kT_\mathrm{r}))^3$
$T_\mathrm{m}, T_\mathrm{r}$	K	matter and radiation temperatures	
$\mathcal{W}_n$	Hz	width over which the Ly-n wings are optically thick for true absorption	Eq. (4.35)
$\mathcal{W}$	Hz	width over which the Lyα wings are optically thick for true absorption	$\mathcal{W} = \mathcal{W}_2$
W	1	dimensionless width over which Lyα is optically thick for true absorption	$W = h\mathcal{W}/(kT_\mathrm{r})$

Table 4.1 (continued)

Symbol	Units	Description	Equation
$x_{\rm D}$	1	abundance of deuterium relative to total hydrogen nuclei	$x_{\rm D} = N_{\rm D}/N_{\rm H}$
x_{nl}	1	fraction of hydrogen in the state $[n, l]$	$x_{nl} = N_{{\rm H}(n,l)}/N_{\rm H}$
x_e	1	abundance of free electrons relative to total hydrogen nuclei	$x_e = N_e/N_{\rm H}$
x	1	detuning from line center (when considering a single line),	$x = (\nu - \nu_n)/(\nu_n \Delta_{\rm H})$
		or from ν_c (when considering line overlap), in Doppler units	$x = (\nu - \nu_c)/(\nu_c \Delta_{\rm H})$
x_n	1	detuning between Ly-n and Ly-continuum frequencies in Doppler widths	$x_n = (\nu_n - \nu_c)/(\nu_c \Delta_{\rm H})$
y	1	same as x OR detuning from the Lyα frequency in units of $kT_{\rm r}/h$	$y = h(\nu - \nu_{{\rm Ly}\alpha})/(kT_{\rm r})$
Γ_{np}	$\rm s^{-1}$	width (or inverse lifetime) of the np state	
$\Delta_{\rm X}$	1	dimensionless Doppler width for a scattering species of mass $m_{\rm X}$	$\Delta_{\rm X} = \sqrt{2kT_{\rm m}/(m_{\rm X}c^2)}$
$\Delta\nu_e$	Hz	rms frequency shift during an electron scattering event near Lyα	$\Delta\nu_e = \nu_{{\rm Ly}\alpha}\Delta_e$
η_e	$\rm Hz^{-1}$	differential optical depth for Thomson scattering near Lyman-α	Eq. (4.50)
$\nu_{{\rm Ly}\alpha}$ $(\nu_{\rm H}, \nu_{\rm D})$	Hz	Lyman-α resonant frequency (in hydrogen or deuterium specifically)	
ν_c	Hz	Lyman-limit frequency	$\nu_c = \frac{4}{3}\nu_{{\rm Ly}\alpha}$
ν_n	Hz	Lyman-n resonant frequency	$\nu_n = (1 - n^{-2})\nu_c$
$\sigma_{\rm T}$	$\rm cm^2$	Thomson cross section	
σ_0	$\rm cm^2$	photoionization cross section from the ground state, at threshold	Eq. (4.89)
τ_n	1	Sobolev optical depth in the Lyman-n resonance line	Eq. (4.6)
$\tau_{{\rm Ly}\alpha}$	1	Sobolev optical depth in the Lyman-α line	$\tau_{{\rm Ly}\alpha} = \tau_2$
τ_c	1	Lyman continuum optical depth per Doppler width near threshold	Eq. (4.101)
$\varphi_n(\nu)$	$\rm Hz^{-1}$	line profile for the Ly-n transition	
$\phi_{\rm V}(x; a)$	1	dimensionless Voigt profile, with Voigt parameter a	Eq. (4.10)
$\phi_n(x)$	1	dimensionless Doppler profile centered at the Ly-n frequency	$\phi_n(x) = \pi^{-1/2}{\rm e}^{-(x-x_n)^2}$
$\phi_c(x)$	1	non-normalized dimensionless profile for continuum absorption near threshold	Eq. (4.93)

4.B Appendix: Resonant scattering in a Doppler core dominated line[8]

We showed in Section 4.4.1 that only Lyα, Lyβ and Lyγ decays affect recombination to a significant level. The exact value of the escape probability in higher-order lines is therefore irrelevant to the problem of primordial recombination. It may however be important in other environments, such as the interstellar medium or stellar atmospheres, to compute the change in escape probability due to partial frequency redistribution in resonant scattering events. This appendix provides a generalization of the Sobolev escape probability for Doppler core dominated optically thick lines (i.e., with optically thin damping wings) with partial frequency redistribution. We also develop a method of solution based on expansion of the radiative transfer equation on the Hermite polynomials basis. We do not consider stimulated emission nor stimulated scattering.

4.B.1 The radiative transfer equation in the presence of partial frequency redistribution

In the absence of non-resonant processes, the most general radiative transfer equation in the vicinity of a resonant line was given in Eq. (4.32). We consider a line (with resonant frequency ν_0) with optically thin damping wings. We can use the Doppler core approximation for the line profile:

$$\phi(\nu) = \frac{1}{\sqrt{\pi}\Delta\nu_{\rm D}} \exp\left[-\left(\frac{\nu-\nu_0}{\Delta\nu_{\rm D}}\right)^2\right], \tag{4.148}$$

where $\Delta\nu_{\rm D} \equiv \nu_0\sqrt{2kT/(mc^2)}$ is the Doppler width of the line, m being the mass of the scatterers. Provided $h\nu_0 \ll \sqrt{mc^2kT}$, we can neglect approximate the exponential factors by unity in Eq. (4.32). The scattering redistribution kernel $R_n(\nu,\nu') = \phi_n(\nu')p_n(\nu|\nu')$ can be taken to be the $R_{\rm I}$ kernel for zero natural line width [89]. Finally, as long as the line is narrow ($\Delta\nu_{\rm D} \ll \nu_0$, always true if the scatterers are non-relativistic), one can make the steady-state approximation and neglect the time dependence in this problem. Making the change of variables

$$x \equiv \frac{\nu-\nu_0}{\Delta\nu_{\rm D}}, \tag{4.149}$$

the time-steady radiative transfer equation for the photon occupation number $f(x)$ becomes:

$$\frac{{\rm d}f}{{\rm d}x} = \tau\phi(x)\left[f(x) - f_{\rm eq}\right] + p_{\rm sc}\,\tau\int\left[\phi(x)\phi(x') - R_{\rm I}(x,x')\right]f(x'){\rm d}x', \tag{4.150}$$

[8]This work is unpublished.

where $\phi(x) \equiv \frac{1}{\sqrt{\pi}} \mathrm{e}^{-x^2}$ is the dimensionless Doppler profile and $R_{\mathrm{I}}(x, x')$ is the dimensionless scattering kernel for zero natural width. It is symmetric in in its arguments when recoil is ignored, and satisfies $\int R_{\mathrm{I}}(x, x') \mathrm{d}x' = \phi(x)$. The scattering kernel is a combination of the kernel for isotropic scattering $R_{\mathrm{I-A}}$ and the one for dipolar scattering $R_{\mathrm{I-B}}$, given in Eqs. (3.11.3) and (3.11.5) of Ref. [89]:

$$R_{\mathrm{I}}(x, x') = (1 - \chi) R_{\mathrm{I-A}}(x, x') + \chi R_{\mathrm{I-B}}(x, x'), \tag{4.151}$$

with $\chi \in [0, 1]$. The value of χ depends on the angular probability distribution of scattering directions in the atom's rest frame, $g(\mathbf{n}'|\mathbf{n})$, where $\mathbf{n}$ and $\mathbf{n}'$ are the direction of propagation of the incoming and outgoing photons respectively. It can be found by decomposing g on the basis:

$$\begin{aligned} g(\mathbf{n}'|\mathbf{n}) &= (1 - \chi) g_{\mathrm{iso}}(\mathbf{n}'|\mathbf{n}) + \chi g_{\mathrm{dip}}(\mathbf{n}'|\mathbf{n}) & (4.152) \\ &\equiv (1 - \chi) \frac{1}{4\pi} + \chi \frac{3}{16\pi} \left(1 + (\mathbf{n} \cdot \mathbf{n}')^2\right). & (4.153) \end{aligned}$$

The value of χ depends in general on the fine and hyperfine splitting of the levels of the considered transition. The boundary condition for f is $f(+\infty) = f_+$. Using the linearity of the equation, and the relation $\int \left[\phi(x)\phi(x') - R(x, x')\right] \mathrm{d}x' = 0$, we can simplify Eq. (4.150) further by defining:

$$\xi(x) \equiv \frac{f(x) - f_+}{f_{\mathrm{eq}} - f_+}, \tag{4.154}$$

which satisfies the equation:

$$\frac{\mathrm{d}\xi}{\mathrm{d}x} = \tau \ \phi(x) \left[\xi(x) - 1\right] + \tau \ p_{\mathrm{sc}} \int \left[\phi(x)\phi(x') - R(x, x')\right] \xi(x') \mathrm{d}x', \tag{4.155}$$

with boundary condition $\xi(+\infty) = 0$.

Let us now try to qualitatively understand what we expect to happen when accounting for partial frequency redistribution. The differential probability for a scattered photon to have frequency x' given that the incoming photon had frequency x is $p(x'|x) = \phi(x')$ in the case of complete redistribution, and $p(x'|x) = R(x, x')/\phi(x)$ in the case of partial frequency redistribution. This allows us to compute the mean and variance of the frequency of the scattered photon frequency, as a function of that of the incoming photon. In the case of complete redistribution, we have

$$\langle x' \rangle_{\mathrm{CR}} = 0, \quad \langle x'^2 \rangle_{\mathrm{CR}} = \frac{1}{2}, \tag{4.156}$$

independently of the frequency of the incoming photon. In the case of partial frequency redistribution, one can show either using the expressions given by Hummer [89] or the expansion derived

below, Eq. (4.175), that

$$\langle x' \rangle_{\rm PR} = 0, \quad \langle x'^2 \rangle_{\rm PR} = \frac{1}{3}\left[\left(1+\frac{\chi}{5}\right)x^2 + 1 - \frac{\chi}{10}\right]. \tag{4.157}$$

The mean outgoing photon frequency vanishes because forward ($x' = x$) and backward ($x' = -x$) scattering events are equally probable. The variance of the scattered photon frequency, however, increases with the distance of the incoming photon frequency from the resonant frequency. Near line center, $\langle x'^2 \rangle_{\rm PR} < \langle x'^2 \rangle_{\rm CR}$ so we expect photons to "pile up" a little more near line center. Several Doppler widths away from line center, $\langle x'^2 \rangle_{\rm PR} > \langle x'^2 \rangle_{\rm CR}$ so we expect photons in the wings to be re-scattered towards line center. Since the photon occupation number on the red side of the line is much larger (for an optically thick line) than that on the blue side, we therefore expect a net flux of photons from the red side of the line to the line center. In other words, partial redistribution will re-inject photons from the blue side of the line back into the line center where they are more likely to be absorbed, and therefore decrease the escape probability. Note, finally, that the effect will be more pronounced for isotropic scattering due to the enhanced probability of backward (and forward) scattering.

We now compute the change in escape probability. We will see that the qualitative features described above are indeed recovered in the exact solution (see Figs. 4.8 and 4.9).

4.B.2 Escape probability

From Eq. (4.42), the net decay rate in the line is

$$\begin{aligned} \dot{x}_{u\to l} &= \frac{g_u}{g_l} x_l A_{u,l} \int \phi(x)[f_{\rm eq} - f(x)]{\rm d}x = \frac{g_u}{g_l} x_l A_{u,l} \int \phi(x)[1-\xi(x)]{\rm d}x \times [f_{\rm eq} - f_+] \\ &\equiv P_{\rm esc}(\tau, p_{\rm sc}) A_{u,l} \left[x_u - \frac{g_u}{g_l} x_l f_+\right], \end{aligned} \tag{4.158}$$

where u and l denote the upper and lower levels. The last line defines the escape probability:

$$P_{\rm esc}(\tau, p_{\rm sc}) \equiv 1 - \overline{\xi} = \frac{\xi(-\infty)}{\tau}, \tag{4.159}$$

where $\overline{\xi} \equiv \int \phi(x)\xi(x)dx$ and we integrated Eq. (4.155) from $-\infty$ to $+\infty$ to obtain the second equality. When $p_{\rm sc} = 0$ (complete redistribution), Eq. (4.155) is a simple ODE that can be solved analytically; in that case $\xi(-\infty) = 1 - {\rm e}^{-\tau}$ and we recover the standard Sobolev escape probability. In the general case, Eq. (4.155) is an integro-differential equation, which does not have any analytic solutions, and therefore requires solving by a numerical method.

Before explaining our method of solution, we first relate our expression for the escape probability to that derived by Switzer & Hirata [56] in the context of helium recombination. In the absence of

continuum absorption, Switzer & Hirata define the function

$$\xi^{\rm SH} \equiv \frac{f - f_+}{f_{\rm (em)} - f_+}, \tag{4.160}$$

where $f_{\rm (em)}$ was defined in Eq. (4.15) [this definition was given for a Lyman transition in hydrogen but can be easily generalized to any resonant line]. We showed in Section 4.2.2.1 that when the rate of expansion is much smaller than the inverse lifetimes of the excited states, the following relation was satisfied [see Eq. (4.22)]: $(1-p_{\rm sc})f_{\rm (em)} = f_{\rm eq} - p_{\rm sc}\overline{f}$. This allows us to express the function $\xi^{\rm SH}$ as a function of our function ξ:

$$\xi^{\rm SH} = \frac{(1-p_{\rm sc})\xi}{1-p_{\rm sc}\overline{\xi}}. \tag{4.161}$$

The expression derived in Ref. [56] for the escape probability

$$P_{\rm esc}^{\rm SH} = \frac{(1-p_{\rm sc})(1-\overline{\xi}^{\rm SH})}{1-p_{\rm sc}(1-\overline{\xi}^{\rm SH})} \tag{4.162}$$

can then be shown to be exactly equivalent to our expression, Eq. (4.159). The advantage of our formulation (besides a simpler expression for the escape probability) is that our function ξ is always strictly positive, even when $p_{\rm sc} \to 1$, whereas $\xi^{\rm SH} \to 0$ when $p_{\rm sc} \to 1$ and the escape probability as given by Ref. [56] is the ratio of two small numbers in that limit.

4.B.3 Hermite polynomial expansion of the scattering kernel

Explicit expressions for the angle averaged scattering redistribution kernel are given in [89]. It is however easier to start off with the angle-dependent scattering kernel, which in the case of zero natural line width is [99, 89]:

$$R_{\rm I}(x, \mathbf{n}, x', \mathbf{n}') = \frac{g(\mathbf{n}'|\mathbf{n})}{4\pi^2 \sin\gamma} {\rm e}^{-x'^2 - (x - x'\cos\gamma)^2 \csc^2\gamma}, \tag{4.163}$$

where γ is the angle between $\mathbf{n}$ and $\mathbf{n}'$, which are the directions of propagation of the incoming and outgoing (scattered) photon respectively, and $g(\mathbf{n}'|\mathbf{n})$ is the probability distribution of $\mathbf{n}'$ given $\mathbf{n}$ (s.t. $\int g(\mathbf{n}'|\mathbf{n}){\rm d}\mathbf{n}' = 1$).

We define the sequence:

$$u_n(x') \equiv \frac{1}{\sqrt{\pi}} \int_{-\infty}^{+\infty} {\rm e}^{-(x - x'\cos\gamma)^2 \csc^2\gamma} H_n(x){\rm d}x, \tag{4.164}$$

where H_n is the n-th Hermite polynomial. Using the recursion relation

$$H_n(x) = 2xH_{n-1}(x) - 2(n-1)H_{n-2}(x), \tag{4.165}$$

integrating by parts and using the property

$$H'_{n-1}(x) = 2(n-1)H_{n-2}(x), \tag{4.166}$$

we obtain the recursion relation:

$$u_n(x') = 2x' \cos\gamma \; u_{n-1}(x') - 2(n-1)\cos^2\gamma \; u_{n-2}(x'). \tag{4.167}$$

This is the recursion relation satisfied by $\cos^n\gamma \; H_n(x')$. Since $u_0(x') = \sin\gamma H_0(x')$ and $u_1(x') = \sin\gamma\cos\gamma H_1(x')$, we conclude that

$$u_n(x') = \sin\gamma\cos^n\gamma H_n(x'). \tag{4.168}$$

We therefore obtain the relation:

$$\frac{1}{\sqrt{\pi}}\int R_{\rm I}(x,\mathbf{n},x',\mathbf{n}')H_n(x)\mathrm{d}x = \frac{g(\mathbf{n}'|\mathbf{n})}{4\pi^2}\cos^n\gamma \mathrm{e}^{-x'^2}H_n(x'). \tag{4.169}$$

From the orthogonality relation of the Hermite polynomials

$$\frac{1}{\sqrt{\pi}}\int_{-\infty}^{+\infty}\mathrm{e}^{-x^2}H_n(x)H_m(x)\mathrm{d}x = \delta_{nm}2^n n!, \tag{4.170}$$

we deduce the decomposition of $R_{\rm I}(x,\mathbf{n},x',\mathbf{n}')$ on the Hermite basis:

$$R_{\rm I}(x,\mathbf{n},x',\mathbf{n}') = \frac{g(\mathbf{n}'|\mathbf{n})}{4\pi^2}\mathrm{e}^{-x^2}\mathrm{e}^{-x'^2}\sum_{n=0}^{+\infty}\frac{\cos^n\gamma}{2^n n!}H_n(x)H_n(x'). \tag{4.171}$$

The angle-averaged redistribution kernel can be obtained by integrating over angles $\mathbf{n},\mathbf{n}'$ [89]:

$$\begin{aligned} R_{\rm I}(x,x') &= 8\pi^2\int_0^\pi R_{\rm I}(x,\mathbf{n},x',\mathbf{n}')\sin\gamma\mathrm{d}\gamma \\ &= \frac{\mathrm{e}^{-x^2}\mathrm{e}^{-x'^2}}{\pi}\sum_{p=0}^{+\infty}\frac{1}{2^{2p}(2p)!}\int_{-1}^{1}2\pi g(\mu)\mu^{2p}\mathrm{d}\mu \; H_{2p}(x)H_{2p}(x'), \end{aligned} \tag{4.172}$$

where we used the fact that $g(\mathbf{n}'|\mathbf{n})$ is a function of the dot product $\mathbf{n}\cdot\mathbf{n}' = \cos\gamma$ only, and therefore all its odd moments vanish.

For an isotropic angular distribution, $g_{\rm iso}(\mu) = \frac{1}{4\pi}$, we have:

$$\int_{-1}^{1}2\pi g_{\rm iso}(\mu)\mu^{2p}\mathrm{d}\mu = \frac{1}{2p+1}, \tag{4.173}$$

whereas for the dipolar angular distribution, $g_{\rm dip}(\mu) = \frac{3}{16\pi}(1+\mu^2)$, we have:

$$\int_{-1}^{1} 2\pi g_{\rm dip}(\mu)\mu^{2p}\mathrm{d}\mu = \frac{3(p+1)}{(2p+1)(2p+3)}. \tag{4.174}$$

With $g = (1-\chi)g_{\rm iso} + \chi g_{\rm dip}$, we obtain the decomposition of the scattering kernel on the Hermite polynomial basis:

$$R_{\rm I}(x,x') = \phi(x)\phi(x')\sum_{p=0}^{+\infty}\left(1+\frac{\chi\ p}{2p+3}\right)\frac{H_{2p}(x)H_{2p}(x')}{2^{2p}(2p+1)!}. \tag{4.175}$$

Such a decomposition was already worked out in Refs. [100, 101] in the case of isotropic scattering (with a missing factor of $1/(2p+1)$ in Ref. [100]).

4.B.4 Solution of the steady-state radiative transfer equation with scattering

Given the quite simple decomposition of the scattering kernel on the Hermite polynomial basis derived above, we suggest a method of solution to the time-steady radiative transfer equation including scattering, Eq. (4.155).

The Hermite polynomials form an orthonormal basis, and we can decompose the function ξ on that basis:

$$\xi = \sum_{n=0}^{+\infty} a_n H_n(x). \tag{4.176}$$

Using the decomposition (4.175) and the orthogonality relation (4.170), the radiative transfer equation Eq. (4.155) therefore reads:

$$\frac{\mathrm{d}\xi}{\mathrm{d}x} = \tau\ \phi(x)\left[a_0 - 1 + \sum_{n=1}^{+\infty} a_n H_n(x) - p_{\rm sc}\sum_{p=1}^{+\infty}\left(1+\frac{\chi p}{2p+3}\right)\frac{a_{2p}}{2p+1}H_{2p}(x)\right]. \tag{4.177}$$

The formal solution to this equation is:

$$\xi(x) = -\int_x^{+\infty}\frac{\mathrm{d}\xi}{\mathrm{d}x'}\mathrm{d}x'. \tag{4.178}$$

Using the defining relation for Hermite polynomials,

$$H_n(x) = \mathrm{e}^{x^2}(-1)^n\frac{\mathrm{d}}{\mathrm{d}x^n}\left(\mathrm{e}^{-x^2}\right), \tag{4.179}$$

we can easily show that, for $n > 0$,

$$\int_x^{+\infty} \phi(x')H_n(x')\mathrm{d}x' = \phi(x)H_{n-1}(x). \tag{4.180}$$

The formal solution is therefore:

$$\xi(x) = \tau\ (1-a_0)\frac{1}{2}\mathrm{erfc}(x) + \tau\ \phi(x)\left[-\sum_{n=1}^{+\infty} a_n H_{n-1}(x) + p_{\mathrm{sc}} \sum_{p=1}^{+\infty} \left(1 + \frac{\chi p}{2p+3}\right) \frac{a_{2p}}{2p+1} H_{2p-1}(x)\right]. \tag{4.181}$$

To close the system we need to make sure that the coefficients of ξ on the Hermite basis are those we started with:

$$a_n = \frac{1}{\sqrt{\pi}2^n n!} \int_{-\infty}^{+\infty} \mathrm{e}^{-x^2} H_n(x)\xi(x)\mathrm{d}x. \tag{4.182}$$

We need to establish some preliminary results first. We define the sequence:

$$\begin{aligned} v_p &\equiv \frac{1}{\sqrt{\pi}} \int_{-\infty}^{+\infty} \mathrm{e}^{-2x^2} H_{2p}(x)\mathrm{d}x & (4.183)\\ &= u_{2p}\left(x' = 0; \gamma = \frac{\pi}{4}\right), & (4.184) \end{aligned}$$

where $u_n(x';\gamma)$ was defined in Eq. (4.164). From Eq. (4.168), we have

$$v_p = \frac{1}{\sqrt{2}} \frac{1}{2^p} H_{2p}(0) = (-1)^p \frac{1}{\sqrt{2}} \frac{(2p)!}{2^p p!}, \tag{4.185}$$

from the well known values of the Hermite numbers $H_{2p}(0)$. We can show the following relations:

$$\begin{aligned} \frac{1}{\sqrt{\pi}} \int_{-\infty}^{+\infty} \mathrm{e}^{-x^2} H_{2q}(x)\mathrm{erfc}(x)\mathrm{d}x &= \delta_{q0} & (4.186)\\ \frac{1}{\sqrt{\pi}} \int_{-\infty}^{+\infty} \mathrm{e}^{-x^2} H_{2q+1}(x)\mathrm{erfc}(x)\mathrm{d}x &= -\frac{2}{\sqrt{\pi}} v_q & (4.187)\\ \frac{1}{\sqrt{\pi}} \int_{-\infty}^{+\infty} \mathrm{e}^{-2x^2} H_{2q+1}(x)H_{2p}(x)\mathrm{d}x &= 0 & (4.188)\\ \frac{1}{\sqrt{\pi}} \int_{-\infty}^{+\infty} \mathrm{e}^{-2x^2} H_{2q}(x)H_{2p}(x)\mathrm{d}x &= v_{p+q} & (4.189)\\ \frac{1}{\sqrt{\pi}} \int_{-\infty}^{+\infty} \mathrm{e}^{-2x^2} H_{2q+1}(x)H_{2p-1}(x)\mathrm{d}x &= -v_{p+q}. & (4.190) \end{aligned}$$

We finally obtain the system of equations satisfied by the coefficients $\{a_n\}$:

$$\begin{aligned} a_{2q} &= \frac{1}{2}\tau(1-a_0)\delta_{q0} - \frac{\tau}{2^{2q}(2q)!\sqrt{\pi}} \sum_{p=0}^{+\infty} v_{p+q} a_{2p+1}, & (4.191)\\ a_{2q+1} &= \frac{\tau/\sqrt{\pi}}{2^{2q+1}(2q+1)!} \left\{ -(1-a_0)v_q + \sum_{p=1}^{+\infty} \left[1 - \frac{p_{\mathrm{sc}}}{2p+1}\left(1 + \frac{\chi\ p}{2p+3}\right)\right] v_{p+q} a_{2p} \right\}. & (4.192) \end{aligned}$$

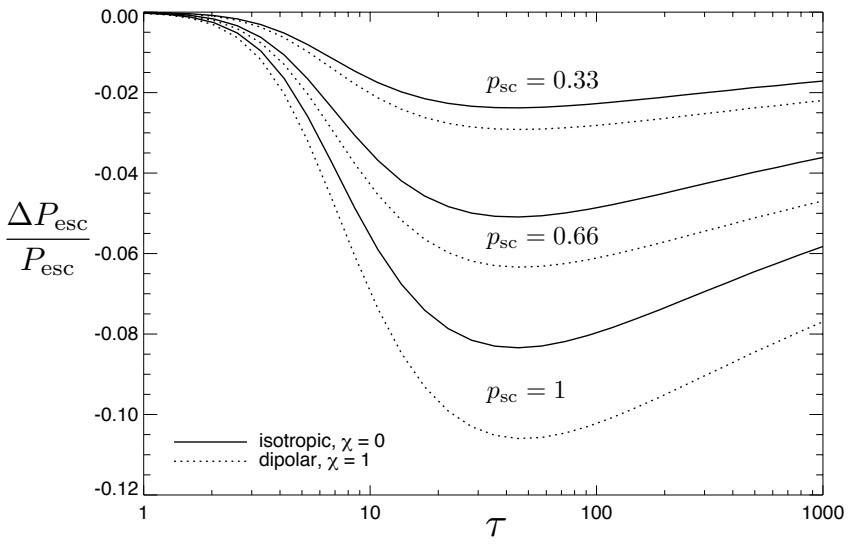

Figure 4.8: Decrease in the escape probability due to partial frequency redistribution [the quantity plotted is $\Delta P_{\rm esc}/P_{\rm esc} \equiv P_{\rm esc}(\tau, p_{\rm sc})/P_{\rm esc}(\tau, p_{\rm sc} = 0) - 1$]. The effect is more pronounced for dipolar scattering than isotropic scattering due to the higher probability of backward scattering.

This is in principle an infinite system of linear equations with an infinite number of unknowns. Our approximation of order N consists in truncating it to the $N + 1$ unknowns $\{a_0, ..., a_N\}$, i.e., solving the system (4.191), (4.192) where we set $a_n = 0$ for $n > N$.

Once we obtain the coefficients $\{a_0, ..., a_N\}$, we use the expression (4.181) for $\xi(x)$ to compute $\xi(-\infty)$ rather than the initial decomposition (4.176), which, when truncated at a finite N, is infinite at $x \to \pm\infty$. We therefore obtain the desired escape probability:

$$P_{\rm esc} = \frac{\xi(-\infty)}{\tau} = 1 - a_0. \tag{4.193}$$

We check the convergence of our method with the known analytic solution in the case $p_{\rm sc} = 0$:

$$P_{\rm esc}(\tau, p_{\rm sc} = 0) = \frac{1 - {\rm e}^{-\tau}}{\tau} \approx \frac{1}{\tau}, \quad \tau \gg 1. \tag{4.194}$$

We find that the approximation has converged to the analytic solution with a relative accuracy of 10^{-4} for $N \gtrsim 30 \log_{10}(\tau)$.

We show the resulting change in escape probability as function of the optical depth and $p_{\rm sc}$ in Fig. 4.8. We see that partial redistribution leads to a systematic *decrease* of the escape probability, as we had anticipated (see discussion at the end of Section 4.B.1). The magnitude of the relative decrease is no larger than $\sim 10\%$, reached for $\tau \sim 50, p_{\rm sc} = 1$ and $\chi = 1$. We also show the function $\xi(x)$ in Fig. 4.9 as an illustration of the qualitative argument given in Section 4.B.1.

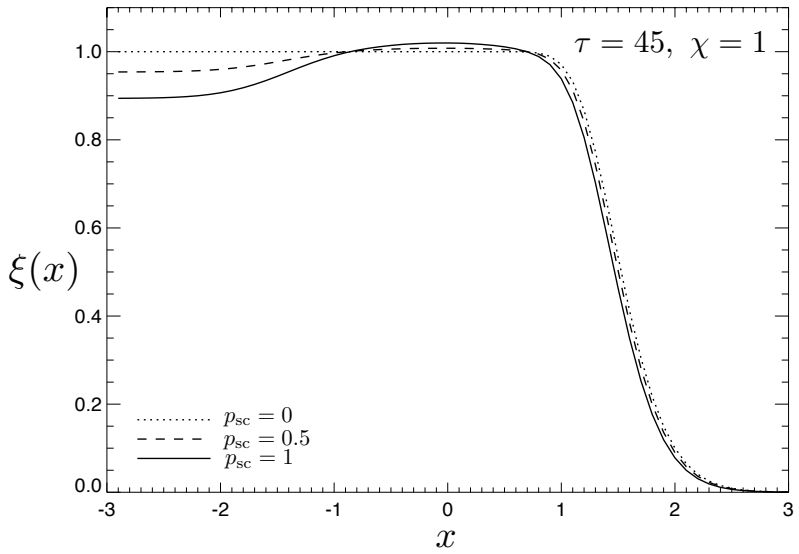

Figure 4.9: Normalized photon occupation number ξ as defined in Eq. (4.154) as a function of frequency in Doppler width units, for Sobolev optical depth $\tau = 45$ and dipolar scattering. Partial redistribution during resonant scattering events re-injects photons from the red side of the line back into line center, where they get absorbed.

Chapter 5

A fast and highly accurate primordial hydrogen recombination code[1]

5.1 Introduction

Previous works have all concentrated on one or a few aspects of the primordial recombination problem. Producing a complete and fast recombination code has so far been hindered by the computational burden previously associated with the high-n problem. Given that this problem is now solved, and that it seems that the main radiative transfer effects have now all been identified, it is timely to deliver a single code that computes an accurate hydrogen and helium recombination history and incorporates all the relevant physics. The purpose of this chapter is to introduce our new recombination code, HyRec, which is publicly available[2], and can compute a highly accurate recombination history (with errors at the level of a few times 10^{-3} for helium recombination and a few times 10^{-4} for hydrogen recombination) in only ~ 2 seconds on a standard laptop. Our code does not account for collisional transitions in hydrogen, as their rates are poorly known. When accurate rates are available and if collisional transitions are shown to significantly impact recombination, we will update our code with the appropriate effective rates.

Recently, a similar work has been carried out by Chluba & Thomas [102], also relying on the effective MLA method presented in Chapter 3. The code they present includes the same physics as ours. The main difference is the treatment of radiative transfer. In Ref. [102], an "order zero" recombination history is first computed, with a simple treatment of radiative transfer. The radiative transfer equation is then solved, given this order zero history. Corrections to the net decay rates

[1] This chapter is adapted from the paper *HyRec: A fast and highly accurate primordial hydrogen and helium recombination code*, Y. Ali-Haïmoud & C. M. Hirata, Phys. Rev. D **83**, 043513 (2011). The section on helium recombination was not included as it is Christopher Hirata's work but the reader is encouraged to read it in the published paper. Reproduced here with permission, copyright (2011) by the American Physical Society.

[2] HyRec is available for download at the following url: http://www.tapir.caltech.edu/∼yacine/hyrec/hyrec.html.

to the ground state are then evaluated, and used to compute a corrected recombination history. This procedure can in principle be iterated, but because the corrections are small, it is essentially converged after one or two iterations. Our solution, on the other hand, is non-perturbative, in the sense that we solve *simultaneously* for the radiation field and the recombination history. A detailed code comparison is in progress, and a full error budget will be presented once it is completed.

In Chapter 4 we briefly evoked the connection between resonant line processes and two-photon transitions. We considered line profiles in the resonant approximation near resonances, since we were mainly studying other (non-resonant) processes that turned out to be negligible. At the level of precision required by *Planck*, two-photon processes must be treated accurately, with correct profiles and a full time-dependent radiative transfer calculation [49, 51, 52].

This chapter is organized as follows. Two-photon processes and frequency diffusion are formally described in Section 5.2. In Section 5.3, we present our numerical solution for the radiative transfer equation. We use a new method of solution, extending that of Ref. [49] to account for frequency diffusion, that allows to solve for the atomic populations and the radiation field simultaneously. We conclude in Section 5.4. Appendix 5.A describes our ordinary differential equation (ODE) integrator and Appendix 5.B lists the numerically stable radiative transfer equations used in the latest version of HyRec[3].

Throughout this chapter we use a flat background ΛCDM cosmology with $T_0 = 2.728$ K, $\Omega_b h^2 = 0.022$, $\Omega_m h^2 = 0.13$, $\Omega_\Lambda h^2 = 0.343$, $Y_{\rm He} = 0.24$ and $N_{\nu,\rm eff} = 3.04$.

5.2 Two-photon processes: formal description

5.2.1 Overview

It is well known since the first works on primordial recombination that $2s \to 1s$ two-photon decays significantly contribute to the recombination dynamics [31, 32]. Even with a relatively low decay rate, the forbidden $2s \to 1s$ decays are indeed comparable in efficiency to the highly self-absorbed Lyman-α transition; in fact, more than half of hydrogen atoms have formed through the $2s \to 1s$ channel [70]. This process was traditionally accounted for with the total $2s \to 1s$ decay rate in vacuum, $\Lambda_{2s,1s} \approx 8.22$ s^{-1}, with a two-photon absorption rate obtained by detailed balance considerations. For the level of accuracy required for future CMB experiments, one needs to account for stimulated two-photon decays [47] and non-thermal absorptions [48, 49].

Recently, it was suggested that two-photon decays from higher lying ns and nd states may also lead to percent level corrections to the recombination history [50]. Inclusion of such decays presents an additional conceptual difficulty which was not present for the $2s \to 1s$ decays: the problem of double-counting. Indeed, there is no fundamental difference between a sequence of two allowed

[3] I will upload this version online within the next few days.

one-photon transitions $nl \to n'p$, $n'p \to 1s$, with $1 < n' < n$, and a two-photon decay from the nl state near resonance (i.e., where the energy of the two photons are near $E_{nn'}$ and $E_{n'1}$ respectively). Approximate solutions were presented in Refs. [50, 103, 51] (for a review, see Ref. [49]). The double-counting problem as well as the reabsorption problem were resolved with a numerical approach, solving the radiative transfer equations for the photon field in Ref. [49], which also provided analytic approximations to check the validity of the numerical result. In this work, we will use the same numerical method as in Ref. [49], which we extend to account for frequency diffusion near the Lyα line. In this section, we review the formalism presented in Ref. [49] and how to solve the double counting problem. In Section 5.3 we will describe our numerical method for solving simultaneously the radiative transfer equation and the evolution of the atomic level populations.

5.2.2 Two-photon decays and Raman scattering

We start by defining the coefficient:

$$\frac{d\Lambda_{nl}}{d\nu} \equiv \frac{\alpha_{\rm fs}^6 \nu^3 \nu'^3}{108(2l+1)E_I^6} |\mathcal{M}(\nu)|^2, \tag{5.1}$$

where the matrix element $\mathcal{M}(\nu)$ is given by Eq. (B5) of Ref. [49], and $\nu' \equiv |\nu - \nu_{n1}|$, where ν_{n1} is the frequency of the Ly-n transition. For $\nu < \nu_{n1}$, $d\Lambda_{nl}/d\nu$ is the rate of spontaneous two-photon decays from nl per frequency interval. For $\nu > \nu_{n1}$, $d\Lambda_{nl}/d\nu \times f_{\nu'}$ (where f_ν is the photon occupation number at frequency ν) is the rate of spontaneous Raman scatterings per frequency interval per atom initially in nl (in the notation of Ref. [49], $d\Lambda_{nl}/d\nu = dK_{nl}/d\nu$ for $\nu > \nu_{n1}$). The function $d\Lambda_{nl}/d\nu$ is continuous across $\nu = \nu_{n1}$, where it vanishes.

We can now write the net rate of $nl \leftrightarrow 1s$ two-photon transitions per frequency interval per hydrogen atom, for which the highest energy photon has frequency $\nu < \nu_{n1}$:

$$\Delta_{nl}(\nu < \nu_{n1}) = \frac{d\Lambda_{nl}}{d\nu}\Big[x_{nl}(1+f_{\nu'})(1+f_\nu) - \frac{g_{nl}}{g_{1s}} x_{1s} f_{\nu'} f_\nu\Big]. \tag{5.2}$$

For $\nu > \nu_{n1}$, the appropriate rate is that of Raman scattering events:

$$\Delta_{nl}(\nu > \nu_{n1}) = \frac{d\Lambda_{nl}}{d\nu}\Big[x_{nl} f_{\nu'}(1+f_\nu) - \frac{g_{nl}}{g_{1s}} x_{1s}(1+f_{\nu'}) f_\nu\Big], \tag{5.3}$$

In both cases, we can assume that the photon occupation number for the low-energy photons is that of a blackbody, since the optical depth for two-photon absorption of the low-energy photons is tiny (for a discussion, see Ref. [49]). We therefore set $f_{\nu'} = (\mathrm{e}^{h\nu'/T_{\rm r}} - 1)^{-1}$. Moreover, the photon occupation number for frequencies $\nu > \nu_{\rm Ly\alpha}/2$ is much smaller than unity: $f_\nu \ll 1$. This means that we can neglect stimulated emission by the high-energy photons in Eqs. (5.2) and (5.3). Given these considerations, the net rate of two-photon transitions can be written in the following form, valid for

both $\nu < \nu_{n1}$ and $\nu > \nu_{n1}$:

$$\Delta_{nl}(\nu) = \frac{d\Lambda_{nl}}{d\nu}\left|\mathrm{e}^{h(\nu-\nu_{n1})/T_\mathrm{r}} - 1\right|^{-1}\left[x_{nl} - \frac{g_{nl}}{g_{1s}}x_{1s}\mathrm{e}^{h(\nu-\nu_{n1})/T_\mathrm{r}}f_\nu\right]. \tag{5.4}$$

5.2.3 Resonant scattering in Lyman-α

We now consider pure scattering events,

$$\mathrm{H(1s)} + \gamma \rightarrow \mathrm{H(1s)} + \gamma. \tag{5.5}$$

In the low-frequency limit this corresponds to the familiar Rayleigh scattering phenomenon; the cross section however has resonances at the Lyman-series lines, which correspond to resonant Rayleigh scattering.

Rayleigh scattering events conserve the photon frequency in the atom's rest frame. In the co-moving frame (frame in which the CMB appears isotropic), the frequency of the scattered photon appears shifted due to the thermal motions of the scatterers. The frequencies of the incoming and outgoing photons are however statistically correlated. Mathematically, there is a definite probability distribution $p(\nu, \nu')$, such that $p(\nu, \nu')d\nu'$ is the probability that the outgoing photon has frequency in $[\nu', \nu' + d\nu']$ given that the incoming photon had frequency ν, and this function generally depends on both ν and ν'. For $T_\mathrm{m} \ll h\nu$, which is the case near the Lyman lines, the variance of the frequency shifts imparted by thermally moving atoms is given by:

$$\langle \delta\nu^2 \rangle \equiv \int (\nu' - \nu)^2 p(\nu, \nu')d\nu' = \frac{2T_\mathrm{m}}{m_\mathrm{H}c^2}\nu^2. \tag{5.6}$$

The rate of injection of photons per frequency interval at frequency ν, due to resonant Rayleigh scattering in Ly-α, can be written in the general form (neglecting stimulated scatterings):

$$\Delta_{1s}(\nu) = x_{1s}\left[\int f_{\nu'}R(\nu', \nu)d\nu' - \int f_\nu R(\nu, \nu')d\nu'\right], \tag{5.7}$$

where $R(\nu, \nu') = \frac{d\Lambda_{1s}}{d\nu}p(\nu, \nu')$ is the differential rate of scatterings per hydrogen atom in the ground state, per unit frequency interval for both the incoming and outgoing photons (it has units of $\mathrm{s}^{-1}\mathrm{Hz}^{-2}$). The scattering kernel must respect detailed balance:

$$R(\nu, \nu')\mathrm{e}^{-h\nu/T_\mathrm{m}} = R(\nu', \nu)\mathrm{e}^{-h\nu'/T_\mathrm{m}}. \tag{5.8}$$

To be fully general one should compute the scattering kernel from first principles. However, simplifications can be easily made in various regimes.

Far from any resonance, the rate of redshifting due to the Hubble expansion is much larger than

the rate of frequency diffusion due to scattering (see for example the discussion in Section 4.2.2.3). We can neglect Rayleigh scattering there, and set $\Delta_{1s}(\nu) = 0$.

Near Lyman resonances, we have

$$\frac{d\Lambda_{1s}}{d\nu}(\nu \approx \nu_{n1}) \approx 3A_{np,1s}p_{\rm sc}^{n}\phi_{V,n}(\nu), \tag{5.9}$$

where $p_{sc}^{n} = A_{np,1s}/\Gamma_{np}$ is the scattering probability in the Lyman-n line (the complementary events being two-photon absorptions and two-photon photoionizations), and $\phi_{V,n}(\nu)$ is the Voigt profile for the Ly-n line. In the Doppler core, we can approximate the partial redistribution induced by scattering events by a complete redistribution, i.e., approximate $p(\nu, \nu') \approx \phi_{V,n}(\nu) \approx \phi_{D,n}(\nu)$, independent of ν', where ϕ_D is the Doppler profile. This approximation is valid because in the Doppler core, complete redistribution recovers the correct rms frequency shift during scattering events, Eq. (5.6) (if one averages over the frequencies of absorbed photons).

In the damping wings of Lyman resonances above Lyα, the rate of scattering events is of the same order as the rate of two-photon absorptions. Each scattering event shifts the photon frequency by a very small amount compared to the width over which the radiation field varies ($\delta\nu_{\rm rms}/\nu \sim 2.5\times10^{-5}$). Partial redistribution is therefore essentially coherent in the comoving frame, i.e., $p(\nu, \nu') \approx \delta(\nu' - \nu)$, which implies $\Delta_{1s}(\nu) \approx 0$. For a more quantitative argument, see Section 4.4.2.

The only frequency regime where Rayleigh scattering affects the radiation field in a non-trivial way is in the damping wings of Lyα. In this line, indeed, scattering events are much more frequent than two-photon absorption events (by a factor of $\sim 10^4$). Resonant scattering therefore leads to a significant diffusion in frequency. Because the frequency shifts are small compared to the width over which the radiation field varies, the integral scattering operator can be approximated by a second-order differential operator — a Fokker-Planck operator [92, 90, 45, 46]. For the purpose of numerical implementation, the relevant properties are (i) the fact that this operator is nearly local (it only connects neighboring bins in frequency), (ii) it must respect detailed balance, and (iii) the diffusion rate must be correct. We will explain our numerical method for the implementation of Lyman-α diffusion in Section 5.3.1.

We note that a number of analytic treatments of Lyman-α scattering in the recombination epoch have been proposed in the past [104, 93, 94, 105, 90]. However, since two-photon emission and absorption act on the same region of frequency space, and since both processes involve high optical depth, an accurate recombination history can only be obtained by considering all processes simultaneously.

5.2.4 The radiative transfer equation

The radiative transfer equation for the photon occupation number is:

$$\frac{\partial f_\nu}{\partial t} - H\nu\frac{\partial f_\nu}{\partial \nu} = \frac{c^3 n_{\rm H}}{8\pi\nu^2}\left[\sum_{n\geq 2,l}\Delta_{nl}(\nu) + \Delta_{1s}(\nu)\right], \tag{5.10}$$

where the left-hand side is the derivative of the photon occupation number along a photon trajectory in the expanding universe, and the prefactor on the right-hand side converts the number of photons per unit frequency per hydrogen atom to the photon occupation number (see Section 4.2).

5.2.5 Inclusion in the effective multilevel atom rate equations

5.2.5.1 Formal two-photon decay rates

As mentioned earlier, including two-photon decays from states with $n > 2$ and Raman scattering events poses a double-counting problem. In principle, to avoid this double counting issue, one should discard "1+1" decays (or decays following an absorption event, which is like a Raman scattering event on resonance) altogether. If one were to pursue this idea, one should not consider the p states at all anymore (as they are formally only intermediate states in two-photon processes), but consider all s and d states as "interface states" and allow for two-photon recombinations to the ground state. The two-photon $nl \leftrightarrow 1s$ transition rates would then become:

$$\dot{x}_{nl}\big|_{1s}^{(2\gamma)} = -\dot{x}_{1s}\big|_{nl}^{(2\gamma)} = x_{1s}\tilde{R}^{\rm total}_{1s,nl} - x_{nl}\tilde{R}^{\rm total}_{nl,1s}, \tag{5.11}$$

where the formal transition rates are given by:

$$\tilde{R}^{\rm total}_{1s,nl} \equiv \int \frac{d\Lambda_{nl}}{d\nu}\frac{g_{nl}}{g_{1s}}\left|{\rm e}^{h(\nu_{n1}-\nu)/T_{\rm r}} - 1\right|^{-1} f_\nu d\nu \tag{5.12}$$

and

$$\tilde{R}^{\rm total}_{nl,1s} \equiv \int \frac{d\Lambda_{nl}}{d\nu}\left|{\rm e}^{h(\nu-\nu_{n1})/T_{\rm r}} - 1\right|^{-1} d\nu, \tag{5.13}$$

where the integrals run from $\nu_{n1}/2$ to ν_c. In principle Eq. (5.11)–(5.13), can be included in a standard or effective multilevel atom code, provided one solves simultaneously for the radiation field, using the radiative transfer equation Eq. (5.10).

5.2.5.2 Decomposition into "1+1" transitions and non-resonant contributions

Two-photon decays from higher excited states constitute, however, a correction to the recombination history computed in the standard "1+1" picture, and we would like to implement it as such. We start by formally separating the integrals in Eqs. (5.12) and (5.13) in two contributions: the resonant

pieces, for $\nu \approx \nu_{n'1}$, and a non-resonant piece, for frequencies far enough from any resonance. We therefore rewrite, formally:

$$\begin{aligned} \tilde{R}^{\rm total}_{1s,nl} &= \sum_{n'} \tilde{R}^{(n'p)}_{1s,nl} + \tilde{R}_{1s,nl} \quad \text{and} \\ \tilde{R}^{\rm total}_{nl,1s} &= \sum_{n'} \tilde{R}^{(n'p)}_{nl,1s} + \tilde{R}_{nl,1s}, \end{aligned} \tag{5.14}$$

where the resonant contributions $\tilde{R}^{(n'p)}_{1s,nl}$ and $\tilde{R}^{(n'p)}_{nl,1s}$ are defined in a similar manner as in Eqs. (5.12) and (5.13), but with the integration being carried over a narrow range $\Delta\nu$ near $\nu_{n'1}$, and $\tilde{R}_{1s,nl}$ and $\tilde{R}_{nl,1s}$ are the non-resonant pieces required to complete the total rates. So far the separation is just formal and we have not made any approximation.

5.2.5.3 "1+1" Resonant contribution

We now notice that near a resonance $\nu \approx \nu_{n'1}$, the two-photon differential decay rate $d\Lambda_{nl}/d\nu$ takes on the following form (if $n > n'$):

$$\left.\frac{d\Lambda_{nl}}{d\nu}\right|_{\nu\approx\nu_{n'1}} \approx \frac{1}{4\pi^2} \frac{A_{nl,n'p}A_{n'p,1s}}{(\nu-\nu_{n'1})^2 + (\Gamma_{n'p}/4\pi)^2} = A_{nl,n'p}\frac{A_{n'p,1s}}{\Gamma_{n'p}}\phi_L(\nu-\nu_{n'1};\Gamma_{n'p}), \tag{5.15}$$

where $\Gamma_{n'p}$ is the total inverse lifetime of the state $n'p$, and the Lorentzian profile is given by

$$\phi_L(\Delta\nu;\Gamma) \equiv \frac{\Gamma/(4\pi^2)}{\Delta\nu^2 + (\Gamma/4\pi)^2}. \tag{5.16}$$

For $n < n'$, the first coefficient in Eq. (5.15) should be $g_{n'p}/g_{nl} \times A_{n'p,nl}$ instead of $A_{nl,n'p}$. When accounting for the thermal motions of atoms, the Lorentzian profile should be replaced by a Voigt profile. We can now approximate the resonant pieces with the following expressions, valid for both $n < n'$ and $n > n'$:

$$\tilde{R}^{(n'p)}_{1s,nl} \approx 3A_{n'p,1s}\overline{f}_{\nu_{n'1}}\frac{R_{n'p,nl}}{\Gamma_{n'p}} \tag{5.17}$$

and

$$\tilde{R}^{(n'p)}_{nl,1s} \approx R_{nl,n'p}\frac{A_{n'p,1s}}{\Gamma_{n'p}}, \tag{5.18}$$

where $\overline{f}_{\nu_{n'1}}$ is the photon occupation number averaged over the Voigt profile near the resonance $\nu \approx \nu_{n'1}$. Eqs. (5.17) and (5.18) are exactly what one would obtain in the "1+1" picture after "factoring out" the p states (with a procedure similar to what is used to get rid of the "interior" states in the EMLA method). Having these resonant rates is exactly equivalent to having optically thin one-photon transitions between the nl and $n'p$ states, with rates $R_{nl,n'p}(T_{\rm r})$ and $R_{n'p,nl}(T_{\rm r})$,

and optically thick Lyman transitions, with net rate:

$$\dot{x}_{n'p}\big|_{1s} = -\dot{x}_{1s}\big|_{n'p} = A_{n'p,1s}\left(3x_{1s}\overline{f}_{\nu_{n'p}} - x_{n'p}\right). \tag{5.19}$$

To obtain the net decay rates in the Lyman transitions, one then needs to solve for the radiation field in the immediate vicinity of Lyman resonances. If the frequency region for which two-photon transitions are considered as "resonant" is narrow enough, this can be done in the Sobolev approximation. Indeed, all the relevant conditions are met (see also discussion in Ref. [49]; for more details on the Sobolev approximation, see Section 4.2.4):

First, the two-photon absorption and emission profiles can both be approximated by the same resonance profile Eq. (5.15). This relies on the assumption that the blackbody radiation field varies little across the "resonant" region, and requires for its width to satisfy $\Delta\nu \ll T_{\rm r}/h$.

Secondly, we argued in Section 5.2.3 that one could assume complete frequency redistribution for resonant scattering near the Doppler core of Lyman resonances. The "resonant" region should therefore not exceed a few Doppler widths.

Finally, if we consider regions in frequency narrow enough around the resonances, we can use the steady-state approximation. This requires $\Delta\nu/\nu \ll 1$.

We can see that considering the "resonant" region around each Lyman resonance to be a few Doppler widths wide meets all the requirements.

An additional assumption required here is that excited states are near Boltzmann equilibrium, which is very accurate at redshifts for which two-photon processes are important. In the Sobolev approximation, and in the limit of large Sobolev optical depth, Eq. (5.19) becomes the standard Lyman decay rate Eq. (3.8), where f^{+}_{np} is the photon occupation number incoming on the resonance, preprocessed by two-photon processes and diffusion in the blue damping wing of the line.

The Sobolev approximation is probably the least accurate for Lyα decays where partial redistribution due to resonant scattering is important. However, the large optical depth to two-photon absorptions in the Lyman-α blue damping wing, in conjunction with frequent scattering events, drive the radiation field to the equilibrium value $f_\nu = x_{n'p}/(3x_{1s})\mathrm{e}^{-h(\nu-\nu_{n'1})/T_{\rm m}}$ over several Doppler widths (of the order of 40 Doppler widths, see Fig. 4.1 and accompanying discussion in Section 4.2). As a consequence the net decay rate in the core of the resonance is very small anyway. We checked that in the presence of two-photon transitions and frequency diffusion, even setting $\dot{x}_{n'p}\big|_{1s} = 0$ instead of the expression given by Eq. (5.19) leads to relative changes to the recombination history of at most 7×10^{-4}. Given that frequency diffusion leads to corrections of a few percent at most to the decay rate in Lyα when radiative transfer is treated carefully even at the line center [45], we can be confident that using the Sobolev approximation for the resonant contributions of two-photon decays is accurate to better than 10^{-4}.

5.2.5.4 "Pure two-photon" non-resonant contribution

In the previous section we discussed how two-photon decays within a few Doppler widths of Lyman resonances can in fact be accounted for in the standard "1+1" picture. To evaluate the non-resonant pieces, $\tilde{R}_{1s,nl}$ and $\tilde{R}_{nl,1s}$, we need to solve the radiative transfer equation, Eq. (5.10), to obtain the photon occupation number. The subject of Section 5.3 is to describe our numerical method of solution.

Note that choosing the "resonant" regions to be a few Doppler widths has an additional advantage. Since a Doppler width is $\sim 10^3$ times wider than the natural width of Lyman lines, it is not necessary to account for the pole displacements in the computation of the differential two-photon decay rates in the non-resonant region. In addition, the fraction of two-photon decays that are considered non-resonant will be small (of the order of $\Gamma_{np}/(4\pi^2)/\Delta\nu$, where $\Delta\nu$ is the width of the "resonant" region). For $\Delta\nu$ of a few Doppler widths, this fraction is $\sim 10^{-4}$. This means that the "pure" two-photon decay rates $\tilde{R}_{nl,1s}$ are much smaller than the total inverse lifetime of the nl state, Γ_{nl}, which is required to simplify the effective MLA model to an effective four-level atom model as we discussed in Section 3.4.4.

As a final note, we want to emphasize why the final result is independent of the exact boundary between "resonant" and "non-resonant" regions, so long as the resonant regions are a few Doppler widths wide. If one were to increase the width of the "resonant" region, then the "pure" two-photon transition rates $\tilde{R}_{nl,1s}$ and $\tilde{R}_{1s,nl}$ would decrease, mainly because of the change of the integration region in the blue wings of the resonance – in the red wing, the radiation field has reached near equilibrium with the line and the net rate of decays immediately blueward of line center is very small anyway. This decrease would be nearly exactly compensated by the increase of what is considered as "1+1" decays, as the photon occupation number incoming on the Lyman resonances, f_{np}^{+}, would be decreased due to the smaller optical depth due to "pure" two-photon absorptions in the blue wing. Hirata (2008) checked the independence of the result from the exact value chosen for the width of the "resonant" region, and found that even changing this width by a factor of 9 lead to relative changes of at most 4×10^{-4} in the recombination history.

5.3 Numerical solution of the radiative transfer equation

5.3.1 Discretization of the radiative transfer equation

To solve the radiative transfer equation [Eq. (5.10)] numerically in the "non-resonant" frequency region, we follow the method of Hirata (2008), and extend it to also account for frequency diffusion.

We will consider the radiation field in the vicinity of N frequency "spikes" ν_b, for $b = 1, 2, ... N$. Each spike has an associated width $\Delta\nu_b$ (which is just the separation between consecutive spikes if

they are linearly spaced, for example).

We use the discretized differential two-photon rate:

$$\left.\frac{d\Lambda_{nl}}{d\nu}\right|_{\rm used} = \sum_b A_{nl,b}\delta_\epsilon(\nu-\nu_b), \tag{5.20}$$

where we use the coefficients

$$A_{nl,b} \equiv \int_{\Delta\nu_b} \frac{d\Lambda_{nl}}{d\nu} d\nu, \tag{5.21}$$

where the integral is carried over the frequency region associated with the spike $\Delta\nu_b$. The function $\delta_\epsilon(\nu-\nu_b)$ in Eq. (5.20) should be understood as a sharp profile centered at ν_b, which integrates to unity, and has support in $[\nu_b-\epsilon,\nu_b+\epsilon]$. The solution we derive is in the limit $\epsilon\to 0$, for which $\delta_\epsilon\to\delta$, the Dirac delta function. Doing so, we are simply approximating the optical depth as concentrated in discrete frequencies instead of being a smooth function.

The main new contribution of the present work is the discretization method for the scattering operator. We use the discretized scattering kernel

$$\left.R(\nu,\nu')\right|_{\rm used} = \sum_{b,b'} R_{b,b'}\delta_\epsilon(\nu-\nu_b)\delta_\epsilon(\nu'-\nu_{b'}). \tag{5.22}$$

We enforce detailed balance:

$$R_{b,b'}{\rm e}^{-h\nu_b/T_{\rm m}} = R_{b',b}{\rm e}^{-h\nu_{b'}/T_{\rm m}}. \tag{5.23}$$

We moreover use the diffusion approximation for resonant scattering. This allows us to assume that the numerical scattering kernel $R_{b,b'}$ is non-vanishing only for neighboring bins, $b'=b\pm 1$. In order to obtain the correct diffusion rate, we set

$$(\nu_{b+1}-\nu_b)^2 R_{b,b+1} + (\nu_{b-1}-\nu_b)^2 R_{b,b-1} = 3\frac{A_{2p,1s}^2}{4\pi^2(\nu-\nu_{{\rm Ly}\alpha})^2}\Delta\nu_b\frac{2T_{\rm m}}{m_{\rm H}c^2}\nu_{{\rm Ly}\alpha}^2, \tag{5.24}$$

where we used the damping wing approximation for the absorption profile (and approximate $\nu_b^2\approx\nu_{{\rm Ly}\alpha}^2$ in the multiplicative factor).

As boundary conditions, we assume a vanishing photon flux due to diffusion at the boundaries of our domain, i.e.,, formally, $R_{1,0}=R_{N,N+1}=0$ (in fact we set these conditions at the boundaries of the diffusion domain, smaller than the entire frequency domain considered). Using Eq. (5.24), we then obtain $R_{1,2}$ and $R_{N,N-1}$. Using iteratively Eqs. (5.23) and (5.24), we can then obtain all the coefficients of the numerical diffusion kernel, starting from the boundaries, and up to line center. Denoting b_1 the highest bin below Ly-α and b_1+1 the first bin above Ly-α, we obtain all coefficients up to $R_{b_{{\rm Ly}\alpha},b_1}$ on the red side of Ly-α, and up to $R_{b_{{\rm Ly}\alpha},b_1+1}$ on the blue side (we do not follow the radiation field at the central bin $b_{{\rm Ly}\alpha}$ but can still define these coefficients). Note that with this

method we cannot ensure that the diffusion rate at the central bin is correct. However, the exact value of the diffusion rate at line center does not matter, as long as it is high enough to ensure that the photon occupation number reaches the equilibrium spectrum $f_\nu \propto \mathrm{e}^{-h\nu/T_\mathrm{m}}$.

5.3.2 Solution of the discretized radiative transfer equation

To simplify the notation, we define the following rate coefficients:

$$\begin{aligned} R_{nl,b} &\equiv \left.\frac{d\Lambda_{nl}}{d\nu}\right|_{\nu_b} \left|\mathrm{e}^{h(\nu_b-\nu_{n1})/T_\mathrm{r}}-1\right|^{-1}\Delta\nu_b \quad \text{and} \\ R_{b,nl} &\equiv \frac{g_{nl}}{g_{1s}}\mathrm{e}^{h(\nu_b-\nu_{n1})/T_\mathrm{r}}R_{nl,b}. \end{aligned} \tag{5.25}$$

This coefficients can be thought of as transition rates between bound states and a set of "virtual" levels with associated energies $E_b = h\nu_b$ [49]. We define the total Sobolev optical depth in the b-th frequency spike:

$$\Delta\tau_b \equiv \frac{c^3 n_\mathrm{H} x_{1s}}{8\pi\nu_b^3 H}\left(\sum_{nl} R_{b,nl} + \sum_{b'=b\pm1} R_{b,b'}\right). \tag{5.26}$$

We also define the average photon occupation number near ν_b:

$$\overline{f}_{\nu_b} \equiv \int_{\nu_b-\epsilon}^{\nu_b+\epsilon} \delta_\epsilon(\nu-\nu_b) f_\nu d\nu. \tag{5.27}$$

Finally, we define the equilibrium photon occupation number at the b-th frequency spike:

$$f_{\nu_b}^\mathrm{eq} \equiv \frac{\sum_{nl} x_{nl} R_{nl,b} + x_{1s}\sum_{b'}\overline{f}_{\nu_{b'}} R_{b',b}}{x_{1s}\left(\sum_{nl} R_{b,nl} + \sum_{b'} R_{b,b'}\right)}. \tag{5.28}$$

In the vicinity of ν_b, the discretized radiative transfer equation becomes:

$$\frac{1}{H\nu_b}\frac{\partial f_\nu}{\partial t} - \frac{\partial f_\nu}{\partial \nu} = \Delta\tau_b \delta_\epsilon(\nu-\nu_b)\left[f_{\nu_b}^\mathrm{eq} - f_\nu\right]. \tag{5.29}$$

In the limit that the support of the delta function becomes vanishingly small, $\epsilon \to 0$, the discretized radiative transfer equation can be solved in the steady-state approximation, and one can neglect the time derivative. This is similar to the commonly used Sobolev approximation, except that we are now making this approximation in the vicinity of an artificially introduced spike (as opposed to a true resonance line), for the purposes of numerical resolution. Another conceptual difference is that the equilibrium photon occupation number also depends on the averaged value of the radiation field at neighboring bins, because of frequency diffusion. Given the photon occupation number at the blue edge of the b-th spike, $f_{\nu_b+\epsilon}$, this equation has a well-known solution f_ν. The quantities of interest for us are the photon occupation number at the red edge of the spike $f_{\nu_b-\epsilon}$ and the average photon occupation number in the spike $\overline{f}_{\nu_b}$. They are given by the following expressions (for a derivation,

see Section 4.2.4):

$$f_{\nu_b-\epsilon} = f_{\nu_b+\epsilon}\mathrm{e}^{-\Delta\tau_b} + f^{\mathrm{eq}}_{\nu_b}\left(1-\mathrm{e}^{-\Delta\tau_b}\right), \tag{5.30}$$

and

$$\overline{f}_{\nu_b} = \Pi_b f_{\nu_b+\epsilon} + (1-\Pi_b) f^{\mathrm{eq}}_{\nu_b}, \tag{5.31}$$

where Π_b is the Sobolev escape probability from the b-th spike:

$$\Pi_b \equiv \frac{1-\mathrm{e}^{-\Delta\tau_b}}{\Delta\tau_b}. \tag{5.32}$$

We now use the variables

$$x_b \equiv x_{1s}\overline{f}_{\nu_b}. \tag{5.33}$$

As explained in Ref. [49], x_b can be interpreted as the population of the virtual level b. One should however keep in mind that this is is just a convenient rewording for the radiation field intensity.

Using the definition of $f^{\mathrm{eq}}_{\nu_b}$, Eq. (5.28), we can rewrite Eq. (5.31) in the form:

$$T_{b,b}x_b = \sum_{nl} x_{nl}R_{nl,b} + \sum_{b'=b\pm1} x_{b'}R_{b',b} + s_b, \tag{5.34}$$

where we have defined:

$$\begin{aligned} T_{b,b} &\equiv \frac{1}{1-\Pi_b}\left(\sum_{nl} R_{b,nl} + \sum_{b'=b\pm1} R_{b,b'}\right) \quad \text{and} \\ s_b &\equiv \Pi_b x_{1s} f_{\nu_b+\epsilon} T_{b,b}. \end{aligned} \tag{5.35}$$

We only follow two-photon decays in the damping wings of resonances, but we should still account for frequency diffusion between line center and the neighboring bins. At the Lyman-α line center, the radiation field is in equilibrium with the $2p/1s$ ratio: $f_{\nu_{\mathrm{Ly}\alpha}} = x_{2p}/(3x_{1s})$. If b_1 is the highest frequency bin below Ly-α, (and b_1+1 is the first bin above Ly-α), we therefore define the transition rates with $2p$:

$$R_{2p,b_1} = \frac{1}{3}R_{b_{\mathrm{Ly}\alpha},b_1} \quad \text{and} \quad R_{2p,b_1+1} = \frac{1}{3}R_{b_{\mathrm{Ly}\alpha},b_1+1}. \tag{5.36}$$

Provided that we set $R_{b_1,b_1+1} = R_{b_1+1,b_1} = 0$, Eq. (5.34) remains valid for $b = b_1, b_1+1$. Adding these transitions with the central frequency bin will ensure that the photon occupation number is driven to its equilibrium value near line center, $f^{\mathrm{eq}}_{\nu} = x_{2p}/(3x_{1s})\mathrm{e}^{-h(\nu-\nu_{\mathrm{Ly}\alpha})/T_{\mathrm{m}}}$.

We now use Eq. (3.52) for the populations x_{nl} with $n \geq 3$. We define the coefficients, for $i = 2s, 2p$:

$$T_{b,i} \equiv -R_{i,b} - \sum_{n\geq3,l} \frac{g_{nl}}{g_i}\mathrm{e}^{-E_{n2}/T_{\mathrm{r}}} P^i_{nl}(T_{\mathrm{r}}) R_{nl,b}. \tag{5.37}$$

We define the new source vector:

$$S_b \equiv s_b + x_e^2 \sum_{n\geq 3,l} \frac{g_{nl}}{g_e} \mathrm{e}^{-E_n/T_\mathrm{r}} P^e_{nl}(T_\mathrm{r}) R_{nl,b}. \tag{5.38}$$

In practice, we use $S_b = s_b$ as we approximate $P^e_{nl} = 0$ (see discussion in Section 3.4.4). We also define the coefficients

$$T_{b,b\pm1} \equiv -R_{b\pm1,b}. \tag{5.39}$$

The discretized radiative transfer equation then takes the final form:

$$T_{b,2s}x_{2s} + T_{b,2p}x_{2p} + \sum_{b'=b-1}^{b+1} T_{b,b'}x_{b'} = S_b. \tag{5.40}$$

5.3.3 Populations of the excited states

Given the radiation field, we can now compute the two-photon transition rates. Using Eqs. (5.12) and (5.13) limited to the "non-resonant" frequency region, we obtain, after discretization:

$$\tilde{R}_{nl,1s} = \sum_b R_{nl,b} \quad \text{and} \quad \tilde{R}_{1s,nl} = \sum_b \overline{f}_{\nu_b} R_{b,nl}. \tag{5.41}$$

The effective transition rates from the $i = 2s$ and $2p$ states to the ground state are therefore, according to the discussion in Section 3.4.4, and using the definition of $T_{b,i}$ Eq. (5.37):

$$\tilde{\mathcal{R}}_{i,1s} = -\sum_b T_{b,i} + \sum_n \frac{g_{np}}{g_i} R_{\mathrm{Lyn}} \mathrm{e}^{-E_{n2}/T_\mathrm{r}} P^i_{np}(T_\mathrm{r}), \tag{5.42}$$

where the first term accounts for two-photon transitions and the second term for escape from Lyman lines, where $R_{\mathrm{Lyn}} = (\nu_n/\nu_2)^3 R_{\mathrm{Ly}\alpha}$ and $R_{\mathrm{Ly}\alpha}$ was defined in Eq. (2.20) (it is understood that $P^{2s}_{2p} = 0$ and $P^{2p}_{2p} = 1$; also, in practice for $n \geq 3$ we use $P^{2s}_{ns} = 1 - P^{2p}_{ns} = 0$, $P^{2s}_{np} = 1 - P^{2p}_{ns} = 1$, $P^{2s}_{nd} = 1 - P^{2p}_{nd} = 0$, see discussion in Section 3.4.4). The effective transition rate for the reverse process is given by:

$$\tilde{\mathcal{R}}_{1s,i} = -\sum_b T_{i,b}\overline{f}_{\nu_b} + 3\sum_n R_{\mathrm{Lyn}} P^i_{np}(T_\mathrm{r}) f^+_{np}, \tag{5.43}$$

where we have defined the coefficients, for $i = 2s, 2p$:

$$T_{i,b} \equiv \frac{g_i}{g_{1s}} \mathrm{e}^{h(\nu_b - \nu_{21})/T_\mathrm{r}} T_{b,i}. \tag{5.44}$$

For a given radiation field and free electron fraction, we can now obtain an equation for the populations of the excited states $2s, 2p$. We do so in the steady-state approximation, i.e., setting $\dot{x}_i = 0$

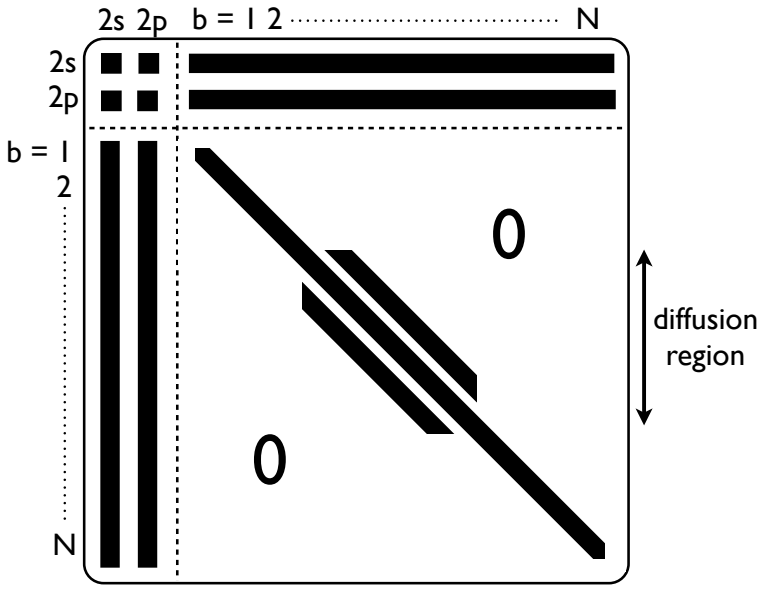

Figure 5.1: Sparsity pattern of the linear system solved for evolving simultaneously the level populations and the radiation field, in the presence of two-photon transtions and frequency diffusion.

for $i = 2s, 2p$ in Eqs. (3.47) and (3.48). We first define the 2×2 matrix of elements

$$\begin{aligned} T_{i,i} &\equiv \mathcal{B}_i + \mathcal{R}_{i,j} + \tilde{\mathcal{R}}_{i,1s} \quad \text{and} \\ T_{i,j} &\equiv -\mathcal{R}_{i,j}, \quad j \neq i. \end{aligned} \tag{5.45}$$

We also define the source vector of elements

$$S_i \equiv n_{\rm H} x_e^2 \mathcal{A}_i + 3 \sum_{n \geq 2} R_{{\rm Ly}n} P^i_{np}(T_{\rm r}) f^+_{np}. \tag{5.46}$$

The steady-state equation for each state i translates into the linear equation:

$$\sum_{j=2s,2p} T_{i,j} x_j + \sum_b T_{i,b} x_b = S_i, \quad i = 2s, 2p. \tag{5.47}$$

5.3.4 Evolution of the coupled system of level populations and radiation field

We now have all the necessary pieces to evolve simultaneously the level populations and the radiation field, and compute the free electron fraction. In this section we summarize the procedure and recall the main equations. We start with an initially thermal radiation field, $f_\nu = {\rm e}^{-h\nu/T_{\rm r}}$. At each time step, we do the following computations:

1. We obtain the photon occupation number incoming on each bin b assuming free streaming

between frequency spikes:

$$f_{\nu_b+\epsilon}(z) = f_{\nu_{b+1}-\epsilon}\left(z' = (1+z)\frac{E_{b+1}}{E_b} - 1\right). \tag{5.48}$$

We also obtain in the same way the incoming photon occupation number at the Ly-n transitions, f_{np}^{+}.

2. We solve for the populations of the $2s$ and $2p$ states and the average photon occupation number at each frequency spike $\overline{f}_{\nu_b} = x_b/x_{1s}$ *simultaneously* by solving the coupled linear system given by Eqs. (5.40) and (5.47). Even with a large number of bins for the radiation field ($N = 311$ in our fiducial case), this system is easily solved because the matrix of coefficients $T_{b,b'}$ is tridiagonal and the overall system has the particular sparsity pattern shown in Fig. 5.1. Such a sparse system can be solved in $\mathcal{O}(N)$ operations (specifically, we can solve the system in $\sim 16N$ operations).

3. We update the photon occupation number at the red side of each spike, $f_{\nu_b-\epsilon}$, using Eq. (5.30). At the red side of Lyman resonances, we use $f_{np}^{-} = x_{np}/(3x_{1s})$, valid in the optically thick limit, where the np state is assumed to be in Boltzmann equilibrium with $2s$ for $n \geq 3$.

4. After step #2, we can obtain the function $\dot{x}_e(z, x_e)$ through Eq. (3.49) or[4] (3.50). This allows us to evolve the free electron fraction to the next time-step.

Note that for numerical stability at early times, it is better to implement the above equations in terms of photon distortion and deviations from Boltzmann equilibrium. We present the appropriate equations in Appendix 5.B.

5.3.5 Implementation, convergence tests and results

We evolve the free electron fraction during hydrogen recombination in several phases. We use even steps in $\ln a$ (where $a = (1+z)^{-1}$ is the scale factor), with $\Delta \ln a = 8.5 \times 10^{-5}$. We describe our ODE integrator in Appendix 5.A.

- We checked that hydrogen and helium recombination never overlap and can be followed separately (to an accuracy of a few times 10^{-4}). We therefore start computing the hydrogen recombination history once helium is completely recombined. Quantitatively, we start hydrogen recombination once the fractional abundance of He^{+} ions is less than 10^{-4} relative to hydrogen. If this criterion is met earlier than $z = 1650$ we only switch on the hydrogen recom-

[4]Eq. (3.49) contains near exact cancellations but Eq. (3.50) contains a large number of terms for which numerical roundoff errors can add up. We checked that both equations give the same result within numerical roundoff errors. We use Eq. (3.49) in the final code simply because it is more compact.

bination computation at $z = 1650$. We checked that at this redshift the exact free electron fraction differs from the Saha equilibrium value by no more than a few times 10^{-4} anyway.

- In the first phases of hydrogen recombination, we use the post-Saha expansion described in Appendix 5.A.1. We do so as long as the free electron fraction differs from the Saha value by $\Delta x_e < 5 \times 10^{-5}$. We checked that explicitly integrating the ODE for x_e instead (with a much smaller time-step, as the ODE is stiff at early times) leads to maximum changes of $\Delta x_e/x_e \lesssim 3 \times 10^{-4}$.

- From then on and until $z = 700$ we solve simultaneously for the level populations and radiative transfer with two photon processes and diffusion as described in this section.

- For $z < 700$, we use the simple EMLA equations, with simple decay rates from $2s$ and $2p$ only (i.e., not accounting for higher order Lyman lines and radiative transfer effects). We checked that moving the last switch to $z = 400$ instead of 700 leads to maximum changes $|\Delta x_e|/x_e < 10^{-4}$.

- For the matter temperature evolution, we use the asymptotic solution of Hirata [49] [it can be obtained by setting $\dot{T}_\mathrm{m} = -HT_\mathrm{m}$ in Eq. (2.26)] as long as $1 - T_\mathrm{m}/T_\mathrm{r} < 5 \times 10^{-4}$. Depending on cosmology, this corresponds to $750 < z < 950$. After that we switch to solving for x_e and T_m simultaneously by using Eq. (2.26).

All the checks mentioned above were made for a wide range of cosmological parameters.

Our fiducial parameters for the numerical solution of radiative transfer are $N = 311$ frequency bins extending from $\nu_{\mathrm{Ly}\alpha}/2$ to $\nu_{\mathrm{Ly}\gamma}$, and a diffusion region with 80 bins extending to $\Delta\nu/\nu_{\mathrm{Ly}\alpha} = \pm 1.7 \times 10^{-2}$. The minimal spacing between bins is $\min[\ln(\nu_{b+1}/\nu_b)] = 8.5 \times 10^{-5}$, which sets the largest step in $\ln a$ that we can take (this is also half of the width $\Delta\nu/\nu$ of the "resonant" region around Lyα). We checked (for the fiducial cosmology only) that reducing the diffusion region to $\Delta\nu/\nu_{\mathrm{Ly}\alpha} = \pm 1 \times 10^{-2}$ leads to changes $|\Delta x_e|/x_e < 6 \times 10^{-6}$. Reducing the diffusion region to $\Delta\nu/\nu_{\mathrm{Ly}\alpha} = \pm 5 \times 10^{-3}$ leads to changes $|\Delta x_e|/x_e < 4 \times 10^{-5}$. We checked that using a 10 times finer frequency grid in the diffusion region (and a 10 times smaller time-step) leads to maximum changes $|\Delta x_e|/x_e \approx 1.5 \times 10^{-4}$ at $z \approx 900$.

We are therefore confident that our numerical treatment is converged at the level of a few parts in 10^4.

We show in Fig. 5.2 the changes in the recombination history due to two-photon processes. We find that including two-photon transitions from the initial states $2s, 3s, 3d, 4s$ and $4d$ is sufficient for the level of accuracy required — we checked that including two-photon transitions from $5s$ and $5d$ leads to a maximum change $\Delta x_e/x_e \sim 8 \times 10^{-5}$ at $z \sim 1200$ and can therefore be neglected. The effect of frequency diffusion in the Lyα line is shown in Fig. 5.3.

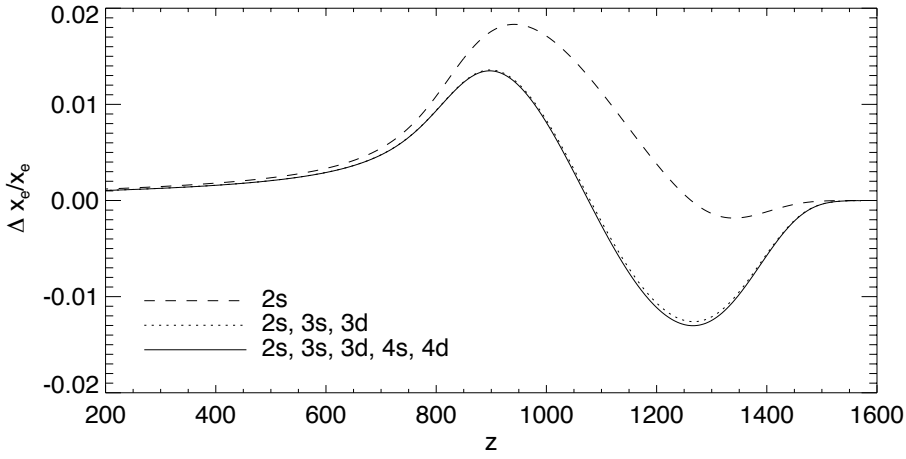

Figure 5.2: Changes in the recombination history when including two-photon decays and Raman scattering (no diffusion), compared to our "base" model. The line labeled "$2s$" shows the changes in x_e when one properly accounts for stimulated $2s \rightarrow 1s$ decays, as well as absorptions of distortion photons and Raman scattering from $2s$. The other lines show the cumlative correction when adding two-photon transitions from higher levels.

We compared our results to the two-photon MLA code of Hirata [49], as well as to the results of Hirata & Forbes [45] for frequency diffusion. For this comparison, we use $n_{\rm max} = 30$. The result of the comparison is shown in Fig. 5.4. The maximum difference between the codes for $700 < z < 1600$ is $|\Delta x_e|/x_e = 0.0005$. The increase of the relative difference at late times is most likely due to small differences in the bound-free rates, which are computed with different methods (we use the recursion relations of Ref. [81] whereas Hirata (2008) directly integrates the products of wave functions to compute matrix elements). This difference remains even when switching off two-photon processes. The $\sim 3 \times 10^{-5}$ kink at $z \sim 1570$ is a startup transient due to switching from the post-Saha solution to solving the full ODE. The kink at $z = 1350$ is due to the Lyβ photons emitted at $z = 1600$ starting to redshift into Lyα. Overall, the agreement is excellent ($|\Delta x_e|/x_e < 10^{-4}$ for $z > 900$), even though the codes use different methods to compute atomic rates and different approaches for solving the MLA problem and treating Lyα frequency diffusion.

5.4 Conclusions

We have presented a complete treatment of primordial hydrogen and helium recombination (see description in Ref. [62]), including all the effects that have been shown to be important so far. Our computation accounts for the multilevel character of hydrogen and the non-equilibrium of angular momentum substates, radiative feedbacks, two-photon transitions, and frequency diffusion in Lyα for hydrogen recombination. For helium recombination, we account for HI continuum opacity in the He I $2^1P^o - 1^1S$ line, decays in the $2^3P^o - 1^1S$ intercombination line, and feedback between these

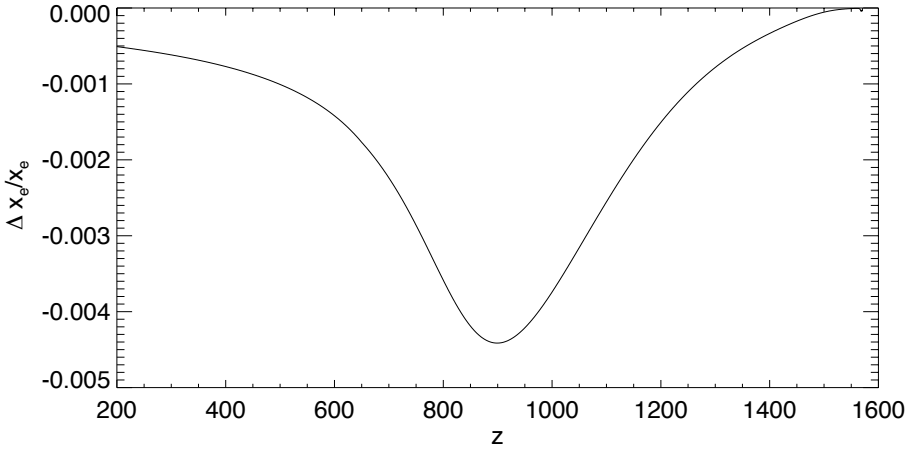

Figure 5.3: Changes in the recombination history when including frequency diffusion in Lyman-α, compared to a model with two-photon transitions but no diffusion.

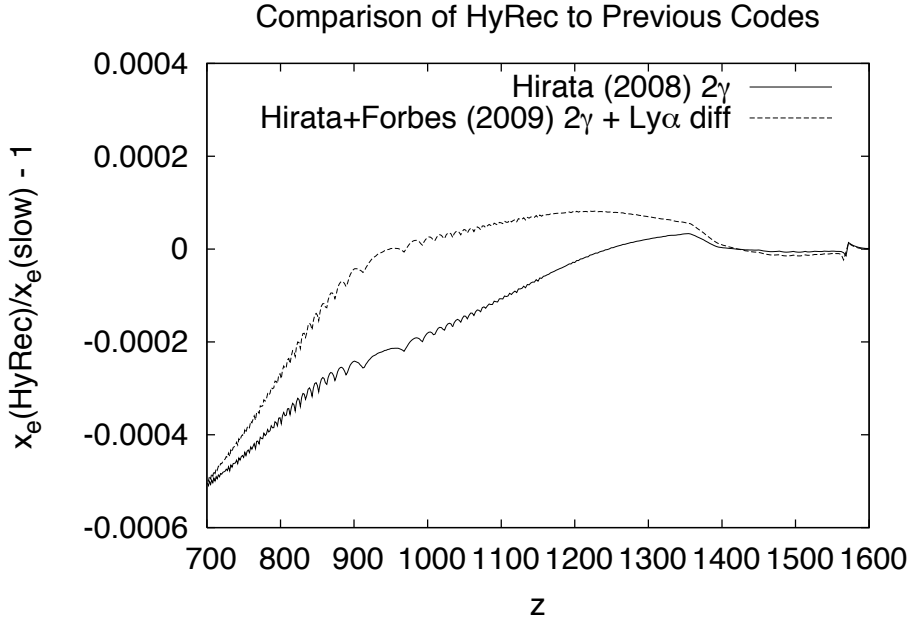

Figure 5.4: Comparison of HyRec with the MLA+two-photon code of Hirata (2008) and to the results of Hirata & Forbes (2009) who account for Lyα diffusion. See text for comments. Figure provided by Christopher Hirata.

lines. We have implemented all these effects in a single recombination code, HyRec, which can compute a recombination history in ~ 2 seconds on a standard laptop for a given set of cosmological parameters. Provided collisional transitions can be neglected (which remains to be established), we estimate the errors of our computation to be a few times 10^{-3} during helium recombination and a few times 10^{-4} during hydrogen recombination, including both numerical errors and errors due to the assumptions and approximations made for physical effects. If collisional transitions are shown to have a significant effect on recombination, our code can be easily updated to account for them with very little loss of computational efficiency.

It has been argued that corrections to the recombination history due to radiative transfer effects are relatively independent of cosmology [106], and that one could therefore compute them once and use the resulting correction function to account for them for any given cosmology. Alternatively, one might run a grid of recombination histories for different cosmologies and construct a fitting function [33, 77]. Our point of view here is that the physics of primordial recombination is simple enough, and an exact calculation from first principles is now fast enough that there should be no reason to use fudge factors and approximate correction functions. This is especially relevant if one wishes to extend the standard recombination calculation by introducing "exotic" new physics. We would like to emphasize that the fast computation presented here, using the EMLA method, is very well adapted for the computation of the recombination history, but that the standard MLA approach and fast interpolation methods may still be useful for the computation of the recombination spectrum.

We believe our code is accurate enough (aside from neglecting collisional transitions) and has a sufficiently small runtime to be incorporated in Monte Carlo Markov chains for upcoming CMB data analysis from the *Planck* mission.

5.A Appendix: Numerical integration of the recombination ODE

5.A.1 Post-Saha expansion at early phases of hydrogen recombination

At the highest redshifts, the ODE describing hydrogen recombination is stiff, and we follow the recombination history using perturbation theory around the Saha approximation, which we describe here. The free electron fraction is very close to the Saha equilibrium value: $x_e = x_e^{\rm S} + \Delta x_e$, with

$$\frac{(x_e^{\rm S})^2}{1 - x_e^{\rm S}} = s \equiv g_e {\rm e}^{-E_I/T}, \tag{5.49}$$

where g_e was given in Eq. (2.6) and $T = T_{\rm m} = T_{\rm r}$ at early times. We can therefore Taylor-expand the derivative of the free-electron fraction:

$$\dot{x}_e(x_e, z) \approx \dot{x}_e(x_e^{\rm S}, z) + \Delta x_e \frac{\partial \dot{x}_e}{\partial x_e}\Big|_{x_e^{\rm S}}. \tag{5.50}$$

Note that in Ref. [39], we used the Peebles ODE at early times, which has $\dot{x}_e(x_e^{\rm S}, z) = 0$. However, for a better accuracy, we account for two-photon processes and radiative transfer even at early times in HyRec. In that case, the small distortion developed by the radiation field renders $\dot{x}_e(x_e^{\rm S}, z)$ nonzero. We now approximate the left-hand side by $d(x_e^{\rm S})/dt$, which allows us to obtain an estimate of the departure from Saha equilibrium:

$$\Delta x_e \approx \left[\frac{d(x_e^{\rm S})}{dt} - \dot{x}_e(x_e^{\rm S}, z)\right] \Big/ \frac{\partial \dot{x}_e}{\partial x_e}\Big|_{x_e^{\rm S}}. \tag{5.51}$$

The first term in the numerator in Eq. (5.51) can be obtained analytically by differentiating Eq. (5.49):

$$\frac{d(x_e^{\rm S})}{dt} = -\frac{H(\frac{E_I}{T} - \frac{3}{2})(x_e^{\rm S})^2}{2x_e^{\rm S} + s}. \tag{5.52}$$

For the denominator in Eq. (5.51), we numerically differentiate the derivative $\dot{x}_e$ obtained when accounting for two-photon processes and diffusion, using a one-sided finite difference with $\Delta x_e = 0.01(1 - x_e^{\rm S})$.

We use the post-Saha expansion until the departure from Saha equilibrium reaches $\Delta x_e = 5 \times 10^{-4}$, after which we switch to the numerical integration of the recombination ODE.

5.A.2 Explicit numerical integration at later times

For the sake of computational efficiency, we use a second-order ODE integrator that uses derivatives computed at previous time-steps. This allows us to evaluate derivatives only once at each time-step.

Explicitly, to numerically solve the equation $y'(x) = f(x, y)$, we use evenly spaced steps Δx, and obtain the solution at the $(i+1)$th step as follows:

$$y_{i+1} = y_i + \Delta x \left[1.25 y'_i - 0.25 y'_{i-2}\right], \tag{5.53}$$

where $y'_i = f(x_i, y_i)$ is stored at each time-step for later use. For the case of interest, we have $x = \ln a$, $y = x_e$ and $f = \dot{x}_e/H$.

5.B Appendix: Stable numerical radiative transfer equations

The equations presented in this chapter for the photon occupation number and the excited level populations are prone to numerical instability at early times, when the radiation field and the level populations are nearly thermal, and the source terms are nearly canceling. This is not an important issue for the recombination history itself, but HyRec could also potentially be used to compute the spectral distortion in the Lyman lines, for which such numerical errors can be important. Here we give the equivalent of the equations of Chapter 5 for the photon distortion $\Delta f_\nu \equiv f_\nu - \mathrm{e}^{-h\nu/T_\mathrm{r}}$ and the deviations from Boltzmann equilibrium $\Delta x_i \equiv x_i - \frac{g_i}{g_{1s}}\mathrm{e}^{-E_{21}/T_\mathrm{r}}$, and the deviation of the free electron fraction from the Saha value [defined in Eq. (2.5)], $\Delta x_e \equiv x_e - x_e^\mathrm{S}$. We also define $\Delta x_b \equiv x_b - x_{1s}\mathrm{e}^{-h\nu_b/T_\mathrm{r}}$, $\Delta x_{1s} \equiv x_{1s} - x_{1s}^\mathrm{Saha} = -\Delta x_e$ and $\Delta\mathcal{A}_i \equiv \mathcal{A}_i(T_\mathrm{m}, T_\mathrm{r}) - \mathcal{A}_i(T_\mathrm{m} = T_\mathrm{r}, T_\mathrm{r})$. The nearly canceling terms can be eliminated analytically, and we obtain the following new equations:

- The discretized radiative transfer equation Eq. (5.40) becomes

$$T_{b,2s}\Delta x_{2s} + T_{b,2s}\Delta x_{2p} + \sum_{b'=b-1}^{b+1} T_{b,b'}\Delta x_b = \Pi_b x_{1s}\Delta f_{\nu_b+\epsilon} T_{b,b}. \tag{5.54}$$

- The rate equation for each state $i = 2s, 2p$ Eq. (5.47) becomes

$$\sum_j T_{i,j}\Delta x_j + \sum_b T_{i,b}\Delta x_b = \Delta S_i, \quad \text{where} \tag{5.55}$$

$$\Delta S_i \equiv n_\mathrm{H}\left[\Delta\mathcal{A}_i (x_e^\mathrm{S})^2 + \mathcal{A}_i \Delta x_e (2x_e^\mathrm{S} + \Delta x_e)\right] - \frac{g_i}{g_{1s}}\Delta x_{1s}\mathcal{B}_i \mathrm{e}^{-E_{21}/T_\mathrm{r}} + 3\sum_{n\geq 2} R_\mathrm{Lyn} P^i_{np}\Delta f^+_{np}. \tag{5.56}$$

- Finally, the rate of change of the free electron fraction Eq. (3.49) becomes

$$\Delta\dot{x}_e = -\sum_i \left\{ n_\mathrm{H}\left[\Delta\mathcal{A}_i (x_e^\mathrm{S})^2 + \mathcal{A}_i \Delta x_e (2x_e^\mathrm{S} + \Delta x_e)\right] - \frac{g_i}{g_{1s}}\Delta x_{1s}\mathcal{B}_i \mathrm{e}^{-E_{21}/T_\mathrm{r}} - \Delta x_i \mathcal{B}_i \right\}. \tag{5.57}$$

Chapter 6

Prospects for detection of heavy elements present at the epoch of primordial recombination[1]

6.1 Introduction

Big-bang nucleosynthesis (BBN) is one of the pillars of the hot standard cosmological model. Comparison of BBN theoretical predictions to observed abundances of the lightest nuclei (D, ^{3}He, ^{4}He and ^{7}Li) uniquely determines the only free parameter of standard BBN, the baryon-to-photon ratio $\eta = (5.7 \pm 0.3) \times 10^{-10}$, or equivalently, given the cosmic microwave background (CMB) temperature today $T_0 = 2.73$ K, the baryon abundance $\Omega_b h^2 = 0.021 \pm 0.001$ (see, e.g., Ref. [107]). The latest results from CMB anisotropy measurements by the WMAP satellite are in excellent agreement, with $\Omega_b h^2 = 0.02249^{+0.00056}_{-0.00057}$ [4].

In the standard BBN scenario, elements heavier than lithium are only produced with trace abundances [108]. It has been shown, however, that significant amounts of heavy elements may be produced in inhomogeneous BBN (IBBN) models [109, 110, 111]. IBBN may take place if some non-standard mechanism leads to large baryon-abundance inhomogeneities on small scales, which are allowed by current observations. It is possible to adjust the IBBN parameters to reproduce the observed abundances of light elements, while producing heavier elements with abundances as large as those in the Sun [111, 112]. More generally, it cannot be excluded that some unknown processes may lead to a significant production of metals heavier than lithium. It may therefore be profitable to inquire what empirical constraints to primordial metals might be possible.

Standard methods to constrain metal abundances at high redshifts rely on line emission or absorption measurements, and therefore require some sources to have already formed (typically,

[1] The material in this chapter was reproduced from *Metals at the surface of last scatter*, Y. Ali-Haïmoud, C. M. Hirata & M. Kamionkowski, Phys. Rev. D **83**, 083508 (2011). Reproduced here with permission, copyright (2011) by the American Physical Society.

high-redshift quasars). The intergalactic medium (IGM) is therefore already partially enriched by metals produced in the first stars, and extracting limits on the primordial abundances relies on understanding the complex physics of galactic outflows and gas mixing and correctly modeling the ambient radiation field. It would be of great interest to be able to probe the abundance of metals *before* the formation of Population III stars that enriched the IGM. A few ideas were put forward to probe the metallicity during the dark ages: Ref. [113] suggested using resonant scattering of CMB photons off neutral lithium atoms (later shown to be unobservable because lithium is kept ionized by redshifted Lyman-α photons emitted during primordial hydrogen recombination [114]); Ref. [115] studied the effect of fine-structure transitions of heavy elements in atomic or ionized states on CMB anisotropies; Ref. [116] considered the spectral signatures of carbon and oxygen. In this chapter we assess whether heavy elements present during primordial recombination could be detectable from upcoming CMB experiments.

Primordial recombination has recently been the subject of a renewed interest, due to the impact of uncertainties in the standard theory on the predicted CMB temperature and polarization anisotropy power spectrum. Errors in the free-electron fraction $x_e(z)$ as small as a few tenths of a percent near the peak of the visibility function at redshifts $z \sim 1100$ would induce biases of several standard deviations for cosmological parameters estimated from *Planck* data [19, 106]. This accuracy requirement has motivated abundant work on radiative transfer in the Lyman lines, in particular Lyman-α (see for example Refs. [49, 52, 45, 40] and references therein). The tails of the visibility function are less important, but an accuracy of about a percent is still needed, which required implementing an accurate multilevel–atom formulation of the recombination problem [36, 37, 38, 39]. Such a high sensitivity to the recombination history can be turned into an asset and serve to probe unusual physics taking place during the recombination history as, for example, the presence of primordial heavy elements. In this chapter, we explore this idea, and quantify the impact of neutral metals on the Lyα and Lyβ net decay rates, and of ionized metals on the low-redshift tail of the visibility function.

Below we consider three effects of metals on the recombination history and thus on the CMB visibility function: (1) The removal of Lyman-α photons (and thus acceleration of recombination) by photoionization of metals (Section 6.2); (2) the degradation of Lyman-β photons (and thus acceleration of recombination) by the Bowen resonance-fluorescence mechanism (Section 6.3); and (3) the contribution to the free-electron abundance at late times by low-ionization metals (Section 6.4). We find that effects (2) and (3) provide the biggest impact on CMB power spectra. However, the effects are visible in *Planck* only if the primordial metal abundance is at least a few hundredths of solar for (2) and a few tenths of solar for (3). Given that the Lyman-alpha forest [117] and ultra-metal-poor halo stars [118] constrain the primordial metal abundance to be at least a few orders of magnitude smaller than solar, we conclude that *Planck* will be unable to improve upon current

constraints to the primordial metal abundance or, alternatively, that the standard CMB predictions for *Planck* are robust to primordial metals at the levels allowed by current empirical constraints.

6.2 Effect of neutral metals on the Lyman-α decay rate

All metals (in the proper chemical sense of the term, i.e., not including noble gases, halogens and other nonmetals) have a first ionization energy below 10.2 eV, which corresponds to the Lyα transition in hydrogen. This means that neutral metals can provide continuum opacity in the vicinity of the Lyα line by absorbing Lyα photons in photoionization events. Since the photoejected electrons rapidly thermalize their energy, this results in a net loss of resonant Lyα photons, which would have otherwise been reabsorbed by ground-state hydrogen atoms. The presence of metals can therefore speed up hydrogen recombination by increasing the net rate of Lyman-α decays. A similar process was investigated for primordial helium recombination [55, 57]: in that case the presence of neutral hydrogen leads to continuum opacity in the He I $2^1P^o - 1^1S$ line. To estimate the impact of continuum opacity on the Lyman-α line, we use the analytic treatment presented for He I recombination in Ref. [62].

6.2.1 Continuum opacity in Lyα due to photoionization of neutral metals

The radiative-transfer equation in the vicinity of Lyα for the photon occupation number f_ν, including only true absorptions and emissions (i.e., neglecting resonant scatterings) and continuum opacity is

$$\frac{1}{H\nu_{\mathrm{Ly}\alpha}}\frac{\partial f_\nu}{\partial t} - \frac{\partial f_\nu}{\partial \nu} = \tau_{\mathrm{abs}}\phi(\nu)\left(\frac{x_{2p}}{3x_{1s}} - f_\nu\right) + \eta_c\left(\mathrm{e}^{-h\nu/T_{\mathrm{m}}} - f_\nu\right), \tag{6.1}$$

where we approximated $\nu \approx \nu_{\mathrm{Ly}\alpha}$ in the prefactor on the left-hand side, τ_{abs} is the Sobolev optical depth for true absorption in the Lyα line, $\phi(\nu)$ is the line profile, and η_c is the continuum differential optical depth, given by

$$\eta_c \equiv \frac{n_{\mathrm{M}^0} c\sigma_{\mathrm{pi}}(\nu_{\mathrm{Ly}\alpha})}{H\nu_{\mathrm{Ly}\alpha}}. \tag{6.2}$$

In Eq. (6.2), n_{M^0} is the abundance of neutral metal M^0, and $\sigma_{\mathrm{pi}}(\nu)$ is the photoionization cross section of M^0 at frequency ν. We have assumed that σ_{pi} varies slowly over the Lyα resonance (specifically, over the region which is optically thick for true absorption, which corresponds to a few tens of Doppler widths [49]), so we can approximate $\sigma_{\mathrm{pi}}(\nu) \approx \sigma_{\mathrm{pi}}(\nu_{\mathrm{Ly}\alpha})$. Note that Eq. (6.1) assumes that the ionization state of M^0 is given by the Saha equilibrium equation (this translates in a ratio of continuum emission to absorption rates equal to $\mathrm{e}^{-h\nu/T_{\mathrm{m}}}/f_\nu$), even though this is not strictly correct (see Section 6.2.2).

The net rate of $2p \rightarrow 1s$ decays is then obtained as follows:

$$\dot{x}_{2p\rightarrow 1s} = \frac{8\pi\nu_{\mathrm{Ly}\alpha}^2}{c^3 n_{\mathrm{H}}} \int H\nu\tau_{\mathrm{abs}}\phi(\nu)\left(\frac{x_{2p}}{3x_{1s}} - f_\nu\right) d\nu, \tag{6.3}$$

where the prefactor converts photon occupation numbers to photons per unit frequency per hydrogen atom, and we have approximated $\nu \approx \nu_{\mathrm{Ly}\alpha}$ in the multiplicative factor. Ref. [62] showed that the net decay rate in Lyman-α can be written in the following form:

$$\dot{x}_{2p\rightarrow 1s} = \mathcal{E} \times \dot{x}_{2p\rightarrow 1s}\big|_{\mathrm{std}}, \tag{6.4}$$

where

$$\dot{x}_{2p\rightarrow 1s}\big|_{\mathrm{std}} = \frac{8\pi H\nu_{\mathrm{Ly}\alpha}^3}{c^3 n_{\mathrm{H}}}\left(\frac{x_{2p}}{3x_{1s}} - \mathrm{e}^{-h\nu_{\mathrm{Ly}\alpha}/T_{\mathrm{r}}}\right) \tag{6.5}$$

is the standard net decay rate in Lyα, in the Sobolev approximation, for a large optical depth and assuming an incoming blackbody radiation field, and $\mathcal{E}$ is a correction factor accounting for continuum absorption in the line. The correction factor $\mathcal{E}(\tau_c)$ depends on the single parameter

$$\tau_c \equiv \frac{\tau_{\mathrm{abs}}\Gamma_{2p}\eta_c}{4\pi^2}, \tag{6.6}$$

where Γ_{2p} is the total inverse lifetime of the $2p$ state. The dimensionless parameter τ_c can be interpreted as the continuum optical depth within the part of the Lyα line which is optically thick for true absorption. For $\tau_c \rightarrow 0$, $\mathcal{E}(\tau_c) \rightarrow 1$, and for $\tau_c > 0$, $\mathcal{E}(\tau_c) > 1$, which is what one would expect as continuum opacity increases the net rate of decays in the line, as explained above. For $\tau_c \ll 1$, we have the following approximate expansion (see Eq. (117) of Ref. [62]):

$$\mathcal{E} \approx 1 + 13\tau_c \quad , \quad \tau_c \ll 1. \tag{6.7}$$

In order for primordial metals to change the net decay rate in Lyα by $\sim 1\%$ (which is roughly the level detectable by *Planck*), we therefore need $\tau_c \sim 0.001$ near the peak of the visibility function. Extracting the relevant parameters from the multilevel atom code of Hirata [49], we obtain, for $z = 1100$,

$$\tau_c \approx 0.7 \times 10^{-3}\ \frac{\sigma_{\mathrm{pi}}(\nu_{\mathrm{Ly}\alpha})}{10^{-17}\mathrm{cm}^2}\ \frac{x_{\mathrm{M}^0}}{10^{-9}}, \tag{6.8}$$

where $x_{\mathrm{M}^0} = n_{\mathrm{M}^0}/n_{\mathrm{H}}$ is the abundance of neutral metals relative to hydrogen. We see that for a characteristic photoionization cross section $\sigma_{\mathrm{pi}} = 10^{-17}$ cm^2, a fractional abundance of neutral metals per hydrogen atom as low as $\sim 10^{-9}$ would be potentially detectable.

6.2.2 Ionization state of metals and results

We now turn to the evaluation of the fraction of neutral metals $f_{\mathrm{M}^0} \equiv n_{\mathrm{M}^0}/n_{\mathrm{M}}$. As a first approximation we use the Saha equilibrium value:

$$\frac{(1-f_{\mathrm{M}^0})}{f_{\mathrm{M}^0}}\Big|_{\mathrm{Saha}} = S_{\mathrm{M}} \equiv \frac{g_{\mathrm{M}^+} g_e}{g_{\mathrm{M}^0}} \frac{(2\pi m_e T_{\mathrm{r}})^{3/2}}{n_e h^3} \mathrm{e}^{-\chi_{\mathrm{M}}/T_{\mathrm{r}}}, \tag{6.9}$$

where χ_{M} is the ionization energy of M^0, n_e is the free electron abundance, and the g's are the degeneracy factors for each species[2]. For a standard recombination history, at $z = 1100$, Eq. (6.9) gives (taking the ratio of degeneracy factors to be unity) $f_{\mathrm{M}^0} = 5\times10^{-3}, 10^{-4}, 2\times10^{-6}$ and 5×10^{-8} for $\chi_{\mathrm{M}} = 10$, 9, 8 and 7 eV, respectively, and we can anticipate that only metals with $\chi_{\mathrm{M}} \gtrsim 8$ eV may have some impact on Lyα.

Saha equilibrium assumes that the ionizing radiation field is thermal. During hydrogen recombination, the radiation field develops large distortions in the vicinity of the Lyα line, due to the slow escape of Lyα photons (in fact, thermalization of these distortions is so inefficient that they survive until today [31]). These non-thermal photons increase the ionization rate with respect to its thermal value, and the neutral fraction of metals is therefore smaller than predicted by the Saha equation (see for example Ref. [114] for the case of lithium). The ionization state of the metal M is therefore rather determined by the balance of recombinations and photoionizations (this assumes the steady-state limit, valid so long as the photoionization rate is much larger than the Hubble expansion rate, which is a very good approximation around the peak of the visibility function)

$$n_{\mathrm{M}^+} n_e \alpha_{\mathrm{M}} = n_{\mathrm{M}^0} \beta_{\mathrm{M}}, \tag{6.10}$$

where α_{M} is the $\mathrm{M}^+ \rightarrow \mathrm{M}^0$ recombination coefficient and β_{M} is the $\mathrm{M}^0 \rightarrow \mathrm{M}^+$ photoionization rate. From Eq. (6.10), we obtain the neutral fraction,

$$f_{\mathrm{M}^0} = \left(1 + \frac{\beta_{\mathrm{M}}}{n_e \alpha_{\mathrm{M}}}\right)^{-1}. \tag{6.11}$$

The photoionization rate $\beta_{\mathrm{M}} = \beta_{\mathrm{CMB}} + \beta_{\mathrm{dist}}$ comprises a thermal part, due to photoionizations by CMB photons (from the ground state *and* excited states), which is related to the recombination coefficient through the detailed balance relation

$$\beta_{\mathrm{CMB}} = S_{\mathrm{M}} n_e \alpha_{\mathrm{M}}, \tag{6.12}$$

[2]Here the degeneracy factor g_e is to be understood as the degeneracy of a single electron (i.e.,, 2).

and a non-thermal part, due to photoionizations from the ground state by distortion photons,

$$\beta_{\rm dist} = \int_{\nu_{\rm M}}^{\infty} \sigma_{\rm pi}(\nu) \frac{8\pi\nu^2}{c^3} \Delta f_\nu \, d\nu, \tag{6.13}$$

where $\nu_{\rm M} \equiv \chi_{\rm M}/h$ and $\Delta f_\nu = f_\nu - f_\nu^{\rm (CMB)}$ is the non-thermal distortion to the photon occupation number. The Lyman-α distortion peaks around $z \sim 1400$. We can therefore expect that distortions may start significantly affecting the ionization state of the metal M around redshift $z \sim 1400 \ \chi_{\rm M}/(10.2 \text{ eV})$. As a consequence, we expect the Saha equilibrium approximation to be quite accurate around $z \sim 1100$ for metals with ionization threshold lower than ~ 8 eV. For the more interesting metals with $\chi_{\rm M} \gtrsim 8$ eV, however, spectral distortions will lower the neutral fraction with respect to the Saha value at $z \sim 1100$, making their detection more difficult through the effect considered here (we will consider the effect of additional free electrons due to the presence of ionized metals in Section 6.4).

We have computed the neutral fraction of several metals with atomic number $Z \leq 26$, using the fits of Ref. [119] for the photoionization cross sections, and the CHIANTI database for the recombination coefficients [120, 121]. We have extracted the Lyα distortion[3] from the two-photon code of Hirata [49]. We show the ionization state of beryllium ($\chi_{\rm Be} = 9.32$ eV), boron ($\chi_{\rm B} = 8.30$ eV) and silicon ($\chi_{\rm Si} = 8.15$ eV) as a function of redshift, for a standard recombination history, in Fig. 6.1.

We show in Fig. 6.2 the minimal abundance of metals detectable through its effect on Lyα (i.e., such that $\tau_c \geq 0.001$ at redshift 1100). We see that the smallest detectable abundance would be $x_{\rm Be} \sim 3 \times 10^{-4}$. Due to lack of data, we have not treated the case of other metals with $\chi_{\rm M} > 9$ eV, such as zinc ($\chi_{\rm Zn} = 9.39$), arsenic ($\chi_{\rm As} = 9.79$) and gold ($\chi_{\rm Au} = 9.23$), but do not expect significantly lower detectability thresholds unless they have unusually high photoionization cross sections.

6.3 The Bowen resonance-fluorescence mechanism for oxygen

There is an accidental coincidence between the hydrogen Lyβ line at 1025.72 Å and the O I $2p^4\ {}^3P_2 - 2p^3 3d\ {}^3D_3^o$ line at 1025.76 Å. Lyβ photons may therefore excite neutral oxygen instead of being reabsorbed in the hydrogen line. Neutral oxygen in the $2p^3 3d\ {}^3D_3^o$ state can then either directly decay back to the ground state or first decay to the $2p^3 3p\ {}^3P_2$ state by emitting an infrared photon at 1.13 μm, and subsequently cascade down to the ground state (in principle, atoms in the $2p^3 3d\ {}^3D_3^o$ state can also be excited or photoionized, but there are very few thermal photons energetic enough

[3] In principle, to be self-consistent, one should account for the continuum optical depth due to metal photoionization above Lyα and between $\nu_{\rm M}$ and $\nu_{\rm Ly\alpha}$. Given that we find that this effect should not be detectable anyway, we have not implemented a more subtle treatment.

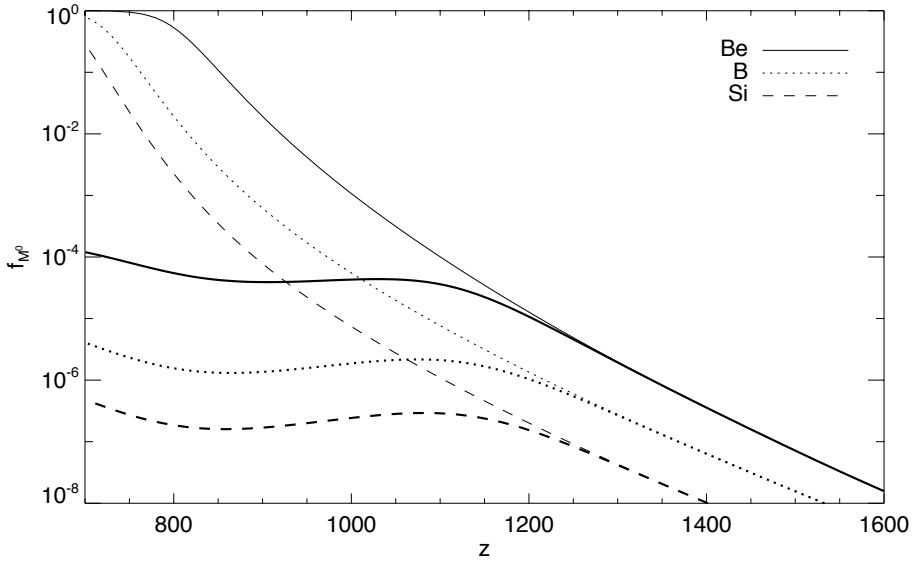

Figure 6.1: Neutral fraction of beryllium, boron and silicon as a function of redshift. Thin lines represent the Saha equilibrium value given by Eq. (6.9). Thick lines represent a more accurate estimate accounting for distortions to the ambient blackbody field near Lyman-α.

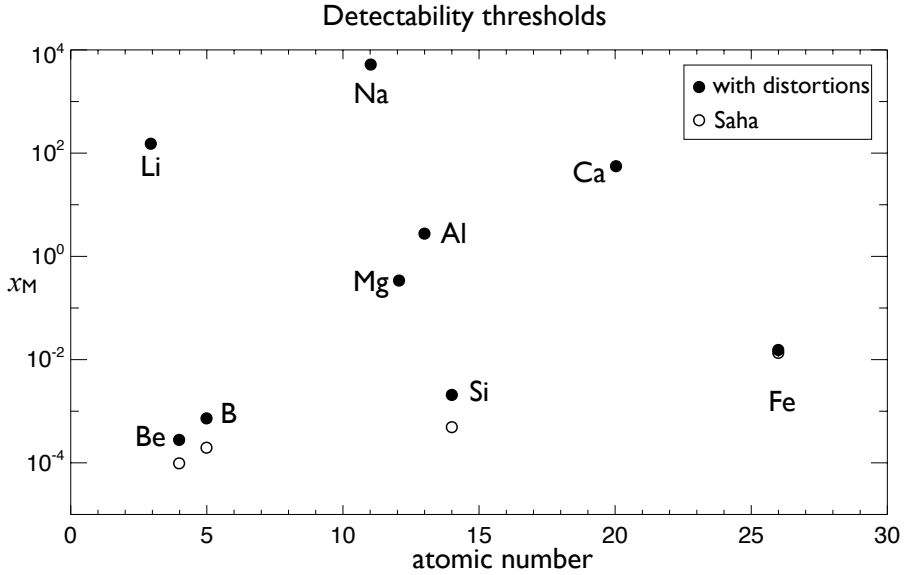

Figure 6.2: Minimum abundance of metals relative to hydrogen needed to result in a continuum optical depth in Lyα $\tau_c \geq 0.001$ at $z = 1100$.

to do so). The probability of the latter series of events (neglecting stimulated decays) is $p_{1.13\mu\mathrm{m}} = A_{1.13\mu\mathrm{m}}/(A_{1.13\mu\mathrm{m}} + A_{1025.76}) \approx 0.3$. Direct decays of excited oxygen to the ground state do not affect radiative transfer in the Lyβ line, as they do not change the number of Lyβ photons. On the other hand, absorptions in the 1025.76 Å line followed by emission of infrared photons degrade Lyβ photons that would otherwise have been reabsorbed by neutral hydrogen. This effect is similar to the continuum opacity in Lyα discussed in Section 6.2, except that this is now a resonant process.

The escape[4] probability in the Lyβ line is enhanced by the probability that a Lyβ photon is absorbed by O I (and then degraded) rather than by H I:

$$\Delta P_{\mathrm{esc}} \approx \frac{\frac{7}{9} n_{\mathrm{OI}}\ A_{1025.76}\ p_{1.13\mu\mathrm{m}}}{3 n_{\mathrm{HI}} A_{3p,1s}} \approx 0.2 \frac{n_{\mathrm{OI}}}{n_{\mathrm{HI}}}, \tag{6.14}$$

where the multiplicative factors are the ratios of the degeneracy factors of the excited levels to those of the ground states. Note that the photon occupation number redward of Lyβ is slightly decreased by this process: $f_- = x_{3p}/(3x_{1s})\,(1 - \Delta P_{\mathrm{esc}})$. However, as long as $\Delta P_{\mathrm{esc}} \ll 1$ this has no detectable impact on radiative transfer redward of Lyβ.

As oxygen and hydrogen have very similar ionization energies, we can assume that they have the same recombination history. More specifically, the ratio of ionized to neutral oxygen rapidly equilibrates to the corresponding ratio for hydrogen because the continuum above the ionization threshold is optically thick. We therefore have $n_{\mathrm{OI}}/n_{\mathrm{OII}} \approx \frac{9}{8} n_{\mathrm{HI}}/n_{\mathrm{HII}}$ [the 9/8 comes from properly accounting for degeneracy factors, see Eq. (6.9)] and as a result we obtain $n_{\mathrm{OI}}/n_{\mathrm{HI}} \approx x_{\mathrm{O}}/(1 - x_e/9) \approx x_{\mathrm{O}}$.

As long as $x_{\mathrm{OI}} \lesssim 10^{-3}$ the damping wings of the O I 1025.76 Å line are optically thin, and the Bowen mechanism can only affect the net decay rate in the Doppler core of the Lyβ line. The latter is very small anyway as the radiation field is very close to equilibrium with the 3p-1s ratio over many Doppler widths near line center. We have modified the escape probability from the Doppler core of Lyβ in the recombination code HyRec [62] according to Eq. (6.14), and found that a minimal abundance of oxygen $x_{\mathrm{O}} \approx 10^{-5}$ is required to affect the recombination history at a potentially detectable level $\Delta x_e/x_e \approx 0.2\%$ at $z \approx 1100$. Note that this would correspond to an enhancement by a factor ~ 200 from the standard escape probability in the Lyβ Doppler core. This stems from the fact that only a tiny fraction of Lyβ decays occur in the Doppler core of the line, whereas most of them take place in the damping wings. The recombination history is therefore highly insensitive to the exact decay rate in the core.

[4]The term "escape" is somewhat misleading in this situation: photons near the Lyβ frequency do not actually escape more from the resonant region (in fact, their overall escape rate is even lower due to a slightly higher optical depth). They rather only "escape" reabsorption by neutral hydrogen.

6.4 Additional free electrons due to ionized metals

If metals remain ionized, they can contribute an additional residual free-electron fraction at late times, $\Delta x_e \sim x_{\mathrm{M}^+}$. In fact we have $\Delta x_e = \frac{1}{2} x_{\mathrm{M}^+}$, as we show below. At late times the evolution of the free-electron fraction is given by

$$\dot{x}_e \approx -n_{\mathrm{H}} \alpha_{\mathrm{B}} x_e x_p = -n_{\mathrm{H}} \alpha_{\mathrm{B}} x_e (x_e - x_{\mathrm{M}^+}). \tag{6.15}$$

Eq. (6.15) is valid because the free electron fraction is many orders of magnitude above the Saha equilibrium value at late time (for a discussion, see Section 2.2.2). If x_e^0 is the unperturbed free electron fraction (i.e., obtained with $x_{\mathrm{M}^+} = 0$) and $x_e = x_e^0 + \Delta x_e$, we obtain

$$\dot{\Delta x_e} = -n_{\mathrm{H}} \alpha_{\mathrm{B}} x_e^0 \left(2\Delta x_e - x_{\mathrm{M}^+}\right), \tag{6.16}$$

which asymptotes to $\Delta x_e = \frac{1}{2} x_{\mathrm{M}^+}$. The *Planck* satellite will be sensitive to fractional changes $\Delta x_e / x_e \sim 1\%$ at late times. Since $x_e \approx 0.3 - 1 \times 10^{-3}$ for $200 \lesssim z \lesssim 700$, we conclude that a potential detection by *Planck* requires a fractional abundance of metals $x_{\mathrm{M}} \gtrsim 10^{-5}$ (in the case that metals remain fully ionized). Note that for a given Ω_b, the presence of metals also modifies the total abundance of hydrogen, n_{H}, throughout the recombination history. However these modifications are degenerate with a mere change of Ω_b of Y_{He} at the level of a few times 10^{-5} and are therefore undetectable.

6.5 Conclusions

We have investigated whether a primordial metal content could sufficiently affect the recombination history to be detectable in upcoming CMB data from *Planck*. We first considered the effect of photoionization of neutral metals by Lyα photons. We showed that although a very small abundance of neutral metals would be enough to significantly affect the net decay rate in Lyα, metals with ionization threshold below Lyα are mostly ionized at $z \sim 1100$, and therefore undetectable. We also considered the Bowen resonance-fluorescence mechanism if primordial oxygen is present. This effect leads to an enhanced escape rate of Lyβ photons and a speed up of recombination. We showed that it could lead to detectable changes for a primordial oxygen abundance of a couple hundredths of solar $x_{\mathrm{O}} \sim 10^{-5}$. Finally, we pointed out that metals that stay ionized until late times provide additional free electrons and therefore change the late-time Thomson scattering optical depth. A fractional abundance $x_{\mathrm{M}} \sim 10^{-5}$ of primordial metals could be detectable through this effect. As a reference, the most abundant metal in the solar photosphere is oxygen ($x_{\mathrm{O}} = 4.9 \times 10^{-4}$), followed by carbon ($x_{\mathrm{C}} = 2.7 \times 10^{-4}$), neon ($x_{\mathrm{Ne}} = 8.5 \times 10^{-5}$), nitrogen ($x_{\mathrm{N}} = 6.8 \times 10^{-5}$), magnesium

($x_{\rm Mg} = 3.4 \times 10^{-5}$), silicon ($x_{\rm Si} = 3.2 \times 10^{-5}$), iron ($x_{\rm Fe} = 3.2 \times 10^{-5}$) and sulfur ($x_{\rm S} = 1.3 \times 10^{-5}$). Other metals have fractional abundances $x_{\rm M} < 10^{-5}$ in the Sun [122]. As carbon, nitrogen, oxygen and neon are neutral at late times (due to their high ionization potential), we conclude that *Planck* could potentially detect primordial metals with an abundance at least a few tenths of solar. This is moreover an optimistic estimate, as the effect of metals is likely to be degenerate with the redshift of reionization or other cosmological parameters.

Given that Lyman-alpha-forest measurements and ultra-metal-poor halo stars suggest a primordial metallicity much smaller than one hundredth solar, we conclude that the CMB can unfortunately not usefully constrain the abundance of primordial metals. At the same time, we also conclude that the CMB predictions for the *Planck* satellite are robust to a primordial metallicity allowed by current empirical constraints.

Part II

Spinning dust radiation

Chapter 7

Introduction

7.1 Motivations

Observational cosmology has entered an era of high precision, exemplified by the most recent temperature results from sensitive cosmic microwave background (CMB) experiments [123, 124, 125, 126]. However, foreground separation and removal remains a major challenge for any CMB measurement (see e.g. Refs. [127, 128]). In addition to the standard Galactic foregrounds, free-free, synchrotron and thermal dust emission (for a description see Box 2 below), an unknown "anomalous" dust-correlated emission has been observed over the last decade, in the microwave region of the spectrum. The anomalous emissions was first interpreted as free-free emission from shock-heated gas in Ref. [129], but Draine & Lazarian [7] showed that this would require an extremely high plasma temperature and a corresponding unrealistic energy injection rate. They proposed instead two possible mechanisms to explain the anomalous microwave emission. One of them is the magnetic dipole emission from thermal fluctuations in the magnetization of interstellar dust grains [130]. The other possible mechanism, on which the present work focuses, is electric dipole radiation from the smallest carbonaceous grains, described in Ref. [8], hereafter DL98b. The physical principle is quite straightforward: dust grains are presumably asymmetric, and thus will have a nonzero electric dipole moment. These grains will spin due to interaction with the ambient interstellar medium (ISM) and radiation field, and thus radiate electromagnetic waves due to the rotation of their electric dipole moment. To get the electric dipole radiation spectrum, one thus needs three ingredients: the quantity of small grains, then their dipole moment, and finally their rotation rates.

Although the observational interest in electric dipole radiation from spinning dust grains has only grown in the last decade, there is a long standing history of theoretical work on the subject. Ref. [131] was the first to consider the possibility that rotating dust grains could be the source of non-thermal radio-noise. Ref. [132] showed that this process was dominated by grains with radius $a \lesssim 10^{-6}$ cm and could lead to radio emission around 10 GHz. Ref. [133] estimated the spinning dust emissivity for thermally rotating grains. The first work to provide a detailed treatment of

rotational excitation of small grains was Ref. [134], where the effect of collisions with gas atoms and absorption and emission of radiation were considered. Ref. [135] evaluated the effect of collisions with ions and "plasma drag" (torques due to the electric field of passing ions).

DL98b provided the first comprehensive study of the rotational dynamics of small grains, including all the previous effects. They evaluated, as a function of grain radius and environmental conditions, rotational damping and excitation rates through collisions, "plasma drag", infrared emission, emission of electric dipole radiation, photoelectric emission and formation of H_2 molecules. The spectra they provided are now widely used in interpreting ISM microwave emission (see for example Refs. [136, 137, 138, 139, 140, 141, 142, 143]) and for CMB foreground analyses (e.g. Refs. [144, 145, 146, 147, 148]). Given that the DL98b models are now a decade old, and the recent surge in interest in anomalous emission, it is timely to revisit the theory of spinning dust emission, including the approximations made in DL98b. This is the purpose of the second part of this thesis.

7.2 Outline of Part II

The remainder of this part is divided into two chapters. Chapter 8 is a reproduction of Y. Ali-Haïmoud, C. M. Hirata & C. Dickinson, Mon. Not. Roy. Astron. Soc. **395**, 1055 (2009), where we describe our formalism for the computation of the grain rotation rate probability distribution, and calculate improved rotational excitation and damping rates for the various processes introduced by Draine & Lazarian. In Chapter 9, the rotation of disk-like grains around a non-principal axis of inertia is considered. This chapter contains mostly unpublished work, and re-derives the results of the paper K. Silsbee, Y. Ali-Haïmoud & C. M. Hirata, Mon. Not. Roy. Astron. Soc. **411**, 2750 (2011) with a quantum mechanical treatment, rather than using classical calculations. Some sections of the published paper are reproduced.

Acknowledgements

I would like to thank Clive Dickinson for initiating this project and helping me understand the basics of spinning dust physics. I also thank Christopher Hirata for his important contributions to the work presented here. Finally, I would like to thank Anthony Readhead for giving me the opportunity to participate in observation runs at the Cosmic Background Imager in the Atacama desert in Chile, during the summer of my first year when this work was started.

Box 2: Standard Galactic foregrounds

Radio emission for the Milky Way is one of the major contaminants for observations of the CMB anisotropy. Here we give a short overview of the physical origin and spectral characteristics of the standard Galactic microwave foregrounds.

• **Thermal free-free emission (Bremsstrahlung)**

Charged particles scatter off each other in the ISM, and in this process, radiate electromagnetic waves. Being the lightest charged particles, free electrons get the largest accelerations and are the primary emitters of free-free radiation. The free-free emissivity in a thermal electron-proton plasma is given by (for a derivation, see Ref. [149])

$$j_\nu^{\rm ff} = \frac{2^4 e^6}{3 m_e^{3/2} c^3} \sqrt{\frac{2\pi}{3kT}} n_e n_p {\rm e}^{-h\nu/(kT)} \overline{g}_{\rm ff}(T,\nu), \tag{7.1}$$

where $\overline{g}_{\rm ff}(T,\nu)$ is the velocity averaged Gaunt factor, which is of order unity for most cases of astrophysical interest. Tabulated velocity-averaged Gaunt factors can be found in Ref. [150]. The essential property of the free-free spectrum is that it is nearly flat up to the cutoff $\nu_{\rm max} = kT/h$, after which it decays exponentially.

• **Synchrotron radiation**

Relativistic electrons circling around the magnetic field lines also radiate energy as they are accelerated. If free electrons have a power-law distribution in energy ${\rm d}N_e \propto E^{-p}{\rm d}E$, as is generally expected for Fermi acceleration in shocks, then the spectrum of synchrotron radiation is also a power law in frequency (for a derivation, see Ref. [149])

$$j_\nu^{\rm synch} \propto \nu^{-s}, \quad s = \frac{p-1}{2}. \tag{7.2}$$

The typical spectral index for Galactic synchrotron radiation is $s \approx 1$.

• **"Thermal" (vibrational) dust emission**

Dust grains in the ISM absorb the visible and ultraviolet starlight, which "heats them up", i.e., puts them in excited vibrational states. The grains then spontaneously decay from the excited states and emit infrared radiation. Grains large enough to reach a steady-state configuration emit as modified blackbodies at temperature $T_d \sim 15 - 20$ K (smaller grains undergo thermal spikes), and the far infrared dust emissivity has the form

$$j_\nu^{\rm dust} \propto \nu^\beta B_\nu(T_d) \propto \nu^{\beta+2}, \quad h\nu \ll kT_d. \tag{7.3}$$

The spectral index β is measured to be $\beta \approx 1.8$ [151, 152].

Below we show the characteristic antenna temperature [$T_\nu \equiv I_\nu c^2/(2k\nu^2)$, where I_ν is the specific intensity] of the standard Galactic foregrounds (figure reproduced from Ref. [153]).

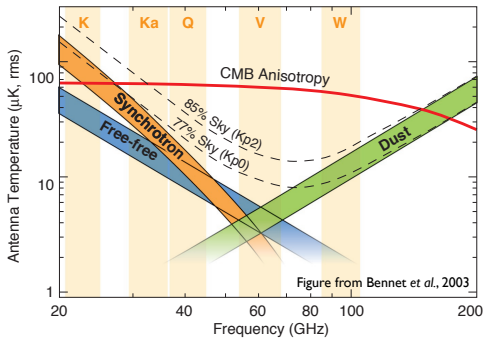

Chapter 8

A refined model for spinning dust radiation[1]

8.1 Introduction

In this chapter, we revisit and update the model of Draine & Lazarian (DL98b) for electric dipole radiation from spinning dust grains. Following DL98b, we consider either spherical grains or disk-like grains rotating about their axis of greatest inertia, leaving the discussion of non-uniformly rotating grains to the next chapter. We concentrate on the rotation rate of the grains; the size distribution has been reconsidered by other authors, and the grain dipole moment distribution should be regarded as a model parameter since one cannot compute it from first principles. We first review the calculation of DL98b for rotational excitation and damping rates. We modify the rotational excitation and damping rates by collisions with neutral species, such that it respects detailed balance in the case where the evaporation temperature is equal to the gas temperature. We include the electric dipole potential when evaluating the effect of collisions with ions. Full hyperbolic trajectories and rotating grains are used when computing the effect of plasma drag. We correct the infrared emission damping rate which was underestimated for a given infrared spectrum. Finally, we use these excitation and damping rates to calculate the grain rotational distribution function by solving the Fokker Planck equation. Updated grain optical properties and size distribution are used throughout this analysis. An Interactive Data Language (IDL) code implementing the formulas in this chapter, SpDust, is available on the web[2], and will hopefully allow for a more thorough exploration of the parameter space, as well as model fitting to observations.

This chapter is organized as follows. In Section 8.2 we remind the reader of the electric dipole radiation formula and give the resulting expected emissivity. In Section 8.3 we discuss the size

[1]The work presented in this chapter was reproduced from the paper *A refined model for spinning dust radiation*, Y. Ali-Haïmoud, C. M. Hirata & C. Dickinson, Mon. Not. Roy. Astron. Soc. **395**, 1055 (2009). Reproduced with permission, copyright (2009) by the Royal Astronomical Society.

[2]SpDust is available for download at http://www.tapir.caltech.edu/∼yacine/spdust/spdust.html.

distribution and dipole moments, along with other grain properties. We then turn to the main thrust of this study, which is the computation of the angular velocity distribution function. The theoretical formalism is exposed in Section 8.4, which presents the Fokker-Planck equation. Sections 8.5–8.9 discuss the various rotational damping and excitation processes: collisions with ions and neutral species, plasma drag, infrared emission, photoelectric emission, and random H_2 formation. The reader interested primarily in the predicted emission may wish to proceed directly to Section 8.10, where we present the resulting emissivity and the effect of various parameters and environment conditions. Our conclusions are given in Section 8.11. Appendix 8.A presents the techniques used to numerically evaluate integrals of rapidly oscillating functions involved in the plasma drag calculation.

8.2 Electric dipole radiation

The power radiated by a dust grain spinning with an angular velocity $\boldsymbol{\omega}$, of electric dipole moment $\boldsymbol{\mu}$, with component $\boldsymbol{\mu}_\perp$ perpendicular to $\boldsymbol{\omega}$, is

$$P = \frac{2}{3}\ \frac{\mu_\perp^2\ \omega^4}{c^3}. \tag{8.1}$$

This power is emitted at the frequency $\nu = \omega/2\pi$.

To get the emissivity of electric dipole radiation per H atom, in $\mathrm{erg\,s^{-1}\,sr^{-1}\,(H\,atom)^{-1}}$, one needs several ingredients:

- The grain size distribution function: $n_{\rm H}^{-1}\mathrm{d}n_{\rm gr}/\mathrm{d}a$, which gives the number of dust grains per unit size per H atom.
- The electric dipole moments as a function of grain size a: $\mu(a)$.
- The angular velocity distribution function, $f_a(\omega)$, which depends upon the grain radius and environmental conditions. It depends on the angular velocity modulus only in a perfectly isotropic environment, with no strong electromagnetic fields forcing the dipole moments to align in some particular direction.

One then readily gets the emissivity of spinning dust grains per H atom:

$$\frac{j_\nu}{n_H} = \frac{1}{4\pi}\ \int_{a_{\rm min}}^{a_{\rm max}} \mathrm{d}a\ \frac{1}{n_{\rm H}}\frac{\mathrm{d}n_{\rm gr}}{\mathrm{d}a}\ 4\pi\omega^2 f_a(\omega)\ 2\pi\ \frac{2}{3}\frac{\mu_{a\perp}^2\omega^4}{c^3}, \tag{8.2}$$

where $\omega = 2\pi\nu$.

8.3 Dust grain properties

8.3.1 Grain shapes

The grains are characterized by their volume-equivalent radius a, such that the grain volume is $4\pi a^3/3$. The radius a is in fact a measure of the number of C atoms in the grain, which we assume to be

$$N_{\rm C} = \frac{4\pi a^3 \rho_{\rm C}}{3 m_{\rm C}} \approx 468\ a_{-7}^3 \tag{8.3}$$

where $\rho_{\rm C} = 2.24{\rm g\ cm}^{-3}$ is the density of ideal graphite and $a_{-7} \equiv a/(10^{-7}\ {\rm cm})$.

We follow Ref. [154], hereafter DL01, for the number $N_{\rm H}$ of H-atoms in the grains [see their Eq. (8)]. Following DL98b, we account for the fact that the smallest grains may be sheet-like[3], as expected for polycyclic aromatic hydrocarbons (PAHs). We assume that this is the case for $a < a_2 = 6$ Å (this corresponds to $N_{\rm C} \approx 100$ carbon atoms, the size of a large PAH). We model them as disks of thickness $d = 3.35$ Å, the interlayer separation in graphite. In many cases, these grains will be rotating primarily around the axis of largest moment of inertia [155], which is perpendicular to the plane of the grain — we will lift this assumption in Chapter 9. When computing various rates, we will usually assume a spherical geometry, with a "surface-equivalent" radius a_s or a "cylindrical excitation-equivalent" radius a_{cx}, defined as :

$$4\pi a_s^2 \equiv \oint {\rm d}S \quad \text{and} \quad 4\pi a_{cx}^4 \equiv \frac{3}{2}\oint \rho^2 {\rm d}S, \tag{8.4}$$

where $\rho \equiv r\sin\theta$ is the distance to the axis of symmetry and ${\rm d}S$ is the surface area element.

Although the assumption of cylindrical grains for $a < a_2$ is not critical, it does have an effect on the spectrum, which is shown in Fig. 8.1.

8.3.2 Size distribution

Following Ref. [156], we adopt the following size distribution for carbonaceous dust, for grain radii $a_{\rm min} = 3.5$ Å$< a < a_{\rm max} = 100$Å:

$$\frac{1}{n_{\rm H}}\frac{dn_{\rm gr}}{da} = D(a) + \frac{C}{a}\left(\frac{a}{a_t}\right)^{\alpha} F(a;\beta,a_t) \times \left\{ \begin{array}{ll} 1, & a_{\rm min} < a < a_t \\ {\rm e}^{-[(a-a_t)/a_c]^3}, & a > a_t \end{array} \right. , \tag{8.5}$$

where

$$F(a;\beta,a_t) = \left\{ \begin{array}{ll} 1+\beta a/a_t, & \beta \geq 0 \\ (1-\beta a/a_t)^{-1}, & \beta < 0 \end{array} \right. . \tag{8.6}$$

[3]DL98b allow for a possible population of linear grains, although they do not actually use them.

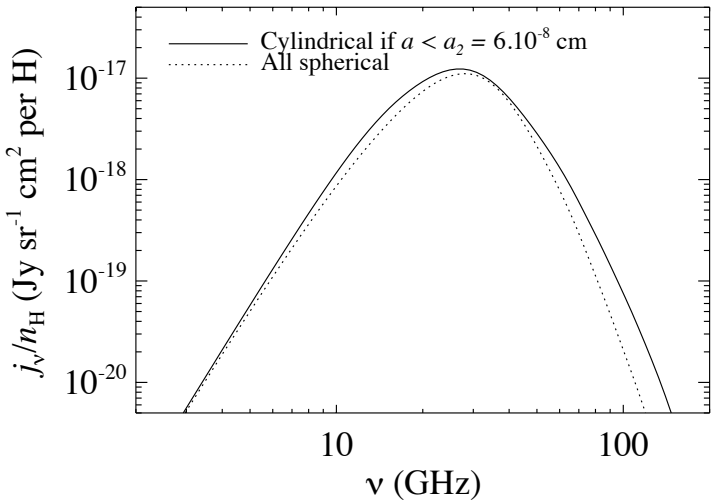

Figure 8.1: Effect of relaxing the assumption of cylindrical grains on the spectrum, for a fiducial cold neutral medium environment [CNM, defined in Eq. (8.176)]. At equal radius, spherical grains have a smaller moment of inertia than the cylindrical ones, which are rotating primarily about their axis of largest moment of inertia. They will thus radiate at slightly higher frequencies. For the CNM, we find an increase of peak frequency $\Delta\nu_{\rm peak}/\nu_{\rm peak} \approx 6\%$. The high-frequency tail of the spectrum is due to the smallest dipole moments of the assumed Gaussian distribution for the intrinsic dipole moments (see Section 8.3.3 and Fig. 8.10). For a spherical distribution of dipole moments, there are fewer grains with a low dipole than for a planar distribution. This explains the decrease in power at high frequencies. For the CNM, this results in a decrease of total emitted power $\Delta j_{\rm tot}/j_{\rm tot} \approx -16\%$.

The function $D(a)$ describes truncated (at 3.5 Å) lognormal grain populations,

$$D(a) = \sum_{i=1}^{2} \frac{B_i}{a} \exp\Big\{ -\frac{1}{2}\Big[\frac{\ln(a/a_{0,i})}{\sigma}\Big]^2\Big\}, \tag{8.7}$$

with the normalizations B_i defined to place a total number $b_{{\rm C},i}$ of carbon atoms per hydrogen nucleus in the i$^{\rm th}$ lognormal population. Here $b_{\rm C,1} = 0.75 b_{\rm C}$, $b_{\rm C,2} = 0.25 b_{\rm C}$, $b_{\rm C}$ being the total carbon abundance per hydrogen nucleus in the lognormal populations, $a_{0,1} = 3.5$ Å, $a_{0,2} = 30$ Å, and $\sigma = 0.4$. This size distribution has a total of six adjustable parameters $(b_C, C, a_t, a_c, \alpha, \beta)$. For a given choice of b_C, the other five parameters can be found in Ref. [157], Table 1.

We consider only carbonaceous grains in this work. The abundance of small silicate grains in the diffuse phases is indeed limited by the absence of the 10 μm band in emission, as discussed in Ref. [157]. Note, however, that Ref. [158] found that as much as $\sim 10\%$ of the interstellar silicate mass could be in the form of ultra-small particles ($a \lesssim 15$Å) without violating any existing observational constraints. While consistent with observations, our assumption is thus not required by them.

8.3.3 Dipole moments

Although only the component of the dipole moment perpendicular to $\boldsymbol{\omega}$ is of importance for the electric dipole emission, the total dipole moment will be needed in coming calculations. In case of spherical grains, we assume the dipole moment and rotation axis are randomly oriented. For cylindrical grains, the dipole moment is mainly oriented in the plane of the grain, perpendicular to the rotation axis.

The dipole moments have two components. First, an intrinsic part $\boldsymbol{\mu}_i$, which results from the addition of dipole moments from individual molecular bonds. For a given grain radius, we assume a multivariate Gaussian distribution, with variance proportional to the number of atoms in the grain, $N_{\rm at} = N_{\rm C} + N_{\rm H}$:

$$P(\mu_i) \propto \begin{cases} \mu_i^2 {\rm e}^{-3\mu_i^2/2\langle\mu_i^2\rangle} & \text{spherical grains} \\ \mu_i {\rm e}^{-\mu_i^2/\langle\mu_i^2\rangle} & \text{disklike grains} \end{cases}, \tag{8.8}$$

with

$$\langle\mu_i^2\rangle = N_{\rm at}\beta^2. \tag{8.9}$$

These are appropriate assumptions if the dipole moments of bonds add in a random-walk fashion, although we caution that this need not be the case. Counterexamples could include dipole moments dominated by a single feature, e.g. a PAH with a single OH group. The formula given above is in that case intended to give an estimate of the total dipole moment, with the value of β tuned to reproduce approximately observed dipole moments for laboratory molecules (see e.g. DL98b, Table 3).

The rms dipole moment per atom, β, is poorly known. Following DL98b, we will take $\beta = 0.38$ Debye as a fiducial value, corresponding to

$$\langle\mu_i^2\rangle|_{a=10^{-7}\ {\rm cm}} = (9.3\ {\rm Debye})^2. \tag{8.10}$$

In addition, for grains with charge Ze, a displacement d between charge centroid and center of mass (e.g. due to asymmetric grain shape or isotopic substitution) may add another, uncorrelated component. We assume that the displacement is proportional to the excitation equivalent radius: $d = \epsilon a_{cx}$, where $\epsilon = 0.01$ (DL98b). In most cases this is negligible compared to the intrinsic component, so we model it as a single value for the sake of simplicity. The total dipole moment is thus given by

$$\mu^2 = \mu_i^2 + (\epsilon Z q_{\rm e} a_{cx})^2, \tag{8.11}$$

where $q_{\rm e}$ is the elementary charge.

8.3.4 Grain charge

The rotational damping and excitation rates will be dependent on the grain charge. DL98b showed that the characteristic timescale for changes in charge is much shorter than the characteristic rotational damping time. We will therefore average the damping and excitation rates over grain charges, as well as the electric dipole moment when computing the power radiated. We therefore need the charge distribution function[4] of the grains as a function of their radius and environmental conditions, $f_a(Z)$.

There are three main processes contributing to grain charging: collisional charging by electrons and ions, which rates we denote $J_e(Z,a)$ and $J_i(Z,a)$, respectively, and photoelectric emission of electrons caused by the impinging radiation, which rate is $J_{pe}(Z,a)$. For every grain radius, the steady state charge distribution function is obtained by solving recursively the following equations:

$$\left[J_i(Z,a) + J_{pe}(Z,a)\right] f_a(Z) = J_e(Z+1,a) f_a(Z+1). \tag{8.12}$$

We use the equations of Ref. [159] for collisional processes, updated with the electron sticking coefficients of Ref. [157], for J_i and J_e. The photoelectric emission rate is computed according to Ref. [157]. The radiation field is taken to be a multiple χ of the average interstellar radiation field $u_{\rm ISRF}$, as estimated in Refs. [160, 161].

8.4 The Fokker-Planck equation

8.4.1 Form of the equation in spherical polar coordinates

The stationary angular velocity distribution function $f_a(\boldsymbol{\omega})$ (such that $f_a(\boldsymbol{\omega})\mathrm{d}^3\boldsymbol{\omega}$ is the probability of the grain's angular velocity being $\boldsymbol{\omega}$ within $\mathrm{d}^3\boldsymbol{\omega}$) is determined from the stationary Fokker-Planck equation. We differ here from DL98b who assumed the distribution was Maxwellian and calculated its approximate rms grain rotation rate $<\omega^2>^{1/2}$. The Fokker-Planck equation is valid in the limit of continuous torques, i.e., if every interaction changing the rotation rate of the grain does so by a small amount $\delta\omega \ll \omega$. This is, therefore, accurate for the largest grains, which have large moments of inertia. But it fails to describe precisely the smallest ones ($a \lesssim 7$ Å), for which DL98b showed that impulsive torques are important (see their Section 7 and Fig. 7). However, we believe that the actual distribution function would differ from the one we calculate only at very high frequencies, where the dust emissivity is dominated by the vibrational emission. Indeed, the occasional impulsive torques on the grains enhance the distribution function for high values of the rotation rate, where the solution of the Fokker-Planck equation predicts an exponential cutoff, as we shall see later. The

[4] We use the same notation for different distribution functions. The context and their argument should make their meaning unambiguous.

peak of the distribution will not be affected significantly, as the variations of the rotation rate of a grain within the peak are not impulsive.

The stationary Fokker-Planck equation is given by (see for example Ref. [162])

$$\frac{\partial}{\partial\omega^i}\left[D^i(\boldsymbol{\omega})f_a(\boldsymbol{\omega})\right]+\frac{1}{2}\frac{\partial^2}{\partial\omega^i\partial\omega^j}\left[E^{ij}(\boldsymbol{\omega})f_a(\boldsymbol{\omega})\right]=0. \tag{8.13}$$

The coefficients are defined as:

$$D^i(\boldsymbol{\omega})\equiv-\lim_{\delta t\to0}\frac{\langle\delta\omega^i\rangle}{\delta t}\quad\text{and}\quad E^{ij}(\boldsymbol{\omega})\equiv\lim_{\delta t\to0}\frac{\langle\delta\omega^i\delta\omega^j\rangle}{\delta t}. \tag{8.14}$$

We assume that the medium is isotropic, and there are no physical processes that allow for a preferred direction, such as a magnetic field. As a consequence, the rotational distribution function only depends upon the magnitude ω of $\boldsymbol{\omega}$. Moreover, in a local orthonormal frame $(\hat{\boldsymbol{e}}_\omega,\hat{\boldsymbol{e}}_\theta,\hat{\boldsymbol{e}}_\phi)$, where ω,θ and ϕ are the usual spherical polar coordinates defining $\boldsymbol{\omega}$, the excitation coefficient takes up the following form:

$$E^{\hat{\omega}\hat{\omega}}=E_\parallel(\omega) \tag{8.15}$$

accounts for fluctuations along $\hat{\boldsymbol{\omega}}$, and

$$E^{\hat{\theta}\hat{\theta}}=E^{\hat{\phi}\hat{\phi}}=E_\perp(\omega) \tag{8.16}$$

accounts for fluctuations perpendicular to $\boldsymbol{\omega}$. The components in the coordinate basis are thus:

$$E^{\omega\omega}=E_\parallel(\omega),\quad E^{\theta\theta}=\frac{E_\perp(\omega)}{\omega^2},\quad E^{\phi\phi}=\frac{E_\perp(\omega)}{\omega^2\sin^2\theta}. \tag{8.17}$$

Moreover, we assume there are no systematic torques, so the damping coefficient is directed along $\boldsymbol{\omega}$ and we have

$$\boldsymbol{D}(\boldsymbol{\omega})=D(\omega)\hat{\boldsymbol{e}}_\omega. \tag{8.18}$$

In the spherical polar coordinate basis, the Fokker-Planck equation then becomes:

$$\frac{1}{\omega^2}\frac{\mathrm{d}}{\mathrm{d}\omega}\left[\omega^2D(\omega)f_a(\omega)\right]+\frac{1}{2\omega^2}\frac{\mathrm{d}^2}{\mathrm{d}\omega^2}\left[\omega^2E_\parallel(\omega)f_a(\omega)\right]-\frac{1}{\omega^2}\frac{\mathrm{d}}{\mathrm{d}\omega}\left[\omega\;E_\perp(\omega)f_a(\omega)\right]=0. \tag{8.19}$$

Integrating once, we get the following first-order differential equation:

$$\frac{\mathrm{d}f_a}{\mathrm{d}\omega}+2\frac{\tilde{D}}{E_\parallel}f_a=0, \tag{8.20}$$

where

$$\tilde{D}\equiv D+\frac{1}{\omega}(E_\parallel-E_\perp)+\frac{1}{2}\frac{\mathrm{d}E_\parallel}{\mathrm{d}\omega}. \tag{8.21}$$

Note that $\tilde{D}$ is simply equal to D if the fluctuations are isotropic and independent of ω.

The coefficients D, $E_\parallel$, $E_\perp$, and therefore $\tilde{D}$ from various independent rotational damping and excitation processes are additive.

A given process is said to respect detailed balance, when, if that process were the only one taking place, the grain would rotate thermally, i.e., $f_a(\omega) \propto \exp(-I\omega^2/2kT)$. As one can see from the Fokker-Planck equation, this implies that this process must satisfy :

$$\tilde{D} = \frac{I\omega}{2kT} E_\parallel. \tag{8.22}$$

Excitation rates are often easier to calculate than damping rates, since they are positive definite and do not rely on near-cancellation of processes that increase versus decreasing ω. Thus in some cases, we will make use of detailed balance (i.e., the fluctuation-dissipation theorem), to obtain the damping rate, knowing the excitation rate.

We can also derive Eq. (8.20) with simpler arguments[5]. The change of the *magnitude* of $\boldsymbol{\omega}$ can be obtained as follows:

$$\begin{aligned}
\delta\omega &\equiv \delta|\boldsymbol{\omega}| = \omega(t+\delta t) - \omega(t) = \sqrt{(\vec{\omega}(t)+\delta\vec{\omega})^2} - \omega(t) = \omega\left[\sqrt{1+2\frac{\vec{\omega}.\delta\vec{\omega}}{\omega^2}+\frac{\delta\vec{\omega}^2}{\omega^2}}-1\right] \\
&= \omega\left[\frac{\vec{\omega}.\delta\vec{\omega}}{\omega^2}+\frac{1}{2}\frac{\delta\vec{\omega}^2}{\omega^2}-\frac{1}{8}\left(2\frac{\vec{\omega}.\delta\vec{\omega}}{\omega^2}\right)^2+\mathcal{O}(\delta\omega^3)\right] = \delta\vec{\omega}.\hat{e}_\omega + \frac{\delta\boldsymbol{\omega}_\perp^2}{2\omega}+\mathcal{O}\left(\frac{\delta\omega^3}{\omega^2}\right).
\end{aligned} \tag{8.23}$$

We therefore obtain, after averaging and taking the time derivative (with $E_\perp(\omega) \equiv \frac{1}{2}\lim_{\delta t\to 0}\frac{\delta\boldsymbol{\omega}_\perp^2}{\delta t}$):

$$\lim_{\delta t\to 0}\frac{\langle\delta\omega\rangle}{\delta t} = -D(\omega)+\frac{E_\perp(\omega)}{\omega}, \tag{8.24}$$

$$\lim_{\delta t\to 0}\frac{\langle\delta\omega^2\rangle}{\delta t} = E_{||}(\omega). \tag{8.25}$$

If we now consider the *one-dimensional* probability distribution for ω, $\mathcal{F}(\omega)$ [such that $\mathcal{F}(\omega)\delta\omega$ is the probability that the rotation rate is ω within $\delta\omega$], it satisfies the one-dimensional stationary Fokker-Planck equation:

$$\frac{\mathrm{d}}{\mathrm{d}\omega}\left[\left(D-\frac{E_\perp}{\omega}\right)\mathcal{F}\right]+\frac{1}{2}\frac{\mathrm{d}^2}{\mathrm{d}\omega^2}\left[E_{||}\mathcal{F}\right]=0, \tag{8.26}$$

which, integrated once, gives (assuming $\mathcal{F}(\omega)$ and its derivative vanish at infinity):

$$\left(D-\frac{E_\perp}{\omega}\right)\mathcal{F}+\frac{1}{2}\frac{\mathrm{d}}{\mathrm{d}\omega}\left[E_{||}\mathcal{F}\right]=0. \tag{8.27}$$

If we know rewrite $\mathcal{F}(\omega) = 4\pi\omega^2 f_a(\omega)$, we directly obtain Eq. (8.20).

[5]This paragraph is not part of the published paper.

8.4.2 Normalized damping and excitation coefficients

We will see in the next section that for collisions with neutral H atoms, at a temperature T, for a spherical dust grain at the same temperature T, the damping and parallel excitation coefficients have the following form:

$$\tilde{D}_H = \frac{\omega}{\tau_{\rm H}} \quad \text{and} \quad E_{||,H} = E_{\perp,H} = \frac{2kT}{I\tau_{\rm H}}, \tag{8.28}$$

where

$$\tau_{\rm H} \equiv \left[n_{\rm H} m_{\rm H} \left(\frac{2kT}{\pi m_{\rm H}} \right)^{1/2} \frac{4\pi a_{cx}^4}{3I} \right]^{-1} \tag{8.29}$$

is the characteristic rotational damping timescale for collisions with neutral H atoms. Note that they respect the detailed balance condition.

We normalize the damping and excitation coefficients of each process to those of collisions with H atoms. Taking DL98b notation, we define, for each process X :

$$F_X(\omega) \equiv \frac{\tau_{\rm H}}{\omega} \tilde{D}_X \tag{8.30}$$

$$G_X(\omega) \equiv \frac{I\tau_{\rm H}}{2kT} E_{\|,X}(\omega). \tag{8.31}$$

A special case is made of the rotational damping through electric dipole radiation (subscript $_{\rm ed}$), because of its specific ω^3 dependence:

$$\left. \frac{\mathrm{d}}{\mathrm{d}t} \left(\frac{1}{2} I\omega^2 \right) \right|_{\rm ed} = \frac{2}{3} \frac{\mu_\perp^2 \omega^4}{c^3}, \tag{8.32}$$

so

$$\left. \frac{\mathrm{d}\omega}{\mathrm{d}t} \right|_{\rm ed} = -D_{\rm ed}(\omega) = -\frac{2}{3} \frac{\mu_\perp^2 \omega^3}{Ic^3} = -\frac{I\omega^3}{3kT} \frac{1}{\tau_{\rm ed}}. \tag{8.33}$$

Here we define, following DL98b:

$$\tau_{\rm ed} \equiv \frac{I^2 c^3}{2kT\mu_\perp^2} \tag{8.34}$$

Using Eqs. (8.30), (8.31) and (8.33) in Eq. (8.20), the final equation for the distribution function is

$$\frac{\mathrm{d}f_a}{\mathrm{d}\omega} + \left[\frac{I\omega}{kT} \frac{F}{G} + \frac{\tau_{\rm H}}{\tau_{\rm ed}} \frac{1}{3G} \frac{I^2\omega^3}{(kT)^2} \right] f_a = 0, \tag{8.35}$$

where

$$F \equiv \sum_X F_X \quad \text{and} \quad G \equiv \sum_X G_X. \tag{8.36}$$

One can see that the conditions to get a thermal, Maxwellian distribution $f_a(\omega) \propto \exp(-I\omega^2/2kT)$ are:

$$F = G \quad \text{and} \quad \frac{\tau_{\rm H}}{G\tau_{\rm ed}} \to 0. \tag{8.37}$$

Otherwise, the general solution to this equation is :

$$f_a(\omega) \propto \exp\left\{ -\int_0^\omega d\omega' \left[\frac{I\omega'}{kT} \frac{F(\omega')}{G(\omega')} \frac{\tau_{\rm H}}{3\tau_{\rm ed} G(\omega')} \frac{I^2\omega'^3}{(kT)^2} \right] \right\}. \tag{8.38}$$

If all F_X's and G_X's are constant, this has a simple form :

$$f_a(\omega) \propto \exp\left[-\frac{F}{G} \frac{I\omega^2}{2kT} - \frac{\tau_{\rm H}}{\tau_{\rm ed}} \frac{1}{3G} \left(\frac{I\omega^2}{2kT} \right)^2 \right]. \tag{8.39}$$

Note that the damping through electric dipole radiation causes the distribution to be non-Maxwellian.

In the general case, some F_X's and G_X's may depend upon ω and one has to compute numerically the resulting distribution function, using Eq. (8.38).

We now turn to the calculation of the various damping and excitation coefficients, due to collisions, plasma drag, infrared emission, photoelectron emission, and random H_2 formation. In the following microphysics sections that form the heart of the calculations, we compute excitation and damping coefficients as a function of grain radius and environmental conditions. We evaluate them numerically for a fiducial cold neutral medium (CNM) environment, defined explicitly in Eq. (8.176).

8.5 Collisional damping and excitation

In this section we correct the results of DL98b, Appendix B, which did not take into account the fact that not all neutrals escape the grain surface when computing the damping rate.
The microphysics of collisions is complex and beyond the scope of this study (for a discussion of the physics and chemistry of PAHs and their relation with the interstellar gas see for example Ref. [163]). We therefore use the following simplifying assumptions:

- The grain is in a stationary state: the rate at which species collide with it is equal to the rate at which they leave its surface.

- We assume that all species (neutrals and ions) colliding with the grain stick and that they depart the grain as neutrals. In extremely dense environments, the colliding species may bounce off the grain surface instead of sticking. This case is discussed at the end of Section 8.5.1.4.

- Even if the impacting species may not collide equiprobably everywhere on the grain's surface (e.g. if the grain is non spherical or if it has a dipole moment), we assume they somehow get re-distributed on the grain surface and leave it equiprobably from any point.

- We assume, as in DL98b, that neutrals leave the grain surface with a thermal velocity distribution in the grain's frame, with a temperature T_{ev} of the order of the infrared emission

characteristic temperature. Unlike DL98b, we estimate T_{ev} as a function of grain radius and ambient radiation field (see Section 8.5.1.4).

Using those assumptions, one can compute the rate of collisional damping and excitation. We will perform the calculations for a spherical grain in the general case. To find the relevant equivalent radius to use for a cylindrical grain, we will carry out the explicit calculation in the case of collisions of a neutral grain with neutral H atoms. Note that as pointed out in DL98b, the rotational excitation in case of collisions has two origins: the random excitation by incoming particles (superscript $^{(in)}$), as well as the random excitation by "evaporating" neutrals (superscript $^{(ev)}$).

8.5.1 General considerations: spherical grain

We use the usual spherical polar coordinates around the spherical grain, taking the rotation axis as a reference. The local phase-space density at the grain surface is:

$$f_{ev}(\boldsymbol{v},\theta) = K(\theta)\exp\Big[-\frac{m(\boldsymbol{v}-\boldsymbol{v}_0)^2}{2kT_{ev}}\Big] \tag{8.40}$$

with the local velocity

$$\boldsymbol{v}_0 \equiv \boldsymbol{\omega}\times\boldsymbol{r} = a\omega\sin\theta\hat{\boldsymbol{e}}_\phi. \tag{8.41}$$

The normalization constant $K(\theta)$ is found by imposing that, locally, the flux of evaporating (and escaping) particles is equal to the flux of colliding particles. Except for the case of ions interacting with the electric dipole of the grain, the flux of colliding particles will be homogenous on the grain surface. If it is not the case, we approximate the local flux by the total rate of collisions $\mathrm{d}N_{coll}/\mathrm{d}t$ divided by the grain area:

$$\frac{1}{4\pi a^2}\frac{\mathrm{d}N_{coll}}{\mathrm{d}t} = K\int v_r\exp\left[-\frac{m(\boldsymbol{v}-\boldsymbol{v}_0)^2}{2kT_{ev}}\right]P_{\rm esc}\,\mathrm{d}^3\boldsymbol{v}, \tag{8.42}$$

where $P_{\rm esc}=1$ for velocities at the grain surface leading to escape, and 0 otherwise.

All particles evaporating from the grain are neutrals. They interact with the grain through the induced dipole potential (we neglect the dipole-induced dipole interaction with the dipole moment of the grain):

$$U(r) = -\frac{1}{2}\alpha\frac{Z_g^2 q_{\rm e}^2}{r^4}, \tag{8.43}$$

where α is the polarizability of the escaping neutral and $q_{\rm e}$ is the elementary charge. The polarizability of hydrogen is a standard result in non-relativistic quantum mechanics and is $\frac{9}{2}a_0^3 = 0.67\,\text{Å}^3$ where a_0 is the Bohr radius [164]. We also take $\alpha = 0.20\text{Å}^3$ for helium[6] [165], and $\alpha = 1.54\text{Å}^3$ for carbon [166], which is important since C^+ is often the dominant ion if the hydrogen is self-shielded.

[6] We assume that all the helium is neutral and $n_{\rm He}/n_{\rm H} = 1/12$.

For molecular hydrogen H_2, we take $\alpha = 0.79 \text{Å}^3$ [167].

8.5.1.1 Computation of P_{esc}

The radial coordinate of the escaping neutral is the solution of the following equation:

$$\dot{r}^2 + V_{\rm eff}(r) \equiv \dot{r}^2 + \frac{a^2}{r^2} v_\parallel^2 - \frac{a^4}{r^4} v_a^2 = \frac{2E}{m}, \tag{8.44}$$

where $v_\parallel$ is the modulus of the tangential velocity at the grain surface and

$$v_a^2 \equiv \frac{Z_g^2 q_{\rm e}^2 \alpha}{m a^4}. \tag{8.45}$$

The effective potential has a maximum at the radius

$$r_a = \sqrt{2}\, a \frac{v_a}{v_\parallel}; \quad V_{eff}(r_a) = \frac{v_\parallel^4}{4 v_a^2}. \tag{8.46}$$

To escape, a neutral needs to have either $a > r_a$ or $2E/m > V_{\rm eff}(r_a)$. These two conditions can be combined to get:

$$P_{\rm esc} = 1 \ \text{ if } \begin{cases} v_r > v_a \\ \text{or} \\ 0 < v_r < v_a \quad \text{and} \quad v_\parallel > \sqrt{2 v_a (v_a - v_r)} \end{cases}, \tag{8.47}$$

where v_r is the radial velocity at the grain surface.

8.5.1.2 Computation of $K(\theta)$

Following DL98b, we define $\epsilon_e^2 \equiv m v_a^2 / 2kT_{ev}$, which describes whether the typical evaporating atom has enough energy to overcome the induced dipole attraction to the grain ($\epsilon_e < 1$) or not ($\epsilon_e > 1$). We also define the ratio of rotational velocity to thermal velocity at the grain surface, which is small compared to unity:

$$\Omega \equiv a\omega \sqrt{\frac{m}{2kT_{ev}}} \sim \left(\frac{m}{m_{\rm grain}} \frac{T_{\rm rot}}{T_{ev}} \right)^{1/2} \ll 1. \tag{8.48}$$

In terms of those dimensionless quantities, we can find the normalization constant K. The right-hand side of Eq. (8.42) can be expanded using the substitution

$$(v_r, v_\theta, v_\phi) = \sqrt{\frac{2kT_{ev}}{m}} \, (u_r, u\cos\psi, u\sin\psi) \tag{8.49}$$

to yield

$$\frac{1}{4\pi a^2}\frac{\mathrm{d}N_{\rm coll}}{\mathrm{d}t} = K\left(\frac{2kT_{ev}}{m}\right)^2\frac{\pi}{2} \times\left[\mathrm{e}^{-\epsilon_e^2}+\mathrm{e}^{-(\Omega\sin\theta)^2}\int_0^{\epsilon_e}2u_r\mathrm{d}u_r\,\mathrm{e}^{-u_r^2}\int_{\sqrt{2\epsilon_e(\epsilon_e-u_r)}}^{\infty}2u\,\mathrm{d}u\,\mathrm{e}^{-u^2}I_0(2u\Omega\sin\theta)\right], \quad (8.50)$$

where

$$I_0(X)=\frac{1}{2\pi}\int_0^{2\pi}e^{X\sin\psi}d\psi = 1+\frac{1}{4}X^2+\mathcal{O}(X^3) \quad (8.51)$$

is a modified Bessel function of the first kind. Expanding to second order in Ω, we get:

$$K=\left(\frac{2kT_{ev}}{m}\right)^{-2}\frac{2}{\pi}\frac{e^{\epsilon_e^2}}{e^{-\epsilon_e^2}+\sqrt{\pi}\epsilon_e\,\mathrm{erf}\,(\epsilon_e)}\frac{1}{4\pi a^2}\frac{\mathrm{d}N_{\rm coll}}{\mathrm{d}t} \quad (8.52)$$

up to corrections of order $\mathcal{O}(\Omega^2)$.

8.5.1.3 Damping and excitation rates

Each escaping neutral particle takes away an angular momentum

$$\boldsymbol{L}=ma(v_\theta\hat{\boldsymbol{e}}_\phi-v_\phi\hat{\boldsymbol{e}}_\theta). \quad (8.53)$$

As P_{esc} is an even function of v_θ, the average of v_θ vanishes. The loss of angular momentum along the z-direction per unit time per unit area is given by

$$\frac{\mathrm{d}L_z}{\mathrm{d}t\,\mathrm{d}S}=-ma\sin\theta\;K\int v_r v_\phi\exp\left[-\frac{m(\boldsymbol{v}-\boldsymbol{v}_0)^2}{2kT_{ev}}\right]P_{esc}\,\mathrm{d}v_r\,\mathrm{d}v_\theta\,\mathrm{d}v_\phi. \quad (8.54)$$

Here we differ from DL98b as we take into account the fact that not all particles escape from the grain. Expanding in Ω and using the expression for K we get, up to corrections of order $\mathcal{O}(\Omega^2)$:

$$\frac{\mathrm{d}L_z}{\mathrm{d}t\,\mathrm{d}S}=-\frac{1}{4\pi}m\sin^2\theta\,\frac{\mathrm{e}^{-\epsilon_e^2}+2\epsilon_e^2}{e^{-\epsilon_e^2}+\sqrt{\pi}\epsilon_e\,\mathrm{erf}\,\epsilon_e}\frac{\mathrm{d}N_{\rm coll}}{\mathrm{d}t}\omega. \quad (8.55)$$

Integrating over the whole grain surface, we find the damping rate

$$D(\omega)=-\frac{1}{I}\frac{\mathrm{d}L_z}{\mathrm{d}t}=\frac{\mathrm{e}^{-\epsilon_e^2}+2\epsilon_e^2}{\mathrm{e}^{-\epsilon_e^2}+\sqrt{\pi}\epsilon_e\,\mathrm{erf}\,\epsilon_e}\frac{2ma^2}{3I}\frac{\mathrm{d}N_{\rm coll}}{\mathrm{d}t}\omega. \quad (8.56)$$

A similar calculation leads to the excitation rate through evaporating particles:

$$E_\parallel{}^{(ev)}(\omega)=\frac{1}{I^2}\frac{\mathrm{d}\Delta L_z^2{}^{(ev)}}{\mathrm{d}t}=\frac{\mathrm{e}^{-\epsilon_e^2}+2\epsilon_e^2}{\mathrm{e}^{-\epsilon_e^2}+\sqrt{\pi}\epsilon_e\,\mathrm{erf}\,\epsilon_e}\frac{2ma^2}{3I^2}\frac{\mathrm{d}N_{\rm coll}}{\mathrm{d}t}\;kT_{ev}=\frac{kT_{ev}}{I\omega}\;D(\omega), \quad (8.57)$$

up to terms quadratic in Ω.

This implies the remarkable relation

$$G_{\rm coll}^{(ev)} = \frac{T_{ev}}{2T} F_{\rm coll}. \tag{8.58}$$

Physically, this occurs because if $T_{ev} = T$ then the collisions with neutrals satisfy detailed balance, Eq. (8.22). The factor of 2 arises since in this case there is an equal contribution to the excitation from incoming and evaporating particles.

We derive a stronger damping rate due to evaporating atoms than DL98b: for $\epsilon_e \ll 1$ this results in no change, but for $\epsilon_e \gg 1$ we find much stronger damping. The physical origin of this is that atoms that evaporate with prograde velocities relative to the local grain surface ($v_\phi > v_{0\phi}$) typically have more angular momentum than atoms that evaporate with retrograde velocities. Therefore the centrifugal potential helps them to escape the grain. DL98b neglected this effect, but for $\epsilon_e \gg 1$ it is dominant.

The excitation rate through incoming particles will be calculated for each case.

8.5.1.4 Evaporation temperature T_{ev}

DL98b assume that the evaporating temperature is a constant, independent of grain size. This accurately describes the largest grains, for which the temperature may be approximated as a constant, obtained from equating the absorbed and emitted energy (DL98b):

$$T_c = \frac{hc}{k} \left[\frac{\langle Q \rangle_* u_*}{8\pi hc Q_0 \lambda_0^\alpha \Gamma(\alpha+4)\zeta(\alpha+4)} \right]^{1/(\alpha+4)} \tag{8.59}$$

where in the infrared the grain absorption efficiency is assumed to be a power-law

$$Q_\nu = Q_0 \left(\frac{\nu}{\nu_0} \right)^\alpha \quad , \quad \lambda_0 = \frac{c}{\nu_0} \tag{8.60}$$

with typically $\alpha = 2$ and $\langle Q \rangle_* u_* \equiv \int {\rm d}\nu Q_\nu u_\nu$. Note that we have $T_c \propto \chi^{1/6}$ and a weak dependence on grain radius as the absorption efficiencies cancel out.

However, the smallest grains undergo sudden thermal spikes after each photon absorption, followed by long intervals during which the grain drops to its vibrational ground state. The neutrals or ions that have stuck to the grain after a collision cannot be thermally ejected from a grain in the ground state so we assume ejection during thermal spikes. A simple assumption is that in this case ejection occurs after a photon absorption and thermalization of the photon's energy. We take

$$E_\gamma = \frac{\int Q_\nu u_\nu {\rm d}\nu}{\int Q_\nu \frac{u_\nu}{h\nu} {\rm d}\nu} \tag{8.61}$$

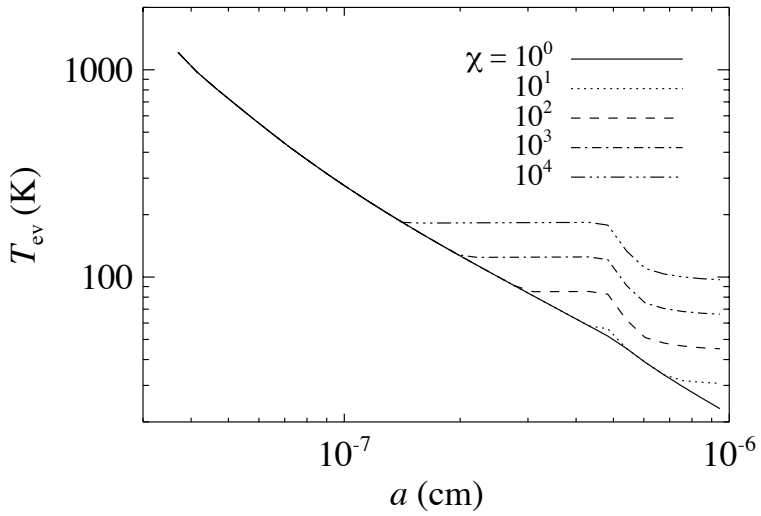

Figure 8.2: Evaporation temperature T_{ev} as a function of grain radius a, for various values of the ambient radiation field u, parameterized by $\chi = u/u_{\rm ISRF}$. The curves join at small radii, for which the grains undergo temperature spikes. The kink at $a = 50$Å results from the DL01 prescription for PAH-graphite optical properties.

as the typical energy of an absorbed photon. Typically, $E_\gamma \approx 5$ eV. We then calculate the corresponding grain temperature following DL01: we solve for T_q such that $\bar{E}(T_q) = E_\gamma$, where

$$\bar{E}(T) = \sum_{j=1}^{N_m} \frac{\hbar\omega_j}{\exp(\hbar\omega_j/kT) - 1} \tag{8.62}$$

is the expectation value of the energy of the grain, and the sum runs over its N_m vibrational degrees of freedom. We take $T_{ev} = \max(T_c, T_q)$ as the evaporation temperature. The result is shown in Fig. 8.2. One can see that we obtain much higher evaporation temperatures than the ones used by DL98b[7]. The effect may be significant on the final spectrum, as can be seen from Fig. 8.3.

High-density, low-radiation field case

The previous treatment is valid only if the rate of photon absorption is high enough to eject all stuck species before all available sites on the grain are occupied. We approximate the number of available sites on the grain by the number of superficial C-atoms :

$$N_{\rm sites} = \begin{cases} N_{\rm C}(a) & \text{for cylindrical grains} \\ \frac{3d}{a} N_{\rm C}(a) & \text{for spherical grains} \end{cases}, \tag{8.63}$$

where $N_{\rm C}(a)$ was defined in Eq. (8.3) and $d = 3.35$Å is the interlayer separation in graphite. The

[7]The mechanism we describe for atomic ejection from grains is called photo-thermo-dissociation (PDT). Ref. [134] also mentions another possible mechanism, photo-dissociation (PD), which is an atomic ejection following the direct interaction of a UV photon with a given C-H bond. PD may lead to even higher ejection temperatures, of order 10,000 K.

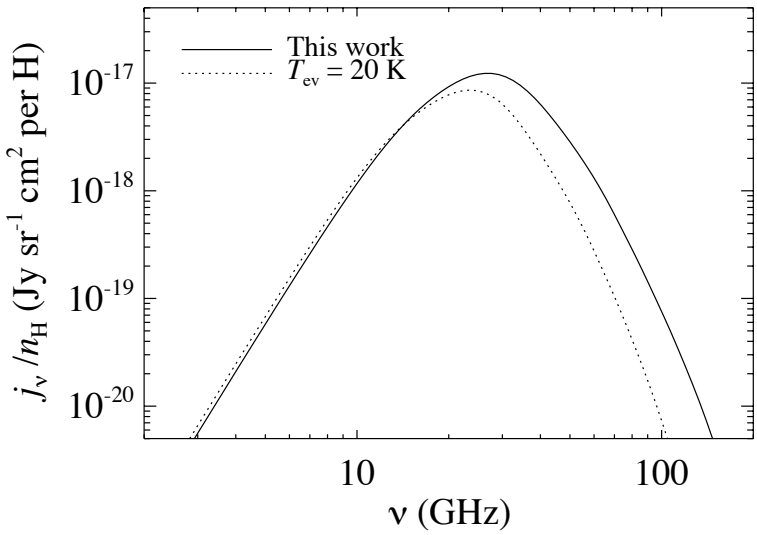

Figure 8.3: Effect of the evaporation temperature model on the spinning dust spectrum for the cold neutral medium [CNM, Eq. (8.176)]. Our prescription results in a much higher evaporation temperature for the smallest grains, compared to DL98b, who assume a constant $T_{ev} = 20$ K for all grain sizes. This leads to a decreased damping rate (see discussion at the end of Section 8.5.1.3) and an increased excitation rate through collisions, and therefore increases the peak frequency of the spectrum.

ratio of collision rate to photon absorption rate is given by :

$$R_{\rm coll/abs} = \frac{n_{\rm H}\sqrt{8kT/\pi m_{\rm H}}}{\int Q_\nu \frac{u_\nu}{h\nu} {\rm d}\nu \; c} \approx 0.1 \times \frac{n_{\rm H}}{30{\rm cm}^{-3}} T_2^{1/2} \chi^{-1} a_{-7}^{-1}. \tag{8.64}$$

In most environments, $R_{\rm coll/abs} \ll N_{\rm sites}$ so there is no accumulation of stuck species. In very dense and dark clouds however, the rate of collisions may become so high compared to the rate of photon absorption that all the sites are occupied. In that case, the assumption that incoming species stick to the grain is no more valid. They will instead bounce off the irregular grain surface. From the fluctuation-dissipation theorem, one expects that, for collisions with neutral species, $F_n = G_n$. Thus, we set the effective evaporation temperature equal to the gas temperature in that case (see Eq. (8.79) and discussion below):

$$T_{ev} = T \quad \text{if} \quad R_{\rm coll/abs} > N_{\rm sites}. \tag{8.65}$$

The actual transition from sticking to elastic collisions should of course be smooth, unlike the discontinuous step we assume here. Our treatment should approximately reflect the physics of collisions except near the transition regime $R_{\rm coll/abs} \sim N_{\rm sites}$.

8.5.2 Collision with neutral H atoms: neutral grain, general grain shape

We assume that the grain is neutral, and has no dipole moment, so there is no interaction whatsoever between the grain and the neutral H atoms (purely geometric cross section). The phase-space density of incoming H atoms at the grain surface is simply

$$f_{in}(\boldsymbol{v}) = n_{\rm H} \left(\frac{m_{\rm H}}{2\pi kT}\right)^{3/2} {\rm e}^{-m_{\rm H}v^2/2kT}, \tag{8.66}$$

from which one can easily get the excitation rate through incoming particles :

$$\frac{{\rm d}\Delta L_z^2{}^{(in)}}{{\rm d}t\,{\rm d}S} = \int v_n (m_{\rm H}\rho v_\phi)^2 f_{in}(\boldsymbol{v}) {\rm d}^3\boldsymbol{v} \tag{8.67}$$

where v_n is the component of the velocity normal to the grain surface. This evaluates to

$$\frac{{\rm d}\Delta L_z^2{}^{(in)}}{{\rm d}t\,{\rm d}S} = n_{\rm H} m_{\rm H}^2 \rho^2 \frac{\pi}{4} \left(\frac{2kT}{\pi m_{\rm H}}\right)^{3/2}. \tag{8.68}$$

Integrating over the grain surface, we get

$$\frac{{\rm d}\Delta L_z^2{}^{(in)}}{{\rm d}t} = kT n_{\rm H} m_{\rm H} \left(\frac{2kT}{\pi m_{\rm H}}\right)^{1/2} \frac{4\pi a_{cx}^4}{3}, \tag{8.69}$$

where a_{cx} was defined in Eq. (8.4). For a spherical grain, $a_{cx} = a$. For a disk-like grain of thickness d and radius b, spinning around its axis of symmetry, we have

$$a_{cx} = \left[\frac{3}{8} b^3 \ (2d + b)\right]^{1/4}. \tag{8.70}$$

We can write the excitation rate by incoming H atoms as

$$E_{\parallel,{\rm H}}^{(in)} = \frac{kT}{I\tau_{\rm H}}, \tag{8.71}$$

where $\tau_{\rm H}$ was defined in equation (8.29).

The case of evaporating particles is very similar. Assuming the grain surface is at the same temperature T as the gas, the phase-space density of evaporating particles is

$$f_{ev}(\boldsymbol{v}) = n_{\rm H} \left(\frac{m_{\rm H}}{2\pi kT}\right)^{3/2} \exp\left(-\frac{m_{\rm H}(\boldsymbol{v} - \boldsymbol{v}_0)^2}{2kT}\right). \tag{8.72}$$

In that case $P_{\rm esc} = 1$ for all outgoing particles. The same calculation therefore leads to

$$E_{\parallel,{\rm H}}^{(ev)} = \frac{kT}{I\tau_{\rm H}}, \tag{8.73}$$

up to terms of order $\mathcal{O}(\Omega^2)$, which comes from the fact that we did not take into account the slight change of ω after the particle has collided (we assumed the same ω for the incoming and the outgoing particle). Detailed balance ensures that

$$\tilde{D}_{\rm H} = \frac{\omega}{\tau_{\rm H}}. \tag{8.74}$$

Therefore, for non-spherical grains, we will compute collision rates assuming a spherical geometry with radius a_{cx}. We just showed that this is an exact result for collisions with neutral H atoms. The collision rates are indeed proportional to the area of the grain, but the angular momentum gained depends on $\langle\rho^2\rangle$, so a_{cx} will approximately reflect both dependencies.

8.5.3 Collisions with neutral atoms: charged grains

In that case, the incoming neutrals interact with the same potential as the outgoing particles:

$$U(r) = -\frac{1}{2}\alpha\frac{Z_g^2 q_{\rm e}^2}{r^4}. \tag{8.75}$$

We use the same notation as DL98b and define

$$\epsilon_n \equiv \sqrt{\frac{mv_a^2}{2kT}} \quad \text{and} \quad b_0(v) \equiv a\sqrt{\frac{2v_a}{v}}, \tag{8.76}$$

where v_a was defined in Eq. (8.45).

We recall, from DL98b, that a trajectory with impact parameter b and velocity at infinity v leads to a collision if

$$b \leq b_{\rm max}(v) = \begin{cases} b_0(v) & \text{if } v \leq v_a \\ a\sqrt{1+v_a^2/v^2} & \text{if } v \geq v_a \end{cases}. \tag{8.77}$$

We compute the collision rate

$$\begin{aligned} \frac{{\rm d}N_{\rm coll}}{{\rm d}t} &= n_n \int_0^\infty {\rm d}v\, 4\pi v^3 \pi b_{\rm max}^2(v) \left(\frac{m_n}{2\pi kT}\right)^{3/2} {\rm e}^{-mv^2/2kT} \\ &= n_n 2\pi a^2 \left(\frac{2kT}{\pi m}\right)^{1/2} \left[e^{-\epsilon_n^2} + \sqrt{\pi}\epsilon_n \,{\rm erf}\,\epsilon_n\right]. \end{aligned} \tag{8.78}$$

We can now get the normalized damping and excitation rates for collisions with neutrals:

$$\begin{aligned} F_n &= \frac{n_n}{n_H}\sqrt{\frac{m_n}{m_{\rm H}}}\frac{e^{-\epsilon_n^2} + \sqrt{\pi}\epsilon_n\,{\rm erf}\,\epsilon_n}{e^{-\epsilon_e^2} + \sqrt{\pi}\epsilon_e\,{\rm erf}\,\epsilon_e}\left(e^{-\epsilon_e^2} + 2\epsilon_e^2\right), \\ G_n^{(ev)} &= \frac{T_{ev}}{2T}F_n, \quad \text{and} \\ G_n^{(in)} &= \frac{n_n}{2n_H}\sqrt{\frac{m_n}{m_{\rm H}}}\left(e^{-\epsilon_n^2} + 2\epsilon_n^2\right), \end{aligned} \tag{8.79}$$

where the result for $G_n^{(in)}$ is identical to that of DL98b. Note that when $T = T_{ev}$, $G_n^{(ev)} = G_n^{(in)} = F_n/2$ so the principle of detailed balance holds. Moreover, in the case of a neutral grain, if the only rotational excitation and damping process were collisions with neutral species, then the rotational distribution function would be a Maxwellian. In that case the rotational temperature would be given by $T_{\rm rot} = G_n/F_n \times T = \frac{1}{2}(T + T_{ev})$, the arithmetic mean of the gas and evaporation temperatures, as was already shown in Ref. [155].

This is the contribution of an individual neutral, for a given grain charge. To get the total contribution, one must average over all grain charges (DL98b showed that the charging timescale is much shorter than the collision timescale) and sum over all neutral species, which we take to be atomic and molecular hydrogen, and helium[8] (with $n_{\rm He}/n_{\rm H} = 1/12$).

8.5.4 Collisions with ions: charged grains

The ion interacts with the grain through the Coulomb, electric dipole, and "image charge" potentials. The latter dominates over the Coulomb potential only in the immediate vicinity of the grain surface, so we will neglect it for charged grains. Properly accounting for it would result in a slight increase in both damping and excitation rates as this is an attractive potential. The general solution for this problem, with a rotating electric dipole moment, is still not analytical. Thus, for simplicity, we will only consider the case where the electric dipole moment can be considered as non-rotating, i.e., when the timescale of the collision is short compared to the rotation period of the grain. This is justified as, when the ion reaches the vicinity of the grain surface, the ratio of collision timescale to rotation timescale is approximately $\omega a/v \sim \sqrt{m_i/m_{gr}} \ll 1$. We will assume that the grain is spherical, so that the electric dipole moment is randomly oriented relative to the rotation axis (for cylindrical grains this is not the case but we will assume so for simplicity). Note that when the grain rotates rapidly, the component of the dipole moment perpendicular to the rotation axis averages out, but not the parallel component. Although this problem will be different in nature as this alignment creates anisotropic excitation by collisions, the magnitude of the non-rotating part of the dipole moment will remain of the same order (a factor $1/\sqrt{3}$ smaller only), so our approximation should give a decent idea of what the effect of the dipole moment is on the trajectory.

We assume a spherical geometry with radius a_{cx}. Taking $\boldsymbol{\mu}$ as the polar axis for spherical polar coordinates, the interaction potential of the ion in the Coulomb and dipole field of the grain is given by

$$V(r,\theta) = \frac{Z_g Z_i q_{\rm e}^2}{r} + \frac{Z_i q_{\rm e} \mu \cos\theta}{r^2}. \tag{8.80}$$

The motion in this potential has two obvious constants: the energy E and the angular momentum

[8] Collisions with neutral helium have little effect on the spectrum: the helium contribution dominates F_n and G_n only in the case where the medium is strongly ionized, i.e., when the dominant rotational excitation and damping mechanisms are rather collisions with ions or plasma drag. We include them for completeness.

along the z-axis (along $\boldsymbol{\mu}$), L_z. For this special potential, however, there exists a third constant of the motion. The torque $\dot{\boldsymbol{L}}$ exerted on the ion comes entirely from the second term in the potential and is

$$\dot{\boldsymbol{L}} = -\boldsymbol{r} \times \nabla V(\boldsymbol{r}) = \frac{Z_i q_e \mu \sin\theta}{r^2} \hat{\boldsymbol{e}}_\phi. \tag{8.81}$$

Since the azimuthal component of angular momentum is $\boldsymbol{L} \cdot \hat{\boldsymbol{e}}_\phi = mr^2\dot{\theta}$, we can then determine the overall rate of change of the angular momentum,

$$\frac{\mathrm{d}}{\mathrm{d}t}(L^2) = 2m_i Z_i q_e \mu \sin\theta\, \dot{\theta} = -2m_i Z_i q_e \mu \frac{\mathrm{d}}{\mathrm{d}t}\cos\theta. \tag{8.82}$$

Therefore we find the constant of the motion[9]

$$\mathcal{A} \equiv L^2 + 2m_i Z_i q_e \mu \cos\theta. \tag{8.83}$$

Its value can be determined by taking the incoming trajectory at infinity with approach angle θ_∞,

$$\mathcal{A} = (m_i b v)^2 + 2m_i Z_i q_e \mu \cos\theta_\infty. \tag{8.84}$$

The energy of the trajectory is

$$\frac{1}{2} m_i \dot{r}^2 + V_{\mathrm{eff}}(r) = E \tag{8.85}$$

where $V_{\mathrm{eff}}(r)$ is the sum of the potential $V(r,\theta)$ and the tangential kinetic energy $L^2/2m_i r^2$:

$$V_{\mathrm{eff}}(r) \equiv \frac{Z_g Z_i q_e^2}{r} + \frac{m_i (bv)^2 + 2Z_i q_e \mu \cos\theta_\infty}{2r^2}. \tag{8.86}$$

It is easier to work with the following dimensionless parameters

$$\psi \equiv \frac{Z_g Z_i q_e^2}{a_{cx} kT} \quad , \quad \tilde{\mu} \equiv \frac{Z_i q_e \mu}{a_{cx}^2 kT}. \tag{8.87}$$

Their physical meaning is as follows : $|\psi| \ll 1$ when the thermal energy of the ion dominates over the electrostatic interaction energy, and $|\psi| \gg 1$ when the electrostatic interaction dominates. The sign determines whether the interaction is attractive ($\psi < 0$) or repulsive ($\psi > 0$). $\tilde{\mu}$ is the equivalent quantity for the dipole interaction. Note that we consider only positively charged ions so $\tilde{\mu} > 0$. We also work with the dimensionless variables

$$c = \frac{b}{a_{cx}} \quad , \quad u = \sqrt{\frac{m_i}{2kT}} v. \tag{8.88}$$

[9]This may also be derived by the Hamilton-Jacobi method in spherical polar coordinates.

The effective potential can now be written

$$V_{\rm eff}(r) = kT\left[\psi\ \frac{a_{cx}}{r} + \left(u^2c^2 + \tilde{\mu}\cos\theta_\infty\right)\left(\frac{a_{cx}}{r}\right)^2\right]. \tag{8.89}$$

A study of this potential leads to the following condition for collision:

$$\cos\theta_\infty < X_{\rm max}(c,u) \equiv \tilde{\mu}^{-1}\left(u^2 - u^2c^2 - \psi\right). \tag{8.90}$$

Note that if $X_{max} < -1$, then there is never collision, for any angle. If $X_{max} > 1$, then all angles lead to a collision. We define

$$X(c,u) \equiv \max\left\{-1, \min\left[1, X_{\rm max}(c,u)\right]\right\}. \tag{8.91}$$

Now, we can compute the collision rate

$$\begin{aligned}\frac{{\rm d}N_{\rm coll}}{{\rm d}t} &= n_i\int 2\pi v^3{\rm d}v\,2\pi b{\rm d}b\left(\frac{m_i}{2\pi kT}\right)^{3/2}{\rm e}^{-m_iv^2/2kT}(X+1)\\ &= 2n_i\sqrt{\frac{2\pi kT}{m_i}}a_{cx}^2\int 2u^3{\rm e}^{-u^2}{\rm d}u\ 2c\ {\rm d}c\ \frac{X+1}{2}.\end{aligned} \tag{8.92}$$

We can also get the excitation rate by incoming ions

$$\begin{aligned}\frac{{\rm d}\Delta L_z^2}{{\rm d}t} &= n_i\int\frac{(mbv)^2}{3}2\pi v^3{\rm d}v\,2\pi b{\rm d}b\left(\frac{m_i}{2\pi kT}\right)^{3/2}{\rm e}^{-m_iv^2/2kT}(X+1)\\ &= \frac{2n_im_i^2a_{cx}^4}{3\pi}\left(\frac{2\pi kT}{m_i}\right)^{3/2}\int u^5{\rm e}^{-u^2}{\rm d}u\ 4c^3{\rm d}c\ \frac{X+1}{2}.\end{aligned} \tag{8.93}$$

These integrals can be evaluated explicitly and one then gets, for the charged grains $Z_g \neq 0$

$$\begin{aligned}F_i(Z_g\neq 0) &= \frac{n_i}{n_{\rm H}}\sqrt{\frac{m_i}{m_{\rm H}}}\frac{{\rm e}^{-\epsilon_i^2}+2\epsilon_i^2}{{\rm e}^{-\epsilon_i^2}+\sqrt{\pi}\epsilon_i\,{\rm erf}\,\epsilon_i}\ g_1(\psi,\tilde{\mu}),\\ G_i^{(ev)}(Z_g\neq 0) &= \frac{T_{ev}}{2T}F_i(Z_g\neq 0), \quad \text{and}\\ G_i^{(in)}(Z_g\neq 0) &= \frac{n_i}{2n_{\rm H}}\sqrt{\frac{m_i}{m_{\rm H}}}\ g_2(\psi,\tilde{\mu}),\end{aligned} \tag{8.94}$$

where we have defined $g_1(\psi,\tilde{\mu}) =$

$$\begin{cases}\begin{cases}1-\psi & \psi<0\\ {\rm e}^{-\psi}\sinh\tilde{\mu}/\tilde{\mu} & \psi>0\end{cases} & ,\ \tilde{\mu}\le|\psi|\\ \dfrac{1-{\rm e}^{-(\psi+\tilde{\mu})}+\tilde{\mu}-\psi+\frac{1}{2}(\tilde{\mu}-\psi)^2}{2\tilde{\mu}} & ,\ \tilde{\mu}>|\psi|,\end{cases} \tag{8.95}$$

and $g_2(\psi,\tilde{\mu}) =$

$$\begin{cases} 1-\psi+\psi^2/2+\tilde{\mu}^2/6 & \psi<0 \\ \mathrm{e}^{-\psi}\sinh\tilde{\mu}/\tilde{\mu} & \psi>0 \end{cases} \quad , \ \tilde{\mu}\le|\psi| \\ \frac{1-\mathrm{e}^{-(\psi+\tilde{\mu})}+\tilde{\mu}-\psi+\frac{1}{2}(\tilde{\mu}-\psi)^2+\frac{1}{6}(\tilde{\mu}-\psi)^3}{2\tilde{\mu}} \quad , \ \tilde{\mu}>|\psi|. \tag{8.96}$$

Note that these functions coincide with the functions $g_1(\psi),\ g_2(\psi)$ defined in DL98b for $\tilde{\mu}=0$. We also defined $\epsilon_i^2 \equiv Z_g^2 q_\mathrm{e}^2 \alpha_i/2a^4 kT_{ev}$ (here α_i is the polarizability of species i after it neutralizes on the grain surface, e.g. when considering collisions with the C^+ ion we take the polarizability of the neutral C atom). Note that even when $T_{ev}=T$, $F_i \neq G_i$ as the incoming and outgoing particles are in different ionization states; detailed balance does not apply since realistic ISM phases are not in Saha equilibrium. Numerically, one has (with $T_2 \equiv T/100\mathrm{K}$)

$$\psi \approx 170\ Z_g\ a_{-7}^{-1}\ T_2^{-1} \tag{8.97}$$

$$\tilde{\mu} \approx 30\ \frac{\langle\mu^2\rangle^{1/2}|_{10^{-7}\mathrm{cm}}}{9.3\ \mathrm{Debye}}\ a_{-7}^{-1/2}\ T_2^{-1}. \tag{8.98}$$

From these values, one can see that in general the effect of the dipole moment cannot be neglected *a priori*, as $\tilde{\mu}$ is not small compared to unity. However, in general $\tilde{\mu}<|\psi|$. This implies that, for negatively charged grains, the dipole moment has little or no effect on the excitation and damping rate. For positively charged grains, the damping and excitation rate are both increased by the huge factor $\sinh\tilde{\mu}/\tilde{\mu}$, but still remain extremely small due to the Coulomb repulsion, which shows in the factor $\mathrm{e}^{-\psi}$.

We therefore conclude that DL98b approximation of neglecting the effect of the electric dipole moment on the trajectory of ions, is essentially valid in the case of collisions with charged grains. It only has a significant effect for positively charged grains, for which the Coulomb repulsion implies an extremely small rate of collisions with ions anyway. We still account for the electric dipole moment for the sake of completeness.

8.5.5 Collisions with ions, neutral grain

In that case the Coulomb potential vanishes, and the "image charge" potential has to be taken into account. We carry the calculation using the same assumptions as in the previous section: slowly rotating spherical grain, with radius a_{cx}. Taking $\boldsymbol{\mu}$ as the polar axis for spherical polar coordinates, the interaction potential of the ion in the dipole and induced dipole field of the grain is given by

$$V(r,\theta) = -\frac{Z_i^2 q_\mathrm{e}^2 a_{cx}^3}{2r^2(r^2-a_{cx}^2)} + \frac{Z_i q_\mathrm{e}\mu\cos\theta}{r^2}. \tag{8.99}$$

The considerations that lead to the third constant of motion $\mathcal{A}$ hold again. The energy of the trajectory is

$$\frac{1}{2}m\dot{r}^2 + V_{\rm eff}(r) = E \tag{8.100}$$

where $V_{\rm eff}(r)$ is given by

$$V_{\rm eff}(r) \equiv -\frac{Z_i^2 q_{\rm e}^2 a^3}{2r^2(r^2-a^2)} + \frac{m(bv)^2 + 2Z_i q_{\rm e}\mu\cos\theta_\infty}{2r^2}. \tag{8.101}$$

Following DL98b, we define the dimensionless parameter

$$\phi^2 \equiv \frac{2Z_i^2 q_{\rm e}^2}{a_{cx}kT}, \tag{8.102}$$

which describes whether the image charge attraction dominates over the thermal energy ($\phi \gg 1$) or the thermal energy dominates ($\phi \ll 1$). The effective potential can be written

$$V_{\rm eff}(r) = kT\left[-\frac{\phi^2 a_{cx}^4}{4r^2(r^2-a_{cx}^2)} + \left(u^2c^2 + \tilde{\mu}\cos\theta_\infty\right)\left(\frac{a_{cx}}{r}\right)^2\right], \tag{8.103}$$

where $\tilde{\mu}$, c, and u were defined in Eqs. (8.87) and (8.88).
A study of this potential leads to the following condition for collision:

$$\cos\theta_\infty < X_{\rm max}(c,u) \equiv \tilde{\mu}^{-1}\left(u^2 - u^2c^2 + \phi u\right). \tag{8.104}$$

The collision and excitation rates are obtained as in Eqs. (8.91), (8.92) and (8.93). One can then obtain the normalized damping and excitation rates for collisions of ions with a neutral grain:

$$F_i(Z_g=0) = \frac{n_i}{n_H}\sqrt{\frac{m_i}{m_{\rm H}}}\,h_1(\phi,\tilde{\mu}), \tag{8.105}$$

$$G_i^{(ev)}(Z_g=0) = \frac{T_{ev}}{2T}F_i(Z_g=0), \tag{8.106}$$

$$G_i^{(in)}(Z_g=0) = \frac{n_i}{2n_H}\sqrt{\frac{m_i}{m_{\rm H}}}\,h_2(\phi,\tilde{\mu}), \tag{8.107}$$

where we have defined

$$h_1(\phi,\tilde{\mu}) \equiv \frac{1}{2} + \frac{\tilde{\mu}}{4} + \frac{2+\phi^2}{4\tilde{\mu}}\left(1-{\rm e}^{-u_0^2}\right) - \frac{\phi u_0}{4\tilde{\mu}}{\rm e}^{-u_0^2} + \frac{\pi^{1/2}\phi}{2}\left(1+\frac{3-2\tilde{\mu}}{4\tilde{\mu}}\,{\rm erf}\,u_0\right), \tag{8.108}$$

$$h_2(\phi,\tilde{\mu}) \equiv \frac{1}{2} + \frac{3\pi^{1/2}}{4}\,\phi + \frac{\phi^2}{4} + \frac{\tilde{\mu}^2}{12} + \frac{\tilde{\mu}}{4} + \frac{1+\phi^2}{2\tilde{\mu}}(1-{\rm e}^{-u_0^2}) + \frac{2\tilde{\mu}\phi^2 + \phi(2\tilde{\mu}-7)u_0}{16\tilde{\mu}}{\rm e}^{-u_0^2} + \frac{\pi^{1/2}\phi}{32\tilde{\mu}}\left(4\tilde{\mu}^2 - 12\tilde{\mu} + 15 + 2\phi^2\right){\rm erf}\,u_0, \tag{8.109}$$

$$u_0 \equiv \frac{-\phi + \sqrt{\phi^2+4\tilde{\mu}}}{2}. \tag{8.110}$$

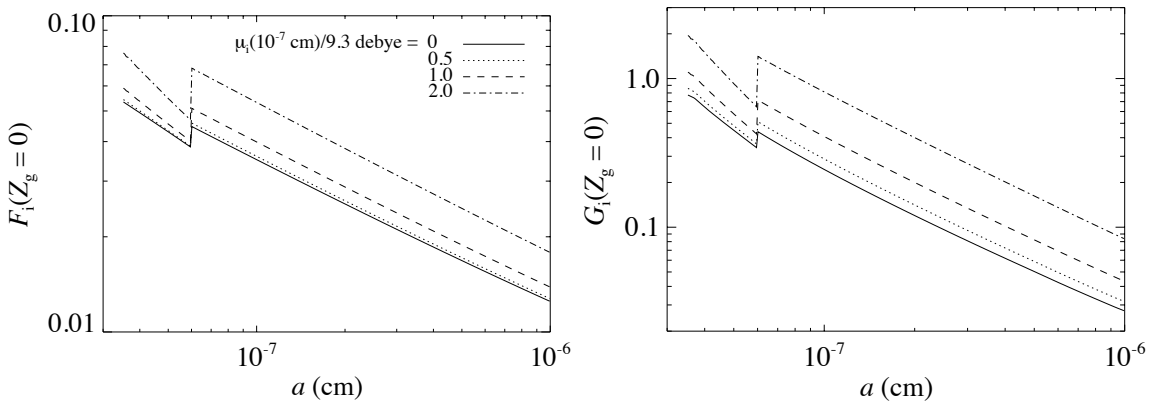

Figure 8.4: $F_i(Z_g = 0)$ (left panel) and $G_i(Z_g = 0)$ (right panel) for several values of the electric dipole moment, in CNM conditions, Eq. (8.176).

Note that in the limit $\tilde{\mu} \to 0$ we recover DL98b result, as

$$h_1(\phi, \tilde{\mu} \to 0) = 1 + \frac{\pi^{1/2}}{2}\phi + \mathcal{O}(\tilde{\mu}^3), \tag{8.111}$$

$$h_2(\phi, \tilde{\mu} \to 0) = 1 + \frac{3\pi^{1/2}}{4}\ \phi + \frac{\phi^2}{2} + \mathcal{O}(\tilde{\mu}^2). \tag{8.112}$$

However, the parameter $\tilde{\mu}$ is not small in general, as we saw in Eq. (8.98), so the effect of the dipole moment on the trajectory cannot be neglected. Note that we also have $\phi \approx 18\ a_{-7}^{-1/2} T_2^{-1/2}$. The net effect of the dipole moment is to increase the collision and excitation rates, as can be seen from Fig. 8.4. In contrast to the case of charged grains, the electric dipole moment does have a significant effect and cannot be discarded.

The effect of the dipole moment is always to increase both the collision and excitation rates, for both charged and neutral grains. This can be understood as follows. When the dipole moment vanishes, ions with a given velocity at infinity v collide with the grain if their impact parameter is such that $b < b_{\max}(v)$. The effect of the dipole moment is to make a smooth transition from non-colliding to colliding trajectories: all ions with impact parameter $b < b_1(v)$ collide with the grain, a fraction $(X(b, v) + 1)/2$ of those for which $b_1(v) < b < b_2(v)$ do collide, and none of the ions with $b > b_2(v)$ collide. b_1 and b_2 are such that $b_1 < b_{\max} < b_2$. As a result, a fraction of trajectories for which $b_1(v) < b < b_{\max}(v)$ do not lead to collision anymore (compared to the vanishing dipole case), and a fraction of trajectories $b_{\max}(v) < b < b_2(v)$ now lead to collision. The suppressed colliding trajectories have a lower rate of collision and angular momentum than the added colliding trajectories. Thus the net effect of the dipole moment is to increase the collision and rotational excitation rates.

8.6 Plasma drag

DL98b computed the effect of torques from passing ions on the electric dipole moments of the dust grains, which they named "plasma drag". They computed this effect for straight-line trajectories (the "Born approximation"). Here we include the full hyperbolic trajectory in the case of charged grains. We also account for the rotation of the grain explicitly. Moreover, we do not include trajectories leading to collisions, as they will give away their entire angular momentum through collision, which we already accounted for. A precise calculation is important because plasma drag is one of the major excitation processes in some environments.

We will find that the straight-line approximation usually overestimates the plasma drag. In the case of positively charged grains, there is a range of impact parameters where the ion trajectory is deflected away from the grain, thereby suppressing angular momentum transfer. For negatively charged grains, ions can be focused by electrostatic attraction. Ref. [135] argued that this is not a significant correction because the increased torque during close approach balances the shorter interaction time since the ion gains kinetic energy as it is attracted to the grain; however, we will see that in these cases there is a cancellation of angular momentum transfer in different parts of the trajectory that leads to reduced drag. For very special cases, the grain can corotate with the ion during close approach leading to an enhancement of the plasma drag, but this occurs for only a narrow range of impact parameters and does not compensate for the reduction of plasma drag that we find in other regimes.

As in DL98b, we find it easiest to directly compute the plasma excitation G_p and use the fluctuation-dissipation theorem to infer $F_p = G_p$.

8.6.1 Charged grain

We consider the trajectories of positively charged ion (charge $Z_i > 0$) in the electric potential of a charged dust grain (charge $Z_g \neq 0$). The trajectories are not strictly hyperbolic due to the presence of the electric dipole potential (see Section 8.5.4). However, we saw that it has little influence on collisions and we will neglect its effect on the trajectory here, assuming they are hyperbolic and determined by the Coulomb potential only. The eccentricity of the hyperbolic trajectory of the ion will be denoted e (as opposed to the elementary charge $q_{\rm e}$).

Let the ion trajectory (a hyperbola) be in the $(\hat{\boldsymbol{e}}_y, \hat{\boldsymbol{e}}_z)$ plane, symmetric about the $\hat{\boldsymbol{e}}_y$ axis. The ion position is given by

$$\boldsymbol{r} = r\hat{\boldsymbol{e}}_r = r(\alpha)\left(\cos\alpha\,\hat{\boldsymbol{e}}_y + \sin\alpha\,\hat{\boldsymbol{e}}_z\right). \tag{8.113}$$

The hyperbolic trajectory of impact parameter b and velocity at infinity v can be described in polar

coordinates as

$$\begin{aligned} r(\alpha) &= \frac{p}{e\cos\alpha - 1} \qquad \alpha \in (-\alpha_e, \alpha_e) \qquad (Z_g > 0), \\ r(\alpha) &= \frac{p}{1 - e\cos\alpha} \quad \alpha \in (\alpha_e, 2\pi - \alpha_e) \quad (Z_g < 0); \end{aligned} \tag{8.114}$$

the eccentricity and semilatus rectum of the trajectory are

$$e = \sqrt{1 + \left(\frac{m_i b v^2}{Z_i Z_g q_e^2}\right)^2} \quad \text{and} \quad p = b\sqrt{e^2 - 1}. \tag{8.115}$$

The range of longitudes α of the trajectory are determined by the limiting case

$$\alpha_e \equiv \arccos\frac{1}{e}. \tag{8.116}$$

The longitude can be related to the true anomaly f familiar from planetary dynamics by $\alpha = f$ for repulsive ($Z_g > 0$) cases and $\alpha = \pi + f$ for attractive ($Z_g < 0$) cases. We will need the following expression for the time $t(\alpha)$, valid in both cases (for the case of an attractive potential, see e.g. Ref. [168], Eq. (2.4.12)):

$$t(\alpha) = \frac{b}{v}\frac{1}{e+1}\left[\sqrt{\frac{e+1}{e-1}}\ln\left|\frac{\tan\frac{\alpha}{2} + \sqrt{\frac{e-1}{e+1}}}{\tan\frac{\alpha}{2} - \sqrt{\frac{e-1}{e+1}}}\right| - \frac{2e\tan\frac{\alpha}{2}}{\tan^2\frac{\alpha}{2} - \frac{e-1}{e+1}}\right]. \tag{8.117}$$

In order to characterize the torque on the grain, we must first take the unit vector in the direction of grain rotation,

$$\hat{\boldsymbol{e}}_\omega = \sin\theta\cos\phi\,\hat{\boldsymbol{e}}_x + \sin\theta\sin\phi\,\hat{\boldsymbol{e}}_y + \cos\theta\,\hat{\boldsymbol{e}}_z, \tag{8.118}$$

so that $\boldsymbol{\omega} = \omega\hat{\boldsymbol{e}}_\omega$. We use (θ, ϕ) to parameterize the (general) direction of rotation. We define the other two axes:

$$\hat{\boldsymbol{e}}_\theta = \cos\theta\cos\phi\,\hat{\boldsymbol{e}}_x + \cos\theta\sin\phi\,\hat{\boldsymbol{e}}_y - \sin\theta\,\hat{\boldsymbol{e}}_z \tag{8.119}$$

$$\text{and} \qquad \hat{\boldsymbol{e}}_\phi = -\sin\phi\,\hat{\boldsymbol{e}}_x + \cos\phi\,\hat{\boldsymbol{e}}_y. \tag{8.120}$$

In this system the electric dipole moment of the grain is

$$\boldsymbol{\mu} = \mu_\parallel\hat{\boldsymbol{e}}_\omega + \mu_\perp\left[\cos(\omega t + \chi)\hat{\boldsymbol{e}}_\theta + \sin(\omega t + \chi)\hat{\boldsymbol{e}}_\phi\right], \tag{8.121}$$

where $t = 0$ is taken to be the time when the ion is at the closest approach (i.e., $\boldsymbol{r} \parallel \hat{\boldsymbol{e}}_y$) and $\chi \in [0, 2\pi)$ is the random angle that $\boldsymbol{\mu}_\perp$ makes with $\hat{\boldsymbol{e}}_\theta$ at that time.

The ion electric field exerts a torque on the grain dipole moment:

$$I\frac{\mathrm{d}\boldsymbol{\omega}}{\mathrm{d}t} = \boldsymbol{\mu}\times\boldsymbol{E} = -I\frac{Z_i q_\mathrm{e}}{r^2}\boldsymbol{\mu}\times\hat{\boldsymbol{e}}_r. \tag{8.122}$$

Using the conservation of angular momentum, $r^2\dot{\alpha} = bv$, we can rewrite:

$$\frac{\mathrm{d}\boldsymbol{\omega}}{\mathrm{d}\alpha} = -\frac{Z_i q_\mathrm{e}}{Ibv}\boldsymbol{\mu}\times\hat{\boldsymbol{e}}_r. \tag{8.123}$$

We project that along the direction of $\hat{\boldsymbol{e}}_\omega$:

$$\frac{\mathrm{d}\omega_\parallel}{\mathrm{d}\alpha} = -\frac{Z_i q_\mathrm{e}\mu_\perp}{Ibv}\big[\cos(\omega t+\chi)\cos\alpha\cos\phi - \sin(\omega t+\chi)\left(\cos\alpha\cos\theta\sin\phi - \sin\alpha\sin\theta\right)\big]. \tag{8.124}$$

Expanding the sines and cosines, we integrate over the trajectory. We keep only the parts of the integral for which the inbound and outbound parts do not cancel, i.e., those which are even under $\alpha\to-\alpha$ ($Z_g>0$) or $\alpha\to2\pi-\alpha$ ($Z_g<0$); note that $t(\alpha)$ is even. We are then left with

$$\delta\omega_\parallel = \frac{Z_i q_\mathrm{e}\mu_\perp}{Ibv}\Big[(\sin\chi\cos\theta\sin\phi - \cos\chi\cos\phi)\int\cos\omega t\cos\alpha\mathrm{d}\alpha - \cos\chi\sin\theta\int\sin\omega t\sin\alpha\mathrm{d}\alpha\Big]. \tag{8.125}$$

In order to find the plasma excitation coefficient, we need to sum $\delta\omega_\parallel^2$ over collisions. We begin by averaging $\delta\omega_\parallel^2$ over solid angles for (θ,ϕ) and over angles for χ. The result is

$$\langle\delta\omega_\parallel^2\rangle = \frac{1}{3}\left(\frac{2Z_i q_\mathrm{e}\mu_\perp}{Ibv}\right)^2\mathcal{I}\left(\frac{\omega b}{v}, e, Z_g\right). \tag{8.126}$$

We have defined the integral

$$\mathcal{I}\left(\frac{\omega b}{v}, e, Z_g\right) \equiv \left(\int\cos\omega t\cos\alpha\mathrm{d}\alpha\right)^2 + \left(\int\sin\omega t\sin\alpha\mathrm{d}\alpha\right)^2, \tag{8.127}$$

where the integration limits are given by $0<\alpha<\alpha_e$ ($Z_g>0$) or $\alpha_e<\alpha<\pi$ ($Z_g<0$). Note that $\mathcal{I}$ only integrates over the inbound part of the trajectory; the outbound part is equal by symmetry.

The excitation rate due to plasma drag is then given by:

$$\frac{\mathrm{d}\Delta\omega_\parallel^2}{\mathrm{d}t} = \int_0^\infty\mathrm{d}v\int_{b_\mathrm{max}(v)}^\infty 2\pi b\,\mathrm{d}b\,n_i\,4\pi v^3\left(\frac{m_i}{2\pi kT}\right)^{3/2}\mathrm{e}^{-\frac{m_i v^2}{2kT}}\frac{1}{3}\left(\frac{2Z_i q_\mathrm{e}\mu_\perp}{Ibv}\right)^2\mathcal{I}\left(\frac{\omega b}{v}, e, Z_g\right), \tag{8.128}$$

where $b_\mathrm{max}(v)$, the maximum impact parameter for collision to occur, is defined as

$$b_\mathrm{max}(v) = \begin{cases} 0 & mv^2/2kT \le \psi \\ a_{cx}\sqrt{1-(2kT/mv^2)\psi} & mv^2/2kT > \psi \end{cases} \tag{8.129}$$

where $\psi = Z_g Z_i q_e^2 / a_{cx} kT$.

Note that technically the integration over impact parameters should stop at the Debye length

$$\lambda_D = \sqrt{\frac{kT}{4\pi n_e q_e^2}} \approx 398 \left(\frac{T_2}{n_e / 0.03 \mathrm{cm}^{-3}} \right)^{1/2}. \tag{8.130}$$

We will see below, however, that the integrand vanishes exponentially for

$$b > v/\omega \approx 4.5 \times 10^{-6} a_{-7}^{5/2} \sqrt{\frac{m_\mathrm{H}}{m_i}} \frac{v}{v_\mathrm{th}} \frac{\omega_\mathrm{th}}{\omega} \ \mathrm{cm} \tag{8.131}$$

which is much smaller than the Debye length. Converting this into an excitation coefficient, we find

$$G_p = \frac{n_i}{n_\mathrm{H}} \sqrt{\frac{m_i}{m_\mathrm{H}}} \left(\frac{Z_i q_\mathrm{e} \mu_\perp}{a_{cx}^2 kT} \right)^2 \times g_p \left(\psi, \sqrt{\frac{m_i a_{cx}^2}{2kT}} \omega \right), \tag{8.132}$$

where

$$g_p(\psi, \Omega) \equiv \int_0^\infty 2u \mathrm{e}^{-u^2} \mathrm{d}u \int_{\frac{b_\mathrm{max}}{a_{cx}}}^\infty \frac{\mathrm{d}c}{c} \mathcal{I} \left(\frac{\Omega c}{u}, e, Z_g \right), \tag{8.133}$$

where the eccentricity is given by

$$e = \sqrt{1 + \left(\frac{2cu^2}{\psi} \right)^2}. \tag{8.134}$$

Note that we recover DL98b result[10] in the limit $\mathcal{I} = 1$.

This expression has to be averaged over the grain charge and summed over all present ions.

Straight line limit for $\mathcal{I}$

In the limit $e \to \infty$, it is easier to express the integrals as a function of time, using

$$\cos\alpha = \frac{y}{\sqrt{y^2 + z^2}} = \frac{b}{\sqrt{b^2 + (vt)^2}}, \tag{8.135}$$

$$\sin\alpha = \frac{v\ t}{\sqrt{b^2 + (vt)^2}}, \quad \text{and} \tag{8.136}$$

$$\mathrm{d}\alpha = \frac{1}{1 + \left(\frac{vt}{b}\right)^2} \frac{v}{b} \mathrm{d}t. \tag{8.137}$$

In this case, the first integral for $\mathcal{I}$ reduces to

$$\int \cos\omega t \cos\alpha \, \mathrm{d}\alpha = \frac{v}{b} \int_0^\infty \frac{\cos\omega t \, \mathrm{d}t}{[1 + (vt/b)^2]^{3/2}} = \frac{\omega b}{v} K_1 \left(\frac{\omega b}{v} \right), \tag{8.138}$$

[10] DL98b include a term due to the parallel component of $\boldsymbol{\mu}$ which is not relevant as it only leads to excitation perpendicular to $\boldsymbol{\omega}$.

where K_1 is a modified Bessel function of the second kind. [Here we used Eq. (9.6.25) of Ref. [169] with $\nu = 1$, $z = 1$, and $x = \omega b/v$.] The other integral is

$$\int \sin\omega t \sin\alpha \, \mathrm{d}\alpha = \frac{v}{b}\int_0^\infty \frac{vt}{b}\frac{\sin\omega t}{[1+(vt/b)^2]^{3/2}}\mathrm{d}t = \int_0^\infty \frac{\tau \sin x\tau \, \mathrm{d}\tau}{(1+\tau^2)^{3/2}}, \tag{8.139}$$

where $x = \omega b/v$. Since $\tau(1+\tau^2)^{-3/2}$ is the derivative of $-(1+\tau^2)^{-1/2}$, we can integrate by parts and find

$$\left.\frac{-\sin x\tau}{\sqrt{1+\tau^2}}\right|_0^\infty + \int_0^\infty \frac{x\cos x\tau \, \mathrm{d}\tau}{\sqrt{1+\tau^2}}. \tag{8.140}$$

The boundary terms evaluate to zero, and the second integral can again be evaluated to $xK_0(x)$ using Eq. (9.6.25) of Ref. [169] with $\nu = 0$ and $z = 1$. Thus we have

$$\mathcal{I} = x^2[K_0^2(x) + K_1^2(x)], \qquad x = \frac{\omega b}{v}. \tag{8.141}$$

Note that when $\omega \to 0$ we recover DL98b result, i.e.,

$$\mathcal{I}\left(\frac{\omega b}{v} = 0, e \to \infty, Z_g\right) = 1. \tag{8.142}$$

We moreover have an exact functional shape for the cutoff at large rotation rates.

Non-rotating grain limit for $\mathcal{I}$

It is straightforward to show that

$$\mathcal{I}\left(\frac{\omega b}{v} = 0, e\right) = 1 - \frac{1}{e^2} \tag{8.143}$$

for both positively and negatively charged grains. Thus, the nearly parabolic trajectories $e - 1 \ll 1$ are suppressed by a factor $\sim 2(e-1)$.

The numerical calculation of $\mathcal{I}$ in the general case is tricky because it involves integrating an oscillating function, the frequency of which goes to infinity at one limit of the integral, as $t(\alpha \to \alpha_e) \to \infty$. We refer the reader to Appendix 8.A for the description of the method used for numerical computation. Fig. 8.5 shows the resulting dimensionless torques. An important feature is that for negatively charged grains, ions with nearly parabolic trajectories may co-rotate with the grain which results in an enhanced torque.

8.6.2 Neutral grain

The exact calculation of the trajectory in the electric dipole potential and the "image charge potential" is intractable analytically, and would require a heavy numerical calculation. Therefore, we

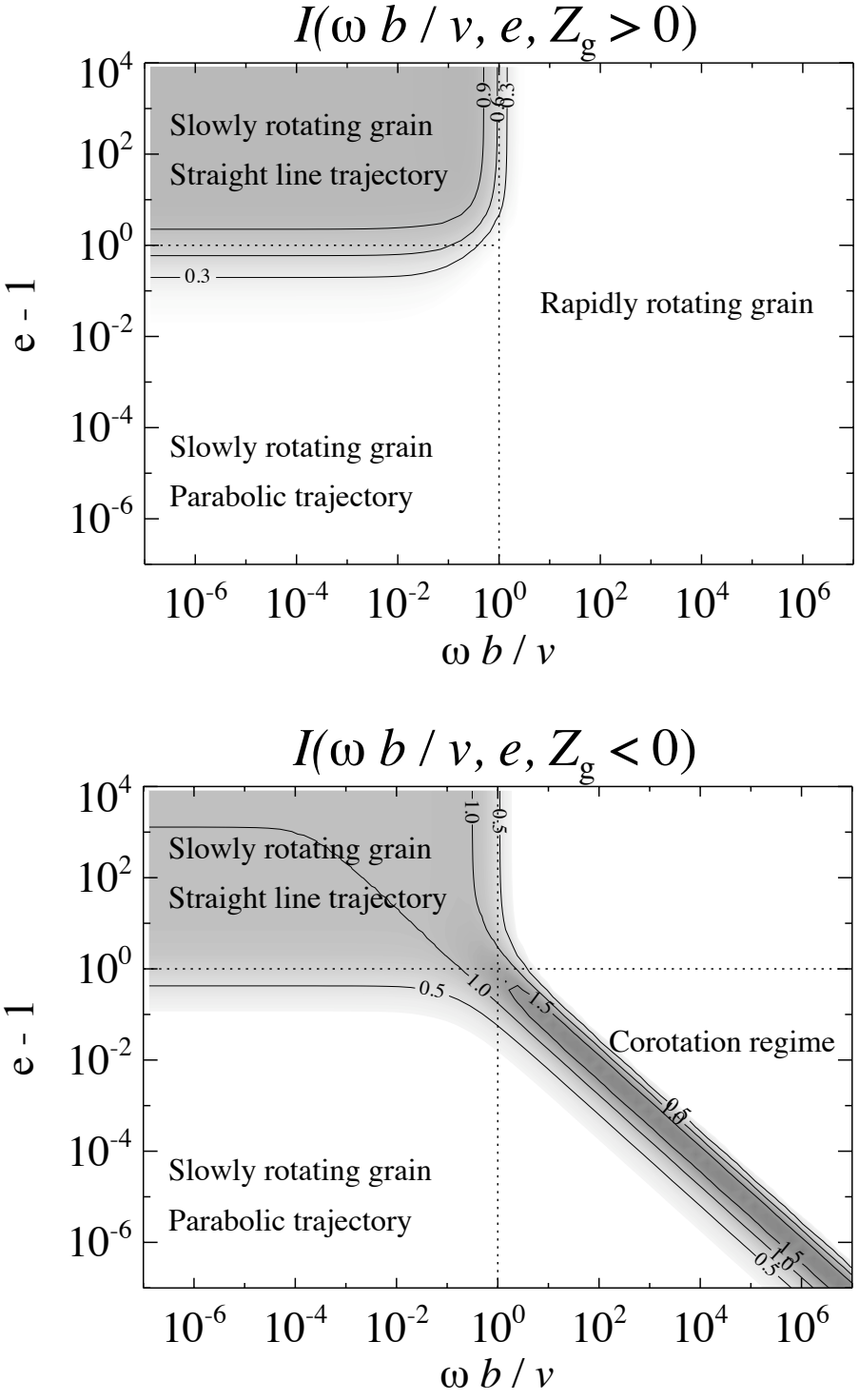

Figure 8.5: Contour levels of $\mathcal{I}(\frac{\omega b}{v}, e, Z_g > 0)$ (top panel) and $\mathcal{I}(\frac{\omega b}{v}, e, Z_g < 0)$ (bottom panel). Both show that $\mathcal{I}$ goes to unity for slowly rotating grain, straightline trajectories, and vanishes for rapidly rotating grains or nearly parabolic trajectory. In the case of negatively charged grains, though, there is a visible co-rotation regime, where $e - 1 \ll 1$ and $\omega b/v(e-1) \sim 1$, for which the ion and the grain approximately co-rotate, enhancing the torque given to the grain.

will make the following simplifications. First, we neglect the effect of the electric dipole moment on the trajectory. This assumption is somewhat cavalier, as we saw previously that the electric dipole moment may significantly affect the ion trajectory in the case of a neutral grain. Furthermore, although trajectories in the "image charge potential" will be curved in general, we will consider them to be straight lines. Thus, we will approximate the torque given to the grain by Eq. (8.126), where $\mathcal{I}$ is given by Eq. (8.141). Colliding trajectories should not be taken into account for the plasma drag excitation rate. Thus, we integrate the torque only over trajectories with impact parameter $b > b_{\max}(v)$, with

$$b_{\max} = a_{cx}\sqrt{1+\frac{\phi}{u}} \tag{8.144}$$

(see DL98b Eq. (B24) and the definition of ϕ Eq. (8.102)). Therefore, in the case of neutral grains, we have

$$G_p(Z_g=0) = \frac{n_i}{n_{\rm H}}\sqrt{\frac{m_i}{m_{\rm H}}}\left(\frac{Z_i q_{\rm e}\mu_\perp}{a_{cx}^2 kT}\right)^2 \times \tilde{g_p}\left(\phi, \sqrt{\frac{m_i a_{cx}^2}{2kT}}\omega\right), \tag{8.145}$$

where

$$\tilde{g_p}\left(\phi,\Omega\right) \equiv \int_0^\infty 2u\mathrm{e}^{-u^2}\mathrm{d}u \int_{\frac{b_{\max}}{a_{cx}}}^\infty \frac{\mathrm{d}c}{c}\mathcal{I}\left(\frac{\Omega c}{u}, e\to\infty\right). \tag{8.146}$$

The inner integral can in fact be evaluated analytically, and Eq. (8.146) can be simplified to[11]

$$\tilde{g_p}\left(\phi,\Omega\right) = 2\Omega\int_0^\infty \sqrt{1+\frac{\phi}{u}}\,K_0\left(\frac{\Omega}{u}\sqrt{1+\frac{\phi}{u}}\right)K_1\left(\frac{\Omega}{u}\sqrt{1+\frac{\phi}{u}}\right)\mathrm{e}^{-u^2}\mathrm{d}u. \tag{8.147}$$

Eq. (8.147) does not have a simple analytic form in the general case. We can however get simple analytic estimates in limiting cases. We first notice that $\phi \approx 18 a_{-7}^{-1/2} T_2^{-1/2} \gg 1$, and therefore for the smallest grains, we have:

$$\tilde{g_p}\left(\phi,\Omega\right) \approx 2\Omega\sqrt{\phi}\int_0^\infty \frac{1}{\sqrt{u}}K_0\left(\frac{\Omega\sqrt{\phi}}{u^{3/2}}\right)K_1\left(\frac{\Omega\sqrt{\phi}}{u^{3/2}}\right)\mathrm{e}^{-u^2}\mathrm{d}u. \tag{8.148}$$

We then obtain that

$$\tilde{g_p}(\Omega\sqrt{\phi}\ll 1) \approx \ln\left(\frac{2}{\Omega\sqrt{\phi}}\right) - \frac{7}{4}\gamma, \tag{8.149}$$

where $\gamma \approx 0.5774$ is Euler's gamma constant, and

$$\tilde{g_p}(\Omega\sqrt{\phi}\gg 1) \approx 6.7(\Omega\sqrt{\phi})^{2/7}\mathrm{e}^{-2.9(\Omega\sqrt{\phi})^{4/7}}. \tag{8.150}$$

We therefore see that rotational excitation by the plasma is exponentially suppressed for grains with rotation rate larger than $\omega_{\max} \sim \sqrt{2kT/(m_i a^2\phi)} \sim 3\times 10^{11}\ T_2^{3/2} a_{-7}^{-3/4}\ \mathrm{sec}^{-1}$.

The normalized excitation rate for plasma drag for cold neutral medium conditions, Eq. (8.176),

[11] This simplification is not present in the published paper.

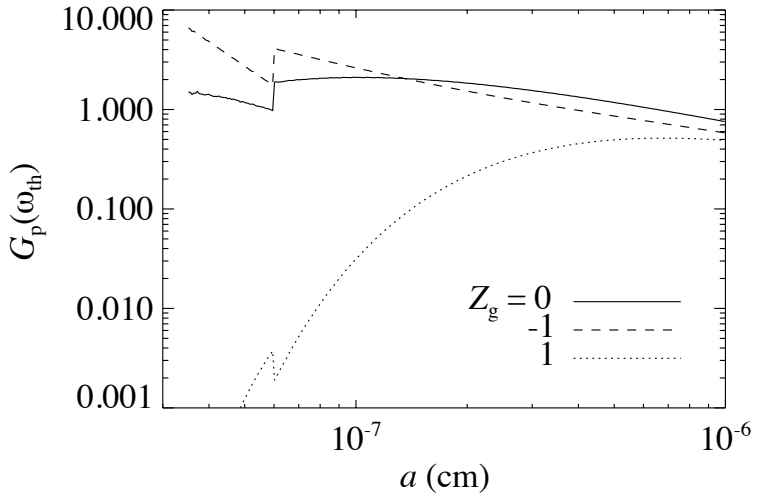

Figure 8.6: Normalized excitation rate due to plasma drag $G_p(\omega_{\rm th})$ for a neutral grain, a positively charged grain, and a negatively charged grain in CNM conditions [Eq. (8.176)], evaluated at the thermal rotation rate $\omega_{\rm th} = (2kT/I)^{1/2}$. All of them are lower than estimated by DL98b. It is clear that the positively charged grains are much less excited than the neutral and negatively charged grains. The kink at 6Å is due to the change of grain shape.

is shown in Fig. 8.6.

8.7 Infrared emission

A dust grain absorbs visible and ultraviolet light and re-emits it in the infrared. A rotating grain will also radiate angular momentum, which damps its rotation. DL98b compute this damping rate by modeling the grain as composed of six rotating dipoles. We give here a more accurate calculation, using the correlation functions of the dipole moment in the grain frame. Our result is a factor of two greater than that of DL98b. We present a classical calculation in this section.

The rates of emission of energy and of angular momentum by a varying electric dipole moment:

$$\dot{E} = \frac{2}{3c^3}\ddot{\boldsymbol{p}}^2 \quad \text{and} \quad \dot{\boldsymbol{L}} = \frac{2}{3c^3}\dot{\boldsymbol{p}} \times \ddot{\boldsymbol{p}}. \tag{8.151}$$

We denote the coordinates of the dipole moment in the frame co-rotating with the grain with unprimed indices, and the ones in the "lab frame" with primed indices. Take a grain rotating around the z-axis, without precession, with angular frequency ω. We have

$$p_x{}' = \cos\omega t\ p_x - \sin\omega t\ p_y, \tag{8.152}$$

$$p_y{}' = \sin\omega t\ p_x + \cos\omega t\ p_y, \tag{8.153}$$

$$p_z{}' = p_z. \tag{8.154}$$

A straightforward calculation leads to the following expressions in the lab frame :

$$\begin{aligned}\ddot{\boldsymbol{p}}^2 &= \ddot{p}_x^2+\ddot{p}_y^2+\ddot{p}_z^2+4\omega\left(\dot{p}_x\ddot{p}_y-\dot{p}_y\ddot{p}_x\right)+\omega^2\left[4\left(\dot{p}_x^2+\dot{p}_y^2\right)-2\left(p_x\ddot{p}_x+p_y\ddot{p}_y\right)\right]\\ &+ 4\omega^3\left(p_x\dot{p}_y-p_y\dot{p}_x\right)+\omega^4\left(p_x^2+p_y^2\right)\end{aligned} \tag{8.155}$$

and

$$\left(\dot{\boldsymbol{p}}\times\ddot{\boldsymbol{p}}\right)_z=\dot{p}_x\ddot{p}_y-\dot{p}_y\ddot{p}_x+\omega\left[2\left(\dot{p}_x^2+\dot{p}_y^2\right)-\left(p_x\ddot{p}_x+p_y\ddot{p}_y\right)\right]+3\omega^2\left(p_x\dot{p}_y-p_y\dot{p}_x\right)+\omega^3\left(p_x^2+p_y^2\right). \tag{8.156}$$

Since we are interested in the statistical properties of the emission, we define the unequal-time dipole moment correlation function in grain coordinates,

$$C_{ij}(\tau)\equiv\left\langle\left(p_i(t)-\langle p_i\rangle\right)\left(p_j(t+\tau)-\langle p_j\rangle\right)\right\rangle, \tag{8.157}$$

where $\langle p_i\rangle=\mu_i$ is just the constant dipole moment of the grain. We further assume statistical spherical symmetry of the dipole moment in the grain coordinates, i.e., $C_{ij}=C\delta_{ij}$. (For a planar grain, the values of the correlation functions depend on the in-plane or out-of-plane character of the vibrational modes and may be anisotropic. However if the infrared emission arises during thermal spikes when the grain is not rotating around its axis of greatest angular momentum, we expect the isotropic analysis to be a good approximation.) The average values of the previous formulae then become[12]

$$\langle\ddot{\boldsymbol{p}}^2\rangle=3C''''(0)-12\omega^2C''(0)+2\omega^4C(0) \tag{8.158}$$

and

$$\langle\dot{\boldsymbol{p}}\times\ddot{\boldsymbol{p}}\rangle_z=-6\omega C''(0)+2\omega^3C(0), \tag{8.159}$$

where $'$ denotes the derivative of the correlation function with respect to τ.

The Wiener-Khintchine Theorem relates the correlation functions to the spectral density S_ν, $C(\tau)=\int_0^\infty S_\nu\cos(2\pi\nu\tau)\mathrm{d}\nu$ (see for example Ref. [162]). Plugging back into Eqs. (8.158) and (8.159), we get

$$\langle\ddot{\boldsymbol{p}}^2\rangle=\int_0^\infty\left[3(2\pi\nu)^4+12\omega^2(2\pi\nu)^2+2\omega^4\right]S_\nu\,\mathrm{d}\nu \tag{8.160}$$

and

$$\langle\dot{\boldsymbol{p}}\times\ddot{\boldsymbol{p}}\rangle_z=\int_0^\infty\left[6\omega(2\pi\nu)^2+2\omega^3\right]S_\nu\,\mathrm{d}\nu. \tag{8.161}$$

Now making use of the assumption that the grain rotates slowly, i.e., that $\nu_{rot}\equiv\omega/2\pi\ll\nu_0\equiv$ typical frequency of emission, in the infrared, we get, at the lowest order in ν_{rot}/ν_0, the average

[12] Expectation values of derivatives such as $\langle\dot{p}_x^2\rangle$ can be expressed in terms of correlation functions via integration by parts. In this case, $\langle\dot{p}_x^2\rangle=\langle\frac{\mathrm{d}}{\mathrm{d}t}(p_x\dot{p}_x)\rangle-\langle p_x\ddot{p}_x\rangle$. The first term vanishes for a stationary process, and the second is $-C''(0)$.

total power and average total rate of radiation of angular momentum:

$$\left\langle \frac{\mathrm{d}E}{\mathrm{d}t} \right\rangle = \frac{2}{3c^3}\langle \ddot{\vec{p}}^2 \rangle = \frac{2}{c^3}\int_0^\infty (2\pi\nu)^4 S_\nu \,\mathrm{d}\nu \tag{8.162}$$

and

$$\left\langle \frac{\mathrm{d}L_z}{\mathrm{d}t} \right\rangle = \frac{2}{3c^3}\left\langle \dot{\boldsymbol{p}} \times \ddot{\boldsymbol{p}} \right\rangle_z = \frac{4\omega}{c^3}\int_0^\infty (2\pi\nu)^2 S_\nu \,\mathrm{d}\nu. \tag{8.163}$$

If one knows the infrared power radiated per steradian per frequency interval F_ν, such that

$$\left\langle \frac{\mathrm{d}E}{\mathrm{d}t} \right\rangle = 4\pi\int_0^\infty F_\nu \,\mathrm{d}\nu, \tag{8.164}$$

one can deduce the rate of angular momentum loss through infrared emission:

$$\left\langle \frac{\mathrm{d}L_z}{\mathrm{d}t} \right\rangle = \frac{2\omega}{\pi}\int_0^\infty \frac{F_\nu}{\nu^2} \,\mathrm{d}\nu. \tag{8.165}$$

This result is twice as big as the one given in DL98b. [The difference occurs because DL98b modeled the dipole fluctuations with six uncorrelated rotating dipoles, one rotating each direction in the xy, yz, and xz planes. They counted the radiated power from all six of these, but only considered the angular momentum loss from two of them (in the xy plane). The dipoles rotating in the xz and yz planes containing the rotation axis also emit net angular momentum however, and if they are considered one recovers the factor of 2.]

This classical treatment does not predict the rotational excitation from the recoil given by individual photons, which is a quantum effect. Each photon has a rotational quantum number $J = 1$, which corresponds to an angular momentum squared $L_\gamma^2 = \hbar^2 J(J+1) = 2\hbar^2$. We therefore have[13]

$$\left\langle \frac{\mathrm{d}\Delta L^2}{\mathrm{d}t} \right\rangle = 3\left\langle \frac{\mathrm{d}\Delta L_z^2}{\mathrm{d}t} \right\rangle = \frac{\mathrm{d}N_{\mathrm{phot}}}{\mathrm{d}t}\; 2\hbar^2 = \frac{2h}{\pi}\int_0^\infty \frac{F_\nu}{\nu} \,\mathrm{d}\nu. \tag{8.166}$$

The normalized damping and excitation rates are then

$$\begin{aligned} F_{\mathrm{IR}} &= \frac{2\tau_{\mathrm{H}}}{\pi I}\int_0^\infty \frac{F_\nu}{\nu^2}\, d\nu \quad \text{and} \\ G_{\mathrm{IR}} &= \frac{h}{3\pi I}\frac{\tau_{\mathrm{H}}}{kT}\int_0^\infty \frac{F_\nu}{\nu} \,\mathrm{d}\nu. \end{aligned} \tag{8.167}$$

We calculate the infrared emissivity of PAHs and small carbonaceous grains using the"thermal continuous" approximation, described in DL01. They indeed show that this treatment leads to spectra very close to those predicted by the exact statistical treatment, and has the advantage of being computationally much faster. We obtain the steady-state energy distribution function and then get the infrared emissivity, as explained in DL01.

[13]This factor of 2 was not included in the original paper and was pointed out in Ref. [170].

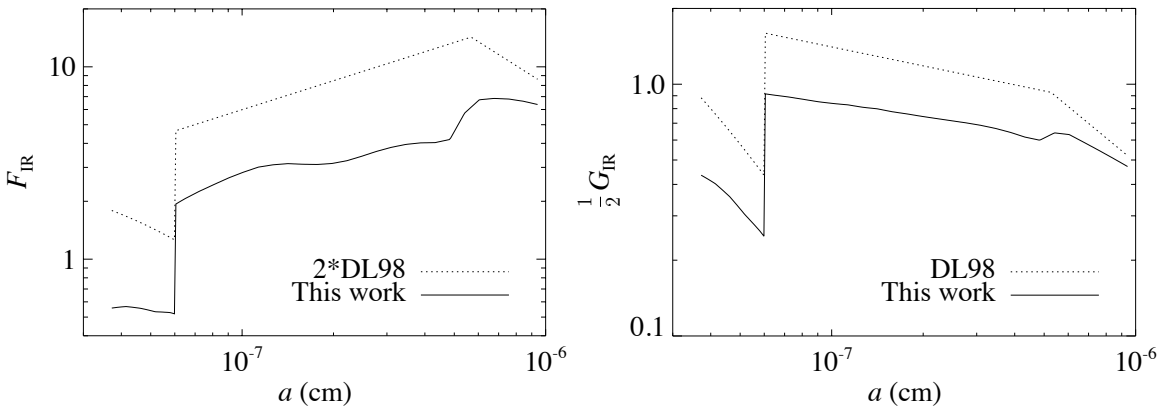

Figure 8.7: Infrared emission damping and excitation coefficients $F_{\rm IR}$, $G_{\rm IR}$, in CNM conditions [Eq. (8.176)], compared with the result of DL98b. The difference is mainly due to differences in grain absorption efficiencies and the calculation of the infrared spectrum. We used absorption efficiencies from Ref. [171] and the model of DL01 to compute the infrared emissivity. The kink at 50 Å in our result is due to a change in optical properties of dust grains. The kink around 50 Å in the DL98b result is due to the change from constant temperature limit (larger grains) to thermal spikes limit (smaller grains). The fact that they coincide is purely chance, and would not be necessarily the case for other environmental conditions. The discontinuity at 6Å is due to the change in grain shape. *Note*: we have plotted $\frac{1}{2}G_{\rm IR} = G_{\rm IR,old}$, which is the result initially used in the paper before we pointed out the missing factor of 2 in Ref. [170]. The correct $G_{\rm IR}$ is now used in the code.

We checked numerically that we recover the result of DL98b for low values of the radiation field intensity: $F_{\rm IR}$, $G_{\rm IR} \propto \chi$. However, their result for high values of the radiation field ($F_{\rm IR} \propto \chi^{2/3}$, $G_{\rm IR} \propto \chi^{5/6}$) relies on the fact that the absorption efficiency $Q_\nu \propto \nu^2$ at the characteristic frequencies of infrared emission. This is not valid anymore for intense radiation fields, which offset the emission spectrum to higher frequencies, where the absorption efficiency has not a simple dependence on frequency anymore. We show the resulting infrared emission and damping coefficients in Fig. 8.7.

8.8 Photoelectric emission

An electron ejected from the grain carries away an angular momentum along the rotation axis (z-axis) equal to:

$$\Delta L_z = m_e \rho \left(v'_\phi - \rho\omega \right), \tag{8.168}$$

where v'_ϕ is its tangential velocity in the grain frame. From this we deduce that

$$F_{pe} = \frac{m_e}{m_{\rm H}} \frac{J_{pe}}{2\pi a_s^2 n_{\rm H} \sqrt{2kT/\pi m_{\rm H}}}, \tag{8.169}$$

where J_{pe} is the photoemission rate and was described in Section 8.3.4. The excitation rate can be obtained by first noticing that the rotational velocity is much smaller than the velocity of ejected

electrons:

$$a\omega \ll v'_\phi \tag{8.170}$$

so that we have, up to small corrections

$$\Delta L_z^2 = m_e^2 \rho^2 v_\phi'^2. \tag{8.171}$$

We assume a cosine-law directional distribution for escaping electrons, so that $\langle v_\phi'^2 \rangle = \frac{1}{4} v_e^2$, where we denote v_e the average velocity of the electron at the grain surface. The latter satisfies

$$\frac{1}{2} m_e v_e^2 - \frac{(Z_g + 1) q_{\rm e}^2}{a_s} = E_{pe}, \tag{8.172}$$

where E_{pe} is the average energy at infinity of the photoejected electron. We finally get

$$\langle \Delta L_z^2 \rangle = m_e^2 \frac{2}{3} \frac{a_{cx}^4}{a_s^2} \frac{1}{4} v_e^2 = \frac{m_e}{3} \frac{a_{cx}^4}{a_s^2} \left[E_{pe} + \frac{(Z_g + 1) q_{\rm e}^2}{a_s} \right]. \tag{8.173}$$

So the normalized excitation rate is

$$G_{pe} = \frac{m_e}{4 n_{\rm H} \left(8\pi m_{\rm H} kT \right)^{1/2} a_s^2 kT} \left[\Gamma_{pe} + \frac{(Z_g + 1) q_{\rm e}^2}{a_s} J_{pe} \right], \tag{8.174}$$

where Γ_{pe} is the heating rate due to photoemission of electrons, obtained from Ref. [157].

8.9 Random H_2 formation

DL98b showed that the random formation of H_2 molecules on the grain surface does not make a major contribution to rotational excitation. We use their result:

$$G_{\rm H_2} = \frac{\gamma}{4} (1 - y) \frac{E_f}{kT} \left[1 + \frac{\langle J(J+1) \rangle \hbar^2}{2 m_{\rm H} E_f a_x^2} \right], \tag{8.175}$$

where γ is the efficiency of H_2 formation, $y = 2 n_{\rm H_2} / n_{\rm H}$, $E_f \approx 0.2$eV is the average translational kinetic energy of the nascent H_2, and $\langle J(J+1) \rangle \approx 10^2$ gives its average angular momentum.

8.10 Resulting emissivity and effect of various parameters[14]

Throughout this section and unless otherwise stated, we will take as a fiducial environment the CNM parameters specified by

$$n_{\rm H} = 30 \text{ cm}^{-3},\ T = 100 \text{ K},\ x_{\rm H} \equiv \frac{n({\rm H}^+)}{n_{\rm H}} = 10^{-3},\ x_{\rm C} \equiv \frac{n({\rm C}^+)}{n_{\rm H}} = 3\times10^{-4},\ \chi \equiv \frac{u}{u_{\rm ISRF}} = 1,\ \gamma = 0. \tag{8.176}$$

We also take the rms intrinsic dipole moment to be

$$\langle \mu_i^2 \rangle^{1/2} \left(a = 10^{-7}{\rm cm}\right) = 9.3 \text{ Debye}. \tag{8.177}$$

For the size distribution parameters, we use those given by Ref. [156] for a ratio of visual extinction to reddening $R_V = 3.1$, and a carbon abundance in the log-normal distributions $b_C = 6\times10^{-5}$.

This section is intended to give some intuition into the effect of various parameters on the spinning dust spectrum. However, the reader should keep in mind that environment parameter space is many-dimensional, and changing several parameters at once may lead to modifications that are not superpositions of the effects described here.

8.10.1 General shape of the rotational distribution function

The rotational distribution function is obtained as described in Section 8.4. We remind the reader that the Fokker-Planck equation is not strictly valid for the smallest grains, for which impulsive torques are important. It however still describes their rotational distribution function with more accuracy than a simple Maxwellian. Moreover, DL98b showed that impulsive torques may be neglected for grain radii $a \geq 7$Å. In Fig. 8.8, we show that the rotational distribution function obtained by the Fokker-Planck equation differs significantly from a Maxwellian. It has a sharper cutoff at high frequencies due to the proper accounting for rotational damping through electric dipole radiation.

In what follows we will analyze the effect of various parameters on the spinning dust emissivity. As can be seen from Eq. (8.38) and the expressions derived next for the normalized damping and excitation rates, the rotational distribution function has complex dependencies on all grain and environmental parameters. To get some intuition on the physics of spinning dust and the influence of each parameter, we will rely on a simplified expression for the rotational distribution function in the following sections:

$$f_a(\omega) \propto \exp\left(-\frac{F}{G}\frac{I\omega^2}{2kT} - \frac{\tau_{\rm H}}{3G\tau_{\rm ed}}\left(\frac{I\omega^2}{2kT}\right)^2\right), \tag{8.178}$$

where we approximate the plasma drag excitation rate (which is in principle a function of ω) by the

[14] The results shown in this section use the initial estimate for $G_{\rm IR}$, which was too low by a factor of 2. This does not change any of the results qualitatively (and only very little quantitatively), and we have therefore not reproduced the whole analysis with the correct $G_{\rm IR}$.

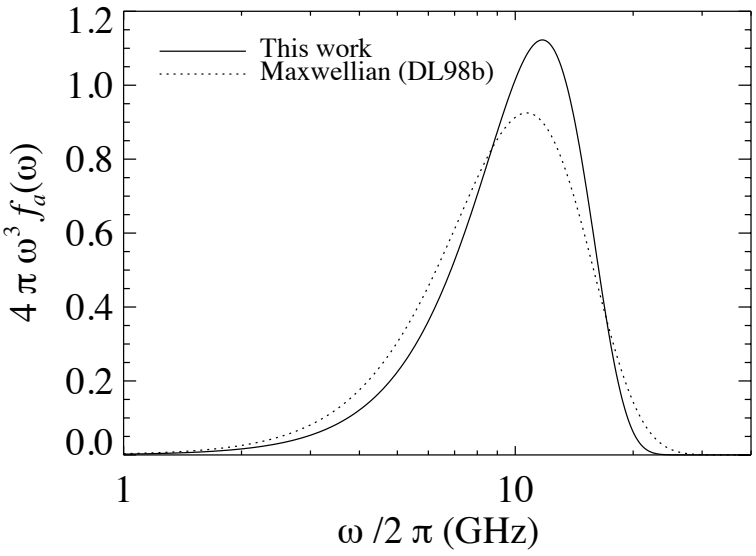

Figure 8.8: Rotational distribution function for a grain radius $a = 7$ Å, in CNM conditions, for a single value of the dipole moment $\mu_i(10^{-7}\mathrm{cm}) = 9.3$ Debye. The plot compares the solution of the Fokker-Planck equation with the DL98b Maxwellian approximation (DL98b Eq. (57) used with our F, G). Note that DL98b prescription gives $(<\omega^2>)^{1/2} = 2\pi \times 10.7$ GHz, which is in excellent agreement with the value we get, $(<\omega^2>)^{1/2} = 2\pi \times 10.9$ GHz. However, the shape of the distribution function is significantly different.

constant

$$G_p \approx G_p(\omega_{\rm th}) \quad , \quad \omega_{\rm th} \equiv \left(\frac{3kT}{I}\right)^{1/2} . \tag{8.179}$$

In our analysis we will also neglect the charge-displacement-induced dipole moment, as it has a minor contribution. Of course the actual rotational distribution function and emissivity are computed using the exact equations developed in this chapter.

For a given grain radius a and intrinsic electric dipole moment μ_i, the power radiated is $P_\nu\,(a;\mu_i) \propto \nu^6 f_a(2\pi\nu;\mu_i)$. It is straightforward, from Eq. (8.178), to show that the peak frequency is given by

$$\nu_{\rm peak} \approx \left(\frac{2}{1+\sqrt{1+\xi}}\frac{G}{F}\right)^{1/2} \frac{1}{2\pi}\sqrt{\frac{6kT}{I}}, \tag{8.180}$$

where we defined the parameter

$$\xi \equiv \frac{8G}{F^2}\frac{\tau_{\rm H}}{\tau_{\rm ed}}, \tag{8.181}$$

which denotes the non-Maxwellian character of the distribution function.

For $\xi \ll 1$, the distribution is nearly Maxwellian,

$$f_a(\omega) \propto \exp\left(-\frac{F}{G}\frac{I\omega^2}{2kT}\right), \tag{8.182}$$

and the peak frequency is given by

$$\nu_{\rm peak} \approx \left(\frac{G}{F}\right)^{1/2} \frac{1}{2\pi}\sqrt{\frac{6kT}{I}} \qquad (\xi \ll 1). \tag{8.183}$$

Moreover, the total power emitted by a single grain $j_a \propto \mu^2 \int \omega^6 f_a(\omega) {\rm d}\omega$ has the following dependence:

$$j_a \propto \mu^2 \left(\frac{G}{F}\right)^2 T^2 \qquad (\xi \ll 1). \tag{8.184}$$

For $\xi \gg 1$ the distribution is strongly non-Maxwellian[15],

$$f_a(\omega) \propto \exp\left(-\frac{\tau_{\rm H}}{3G\tau_{\rm ed}}\left(\frac{I\omega^2}{2kT}\right)^2\right), \tag{8.185}$$

and the peak frequency is given by

$$\nu_{\rm peak} \approx \left(\frac{G\tau_{\rm ed}}{2\tau_{\rm H}}\right)^{1/4} \frac{1}{2\pi}\sqrt{\frac{6kT}{I}} \qquad (\xi \gg 1). \tag{8.186}$$

The total power is then given by

$$j_a \propto \mu^2 \, \frac{G\tau_{\rm ed}}{\tau_{\rm H}} \, T^2 \qquad (\xi \gg 1). \tag{8.187}$$

In Fig. 8.9 we show the rms rotation rate $< \omega^2 >^{1/2}$ as a function of grain radius. As can be expected, the smallest grains are rotating with the greatest angular velocity, as they have the smallest moment of inertia. Consequently, they radiate at the highest frequencies, and constitute the peak of the spectrum. Therefore, we will use Eqs. (8.178) to (8.187) for a grain of radius $a_{\rm min} = 3.5$ Å to evaluate the effect of various parameters on the emissivity.

We finally remind the reader with the dependencies of characteristic timescales:

$$\tau_{\rm H} \propto n_{\rm H}^{-1} T^{-1/2} \quad , \quad \tau_{\rm ed} \propto \mu^{-2} T^{-1}. \tag{8.188}$$

8.10.2 Emissivity

Once the rotational distribution function is known, as a function of the intrinsic electric dipole moment, $f_a(\omega;\mu_i)$, one can get the power radiated by a grain of radius a by averaging over the intrinsic dipole moments Gaussian distribution $P(\mu_i)$ defined in Eq. (8.8). One gets:

$$P_\nu(a) = \int d\mu_i P(\mu_i) \, \frac{2}{3} \, \frac{\mu_\perp^2 \omega^6}{c^3} \, 2\pi \, f_a(\omega;\mu_i) \tag{8.189}$$

[15]Interestingly, Ref. [131] had already obtained a result similar to Eq. (8.185) with a Fokker-Planck equation.

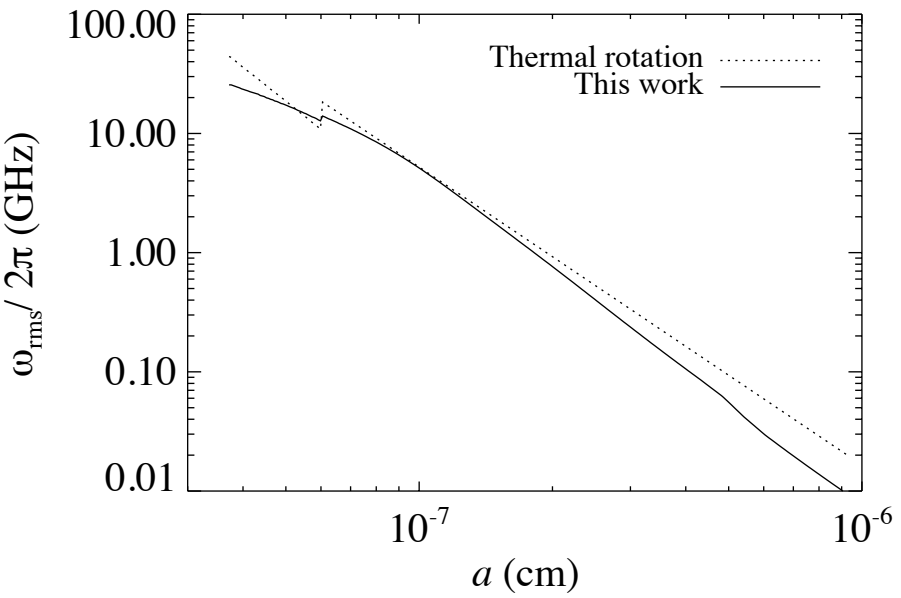

Figure 8.9: rms rotation rate $\omega_{\rm rms} \equiv < \omega^2 >^{1/2}$ as a function of grain radius a, for CNM conditions. The rotation rate the grain would achieve if it were rotating thermally (in that case $\omega_{\rm rms} = \sqrt{3kT/I}$) is also shown. It can be seen that the grains rotate sub-thermally. The kink at 6 Å is due to the change in grain geometry.

where $\mu_\perp^2 = \frac{2}{3}\mu^2$ for spherical grains, and $\mu_\perp^2 = \mu^2$ for cylindrical grains.

The overall effect of averaging over the dipole moments distribution is to broaden the spectrum, as can be seen in Fig. 8.10. The peak frequency remains approximately equal to that of $P_\nu(\mu_i = \langle\mu_i^2\rangle^{1/2})$. We will discuss the effect of the rms intrinsic dipole moment in Section 8.10.3.

The emissivity per H atom is then obtained by integrating the power radiated by each grain over the grain size distribution function, described in Section 8.3.2. The emissivity for the CNM environment is shown in Fig. 8.11. Note that the grain size distribution directly weights the spectrum, and thus needs to be known with accuracy, which is not quite the case yet for the very small grains.

8.10.3 Effect of the rms intrinsic dipole moment $\langle\mu_i^2\rangle^{1/2}$

Varying the rms intrinsic dipole moment affects the spectrum in three main ways. First, it affects the total power radiated, as $P_\nu \propto \mu^2$. Then, it affects the non-Maxwellian character of the distribution function, as $\tau_{\rm ed} \propto \mu^2$. Finally, it affects the rotational damping and excitation rates essentially through plasma drag, which has $G_p \propto \mu^2$ (the effect on G_i is not as important). Throughout the range of values considered,

$$1 \text{ Debye} < \mu_i(10^{-7} \text{ cm}) < 100 \text{ Debye}, \tag{8.190}$$

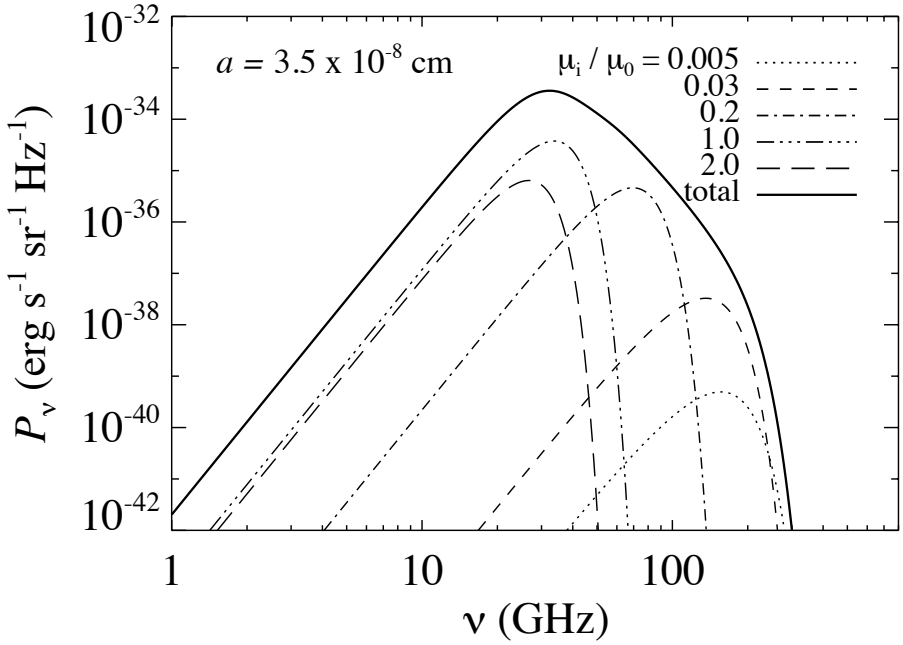

Figure 8.10: Power radiated by one grain of radius $a = 3.5$ Å in CNM conditions. The dotted and dashed lines show the contributions of various values of the intrinsic dipole moment, which is assumed to have a gaussian distribution with rms value $\mu_0 \equiv < \mu_i^2 >^{1/2}$ (a). The solid line is the total power.

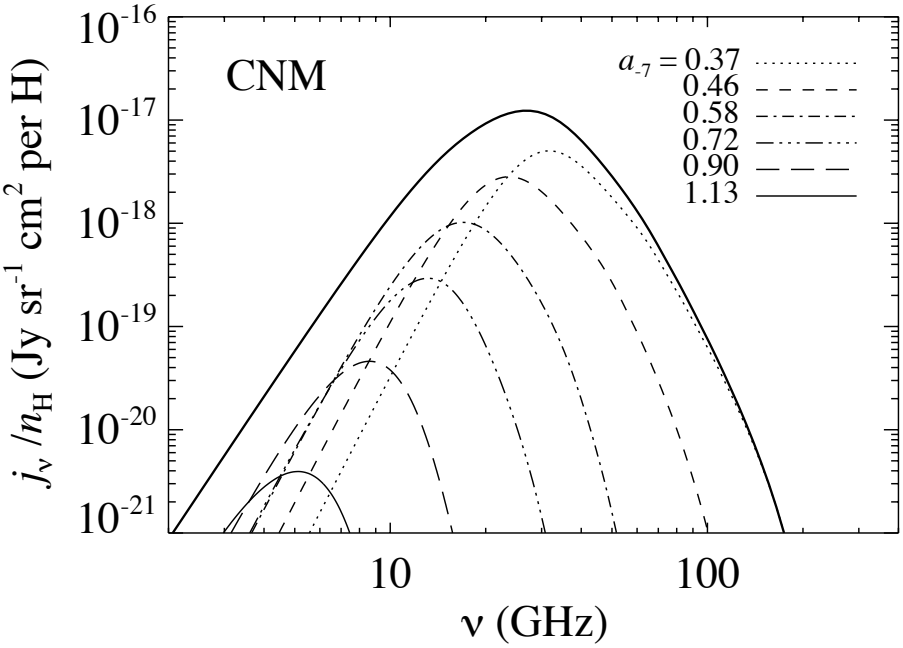

Figure 8.11: Spinning dust emissivity for CNM environment. Contributions from grains of various sizes are shown [$a_{-7} \equiv a/(10^{-7}$ cm)]. The grain size distribution parameters are taken from Ref. [156] with $R_V = 3.1$ and $b_c = 6 \times 10^{-5}$.

and in CNM conditions, the distribution function remains strongly non-Maxwellian: $\xi \gtrsim 60$. Therefore, we can use the strongly non-Maxwellian limit Eq. (8.186) to evaluate the peak frequency.

Low dipole moment limit

For low values of the electric dipole moment, plasma drag has little effect on both the rotational damping and excitation. Therefore, F and G are roughly independent of μ, and, from Eqs. (8.186), (8.187) and $\tau_{\rm ed} \propto \mu^2$, we get

$$\nu_{\rm peak}\left(\mu_i \to 0\right) \quad \propto \quad \mu_i^{-1/2}, \tag{8.191}$$

$$j/n_{\rm H}\left(\mu_i \to 0\right) \quad \to \quad \text{constant}. \tag{8.192}$$

One can see in Fig. 8.12 that Eq. (8.192) is quite accurately satisfied. The total power has a weak dependence on μ_i for low values of the intrinsic dipole moment, but is not strictly independent of it, which comes from the multiple approximations made in this analysis (neglecting the charge-displacement-induced dipole moment, and using Eq. (8.187) for the total power, after integration over the size distribution, instead of the total power radiated by a single grain).

High dipole moment limit

For high values of the electric dipole moment, plasma drag dominates both rotational damping and excitation. Therefore, $G \approx G_p \propto \mu^2$ so we get

$$\nu_{\rm peak}\left(\mu_i \to \infty\right) \quad \to \quad \text{constant}, \tag{8.193}$$

$$j/n_{\rm H}\left(\mu_i \to \infty\right) \quad \propto \quad \mu_i^2, \tag{8.194}$$

which describe approximately the behavior observed in Fig. 8.12.

8.10.4 Effect of number density $n_{\rm H}$

The main effects of the number density are:

- Changing the relative contribution of gas-induced and radiation-induced rotational damping and excitation. For very low number densities, $F_{\rm IR}$ and $G_{\rm IR} \propto \tau_{\rm H} \propto n_{\rm H}^{-1}$ dominate over other rotational damping and excitation rates. For high densities, plasma drag and collisions are dominant. Note that the charge distribution is also modified as the higher the density, the more important is collisional charging compared to photoemission. As a consequence, the grains are positively charged at low densities, and tend to be negatively charged at high densities, due to the higher rate of collisions with electrons.

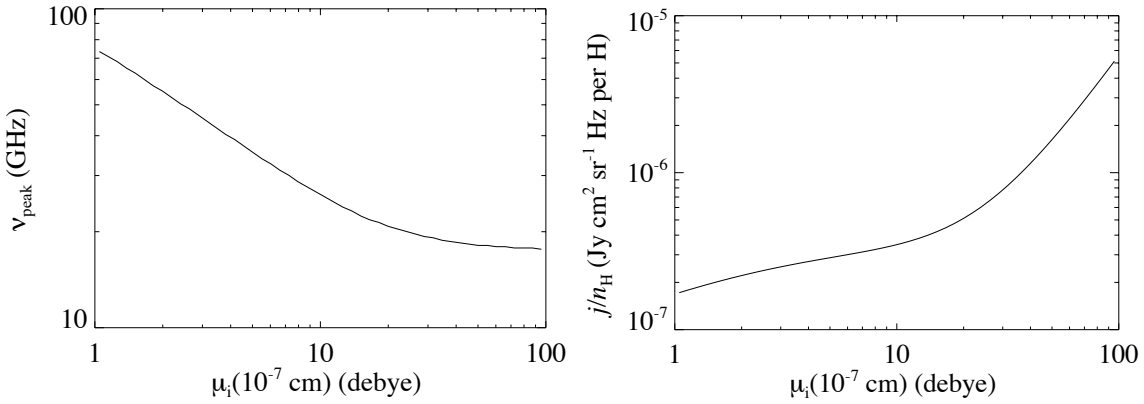

Figure 8.12: Effect of the intrinsic electric dipole moment on the peak frequency and the total spinning dust emission. Environment parameters are set to CNM conditions defined in equation (8.176). Increasing the electric dipole moment decreases the peak frequency and increases the total power radiated.

- Influencing the non-Maxwellian character of the rotational distribution function. The higher the number density, the closer is the distribution function to a Maxwellian. Numerical calculation shows that starting from CNM conditions and varying only $n_{\rm H}$, we transition to the Maxwellian regime ($\xi \lesssim 1$) if $n_{\rm H} \gtrsim 10^5$ cm^{-3}.

Low density limit

For very low number densities, the distribution is highly non-Maxwellian and we can use Eqs. (8.186) and (8.187), with $G = G_{\rm IR}$, to estimate the peak frequency and total power. As $G_{\rm IR}/\tau_{\rm H}$ is independent of $n_{\rm H}$, both the number density and total power should asymptote to a constant value. We can estimate numerically the peak frequency in CNM conditions and get:

$$\nu_{\rm peak}\left(n_{\rm H} \to 0\right) \approx 13 \text{ GHz}, \tag{8.195}$$

$$j/n_{\rm H}\left(n_{\rm H} \to 0\right) \to \text{constant}, \tag{8.196}$$

which is in good agreement with Fig. 8.13.

Intermediate densities

Over the range 10^2 cm$^{-3} \lesssim n_{\rm H} \lesssim 10^4$ cm^{-3}, gas processes are dominant over infrared emission, so F, G are roughly independent of $n_{\rm H}$. In addition, the distribution is still strongly non-Maxwellian. Using Eqs. (8.186) and (8.187), we thus find

$$\nu_{\rm peak}\left(10^2 \text{ cm}^{-3} \lesssim n_{\rm H} \lesssim 10^4 \text{ cm}^{-3}\right) \propto n_{\rm H}^{1/4}, \tag{8.197}$$

$$j/n_{\rm H}\left(10^2 \text{ cm}^{-3} \lesssim n_{\rm H} \lesssim 10^4 \text{ cm}^{-3}\right) \propto n_{\rm H}. \tag{8.198}$$

The kink around $n_{\rm H} \sim 3 \times 10^3$ cm^3 is due to our discontinuous treatment of the evaporation temperature for high densities (see Section 8.5.1.4), and to the replacement of the integration over all grain radii by a discrete summation when numerically computing the spectrum. Therefore the spectra should not be considered as very accurate in that region.

High density limit

For very high number densities, the excitation and damping is dominated by gas processes, and the electric dipole damping becomes negligibly small, so that the rotational distribution function is actually a Maxwellian, although not thermal. Using Eqs. (8.183) and (8.184), we find

$$\nu_{\rm peak}\left(n_{\rm H} \rightarrow \infty\right) \approx 150 \text{ GHz}, \tag{8.199}$$

$$j/n_{\rm H}\left(n_{\rm H} \rightarrow \infty\right) \rightarrow \text{constant}. \tag{8.200}$$

8.10.5 Effect of the gas temperature T

Temperature has a less obvious effect on the spectrum and we need to analyze in detail every damping and excitation process. It turns out the charge distribution of the smallest grains varies very little over the range of temperature considered 1 K $< T <$ 10^5 K and they remain mostly neutral throughout this interval. The distribution remains strongly non-Maxwellian for T greater than a few K.

Low temperature limit

At very low temperatures, the dominant excitation process is collisions with ions. Indeed, the grains being mostly neutral, the ions interact strongly with the electric dipole potential. As $\tilde{\mu} \propto T^{-1}$ and $\phi \propto T^{-1/2}$, one can see from Eqs. (8.107) and (8.109) that $G_i \propto T^{-2}$. Plasma drag has also $G_p \propto T^{-2}$ in principle but this becomes a shallower power law at low temperatures as the interaction timescale becomes longer than the rotation timescale. We find numerically, though, that roughly $G \propto T^{-1.5}$ as G is not strictly equal to G_i (collisions with neutrals are also significant at low temperatures). Using Eqs. (8.183), (8.184), and (8.188) we find

$$\nu_{\rm peak}\left(3 \text{ K} \lesssim \text{T} \lesssim 10^2 \text{ K}\right) \approx 35 \text{ GHz}, \tag{8.201}$$

$$j/n_{\rm H}\left(3 \text{ K} \lesssim \text{T} \lesssim 10^2 \text{ K}\right) \approx \text{constant}. \tag{8.202}$$

Note that for extremely low temperatures, the distribution would become Maxwellian, and one would get, according to Eqs. (8.186) and (8.187),

$$\nu_{\rm peak}\,(T \to 0) \quad \propto \quad T^{1/2}, \tag{8.203}$$

$$j/n_{\rm H}\,(T \to 0) \quad \propto \quad T^{2}, \tag{8.204}$$

which can be guessed at the extreme low temperature end of Fig. 8.13. Temperatures below ~ 3 K are of course unphysical, but for other environmental conditions than those of Eq. (8.176), the behavior discussed above could take place at higher, observed temperatures.

High temperature limit

At very high temperatures, collisions with neutrals are the dominant damping and excitation process. The CNM environment being mostly neutral, $F_n \to 1$ and $G_n \to 1/2$ at high temperatures ($G_n^{(ev)} \propto T_{ev}/T \to 0$). Moreover, the distribution becomes strongly non-Maxwellian, as $\xi \propto T^{1/2}$. We therefore obtain

$$\nu_{\rm peak}(T \to \infty) \quad \approx \quad 200\ T_5^{3/8}\ {\rm GHz}, \tag{8.205}$$

$$j/n_{\rm H}\,(T \to \infty) \quad \propto \quad T^{3/2}. \tag{8.206}$$

Fig. 8.13 shows that these power laws describes the behavior of the peak frequency and total power with very good accuracy.

8.10.6 Effect of the radiation field intensity χ

The radiation field affects the spectrum through only two ways. First of all, it changes the charge distribution of the grains as an increased radiation implies a higher photoemission rate. Second of all, it affects the rate of damping and excitation through infrared emission (and photoelectric emission, but this is subdominant).

Low radiation intensity limit

In a low radiation field, $F_{\rm rad}$ and $G_{\rm rad}$ become negligible. The photoemission charging rate becomes insignificant compared with collisional charging, and the charge distribution function depends only on other environment parameters. Thus, one expects the spectrum to reach an asymptotic shape for very low radiation fields. The distribution is strongly non-Maxwellian, and the dominant excitation mechanism is collisions with ions, whereas the dominant damping mechanisms are plasma drag and

collisions with neutrals. Thus, we find

$$\nu_{\rm peak}(\chi \to 0) \approx 35 \text{ GHz}, \tag{8.207}$$

$$j/n_{\rm H}\,(\chi \to 0) \to \text{constant}. \tag{8.208}$$

The kink around $\chi \sim 2 \times 10^{-2}$ is due to our discontinuous treatment of the evaporation temperature for low intensities of the radiation field. Around $\chi \approx 1 - 10$, the grain becoming more and more positively charged, collisions with ions start being less efficient, even though they remain the dominant excitation mechanism. This results in a slight decrease in both $\nu_{\rm peak}$ and $j/n_{\rm H}$.

High radiation intensity limit

In a high radiation field, $F \approx F_{\rm IR}$, and $G \approx G_{\rm IR}$. Both $F_{\rm IR}$ and $G_{\rm IR}$ are approximately (although not strictly) linear in χ, as shown in DL98b for the thermal spikes limit [see their Eqs. (31) and (44)]. Thus, $\xi \sim \chi^{-1}$ so the distribution becomes Maxwellian. The peak frequency and total emitted power are then given by Eqs. (8.183) and (8.184), which imply that

$$\nu_{\rm peak}(\chi \to \infty) \approx \text{constant}, \tag{8.209}$$

$$j/n_{\rm H}\,(\chi \to \infty) \approx \text{constant}. \tag{8.210}$$

These asymptotic forms are not strictly valid because $F_{\rm IR}$ and $G_{\rm IR}$ are not strictly linear in χ, and do not have a simple dependence on that parameter.

8.10.7 Effect of the ionization fraction $x_{\rm H}$

The hydrogen ionization fraction affects the charge distribution by modifying the contribution from collisions with protons. It also changes the contribution of collisions with ions and neutrals, and plasma drag. Characteristic timescales are left invariant, and $\xi \gg 1$ for any ionization fraction in otherwise CNM conditions.

Low ionization fraction limit

In that limit the rotational distribution function reaches an asymptotic form where collisions with protons and plasma drag due to protons can be neglected. However, there are still C^+ ions in the gas, so collisions with ions and plasma drag may still be important, although the dominant excitation process is collisions with neutrals. We find

$$\nu_{\rm peak}\,(x_{\rm H} \to 0) \approx 30\text{GHz}, \tag{8.211}$$

$$j/n_{\rm H}\,(x_{\rm H} \to 0) \to \text{constant}. \tag{8.212}$$

High ionization fraction limit

In that case collisions with ions are the dominant excitation process. Using Eqs. (8.186) and (8.187) along with $G \approx G_i \propto x_{\rm H}$, we find

$$\nu_{\rm peak}(x_{\rm H} \to 1) \approx 90(x_{\rm H}/0.1)^{1/4}{\rm GHz}, \tag{8.213}$$

$$j/n_{\rm H}\,(x_{\rm H} \to 1) \propto x_{\rm H}. \tag{8.214}$$

8.10.8 Concluding remarks

We remind the reader that all the estimates in the previous section were given by assuming that the peak frequency of the spinning dust spectrum is determined by that of the smallest grains, and that the total power follows the same dependence upon environmental parameters as the power emitted by the smallest grains. Therefore they should be taken as an aid to understand the physics of spinning dust, but not as an accurate description, which requires numerical calculations.

The overall conclusion of this section is that varying a single environmental parameter may change the peak frequency by up to an order of magnitude, and the total emitted power by several orders of magnitude. There is therefore a very large range of possible peak frequencies and total powers that can be produced by spinning dust radiation. Multiphase environments, in particular, could emit very broad spinning dust spectra. Deducing the environment parameters from an observed spectrum could therefore be a difficult task.

We show the spinning dust spectrum for various environments and compare them to the results of DL98b in Fig. 8.14.

8.11 Conclusion

We have presented a detailed analysis of the rotational excitation and damping of small carbonaceous grains. We have refined the calculations of DL98b in the case of collisions, accounting properly for the centrifugal potential which increases the net damping rate. In the case of collisions with ions, we accounted for the effect of the electric dipole potential on the collision cross section. We found that this is a small effect in the case of charged grains, but that it may significantly increase the damping and excitation rates in the case of neutral grains. We evaluated the contribution of "plasma drag" by considering hyperbolic trajectories and rotating grains in the case of charged grains, and straight lines in the case of neutral grains. We corrected the results of DL98b for the damping through infrared emission. Finally, we calculated the rotational distribution function by solving the Fokker-Planck equation.

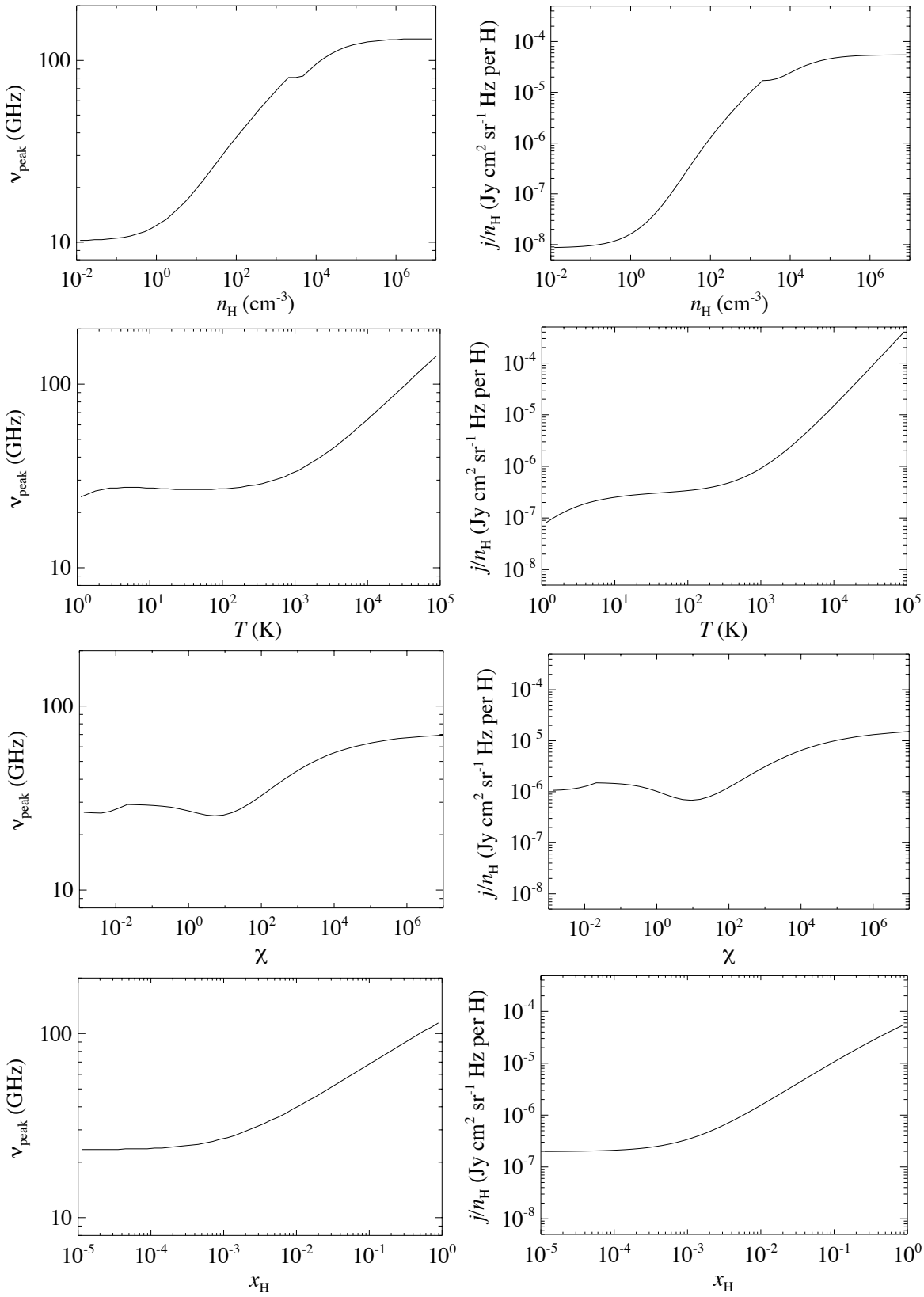

Figure 8.13: Effect of various environmental parameters on the peak frequency and the total spinning dust emission. When one parameter is varied, other environment parameters are set to CNM conditions defined in Eq. (8.176). See Sections 8.10.4 to 8.10.7 for a detailed description.

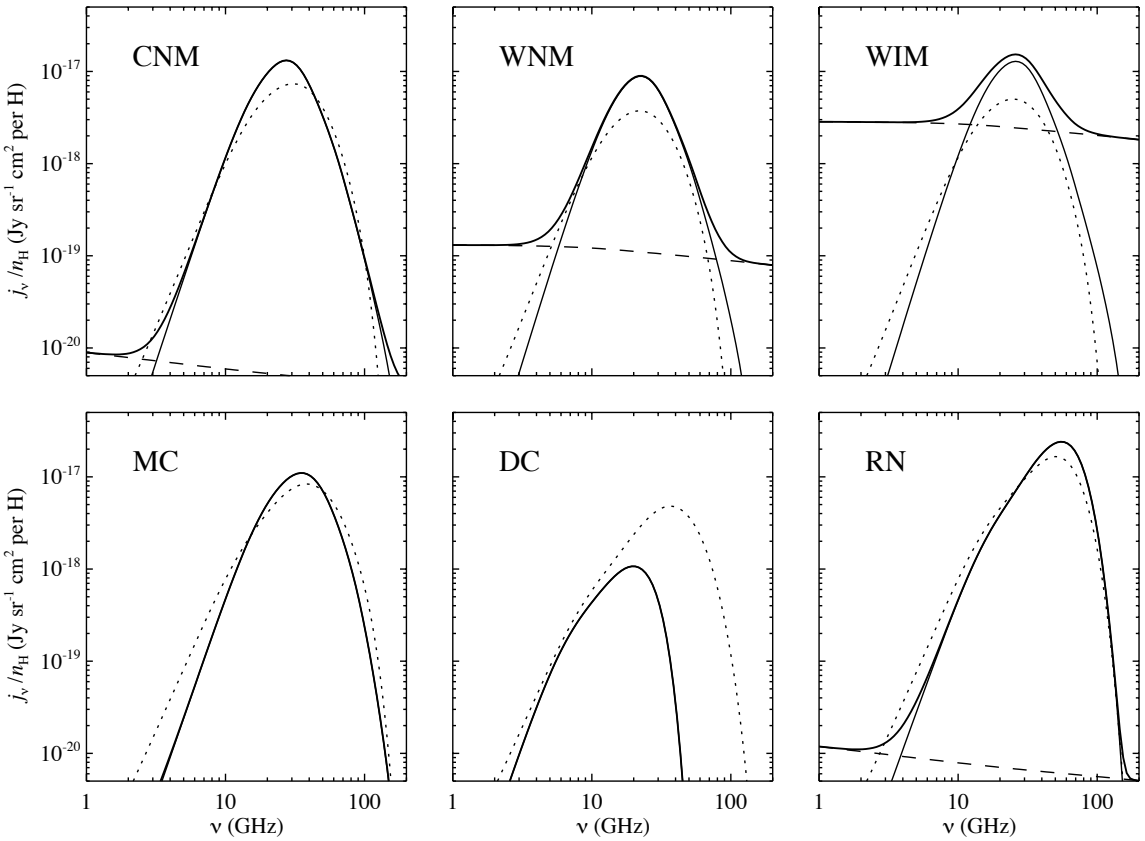

Figure 8.14: Spinning dust spectra for several environmental conditions: cold neutral medium (CNM), warm neutral medium (WNM), warm ionized medium (WIM), molecular cloud (MC), dark cloud (DC) and reflection nebula (RN). The environments are defined in DL98b, Table 1. The thin solid line is the result of our calculation, the dotted line being DL98 prediction, and the dashed line is the free-free emission (the free-free gaunt factor was taken from Ref. [150]). The parameters for the grain size distribution are: $R_V = 3.1,\ b_C = 6 \times 10^{-5}$ for the diffuse CNM, WNM and WIM environments, and $R_V = 5.5,\ b_C = 3 \times 10^{-5}$ for the dense MC, DC and RN environments. The apparent systematic increase of power around the peak frequency for our result is mainly due to the grain size distribution we use, which has an increased number of small grains compared to that used by DL98 (compare e.g. Fig. 2 from Ref. [156] with Fig. 8 from DL98b). Note that for the DC environment, for which rotational excitation and damping is dominated by collisions with neutral species (mainly H_2 molecules), DL98 prediction largely overestimates the peak frequency and total power because they underestimate the damping rate (see Eq. (8.58) and subsequent discussion).

We believe our model provides a much more accurate description of the spinning dust spectrum than previous work. However, we would like to remind the reader of its uncertainties and limitations. First, our model only computes the total intensity of the emitted radiation and not the polarization, which would require an additional study of the alignment mechanisms for PAHs. Secondly, the dust grains properties are poorly known:

- The size distribution and abundance of the smallest grains is uncertain, and in particular the nature of the cutoff at small grain sizes $a \sim a_{\rm min}$ can have a large effect on the spectrum.
- The permanent electric dipole moments of dust grains are not directly constrained by other dust observables. Given that it cannot be computed from first principles, one may regard it as a free parameter (or parameters) of the spinning dust model.

Thirdly, we made some simplified calculations in some cases, as an accurate calculation would have been intractable numerically or substantially complicated the code:

- We used the Fokker-Planck approximation, which starts to break down for our smallest grains because a single collision suffices to change the rotational state. We expect that the main consequence of a full treatment would be a tail in the emission spectrum extending to high frequencies, because impulsive collisions would be able to increase the rotation velocities of the grains to $> 2\nu_{\rm peak}$ before dissipative forces had time to act (an effect missed by the Fokker-Planck treatment). Therefore one should not place too much confidence in the many-order-of-magnitude falloff at ~ 100 GHz seen in most of our models. (In many cases this will be unimportant observationally since at high frequencies the vibrational dust contribution is dominant.)
- In the plasma drag calculation, we neglected the electric dipole potential when evaluating the trajectory of ions, taking the straight-line (neutral grain) or hyperbolic (charged grain) approximation. Relying on the study of collisions with ions, we may expect the dipole moment to have a small effect in the case of a charged grain. On the other hand, its effect in the case of a neutral grain may be more important, as in that case the electric dipole potential provides the dominant interaction.
- We assumed the evaporation temperature for the smallest grains was the "temperature" of the grain just after it has absorbed a UV photon. This is a physically motivated assumption but its validity is not established. The evaporation temperature can have a significant effect on the spectrum, as can be seen from Fig. 8.3 and one should be aware of the uncertainty in this parameter. Also, we assumed that collisions transition from being sticking to elastic, as the density exceeds a given threshold. Our model is therefore inaccurate in the transition region.

- When calculating the infrared emission spectrum of dust grains, we used the DL01 "thermal continuous" approximation, which is not very accurate to describe the low energy part of the spectrum. Whereas these uncertainties are not important if one only wants the spectrum F_ν in the mid-infrared, they may lead to significant errors when calculating the corresponding damping and excitation rates, which are proportional to $\int \nu^{-2} F_\nu \mathrm{d}\nu$ and $\int \nu^{-1} F_\nu \mathrm{d}\nu$, respectively.

- We ignored systematic torques, although this may not be a major omission for the smallest dust grains.

Despite these uncertainties, we believe that this model is the most complete thus far, and will be a useful tool for comparison to observations and testing the spinning dust hypothesis for anomalous microwave emission in various ISM phases.

In this chapter, we have assumed that the smallest, disk-like grains always rotate about their axis of greatest inertia. In the next chapter, we shall see that this assumption is in fact not correct, and that grains are more likely to have their nutation state randomized by frequent absorptions of ultraviolet photons.

8.A Appendix: numerical evaluation of $\mathcal{I}(\frac{\omega b}{v}, e, Z_g)$

The numerical evaluation of $\mathcal{I}$ [defined in Eq. (8.127)] is tricky because it involves integrating an oscillating function which frequency goes to infinity at one limit of the integral, as $t(\alpha \to \alpha_e) \to \infty$. Here we describe our implementation for both the positive and negative grain charges.

8.A.1 Positively charged grains

We first make the change of variable

$$z = \sqrt{\gamma} \cot \frac{\alpha}{2}, \tag{8.215}$$

where $\gamma = (e-1)/(e+1)$. The expression for the time is now:

$$\omega t(z) = \frac{\omega b}{v} \frac{1}{\sqrt{e^2-1}} \left(\ln \frac{z+1}{z-1} + 2e \frac{z}{z^2-1} \right). \tag{8.216}$$

The $\mathcal{I}$-integral is then

$$\mathcal{I} = 4\gamma \left[\Re \int_1^\infty \mathrm{e}^{i\omega t(z)} \frac{z^2-\gamma}{(z^2+\gamma)^2} \mathrm{d}z \right]^2 + 16\gamma^2 \left[\Im \int_1^\infty \mathrm{e}^{i\omega t(z)} \frac{z}{(z^2+\gamma)^2} dz \right]^2. \tag{8.217}$$

The functions inside the integrals are analytical on the complex plane, deprived from the branch cut $[-1,1]$ on the real axis and the two poles $\pm \mathrm{i}\sqrt{\gamma}$. The integrands are at least $\mathcal{O}(z^{-2})$ as $|z| \to \infty$. Moreover, for $y \to 0^+$,

$$\Re \left[\mathrm{i}\omega t(1-\mathrm{i}y) \right] \propto \Re \left[\mathrm{i} \ln \left(-1 + \frac{2\mathrm{i}}{y} \right) - \frac{e}{y} \right] < 0. \tag{8.218}$$

Thus, using the fact that the integral over the lower right part of the complex plane vanish, we can replace our integrals by integrals over the axis

$$z = 1 - \mathrm{i}y, \quad 0 < y < +\infty. \tag{8.219}$$

Note that for $e \to 1$, $\mathcal{I} = \mathcal{O}(e-1)$, as one may expect from almost parabolic trajectories if the grain repels the ion. Also, in the limit $\omega b/v \to 0$, $\mathcal{I} \to (e^2-1)/e^2$.

8.A.2 Negatively charged grains

This time we make the change of variable

$$z = \frac{1}{\sqrt{\gamma}} \tan \frac{\alpha}{2}. \tag{8.220}$$

The expression for the time is now

$$\omega t(z) = \frac{\omega b}{v}\frac{1}{\sqrt{e^2-1}}\left(\ln\frac{z+1}{z-1} - 2e\frac{z}{z^2-1}\right). \tag{8.221}$$

And we have:

$$\mathcal{I} = 4\gamma\left[\Re\int_1^\infty \mathrm{e}^{\mathrm{i}\omega t(z)}\frac{1-\gamma z^2}{(1+\gamma z^2)^2}\mathrm{d}z\right]^2 + 16\gamma^2\left[\Im\int_1^\infty \mathrm{e}^{\mathrm{i}\omega t(z)}\frac{z}{(1+\gamma z^2)^2}\mathrm{d}z\right]^2. \tag{8.222}$$

The functions inside the integrals are analytical on the complex plane, deprived from the branch cut $[-1,1]$ on the real axis and the two poles $\pm\mathrm{i}/\sqrt{\gamma}$. This time $\Re(i\omega t)$ is negative for z close to 1 when $\Im z > 0$. Moreover, the two poles tend to infinity when $e \to 1$ so to avoid integrating too close to the poles, we integrate over the line

$$z = 1 + \mathrm{e}^{\mathrm{i}\pi/4}y, \quad 0 < y < +\infty. \tag{8.223}$$

In that case, the integrals are not simply bounded anymore for nearly parabolic trajectories. One can show, by making the previous change of variables, that

$$\mathcal{I}\left(\frac{\omega b}{v}, e, Z_g < 0\right) = \exp\frac{2\pi\omega b}{v\sqrt{e^2-1}}\,\mathcal{I}\left(\frac{\omega b}{v}, e, Z_g > 0\right). \tag{8.224}$$

This expression is ill behaved for nearly parabolic trajectories, as the exponential factor diverges whereas the $\mathcal{I}$-integral vanishes. In order to avoid numerical problems, in the case of nearly parabolic trajectories, we make the change of variables

$$u = \left(\tan\frac{\alpha}{2}\right)^{-1}. \tag{8.225}$$

The expression for the $\mathcal{I}$-integral is then, for $e - 1 \ll 1$:

$$\begin{aligned}\mathcal{I} \approx\ & 4\left\{\int_0^{\sqrt{\frac{2}{e-1}}}\cos\left[\frac{\omega b}{v}(e-1)(u+\frac{u^3}{3})\right]\frac{u^2-1}{(u^2+1)^2}\mathrm{d}u\right\}^2 \\ & + 16\left\{\int_0^{\sqrt{\frac{2}{e-1}}}\sin\left[\frac{\omega b}{v}(e-1)(u+\frac{u^3}{3})\right]\frac{u}{(u^2+1)^2}\mathrm{d}u\right\}^2\end{aligned} \tag{8.226}$$

Note that in terms of the true anomaly f we have $u = -\tan f/2$ and the expression for the time can be found in Ref. [168], Eq. (2.3.9). Here again we integrate along $u = \mathrm{e}^{\mathrm{i}\pi/6}y$, $0 < y < \infty$, which cancels the $\mathcal{O}(u^3)$ real part of the time and maximizes its positive imaginary part at infinity. Notice that for very small eccentricities, this is mainly a function of $(\omega b/v)(e-1)$.

Chapter 9

Spinning and wobbling dust: Quantum-mechanical treatment [1]

9.1 Introduction

In the previous chapter, following DL98b, we assumed that dust grains were either spherically symmetric, or rotating about their axis of greatest inertia if they are non-spherical. Refs. [170, 172] however showed that in general ISM conditions, the rotational state of grains will be randomized due to rapid energy transfer between vibrational and rotational degrees of freedom following absorption of ultraviolet photons. Not only the emission spectrum is modified for a given total angular momentum, but also the rotational excitation and damping rates and consequently the angular momentum distribution must be re-evaluated. This is the subject of this chapter, where we compute the rotational excitation and damping rates quantum-mechanically (except for collisions). Since DL98b showed that even the smallest grains can be considered as classical rotators (their characteristic angular momentum is much larger than $\hbar$), we will take the classical limit of the rates obtained quantum-mechanically.

9.2 Rotation of a disk-like grain

Here we review the formalism to describe the rotation of a general axisymmetric grain, and the physics that determines the nutation angle distribution.

[1] This chapter follows the same idea as the paper *Spinning dust emission: the effect of rotation around a non-principal axis*, K. Silsbee, Y. Ali-Haïmoud & C. M. Hirata, Mon. Not. Roy. Astron. Soc. **411**, 2750 (2011). Most of the calculations presented in this chapter are original, unpublished work, and reproduce the results of the published paper using quantum-mechanical arguments, rather than a classical treatment. Sections 9.8 and 9.9 are reproduced from the published paper with permission, copyright (2011) by the Royal Astronomical Society.

9.2.1 General description

We focus here on the case of an oblate axisymmetric dust grain, i.e., one with principal moments of inertia $I_1 = I_2 < I_3$. For a planar grain, which is a reasonable model for a PAH, one has $I_3 = 2I_1$. In free solid-body rotation, the conserved quantities are the total angular momentum $\boldsymbol{L}$, and the total rotational energy $E_{\rm rot}$. As a consequence, the the projection of the angular momentum on the grain symmetry axis is also conserved. The energy eigenstates are determined by three quantum numbers: J [a non-negative integer such that the square of the angular momentum is $\hbar^2 J(J+1)$], K ($|K| \leq J$, the projection of $\boldsymbol{L}$ on the symmetry axis is $\hbar K$) and M ($|M| \leq J$, the projection of the angular momentum on a given reference axis is $\hbar M$). The rotational energy corresponding to the eigenstate $|J, K, M\rangle$ is

$$E_{JK} = \frac{\hbar^2}{2I_1} J(J+1) - \frac{\hbar^2}{2}\left(\frac{1}{I_1} - \frac{1}{I_3}\right) K^2. \tag{9.1}$$

Note that in the large J limit, the nutation angle θ (angle between the direction of the angular momentum $\boldsymbol{L}$ and the grain axis of symmetry) is given by $\cos\theta \approx K/J$. To simplify upcoming calculations, it will be useful to introduce the characteristic frequencies

$$\nu_1 \equiv \frac{\hbar}{4\pi I_1}, \tag{9.2}$$

$$\nu_{13} \equiv \frac{\hbar}{4\pi}\left(\frac{1}{I_1} - \frac{1}{I_3}\right), \tag{9.3}$$

so that we can rewrite the rotational energy in the eigenstate $|J, M, K\rangle$ as

$$E_{JK} = h\nu_1 J(J+1) - h\nu_{13} K^2. \tag{9.4}$$

9.2.2 Rotational configuration

For large grains, we expect that energy dissipation will bring the grain to the state of lowest energy at fixed total angular momentum, i.e., a state where the grain is rotating about the axis of greatest inertia, with $K = \pm J$ [see Eq. (9.1)]. For the smallest grains, however, the physics is different. Small grains are stochastically heated to large temperatures (because they have few degrees of freedom) by occasional absorption of ultraviolet photons (see Fig. 8.2). As they cool down by emitting infrared ro-vibrational photons, a rapid energy transfer occurs between rotational and vibrational degrees of freedom. Since the characteristic temperature of the grain (corresponding to IR frequencies) is much larger than the characteristic energy difference between rotational states (corresponding to microwave frequencies), the rotational state of the grain is completely randomized after each thermal spike. It is then important to consider how the time between thermal spikes $\tau_{\rm abs}$ compares to the timescale for changes in grain angular momentum $\tau_{\rm rot}$. The characteristic timescale between UV

Table 9.1: Characteristic timescales for UV photons absorption and rotational damping for idealized interstellar phases. The rotational damping time is shown for grains rotating about their axis of greatest inertia ("case 1", as assumed in DL98b and Ref. [173] — see Chapter 8), and for grains which are randomly oriented with respect to their angular momentum ("case 2", the subject of the present work). All values are for the smallest grains ($a = 3.5\,\text{Å}$ or $N_\text{C} = 20$).

Phase	DC	MC	CNM	WNM	WIM	RN	PDR
τ_abs (sec)	2.0×10^{11}	2.0×10^{9}	2.0×10^{7}	2.0×10^{7}	2.0×10^{7}	2.0×10^{4}	6.6×10^{3}
τ_rot (sec) [case 1]	1.6×10^{7}	9.5×10^{7}	1.9×10^{8}	2.8×10^{8}	2.1×10^{8}	7.0×10^{6}	1.4×10^{6}
τ_rot (sec) [case 2]	1.4×10^{7}	4.1×10^{7}	8.2×10^{7}	1.2×10^{8}	9.0×10^{7}	6.9×10^{6}	1.1×10^{6}

photon absorptions for a grain of volume-equivalent radius a is

$$\tau_\text{abs} = \left[\pi a^2 c \int Q_\text{abs}(a;\nu)\frac{u_\nu}{h\nu}\text{d}\nu\right]^{-1}, \tag{9.5}$$

where $u_\nu = \chi u_{\nu,\text{ISRF}}$ is the ambient radiation field and $\pi a^2 Q_\text{abs}$ is the absorption cross section.

The characteristic rotational damping (or excitation, in steady-state) timescale for such a grain is $\tau_\text{rot} \equiv L\left|\frac{\text{d}L}{\text{d}t}\right|^{-1}$, where L is the characteristic angular momentum of the grain and $\frac{\text{d}L}{\text{d}t}$ is the rotational damping rate evaluated at L. Evaluating τ_rot requires an analysis of the rotational dynamics. The analysis of Chapter 8 suggests

$$\tau_\text{rot} \approx \min\left[\frac{\tau_\text{H}}{F}, \left(\frac{\tau_\text{H}\tau_\text{ed}}{G}\right)^{1/2}\right], \tag{9.6}$$

where F and G are the normalized damping and excitation rates; and τ_H and τ_ed are the idealized characteristic damping timescales through collisions with hydrogen atoms and electric dipole radiation, respectively (see Section 8.4.2 and the next section for their precise definitions; and note that τ_ed is defined for thermally rotating grains, but that the actual dipole damping time varies depending on whether rotation is sub- or super-thermal).[2]

Since the smallest grains rotate fastest and determine the peak of the spinning dust spectrum, we evaluate the above timescales at the smallest grain size $a = 3.5\,\text{Å}$, for the idealized interstellar environments defined in DL98b, Table 1. We show these timescales in Table 9.1, for both the case of $\theta = 0$ (Chapter 8) and for randomized θ (using the formulae in this chapter).

In the diffuse ISM phases (CNM, WNM, WIM), thermal spikes occur with a rate at least ~ 4 to 6 times higher than the processes that change the grain angular momentum. The rate difference is even more pronounced in regions of high radiation intensity (RN, PDR), where the small grains can absorb several hundreds of photons during the time it takes to change their angular momentum. Therefore we expect an isotropic distribution $P(K|J) = 1/(2J+1)$ in these phases. Note that this

[2] In Eq. (9.6) the damping time is typically τ_H/F when linear drag processes dominate. When electric dipole damping dominates, e.g. in the WIM, the angular velocity is typically $(G\tau_\text{ed}/\tau_\text{H})^{1/4}$ times the thermal angular velocity $\omega_\text{th} = (kT/I_3)^{1/2}$ (see Section 8.10.1). Since electric dipole emission torque scales as ω^3 instead of ω, the actual timescale for electric dipole damping is then $\tau_\text{ed}(\omega/\omega_\text{th})^{-2}$, or $(\tau_\text{H}\tau_\text{ed}/G)^{1/2}$.

is *not* true of regions of lower radiation density (DC, MC), where thermal spikes occur every few hundreds to thousands of years and $\tau_{\rm abs} \gg \tau_{\rm rot}$. In such cases, other processes will dominate the distribution of K and the result may be in between complete isotropization (as assumed here) and perfect rotation around the I_3 axis ($|K| = J$; assumed in DL98b and Chapter 8).

9.2.3 Angular momentum distribution

The angular velocity vector $\boldsymbol{\omega}$ is no longer conserved for a non-spherical grain. The proper variable to follow is rather the total angular momentum $\boldsymbol{L}$. In the classical limit $J \gg 1$, we can see $\boldsymbol{L}$ as a continuous stochastic variable, and use the Fokker-Planck equation to compute its probability distribution. In order to maintain a simple connection with previous work, we define the variable

$$\boldsymbol{\Omega} \equiv \frac{\boldsymbol{L}}{I_3}, \tag{9.7}$$

which would be the angular velocity of the grain if if were rotating about its axis of greatest inertia. The Fokker-Planck equation for $f_a(\boldsymbol{\Omega})$ then takes the same form as that described in Section 8.4.1 for $\boldsymbol{\omega}$ and we will not repeat it here. The only subtlety is that the drift and diffusion coefficients must be averaged over the orientation of the grain:

$$D^i(\boldsymbol{\Omega}) = -\Big\langle \lim_{\delta t \to 0} \frac{\langle \delta \Omega^i \rangle}{\delta t} \Big\rangle_K \equiv -\frac{1}{2J+1} \sum_K \lim_{\delta t \to 0} \frac{\langle \delta \Omega^i \rangle}{\delta t}(\boldsymbol{\Omega}, K), \tag{9.8}$$

and similarly $E^{ij}(\boldsymbol{\Omega}) = \langle E^{ij}(\boldsymbol{\Omega}, K) \rangle_K$.

We also define the dimensionless damping and excitation coefficients, for each process X:

$$F_X(\Omega) \equiv \frac{\tau_{\rm H}}{\Omega} \tilde{D}_{\rm X}(\Omega), \tag{9.9}$$

$$G_X(\Omega) \equiv \frac{I_3 \tau_{\rm H}}{2kT} E_{||,X}(\Omega), \tag{9.10}$$

where the characteristic damping time-scale $\tau_{\rm H}$ is given by Eq. (8.29) with the replacement $I \to I_3$ and $\tilde{D}$ was defined in Eq. (8.21).

9.2.4 Form of the principle of detailed balance

In Section 8.4.1, we showed that a simple relation must be satisfied between the drift and diffusion rates due to a thermal process X with characteristic temperature T_X. One must be careful when deriving such a relation in the case of grains for which the nutation state is constantly randomized. The detailed derivation is given in Ref. [170], and we simply outline it here.

Consider the microscopic transition rates $\Gamma_X(J, K \to J', K')$ associated with a process X. If the process is thermal with temperature T_X, the transition rates must preserve the thermal probability

distribution for J and K:

$$P(J,K;T_X) \propto (2J+1)\exp\left[-\frac{\hbar^2}{2I_1 kT_X}J(J+1)\right]\exp\left[\frac{\hbar^2}{2kT_X}\left(\frac{1}{I_1}-\frac{1}{I_3}\right)K^2\right], \tag{9.11}$$

i.e., we must have the following relation between backward and forward transition rates:

$$P(J,K;T_X)\Gamma_X(J,K\rightarrow J',K') = P(J',K';T_X)\Gamma_X(J',K'\rightarrow J,K). \tag{9.12}$$

In the classical limit ($J,|K| \gg 1$) and for non-impulsive torques ($|\Delta J| = |J'-J| \ll J, |\Delta K| = |K'-K| \ll |K|$), we can Taylor-expand this relation in $\Delta J/J, \Delta K/K$. This then allows us to relate the mean rate of change of J,

$$D_J \equiv \frac{\mathrm{d}\langle\Delta J\rangle}{\mathrm{d}t} = \sum_{\Delta J,\Delta K} \Delta J\ \Gamma_X(J,K\rightarrow J+\Delta J, K+\Delta K), \tag{9.13}$$

in which contributions from ΔJ and $-\Delta J$ nearly cancel each other, to the rates of diffusion in J-space and K-space,

$$E_{JJ} \equiv \frac{\mathrm{d}\langle\Delta J^2\rangle}{\mathrm{d}t} = \sum_{\Delta J,\Delta K} \Delta J^2\ \Gamma_X(J,K\rightarrow J+\Delta J, K+\Delta K), \tag{9.14}$$

$$E_{JK} \equiv \frac{\mathrm{d}\langle\Delta J\Delta K\rangle}{\mathrm{d}t} = \sum_{\Delta J,\Delta K} \Delta J\Delta K\ \Gamma_X(J,K\rightarrow J+\Delta J, K+\Delta K). \tag{9.15}$$

The relation obtained is [170]:

$$D_J = \left(\frac{1}{2J}-\frac{\hbar^2 J}{2I_1 kT_X}\right)E_{JJ} + \frac{\hbar^2 K}{2kT_X}\left(\frac{1}{I_1}-\frac{1}{I_3}\right)E_{JK} + \frac{1}{2}\frac{\partial E_{JJ}}{\partial J} + \frac{1}{2}\frac{\partial E_{JK}}{\partial K}. \tag{9.16}$$

The next step is to relate these rates to the coefficients appearing in the Fokker-Planck equation. We recall that in the large-J limit, $\Omega \equiv |\mathbf{\Omega}| = \hbar J/I_3$. Using Eqs. (8.24) and (8.25), we obtain

$$D(\Omega,K) = -\frac{\hbar}{I_3}D_J + \frac{E_\perp(\Omega,K)}{\Omega}, \tag{9.17}$$

$$E_{||}(\Omega,K) = \frac{\hbar^2}{I_3^2}E_{JJ}. \tag{9.18}$$

The final step is to average the obtained relations over K. The final result is [170]:

$$\tilde{D} = \frac{I_3\Omega}{2kT_X}\left[\frac{I_3}{I_1}E_\parallel - \left(\frac{I_3}{I_1}-1\right)\left\langle\frac{K}{J}\frac{\hbar^2 E_{JK}}{I_3^2}\right\rangle_K\right], \tag{9.19}$$

where $\tilde{D}$ was defined in Eq. (8.21). This relation will be useful when computing the damping rate due to interaction of the passing ions with the electric dipole moment of the grain ("plasma drag").

9.3 Quantum mechanical expressions for spontaneous transition rates[3]

9.3.1 Transition frequencies

Consider a decay from the state $|J, K, M, v\rangle$ to the state $|J', K', M', v'\rangle$, where v and v' are the vibrational quantum numbers of the grain in the initial and final states. In the absence of vibration-rotation interactions, the energy of the photon associated with the transition is just $\Delta E = \Delta E_{\rm vib} + \Delta E_{\rm rot}$, where $\Delta E_{\rm vib} \equiv E_v - E_{v'}$, and the change in rotational energy $\Delta E_{\rm rot} \equiv E_{J,K} - E_{J',K'} \equiv \Delta E_{(\Delta J, \Delta K)}$ can be obtained from Eq. (9.4):

$$\Delta E_{(\Delta J,\Delta K)} = -(1 + \Delta J + 2J)\Delta J \; h\nu_1 + (\Delta K + 2K)\Delta K \; h\nu_{13} \tag{9.20}$$

$$\approx -2J\Delta J \; h\nu_1 + 2K\Delta K \; h\nu_{13}, \tag{9.21}$$

where $\Delta J \equiv J' - J$, $\Delta K \equiv K' - K$, and the second line is valid in the large-J and large-K limit.

9.3.2 Decay rates

The spontaneous transition rate from the state $|J, K, M, v\rangle$ to the state $|J', K', M', v'\rangle$ is given by the standard electric dipole formula (see for example Ref. [174])

$$A_{J,K,M,v\rightarrow J',K',M',v'} = \frac{4(\Delta E)^3}{3\hbar^4 c^3} |\langle J', K', M', v'|\hat{\boldsymbol{\mu}}|J, K, M, v\rangle|^2, \tag{9.22}$$

where $\hat{\boldsymbol{\mu}}$ is the electric dipole moment operator and $\Delta E \equiv E(J, K, M, v) - E(J', K', M', v')$ is the energy difference between the initial and final states. The square of the dipole matrix element can be rewritten as

$$|\langle J', K', M', v'|\hat{\boldsymbol{\mu}}|J, K, M, v\rangle|^2 \equiv \sum_{m=-1}^{1} |\langle J', K', M', v'|\hat{\mu}_m|J, K, M, v\rangle|^2, \tag{9.23}$$

where, following Ref. [175], we have used

$$\hat{\mu}_0 \equiv \hat{\mu}_z, \qquad \hat{\mu}_\pm \equiv \frac{\mp\hat{\mu}_x + i\hat{\mu}_y}{\sqrt{2}}. \tag{9.24}$$

We can relate the components of $\hat{\boldsymbol{\mu}}$ in the rotating grain frame [superscript (g)] to those in the "lab" frame (i.e., the frame of reference in which the state $|J, K, M\rangle$ corresponds to an angular momentum

[3] This section is a generalization of Appendix B of Ref. [173].

$\hbar M$ along the z-axis):

$$\hat{\mu}^{(g)}_{m'} = \sum_{m=-1}^{1} \mathcal{D}^{(1)}_{m,m'}(\chi)\hat{\mu}_m, \tag{9.25}$$

where $\mathcal{D}^{(j)}_{m,m'} \equiv \langle j, m(\text{“lab”})|j, m'(\text{grain})\rangle$ is the rotation matrix in the spin-j representation [175], and χ represents the set of three Euler angles. The inverse of Eq. (9.25) is just

$$\hat{\mu}_m = \sum_{m'=-1}^{1} \mathcal{D}^{(1)*}_{m',m}(\chi)\hat{\mu}^{(g)}_{m'}, \tag{9.26}$$

where we have used the fact that $\mathcal{D}^{(j)}$ is unitary. In the absence of rotation-vibration interactions, the electric dipole operator only acts on the vibrational degrees of freedom of the grain, when expressed in the frame of the rotating grain, so we have

$$\langle J', K', M', v'|\hat{\mu}_m|J, K, M, v\rangle = \sum_{m'=-1}^{1} \langle v'|\hat{\mu}^{(g)}_{m'}|v\rangle \int \Psi^*_{J',K',M'}(\chi)\mathcal{D}^{(1)*}_{m',m}(\chi)\Psi_{J,K,M}(\chi)\mathrm{d}^3\chi, \tag{9.27}$$

where we have written the state $|J, K, M, v\rangle$ as a tensor product of a wave function describing the rotational configuration $\Psi_{J,K,M}(\chi)$ and a vibrational eigenstate $|v\rangle$. The rotational wave functions can be expressed in terms of the rotation matrix elements [175]:

$$\Psi_{J,K,M}(\chi) = \sqrt{\frac{2J+1}{8\pi^2}}\mathcal{D}^{(J)}_{M,K}(\chi). \tag{9.28}$$

The integrand in Eq. (9.27) is therefore a product of three rotation matrix elements. Using the symmetries of the rotation matrices and Eq. (4.6.2) of Ref. [175], we obtain

$$\begin{aligned}\langle J', K', M', v'|\hat{\mu}_m|J, K, M, v\rangle &= \sqrt{(2J'+1)(2J+1)}(-1)^{M'+K'+m}\begin{pmatrix} J' & 1 & J \\ -M' & -m & M\end{pmatrix} \\ &\times \sum_{m'=-1}^{1}(-1)^{m'}\langle v'|\hat{\mu}^{(g)}_{m'}|v\rangle\begin{pmatrix} J' & 1 & J \\ -K' & -m' & K\end{pmatrix}.\end{aligned} \tag{9.29}$$

We then obtain the following expression for the spontaneous decay rate:

$$\begin{aligned}A_{J,K,M,v\to J',K',M',v'} = \frac{4(\Delta E)^3}{3\hbar^4c^3}(2J+1)(2J'+1)\sum_{m=-1}^{1}\begin{pmatrix} J' & 1 & J \\ -M' & -m & M\end{pmatrix}^2 \\ \times\left|\sum_{m'=-1}^{1}(-1)^{m'}\langle v'|\hat{\mu}^{(g)}_{m'}|v\rangle\begin{pmatrix} J' & 1 & J \\ -K' & -m' & K\end{pmatrix}\right|^2.\end{aligned} \tag{9.30}$$

Each sum of $3j$ symbols in Eq. (9.30) in fact reduces to a single element, with $m = -\Delta M \equiv M - M'$ and $m' = -\Delta K \equiv K - K'$, respectively. From a basic property of the $3j$ symbol, we see that the

$\Delta K = 0$ transitions are induced by the component of the permanent dipole moment which is parallel to the grain's axis of symmetry, whereas the $\Delta K = \pm 1$ transitions are induced by the perpendicular component of the permanent dipole moment. Explicitly, we have

$$A_{J,K,M,v\rightarrow J',K',M',v'} = \frac{4(\Delta E)^3}{3\hbar^4 c^3}(2J+1)(2J'+1)|\langle v'|\hat{\mu}^{(g)}_{-\Delta K}|v\rangle|^2 f_{JM}(\Delta J,\Delta M) f_{JK}(\Delta J,\Delta K), \quad (9.31)$$

where we have defined

$$f_{JM}(\Delta J,\Delta M) \equiv \left(\begin{array}{ccc} J+\Delta J & 1 & J \\ -(M+\Delta M) & \Delta M & M \end{array} \right)^2 . \quad (9.32)$$

Using Table 2 of Ref. [175], we obtain the following explicit values for the function f:

$$f_{JM}(+1,\pm 1) = \frac{(J\pm M+1)(J\pm M+2)}{(2J+1)(2J+2)(2J+3)} \approx \frac{1}{8J}\left(1\pm\frac{M}{J}\right)^2, \quad (9.33)$$

$$f_{JM}(-1,\pm 1) = \frac{(J\mp M-1)(J\mp M)}{(2J-1)(2J)(2J+1)} \approx \frac{1}{8J}\left(1\mp\frac{M}{J}\right)^2, \quad (9.34)$$

$$f_{JM}(\pm 1,0) = \frac{J_>^2-M^2}{J_>(2J_>-1)(2J_>+1)} \approx \frac{1}{4J}\left(1-\frac{M^2}{J^2}\right), \quad (9.35)$$

$$f_{JM}(0,\pm 1) = \frac{(J\pm M+1)(J\mp M)}{2J(J+1)(2J+1)} \approx \frac{1}{4J}\left(1-\frac{M^2}{J^2}\right), \quad (9.36)$$

$$f_{JM}(0,0) = \frac{M^2}{J(J+1)(2J+1)} \approx \frac{1}{2J}\frac{M^2}{J^2}, \quad (9.37)$$

where $J_> \equiv \max(J, J+\Delta J)$ and we have given both the exact values and approximate expressions in the large-J and large-M limit.

To simplify the computations, we are always free to orient the "lab" frame in such a way that the grain angular momentum is aligned with the z-axis, and $M = J$. We can see from inspection of Eqs. (9.33)–(9.37) that in the large-J limit $f_{JJ}(\Delta M = \Delta J) \approx 1/(2J)$ independently of ΔJ. In the large-J limit, we therefore have, for transitions with $\Delta J = \Delta M$:

$$A_{J,K,J,v\rightarrow J',K',J',v'} \approx \frac{8(\Delta E)^3}{3\hbar^4 c^3}|\langle v'|\hat{\mu}^{(g)}_{-\Delta K}|v\rangle|^2 J f_{JK}(\Delta J,\Delta K). \quad (9.38)$$

Moreover, we see that transitions with $\Delta M \neq \Delta J$ are suppressed by a factor $\sim 1/J^{|\Delta M-\Delta J|}$ with respect to transitions with $\Delta M = \Delta J$.

9.4 Electric dipole emission and radiative damping

In the case where the grain is assumed to rotate about its axis of greatest inertia, the electric dipole emission is monochromatic, at frequency $\omega/(2\pi)$, where ω is the angular velocity of the grain. For

a disk-like grain that wobbles, the emission spectrum, for a given total angular momentum, is more complicated, and we will see that the grain radiates at four different frequencies.

9.4.1 Spontaneous decay rates

Here we consider the purely rotational transitions, i.e., those for which the vibrational state is unchanged ($v' = v$). There are four allowed transitions for spontaneous decay, corresponding to four possible frequencies of emission $\nu_{(\Delta J,\Delta K)} = \frac{1}{h}\Delta E_{(\Delta J,\Delta K)}$:

$$\Delta J = -1,\ \Delta K = 0: \qquad \nu_{(-1,0)} = 2J\nu_1 \approx \frac{I_3}{I_1}\frac{\Omega}{2\pi}, \tag{9.39}$$

$$\Delta J = -1,\ \Delta K = \pm 1: \qquad \nu_{(-1,\pm 1)} = 2J\nu_1 \pm (2K \pm 1)\nu_{13} \approx \left[\frac{I_3}{I_1} \pm \left(\frac{I_3}{I_1} - 1\right)\frac{K}{J}\right]\frac{\Omega}{2\pi}, \tag{9.40}$$

$$\Delta J = 0,\ \Delta|K| = +1: \qquad \nu_{(0,\pm 1)} = (2|K| + 1)\nu_{13} \approx \left(\frac{I_3}{I_1} - 1\right)\frac{|K|}{J}\frac{\Omega}{2\pi}, \tag{9.41}$$

where ν_1 and ν_{13} were defined in Eqs. (9.2) and (9.3) and we recall that $\Omega \approx \hbar J/I_3$ in the large-J limit. We see that in the case of a spherical grain ($I_1 = I_3 \equiv I,\ \nu_{13} = 0$), there is only one emitted frequency, $\nu = \frac{\Omega}{2\pi}$. Also, if we assume that the grain is initially rotating about its axis of greatest inertia ($K = J$), then only the transition $\Delta J = \Delta K = -1$ is allowed (as K' must be between $-J'$ and J'), and it also has frequency $\nu = \frac{\Omega}{2\pi}$ in the large-J limit.

We can now use the formalism developed in Section 9.3 to compute the spontaneous decay rates. To simplify the notation, we first define the in-plane (ip) and out-of-plane (op) components of the permanent electric dipole moment

$$\mu_{\rm op}^2 \equiv |\langle v|\hat{\mu}_0^{(g)}|v\rangle|^2, \quad \mu_{\rm ip}^2 \equiv |\langle v|\hat{\mu}_1^{(g)}|v\rangle|^2 + |\langle v|\hat{\mu}_{-1}^{(g)}|v\rangle|^2 = 2|\langle v|\hat{\mu}_{\pm 1}^{(g)}|v\rangle|^2. \tag{9.42}$$

Using Eq. (9.38) and Eqs. (9.33)-(9.37), we obtain the spontaneous decay rate for purely rotational transitions, in the large-J limit:

$$A_{\Delta J=\Delta M=-1,\Delta K=0} \approx \left(\frac{I_3}{I_1}\right)^3\left(1 - \frac{K^2}{J^2}\right)\frac{2\mu_{\rm op}^2\Omega^3}{3\hbar c^3}, \tag{9.43}$$

$$A_{\Delta J=\Delta M=-1,\Delta K=\pm 1} \approx \left[\frac{I_3}{I_1} \pm \left(\frac{I_3}{I_1} - 1\right)\frac{K}{J}\right]^3\left(1 \mp \frac{K}{J}\right)^2\frac{\mu_{\rm ip}^2\Omega^3}{6\hbar c^3} \tag{9.44}$$

$$A_{\Delta J=\Delta M=0,\Delta|K|=1} \approx \left(\frac{I_3}{I_1} - 1\right)^3\left(\frac{|K|}{J}\right)^3\left(1 - \frac{K^2}{J^2}\right)\frac{\mu_{\rm ip}^2\Omega^3}{3\hbar c^3}. \tag{9.45}$$

9.4.2 Radiated power

In the case that the grain is initially rotating along the axis of greatest inertia ($K = J$), we see that only the transition $\Delta J = \Delta K = -1$ is allowed. The power radiated in this transition is obtained by

multiplying the spontaneous transition rate, Eq. (9.44), by $\Delta E = \hbar\Omega$. In the large-J limit, we find

$$P(K=J) = \frac{2\mu_{\rm ip}^2\Omega^4}{3c^3}, \tag{9.46}$$

independently of the ratio I_3/I_1. This is the same expression as what was obtained classically from the electric dipole formula, Eq. (8.1).

Let us now turn to the case where the orientation of the grain is randomized and K is uniformly distributed in $[-J, J]$. In the large-J limit, we can replace discrete averaging over K by integrals:

$$\frac{1}{2J+1}\sum_{K=-J}^{J} F(K/J) \underset{J\gg 1}{\longrightarrow} \frac{1}{2}\int_{-1}^{1} F(x)\mathrm{d}x. \tag{9.47}$$

For a given a value of J, the transitions $\Delta J = -1$, $\Delta K = 0$ all radiate at $\nu = \frac{I_3}{I_1}\frac{\Omega}{2\pi}$, independently of the initial value of K. Averaging over grain orientation, the power radiated per unit frequency in these transitions is then

$$\left.\frac{\mathrm{d}P}{\mathrm{d}\nu}\right|_{\binom{\Delta J=-1}{\Delta K=0}} = \left(\frac{I_3}{I_1}\right)^3 \frac{4\mu_{\rm op}^2\Omega^4}{9c^3}\delta\left(\nu - \frac{I_3}{I_1}\frac{\Omega}{2\pi}\right). \tag{9.48}$$

Let us now consider the $\Delta J = -1, \Delta K = \pm 1$ transitions. They emit power in the frequency interval

$$\frac{\Omega}{2\pi} < \nu < \left(2\frac{I_3}{I_1}+1\right)\frac{\Omega}{2\pi}. \tag{9.49}$$

Since K is uniformly distributed in $[-J, J]$, we obtain that the power radiated by these transitions per unit frequency is

$$\left.\frac{\mathrm{d}P}{\mathrm{d}\nu}\right|_{\binom{\Delta J=-1}{\Delta K=+1}} = \left.\frac{\mathrm{d}P}{\mathrm{d}\nu}\right|_{\binom{\Delta J=-1}{\Delta K=-1}} = \left(\frac{I_3}{I_1}-1\right)^{-3}\left[2\frac{I_3}{I_1}-1-\frac{2\pi\nu}{\Omega}\right]^2\frac{2\pi}{\Omega}\frac{\mu_{\rm ip}^2(2\pi\nu)^4}{12c^3}, \tag{9.50}$$

where we have made the replacement $K/J = \pm\left(\frac{I_3}{I_1}-1\right)^{-1}\left[\frac{2\pi\nu}{\Omega} - \frac{I_3}{I_1}\right]$. A similar reasoning applied to the $\Delta J = 0, \Delta|K| = 1$ gives us

$$\left.\frac{\mathrm{d}P}{\mathrm{d}\nu}\right|_{\binom{\Delta J=0}{\Delta|K|=1}} = \left(\frac{I_3}{I_1}-1\right)^{-3}\left[\frac{I_3}{I_1}-1-\frac{2\pi\nu}{\Omega}\right]^2\frac{2\pi}{\Omega}\frac{\mu_{\rm ip}^2(2\pi\nu)^4}{3c^3}, \quad 0<\nu<\left(\frac{I_3}{I_1}-1\right)\frac{\Omega}{2\pi}. \tag{9.51}$$

Note that the total power radiated through the latter transition is much smaller than the total power radiated in $\Delta J = -1, \Delta K = \pm 1$ transitions: in the case $I_3 = 2I_1$ we obtain

$$P_{\binom{\Delta J=0}{\Delta|K|=1}} \Big/ \left[P_{\binom{\Delta J=-1}{\Delta K=+1}} + P_{\binom{\Delta J=-1}{\Delta K=-1}}\right] = \frac{1}{174}. \tag{9.52}$$

The total power radiated in $\Delta J = -1, \Delta K = \pm 1$ transitions is of the same order as that radiated

in $\Delta J=-1, \Delta K=0$ transitions:

$$\left[P_{\binom{\Delta J=-1}{\Delta K=+1}}+P_{\binom{\Delta J=-1}{\Delta K=-1}}\right] \Big/ P_{\binom{\Delta J=-1}{\Delta K=0}}=\frac{261}{560}\frac{\mu_{\rm ip}^2}{\mu_{\rm op}^2}. \tag{9.53}$$

The total emitted spectrum is then the sum of the 4 components, Eqs. (9.48–9.51), considered only within their respective range of validity. In the case of $I_1=\frac{1}{2}I_3$, we obtain:

$$\frac{{\rm d}P}{{\rm d}\nu}(\nu|\Omega)=2\pi\frac{\omega^4}{c^3}\left\{\frac{\mu_{\rm ip}^2}{6\Omega}\left(3-\frac{\omega}{\Omega}\right)^2\mathbf{1}_{\Omega<\omega<3\Omega}+\frac{\mu_{\rm ip}^2}{3\Omega}\left(1-\frac{\omega^2}{\Omega^2}\right)\mathbf{1}_{\omega<\Omega}+\frac{4}{9}\mu_{\rm op}^2\delta(\omega-2\Omega)\right\}, \tag{9.54}$$

where $\omega=2\pi\nu$ and the truth function $\mathbf{1}$ is 1 if the subscripted inequality holds and 0 otherwise. We show the power radiated by one grain, for a given angular momentum, in Fig. 9.1. The total power emitted per grain is then (for $I_3=2I_1$):

$$P_{\rm tot}=\frac{2\Omega^4}{3c^3}\left(5\mu_{\rm ip}^2+\frac{32}{3}\mu_{\rm op}^2\right). \tag{9.55}$$

This should be compared to $2\Omega^4\mu_{\rm ip}^2/(3c^3)$ for the case of a grain rotating around it axis of greatest inertia; for an in-plane dipole moment ($\mu_{\rm op}=0$) the emitted power is 5 times higher, whereas for an isotropically distributed dipole moment ($\mu_{\rm ip}^2:\mu_{\rm op}^2=2:1$) the emitted power is ~ 10 times higher.

The emissivity per H atom j_ν (units of $\mathrm{erg\,s^{-1}\,Hz^{-1}\,sr^{-1}}$ per H atom) can then be obtained by integrating over the probability distribution for Ω and the grain size distribution:

$$j_\nu=\frac{1}{4\pi}\int{\rm d}a\frac{1}{n_{\rm H}}\frac{{\rm d}n_{\rm gr}}{{\rm d}a}\int{\rm d}\Omega\frac{dP}{d\nu}(\nu|\Omega)4\pi\Omega^2 f_a(\Omega)=\frac{\omega^4}{c^3}\int{\rm d}a\frac{1}{n_{\rm H}}\frac{{\rm d}n_{\rm gr}}{{\rm d}a}\times$$
$$\left\{\frac{\mu_{\rm op}^2}{9}\pi\omega^2 f_a\left(\frac{\omega}{2}\right)+\frac{\mu_{\rm ip}^2}{3}\int_{\frac{\omega}{3}}^{\omega}\frac{{\rm d}\Omega}{\Omega}\left(3-\frac{\omega}{\Omega}\right)^2\pi\Omega^2 f_a(\Omega)+\frac{2\mu_{\rm ip}^2}{3}\int_{\omega}^{\infty}\frac{{\rm d}\Omega}{\Omega}\left(1-\frac{\omega^2}{\Omega^2}\right)\pi\Omega^2 f_a(\Omega)\right\}, \tag{9.56}$$

where $\omega=2\pi\nu$. This expression should in addition be averaged over magnitudes and orientations of dipole moments.

9.4.3 Radiation-reaction torque with a nonzero CMB temperature

In the previous chapter, we have only accounted for spontaneous rotational decays and hence considered electric dipole radiation as a pure damping process. In practice, however, the ISM is permeated by CMB photons, which can also cause stimulated decays or be absorbed by dust grains. The characteristic frequencies of emission of spinning dust grains are in the range 10 GHz $\lesssim\nu\lesssim$ 100 GHz, which is of the order of the characteristic CMB frequency $\nu_0\equiv kT_0/h\approx 57$ GHz, where $T_0\approx 2.73$ K is the CMB temperature. This implies that the mean occupation number of CMB photons at the frequencies of interest is of order unity, and the rates of stimulated emissions and absorptions are comparable to the spontaneous decay rates. The main effect is to lead to an additional rotational

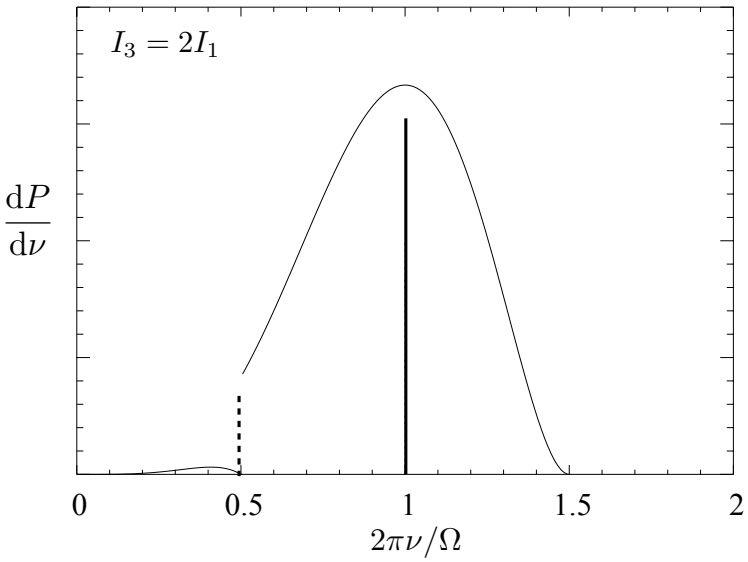

Figure 9.1: Power radiated per unit frequency by a disklike dust grain, for a given $\Omega = \hbar J/I_3$, in arbitrary units, and assuming a randomly oriented grain. The dashed line shows the emitted power for the case of a grain spinning about its axis of greatest inertia.

diffusion.

Let us denote $\eta(E) \equiv \left(\mathrm{e}^{E/(kT_0)} - 1\right)^{-1}$ the occupation number of CMB photons. At the energies of interest, $\eta(E) \sim 1$. We start in a state with $M = J$ and denote $A_{J,K,J\to J',K',J'} \equiv A_{J,K\to J',K'}$ for short.

The average rate of change of the quantity ΔX per unit time, where $\Delta X = \Delta M,\ \Delta J^2$ or $\Delta J \Delta K$, is given by

$$\begin{aligned} \frac{\mathrm{d}\langle \Delta X\rangle}{\mathrm{d}t} &= \sum_{K'} \Delta X\ A_{J,K\to J-1,K'}\left[1+\eta(E_{J,K}-E_{J-1,K'})\right] \\ &+ \sum_{K'} \Delta X\ A_{J+1,K'\to J,K}\ \eta(E_{J+1,K'}-E_{J,K}), \end{aligned} \tag{9.57}$$

where the second term in the first line accounts for stimulated decays and the second line accounts for absorptions from the state $|J,K,J\rangle$ to the state $|J+1,K',J+1\rangle$ and we have not included transitions with $\Delta M \neq \Delta J$ as they are suppressed in the large-J limit.

We now point out that the Einstein-A coefficients are slowly varying functions of J and K, i.e., they change by a fractional amount of order $\sim 1/J$ if changing J or K by 1. If $\Delta E \sim kT_0$, then this is also the case for the photon occupation numbers appearing in Eq. (9.57). To lowest order in $1/J$,

we therefore obtain

$$\frac{\mathrm{d}\langle\Delta M\rangle}{\mathrm{d}t} \approx -\sum_{\Delta K} A_{J,K\rightarrow J-1,K'}, \tag{9.58}$$

$$\frac{\mathrm{d}\langle\Delta J^2\rangle}{\mathrm{d}t} \approx \sum_{\Delta K} A_{J,K\rightarrow J-1,K'}\left[1+2\eta(E_{J,K}-E_{J-1,K'})\right], \tag{9.59}$$

$$\frac{\mathrm{d}\langle\Delta J\Delta K\rangle}{\mathrm{d}t} \approx -\sum_{\Delta K} \Delta K\ A_{J,K\rightarrow J-1,K'}\left[1+2\eta(E_{J,K}-E_{J-1,K'})\right]. \tag{9.60}$$

We see that there is not only rotational damping, but also diffusion associated with electric dipole radiation, even at zero CMB temperature. In the case of a grain rotating about its axis of greatest inertia, we find

$$D_{\mathrm{ed}}(\Omega;K=J) \equiv \frac{\hbar}{I_3}\frac{\mathrm{d}\langle\Delta M\rangle}{\mathrm{d}t} = \frac{2}{3}\frac{\mu_{\mathrm{ip}}^2\Omega^3}{I_3c^3} \tag{9.61}$$

$$E_{||,\mathrm{ed}}(\Omega;K=J) \equiv \frac{\hbar^2}{I_3^2}\frac{\mathrm{d}\langle\Delta J^2\rangle}{\mathrm{d}t} = \frac{\hbar}{I_3}D_{\mathrm{ed}}(\Omega)\left[1+2\eta(\hbar\Omega)\right]. \tag{9.62}$$

The damping rate is identical to that found in Chapter 8. Note that Eq. (9.62) resembles closely the generalized Nyquist theorem [176, 162]. In the limit $\hbar\Omega \ll kT_0$, we obtain the form derived in Chapter 8 for the fluctuation-dissipation theorem, $E_{||,\mathrm{ed}} = 2kT_0/(I_3\Omega)D_{\mathrm{ed}}$.

For a randomly oriented grain, we must evaluate the average of Eqs. (9.58) and (9.59) over K. For $I_3 = 2I_1$, we obtain

$$D_{\mathrm{ed}}(\Omega) = \frac{32}{9}\frac{\mu_{\mathrm{op}}^2\Omega^3}{I_3c^3} + \frac{82}{45}\frac{\mu_{\mathrm{ip}}^2\Omega^3}{I_3c^3} \tag{9.63}$$

$$E_{||,\mathrm{ed}}(\Omega) = \frac{32}{9}\frac{\hbar\Omega^3}{I_3^2c^3}\mu_{\mathrm{op}}^2\left[1+2\eta(2\hbar\Omega)\right] + \frac{\hbar\Omega^3}{3I_3^2c^3}\mu_{\mathrm{ip}}^2\left[\frac{82}{15}+\mathcal{G}\left(\frac{\hbar\Omega}{kT_0}\right)\right], \tag{9.64}$$

where we have defined

$$\mathcal{G}(\lambda) \equiv \int_{-1}^{1}\frac{(2-x)^3(1+x)^2}{\mathrm{e}^{(2-x)\lambda}-1}\mathrm{d}x. \tag{9.65}$$

Moreover, we can evaluate the following quantity, which appears in the principle of detailed balance for a randomly oriented grain, Eq. (9.19):

$$\left\langle\frac{\hbar^2}{I_3^2}\frac{K}{J}\frac{\mathrm{d}\langle\Delta J\Delta K\rangle}{\mathrm{d}t}\right\rangle_K = \frac{\hbar\Omega^3}{3I_3^2c^3}\mu_{\mathrm{ip}}^2\left[\frac{104}{105}+\mathcal{H}(\lambda)\right], \tag{9.66}$$

where we have defined

$$\mathcal{H}(\lambda) \equiv \int_{-1}^{1} x\frac{(2-x)^3(1+x)^2}{\mathrm{e}^{(2-x)\lambda}-1}\mathrm{d}x. \tag{9.67}$$

One can easily check that in the limit $\hbar\Omega \ll kT_0$, the principle of detailed balance as previously derived is indeed satisfied in the form of Eq. (9.19) with $T = T_0$. We now explain why the form (9.19)

is not recovered for a general value of $\hbar\Omega/(kT_0)$. One expects that in the absence of any interactions besides absorptions and emissions of microwave photons, the probability distribution of rotational quantum number should reach thermal equilibrium with a temperature T_0. In that case, the ratio of the population of two neighboring levels is of order $X_{J+1}/X_J \sim \mathrm{e}^{-\hbar\Omega/(kT_0)}$. For $\hbar\Omega \ll kT_0$, we see that this ratio is close to unity and one can treat the population of rotational states as a smoothly varying function, which is an underlying assumption of the Fokker-Planck equation. For $\hbar\Omega \gtrsim kT_0$, however, the population of rotational states would be a rapidly decreasing function, and a Fokker-Planck treatment would not be valid *if no other processes were present*; in that case one should rather solve a coupled rate equation in a matrix form. Due to other rotational excitation and damping processes, however, the characteristic rotation temperature is much larger than the CMB temperature and the level populations are indeed slowly varying with J around the peak of the spectrum. The Fokker-Planck treatment is therefore valid, but one cannot expect the form (9.19) of detailed balance to be satisfied for excitation and damping by emission and absorption of microwave photons. Note, finally, that for all other processes considered, the temperature is much larger than the characteristic emission frequency and the generalized Nyquist theorem takes the form of the standard dissipation-fluctuation theorem.

Normalized damping and excitation rates

In Chapter 8 we had only considered electric dipole radiation as a rotational damping process, which we characterized by the characteristic timescale $\tau_{\rm ed}$. Here we have shown that there is an associated rotational excitation rate. The corresponding dimensionless damping and excitation rates defined in Eqs. (9.9) and (9.10) are given by

$$F_{\rm ed}(\Omega; K=J) = \tau_{\rm H}\frac{2}{3}\frac{\mu_{\rm ip}^2\Omega^2}{I_3c^3}, \tag{9.68}$$

$$G_{\rm ed}(\Omega; K=J) = \frac{\hbar\Omega}{kT}\left[\frac{1}{2}+\eta(\hbar\Omega)\right]F_{\rm ed}(\Omega), \tag{9.69}$$

when the grain is rotating about its axis of greatest inertia, and

$$F_{\rm ed}(\Omega; K \text{ random}) = \tau_H\left[\frac{32}{9}\mu_{\rm op}^2+\frac{82}{45}\mu_{\rm ip}^2\right]\frac{\Omega^2}{I_3c^3}, \tag{9.70}$$

$$G_{\rm ed}(\Omega; K \text{ random}) = \frac{1}{2}\frac{\hbar\Omega}{kT}F_{\rm ed}(\Omega)+\tau_H\frac{\hbar\Omega}{kT}\left[\frac{32}{9}\mu_{\rm op}^2\eta(2\hbar\Omega)+\frac{1}{6}\mu_{\rm ip}^2\mathcal{G}\left(\frac{\hbar\Omega}{kT_0}\right)\right]\frac{\Omega^2}{I_3c^3}, \tag{9.71}$$

when the grain's orientation is randomized.

Evaluation of $\mathcal{G}(\lambda)$

For small values of its argument, the function $\mathcal{G}$ has the asymptotic expansion

$$\mathcal{G}(\lambda \ll 1) = \frac{32}{5\lambda} - \frac{82}{15} + \frac{58}{35}\lambda - \frac{61}{567}\lambda^3 + \mathcal{O}(\lambda^4). \tag{9.72}$$

For general values of λ, one may Taylor-expand the denominator in Eq. (9.65) to obtain

$$\mathcal{G}(\lambda) = \sum_{n=1}^{+\infty} \mathcal{G}_1(n\lambda), \tag{9.73}$$

where

$$\begin{aligned} \mathcal{G}_1(\lambda) \equiv \int_{-1}^{1} (2-x)^3(1+x)^2 \mathrm{e}^{-(2-x)\lambda} \mathrm{d}x &= 2\lambda^{-6}\mathrm{e}^{-\lambda}\left[2\lambda^5 + 4\lambda^4 + \lambda^3 - 15\lambda^2 - 12\lambda + 60\right] \\ &- 6\lambda^{-6}\mathrm{e}^{-3\lambda}\left[9\lambda^3 + 27\lambda^2 + 36\lambda + 20\right]. \end{aligned} \tag{9.74}$$

We use the expansion (9.72) for $\lambda < 1$ and Eq. (9.73) truncated to $n \leq 4$ for $\lambda \geq 1$. This approximates the exact $\mathcal{G}(\lambda)$ to better than 1% accuracy over the whole range $0 < \lambda < +\infty$.

Effect of accounting for rotational excitation

We find that the rotational excitation due to electric dipole radiation is a subdominant process, as it leads to at most a $\sim 20\%$ increase of the peak emissivity in diffuse environments. We therefore only consider the damping associated with electric dipole radiation. As in Chapter 8, we can associate a characteristic electric dipole damping timescale

$$\tau_{\rm ed}(K \text{ random}) = \frac{I_3^2 c^3}{3kT}\left[\frac{32}{9}\mu_{\rm op}^2 + \frac{82}{45}\mu_{\rm ip}^2\right]^{-1}. \tag{9.75}$$

9.5 Plasma excitation and drag

Plasma excitation is the random torquing of dust grains via their interaction with passing ions; plasma drag is the related effect in which a rotating grain spins down by transferring its angular momentum to the surrounding plasma. These processes have been previously computed for uniformly rotating grains in DL98b and Chapter 8.

We consider first the excitation in terms of the power spectrum of the electric field at the position of the grain. Then we consider the drag, which is determined using the detailed balance theorem derived in Section 9.2.4. Finally, we combine this with the analysis of ion trajectories in Chapter 8 to obtain the coefficients $F_{\rm p}(\Omega)$ and $G_{\rm p}(\Omega)$ as a function of the coefficient $G_{\rm p,K=J}(\omega) = F_{\rm p,K=J}(\omega)$ computed in Section 8.6.

Perturbation theory predicts the transition rate $\Gamma_{n\to k}$ for a perturbation depending on time $\hat{V}(t)$ (see e.g. Ref. [164])

$$\Gamma_{n\to k} = \frac{1}{\hbar^2}\mathcal{P}_{V_{kn}}(\nu_{kn}) \ , \tag{9.76}$$

where $h\nu_{kn} \equiv |E_k - E_n|$ and $\mathcal{P}_V(\nu)$ is the power spectrum of the perturbation:

$$\mathcal{P}_{V_{kn}}(\nu) \equiv \lim_{T\to\infty}\frac{1}{T}\left|\int_0^T \mathrm{e}^{2\pi\mathrm{i}\nu t}V_{kn}(t)\mathrm{d}t\right|^2 . \tag{9.77}$$

In the case of a rotating dust grain in a fluctuating electric field, the perturbation operator is given by

$$\hat{V} = -\hat{\boldsymbol{\mu}}.\boldsymbol{\mathcal{E}} \ , \tag{9.78}$$

where $\hat{\boldsymbol{\mu}}$ is the electric dipole operator of the grain and $\boldsymbol{\mathcal{E}}$ is the stochastic electric field produced by the passing ions. Using Eq. (9.26), we rewrite the perturbation as

$$\hat{V} = -\sum_{m=-1}^{1}(-1)^m\hat{\mu}_m\mathcal{E}_{-m} = -\sum_{m=-1}^{1}(-1)^m\mathcal{E}_{-m}\sum_{m'=-1}^{1}\mathcal{D}^{(1)*}_{m'm}(\chi)\hat{\mu}^{(g)}_{m'} \ , \tag{9.79}$$

where we rewrote the components of the dipole moment in the lab frame as a function of those in the grain frame. The matrix element of the perturbation between two states can then be evaluated:

$$\begin{aligned}
\langle J',K',M',v'|\hat{V}|J,K,M,v\rangle &= -\sum_{m=-1}^{1}(-1)^m\mathcal{E}_{-m}\sum_{m'=-1}^{1}\langle v'|\mu^{(g)}_{m'}|v\rangle\langle J',K',M'|D^{1*}_{m'm}(\chi)|J,K,M\rangle \\
&= (-1)^{K'+M'}\sqrt{(2J'+1)(2J+1)}\sum_{m=-1}^{1}\mathcal{E}_{-m}\begin{pmatrix} J' & 1 & J \\ -M' & -m & M\end{pmatrix} \\
&\times \sum_{m'=-1}^{1}(-1)^{m'}\langle v'|\mu^{(g)}_{m'}|v\rangle\begin{pmatrix} J' & 1 & J \\ -K' & -m' & K\end{pmatrix}.
\end{aligned} \tag{9.80}$$

The transition rate induced by the perturbation is therefore

$$\begin{aligned}
\Gamma_{J,K,M,v\to J',K',M',v'} = \frac{(2J'+1)(2J+1)}{\hbar^2}\lim_{T\to\infty}\frac{1}{T}\Bigg|\sum_{m=-1}^{1}\begin{pmatrix} J' & 1 & J \\ -M' & -m & M\end{pmatrix}\int_0^T \mathrm{e}^{\mathrm{i}\frac{\Delta E}{\hbar}t}\mathcal{E}_{-m}(t)\mathrm{d}t \\
\times\sum_{m'=-1}^{1}(-1)^{m'}\langle v'|\mu^{(g)}_{m'}|v\rangle\begin{pmatrix} J' & 1 & J \\ -K' & -m' & K\end{pmatrix}\Bigg|^2 .
\end{aligned} \tag{9.81}$$

If we now assume that the x, y, z components of the electric field are uncorrelated, the terms mixing different values of m in the modulus squared vanish, we obtain, using Eq. (9.30) for the spontaneous

decay rates[4]:

$$\Gamma_{J,K,M,v\to J',K',M',v'} = \frac{3\hbar^2 c^3}{4(\Delta E)^3}\mathcal{P}_{\mathcal{E}}\left(\frac{\Delta E}{h}\right) \times A_{J,K,M,v\to J',K',M',v'} \ , \tag{9.82}$$

where we used the power spectrum of the electric field, which we assumed to be isotropic :

$$\mathcal{P}_{\mathcal{E}}(\nu) \equiv \mathcal{P}_{\mathcal{E}_x}(\nu) + \mathcal{P}_{\mathcal{E}_y}(\nu) + \mathcal{P}_{\mathcal{E}_z}(\nu). \tag{9.83}$$

Before proceeding further, we should emphasize a subtlety regarding the meaning of the electric field power spectrum. The stochastic electric field arises from ions passing nearby the grain. Ions that collide with the grain, however, should not be accounted for, as we already include them in the collisional excitation and damping rates. Therefore only ions which have an impact parameter b large enough not to collide with the grain (typically $b \gtrsim a$) should be accounted for when evaluating the power spectrum $\mathcal{P}_{\mathcal{E}}$. With this knowledge, we can estimate the characteristic cutoff frequency $\nu_{\max}$ of the power spectrum: $\nu_{\max} \sim v_{\rm th}/a \sim \sqrt{2kT/(m_p a^2)} \sim 10^{12}\ T_2^{1/2} a_{-7}^{-1}$ Hz. We therefore see that transitions between different vibrational states will be largely suppressed as they correspond to infrared frequencies $\nu_{\rm IR} \sim 10^{13} - 10^{14}$ Hz for the smallest grains. We therefore only need to consider purely rotational transitions with $v' = v$.

We choose the reference z-axis so that the grain is initially in the state $M = J$. There are in principle 18 possible transitions, $\Delta J = 0, \pm 1$, $\Delta M \leq \Delta J$, $\Delta K = 0, \pm 1$. We saw in Section 9.3 that transitions with $\Delta M < \Delta J$ are suppressed with respect to those with $\Delta M = \Delta J$ in the large J limit. We are left with 8 transitions that change J and/or K. Transitions with $\Delta J = 0$ do not appear in calculations of the diffusion rates $\mathrm{d}\langle \Delta J^2\rangle/\mathrm{d}t$ or $\mathrm{d}\langle \Delta J \Delta K\rangle/\mathrm{d}t$. We therefore only need to consider the 6 transitions $\Delta J = \Delta M = \pm 1, \Delta K = 0, \pm 1$.

In the large-J limit, we find that the transition rates are given by:

$$\Gamma_{\Delta J=\pm 1,\Delta K=0} = \frac{\mu_{\rm op}^2}{2\hbar^2}\mathcal{P}_{\mathcal{E}}\left(\frac{I_3}{I_1}\frac{\Omega}{2\pi}\right)\left(1 - \frac{K^2}{J^2}\right), \tag{9.84}$$

$$\begin{aligned}\Gamma_{\Delta J=\pm 1,\Delta K=\pm 1} &= \frac{\mu_{\rm ip}^2}{8\hbar^2}\mathcal{P}_{\mathcal{E}}(\nu)\left(1 + \Delta J \Delta K \frac{K}{J}\right)^2 \\ &= \frac{\mu_{\rm ip}^2}{8\hbar^2}\mathcal{P}_{\mathcal{E}}(\nu)\left(\frac{I_3}{I_1} - 1\right)^{-2}\left(2\frac{I_3}{I_1} - 1 - \frac{2\pi\nu}{\Omega}\right)^2,\end{aligned} \tag{9.85}$$

where in the last line we have used $\nu \equiv \left(I_3/I_1 - \Delta J \Delta K \left(I_3/I_1 - 1\right)\frac{K}{J}\right)\Omega/(2\pi)$. We can now obtain

[4]Einstein-A coefficients are only defined when the final state has a lower energy than the initial state. Here $A_{J,K,M,v\to J',K',M',v'}$ should just be understood as a compact notation for the right-hand side of Eq. (9.30), which is always well defined.

the diffusion rates

$$E_{JJ}(J,K) \equiv \frac{\mathrm{d}\langle \Delta J^2\rangle}{\mathrm{d}t} = \sum_{\Delta J,\Delta K} (\Delta J)^2 \Gamma_{\Delta J,\Delta K}, \tag{9.86}$$

$$E_{JK}(J,K) \equiv \frac{\mathrm{d}\langle \Delta J \Delta K\rangle}{\mathrm{d}t} = \sum_{\Delta J,\Delta K} \Delta J \Delta K\ \Gamma_{\Delta J,\Delta K}. \tag{9.87}$$

Let us first consider the case where the grain is rotating about its axis of greatest inertia, $K = J$. In this case the $\Delta K = 0$ and $\Delta K = -\Delta J$ transitions are suppressed and we find

$$E_{JJ}(J,J) = E_{JK}(J,J) = \frac{\mu_{\rm ip}^2}{\hbar^2}\mathcal{P}_{\mathcal{E}}\left(\frac{\Omega}{2\pi}\right). \tag{9.88}$$

We have already computed the rate of angular momentum diffusion in this case in Section (8.6). We can therefore relate the electric field power spectrum to the dimensionless diffusion rate $G_{\rm p,K=J}(\omega)$:

$$\mathcal{P}_{\mathcal{E}}(\nu) = \frac{2kTI_3}{\tau_{\rm H}\mu_{\rm ip}^2} G_{\rm p,K=J}(2\pi\nu). \tag{9.89}$$

Note that $G_{\rm p,K=J} \propto \mu_{\rm ip}^2$ so this quantity is well defined even for $\mu_{\rm ip} = 0$.

For a randomly oriented dust grain, we need to evaluate the averages $\langle E_{JJ}\rangle_K$ and $\langle (K/J)E_{KJ}\rangle_K$. In the large-$J$ limit, we can change the discrete sums over K to integrals, and we obtain, for $I_3 = 2I_1$:

$$\hbar^2\langle E_{JJ}\rangle(\Omega) = \frac{2}{3}\mu_{\rm op}^2\mathcal{P}_{\mathcal{E}}\left(\frac{\Omega}{\pi}\right) + \frac{\mu_{\rm ip}^2}{4}\int_{\Omega}^{3\Omega}\mathcal{P}_{\mathcal{E}}\left(\frac{\omega}{2\pi}\right)\left(3-\frac{\omega}{\Omega}\right)^2\frac{\mathrm{d}\omega}{\Omega}, \tag{9.90}$$

and therefore

$$G_{\rm p}(\Omega) = \frac{2}{3}\frac{\mu_{\rm op}^2}{\mu_{\rm ip}^2}G_{\rm p,K=J}(2\Omega) + \frac{1}{4}\int_{\Omega}^{3\Omega}\left(3-\frac{\omega}{\Omega}\right)^2 G_{\rm p,K=J}(\omega)\frac{\mathrm{d}\omega}{\Omega}. \tag{9.91}$$

The rates we have derived are symmetric and do not properly account for the fact that the total angular momentum of the system { grain + ions } should be conserved. In principle there should be a slight asymmetry in the $\Delta J = +1$ and $\Delta J = -1$ rates, translating the fact that a supra-thermally rotating grain will be systematically slowed down by transferring its angular momentum to the bath of thermal ions. To obtain the net damping rate one should therefore not use the face values of the rates computed here, but rather derive it from the diffusion rate through the principle of detailed balance, which takes the form of Eq. (9.19). We therefore obtain the normalized damping rate

$$F_{\rm p}(\Omega) = \frac{4}{3}\frac{\mu_{\rm op}^2}{\mu_{\rm ip}^2}G_{\rm p,K=J}(2\Omega) + \frac{1}{4}\int_{\Omega}^{3\Omega}\frac{\omega}{\Omega}\left(3-\frac{\omega}{\Omega}\right)^2 G_{\rm p,K=J}(\omega)\frac{\mathrm{d}\omega}{\Omega}. \tag{9.92}$$

Notice that $G_{\rm p} < F_{\rm p} < 3G_{\rm p}$. We describe our numerical implementation of the plasma excitation and drag coefficients in Appendix 9.A.

We show the plasma excitation and drag coefficient for a grain containing $N_{\rm C} = 54$ carbon atoms

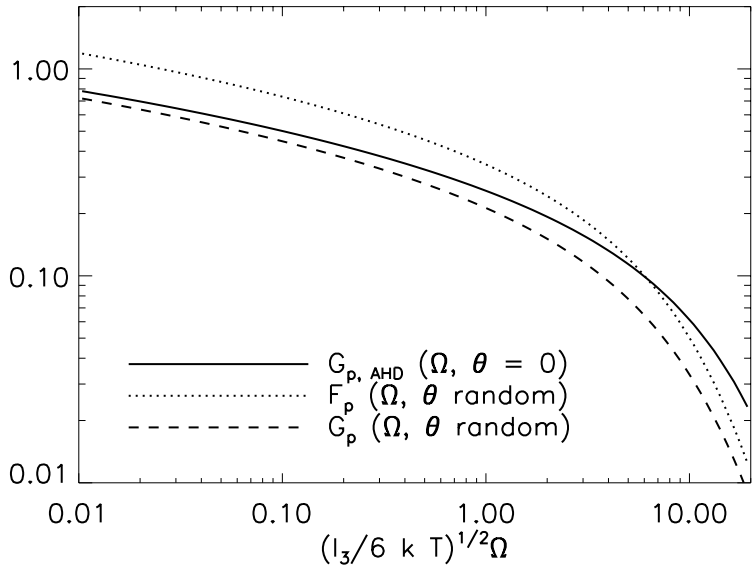

Figure 9.2: Dimensionless plasma excitation and drag coefficients, for $N_{\rm C} = 54$ in the WIM. The curve labelled "$\theta = 0$" corresponds to a grain rotating around its axis of greatest inertia as assumed in Chapter 8; the curves labelled "θ random" correspond to grains with a randomized nutation angle discussed in this chapter.

(equivalent radius $a \approx 5$Å), in WIM conditions (as defined in DL98b) in Fig. 9.2.

9.6 Infrared excitation and damping

Dust grains in the ISM get excited by absorbing ultraviolet photons, which they then degrade into a large number of infrared photons, emitted in ro-vibrational transitions. Because of the $(\Delta E)^3$ factor in the spontaneous rates, for given initial and final vibrational states, transitions with $\Delta J = -1$ have slightly larger rates than transitions with $\Delta J = +1$, and the emission of infrared photons tends to systematically damp out the grain's rotation. This damping is accompanied by a stochastic excitation as infrared photons carry quanta of angular momentum with random projections. We have already computed the damping rate for a grain rotating about its axis of greatest inertia with a classical approach in Section 8.7. In this section, we generalize the quantum treatment of Appendix B of Ref. [173] for randomly oriented disk-like grains.

As in the previous section, we choose a reference frame such that the grain is initially in the $M = J$ rotational state. As for the plasma drag calculation, only the 6 cases $\Delta J = \Delta M = \pm 1, \Delta K = 0, \pm 1$ need to be considered in the large-J limit.

We consider the ro-vibrational transition $v \rightarrow v'$ with change in the rotational configuration $\Delta J, \Delta K$. The energy of the emitted photon is $\Delta E = \Delta E_{\rm vib} + \Delta E_{\rm rot} \equiv h\nu_{\rm vib} + \Delta E_{(\Delta J, \Delta K)}$. Rotational transition energies (typically in the microwaves) are much smaller than vibrational transition energies

(typically in the infrared). We can therefore expand the $(\Delta E)^3$ term in Eq. (9.30) to lowest order in $\Delta E_{(\Delta J,\Delta K)}/\Delta E_{\rm vib}$. The Einstein-A coefficients for the J-changing ro-vibrational transitions are then, in the large-J limit:

$$A_{v\to v';\Delta J=\Delta M=\pm1,\Delta K=0} \approx \frac{2\mu_{||}^2}{3\hbar c^3}(2\pi\nu_{\rm vib})^3\left(1-\frac{K^2}{J^2}\right)\left(1-3\Delta J\frac{I_3}{I_1}\frac{\Omega}{2\pi\nu_{\rm vib}}\right), \quad (9.93)$$

$$A_{v\to v';\Delta J=\Delta M=\pm1,\Delta K=\pm1} \approx \frac{\mu_{\perp}^2}{6\hbar c^3}(2\pi\nu_{\rm vib})^3\left(1+\Delta J\Delta K\frac{K}{J}\right)^2 \times \left\{1+3\frac{\Omega}{2\pi\nu_{\rm vib}}\left[-\Delta J\frac{I_3}{I_1}+\Delta K\frac{K}{J}\left(\frac{I_3}{I_1}-1\right)\right]\right\}, \quad (9.94)$$

where we have defined

$$\mu_{||}^2\equiv|\langle v'|\hat{\mu}_0^{(g)}|v\rangle|^2, \quad \mu_{\perp}^2\equiv|\langle v'|\hat{\mu}_1^{(g)}|v\rangle|^2+|\langle v'|\hat{\mu}_{-1}^{(g)}|v\rangle|^2=2|\langle v'|\hat{\mu}_{\pm1}^{(g)}|v\rangle|^2. \quad (9.95)$$

Note that these differ form $\mu_{\rm ip}^2$ and $\mu_{\rm op}^2$ as we are now considering matrix elements between *different* vibrational states. Classically, they correspond to the power spectrum of the stochastic dipole moment of the grain at the relevant transition frequency (see Section 8.7).

The slight asymmetry between the rates of $\Delta J=+1$ and $\Delta J=-1$ transitions causes a net loss of z-angular momentum, with rate (recalling that transitions with $\Delta M\neq\Delta J$ are suppressed in the large-J limit):

$$\frac{{\rm d}\langle\Delta L_z\rangle}{{\rm d}t}(J,K) = \hbar\frac{{\rm d}\langle\Delta M\rangle}{{\rm d}t}=\hbar\sum_{\Delta J,\Delta K}\Delta J\ A_{v\to v';\Delta J=\Delta M,\Delta K} = -\frac{4}{c^3}(2\pi\nu_{\rm vib})^2\Omega\left\{\frac{I_3}{I_1}\mu_{||}^2\left(1-\frac{K^2}{J^2}\right)+\frac{I_3}{2I_1}\mu_{\perp}^2\left(1-\frac{K^2}{J^2}\right)+\mu_{\perp}^2\frac{K^2}{J^2}\right\}. \quad (9.96)$$

We would like to compare this quantity to the rate of energy loss. For that, we also need the rate of $\Delta J=\Delta M=0$ ro-vibrational transitions, which, to lowest order in $\Delta E_{\rm rot}/\Delta E_{\rm vib}$, are given by:

$$A_{v\to v';\Delta J=\Delta M=0,\Delta K=0} = \frac{4\mu_{||}^2}{3\hbar c^3}(2\pi\nu_{\rm vib})^3\frac{K^2}{J^2}, \quad (9.97)$$

$$A_{v\to v';\Delta J=\Delta M=0,\Delta K=\pm1} = \frac{\mu_{\perp}^2}{3\hbar c^3}(2\pi\nu_{\rm vib})^3\left(1-\frac{K^2}{J^2}\right). \quad (9.98)$$

We can then evaluate the rate of energy loss:

$$\dot{E}(J,K)=-h\nu_{\rm vib}\sum_{\Delta J,\Delta K}A_{v\to v';\Delta J,\Delta K}=-\frac{4}{3}\frac{(2\pi\nu_{\rm vib})^4}{c^3}\left(\mu_{||}^2+\mu_{\perp}^2\right). \quad (9.99)$$

We can now relate the rate of angular momentum loss to the rate of energy loss. In the case $K=J$,

we see that only the last term in Eq. (9.96) contributes and we obtain

$$\frac{\mathrm{d}\langle\Delta L_z\rangle}{\mathrm{d}t}(K=J) = -\frac{4}{c^3}(2\pi\nu_{\rm vib})^2\mu_\perp^2\Omega = \frac{3\mu_\perp^2}{\mu_{||}^2+\mu_\perp^2}\frac{\Omega}{(2\pi\nu_{\rm vib})^2}\dot{E}. \tag{9.100}$$

In the case where the grain orientation is randomized, one must average over K. For $I_3 = 2I_1$, we obtain:

$$\frac{\mathrm{d}\langle\Delta L_z\rangle}{\mathrm{d}t}(K=\text{ random}) = -\frac{4}{c^3}(2\pi\nu_{\rm vib})^2\left[\frac{4}{3}\mu_{||}^2+\mu_\perp^2\right]\Omega = \frac{3\mu_\perp^2+4\mu_{||}^2}{\mu_{||}^2+\mu_\perp^2}\frac{\Omega}{(2\pi\nu_{\rm vib})^2}\dot{E}. \tag{9.101}$$

We see that we obtain an increase in the damping rate by a factor $(1+\frac{4}{3}\frac{\mu_{||}^2}{\mu_\perp^2})$ in comparison to the case $K=J$. In principle one should specify the character of each transition (in-plane, or perpendicular, if $\mu_{||}^2=0$; out-of-plane, or parallel, if $\mu_\perp^2=0$). For simplicity we assume the isotropic case, $\mu_{||}^2=\frac{1}{2}\mu_\perp^2$. In that case, we obtain

$$F_{\rm IR} = \frac{10\tau_{\rm H}}{3\pi I}\int_0^\infty \frac{F_\nu}{\nu^2}\,d\nu, \tag{9.102}$$

where $F_\nu \equiv \frac{1}{4\pi}\frac{\mathrm{d}\dot{E}}{\mathrm{d}\nu}$.

We can now also obtain the rotational excitation rate. Using Eqs. (9.93) and (9.94) to lowest order in $\Omega/(2\pi\nu_{\rm vib})$, we obtain

$$\frac{\mathrm{d}\langle\Delta L_z^2\rangle}{\mathrm{d}t}(J,K) = \frac{2\hbar}{3c^3}(2\pi\nu_{\rm vib})^3\left\{2\mu_{||}^2\left(1-\frac{K^2}{J^2}\right)+\mu_\perp^2\left(1+\frac{K^2}{J^2}\right)\right\}. \tag{9.103}$$

In the case that the grain rotates around its axis of greatest inertia, we have

$$\frac{\mathrm{d}\langle\Delta L_z^2\rangle}{\mathrm{d}t}(K=J) = \frac{\hbar^2}{h\nu_{\rm vib}}\frac{\mu_\perp^2}{\mu_{||}^2+\mu_\perp^2}\dot{E} = \frac{1}{3}\frac{2\hbar^2}{h\nu_{\rm vib}}\dot{E}, \tag{9.104}$$

where in the last equality is valid in the isotropic case. When the grain's nutation state is randomized, we obtain

$$\frac{\mathrm{d}\langle\Delta L_z^2\rangle}{\mathrm{d}t}(K\text{ random}) = \frac{1}{3}\frac{2\hbar^2}{h\nu_{\rm vib}}\dot{E}, \tag{9.105}$$

regardless of the character of the transition. As was explained in Chapter 8, this result can be intuitively understood as follows: each photon carries and angular momentum squared $L_\gamma^2 = 2\hbar^2$. If photons are isotropically emitted, then 1/3 of this quantity leads to a diffusion of the grain's angular momentum along its initial direction.

9.7 Collisions

A quantum mechanical treatment of collisions would be much more complex than that of plasma drag or infrared emission, and we have not carried it. For completeness, we just state the results of Ref. [170], where these rates were derived classically, and we refer the reader to the paper for a complete discussion. For the case of neutral grains and neutral impactors, we have:

$$F_{\rm n}(Z_g = 0) = \frac{5}{3} F_{\rm n,K=J} \quad \text{and} \quad G_{\rm n}(Z_g = 0) = G_{\rm n,K=J}. \tag{9.106}$$

For charged grains and neutral impactors, the normalized damping rate was found to be:

$$F_{\rm n}^{\rm (in)}(Z_g \neq 0) = \left\{ 1 + \frac{2}{3} \left[1 + \left(\frac{r_{\rm c}}{a_{\rm cx}} \right)^2 \right]^{-1} \right\} F_{\rm n,K=J}, \quad \text{where} \quad r_{\rm c} \equiv \sqrt[4]{\frac{Z_g^2 q_e^2 \alpha}{3kT}}. \tag{9.107}$$

r_c is the critical separation at which the induced dipole attraction overwhelms the thermal energy of the gas. The normalized excitation rate is

$$G_{\rm n}(Z_g \neq 0) = G_{\rm n,K=J}. \tag{9.108}$$

The case of ion impacts is left unchanged from Chapter 8.

9.8 Results

To avoid lengthy repetitions, we will refer to the case where grains are spinning around their axis of greatest inertia (as treated by DL98b and in Chapter 8) by "case 1" (or "$\theta = 0$" in figures), and to the case where the relative orientation of the grain and the angular momentum is randomized (as discussed in the present chapter) by "case 2" (or "θ random" in figures).

9.8.1 Angular momentum distribution

We saw in Section 9.4.2 that, at equal angular momentum, the total power radiated by a disk-like grain in case 2 was 5 times (in the case $\mu_{\rm op} = 0$) to ~ 10 times ($\mu_{\rm ip}^2 : \mu_{\rm op}^2 = 2 : 1$) higher than the power radiated in case 1. This ratio goes even higher as one increases the $\mu_{\rm op}^2 : \mu_{\rm ip}^2$ ratio. However, the angular momentum distribution is different in each case, and, as $P \propto L^4$, the ratio of the total power emitted will really be

$$\frac{P_{\rm case2}}{P_{\rm case1}} \approx 10 \frac{\langle L^2 \rangle_{\rm case2}^2}{\langle L^2 \rangle_{\rm case1}^2}. \tag{9.109}$$

In what follows we show that $\langle L^2 \rangle_{\rm case2} < \langle L^2 \rangle_{\rm case1}$.

First of all, we showed in earlier sections that the damping rates are generally higher for grains

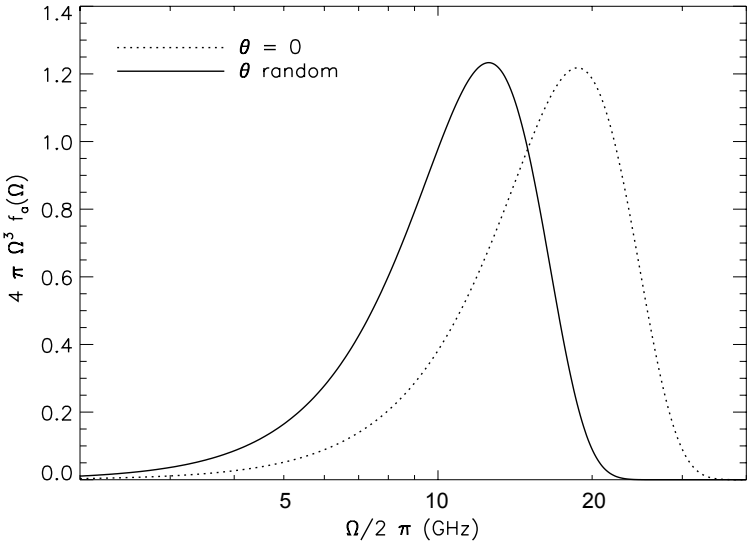

Figure 9.3: Probability distribution function for the parameter $\Omega = L/I_3$, for a grain of radius $a = 5\,\text{Å}$, in WIM conditions, with $\mu_{\rm ip}^2 : \mu_{\rm op}^2 = 2 : 1$, and with dipole moment per atom $\beta = 0.38$ Debye.

spinning around a non-principal axis of inertia. This can be understood heuristically as follows: for a given angular momentum $L = \hbar J$, the rotational energy $E_{\rm rot}(J, K)$ was given in Eq. (9.1). Averaging over the nutation angle (i.e., averaging over K), we find that

$$\langle E_{\rm rot}\rangle(J) = \frac{L^2}{2I_1} - \frac{1}{3}\frac{L^2}{2}\left(I_1^{-1} - I_3^{-1}\right). \tag{9.110}$$

In the case of a disk-like grain, ($I_3 = 2I_1$) this is

$$\langle E_{\rm rot}\rangle(J) = \frac{5}{3}\frac{L^2}{2I_3} = \frac{5}{3}E_{\rm rot}(J, K = J). \tag{9.111}$$

Therefore, we may expect that, when in contact with a bath of a characteristic energy, grains with a randomly oriented rotation axis will have an rms angular momentum of the order of $\sim \sqrt{3/5} \approx 0.77$ that of grains rotating around their axis of greatest inertia. This is indeed what we found in the case of collisions of neutral grains with neutral impactors, or emission of infrared photons, for which we showed that G was unchanged but F was increased by a factor of 5/3. We also showed that the normalized plasma damping and excitation rates satisfied $1 < F_{\rm p}/G_{\rm p} < 3$.

More importantly, the characteristic radiation-reaction damping time $\tau_{\rm ed}$ was found to be shorter in case 2. We have

$$\frac{\tau_{\rm ed}(\text{case 2})}{\tau_{\rm ed}(\text{case 1})} = \frac{\mu_{\rm ip}^2}{\frac{41}{15}\mu_{\rm ip}^2 + \frac{16}{3}\mu_{\rm op}^2}. \tag{9.112}$$

In the case where radiation-reaction is the dominant rotational damping mechanism, which is the

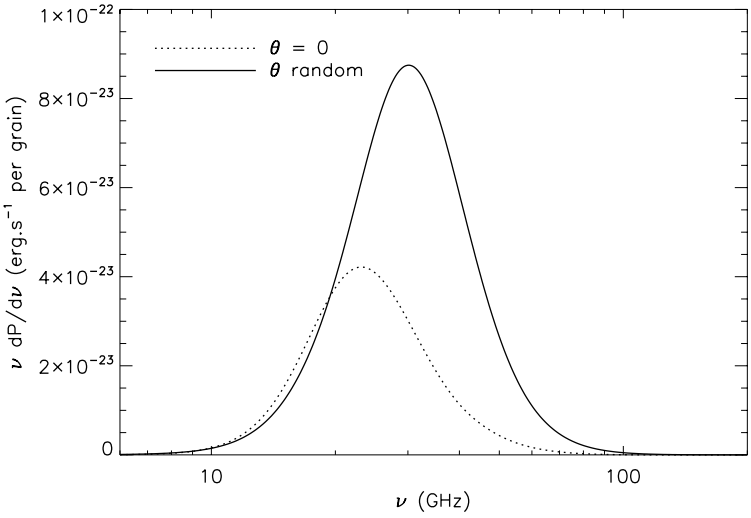

Figure 9.4: Power radiated by a grain of radius $a = 5\,\text{Å}$, in WIM conditions, with $\mu_{\rm ip}^2 : \mu_{\rm op}^2 = 2 : 1$, and with dipole moment per atom $\beta = 0.38$ Debye.

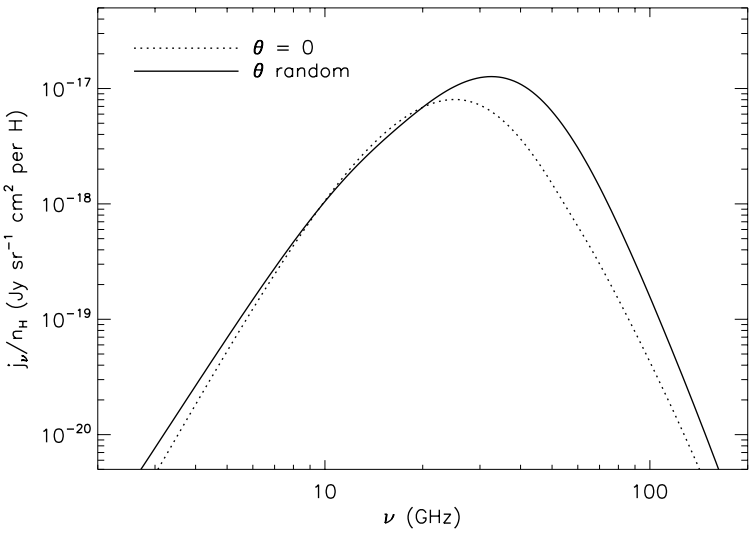

Figure 9.5: Spinning dust emissivity in WIM environment.

case for the smallest grains in diffuse phases of the ISM, we showed in Section 8.10.1 that the rms angular momentum is proportional to $\tau_{\rm ed}^{1/4}$. Numerically, we have

$$\frac{\tau_{\rm ed}^{1/4}(\text{case 2})}{\tau_{\rm ed}^{1/4}(\text{case 1})} \approx \begin{cases} 0.78 & \mu_{\rm op}=0, \\ 0.66 & \mu_{\rm ip}^2:\mu_{\rm op}^2=2:1. \end{cases} \tag{9.113}$$

From these considerations, we therefore expect that in the same environment, the characteristic angular momentum in case 2 will be ~ 0.66–0.78 times the one in case 1.

We show in Fig. 9.3 the angular momentum distribution for a grain of volume equivalent radius $a = 5$ Å, in WIM conditions, with $\mu_{\rm ip}^2 : \mu_{\rm op}^2 = 2 : 1$, and with dipole moment per atom $\beta = 0.38$ Debye. The rms angular momentum in case 2 is ~ 0.67 times the one in case 1.

9.8.2 Change in emissivity

At a given angular momentum, the power radiated in case 2 peaks at a frequency approximately twice higher than the power radiated in case 1 (see discussion in Section 9.4.2).

Therefore, and in view of the preceding section, we expect that the total power radiated in case 2 will peak at a frequency $\sim 2\times 0.7 \sim 1.4$ times higher and will integrate to a total power $\sim 10\times(0.7)^4 \sim 2$ times the power radiated in case 1. This is indeed what we find, as can be seen in Fig. 9.4.

The overall spinning dust emissivity follows the same trends, as can be seen in Fig. 9.5 for the WIM, and in Fig. 9.6 for other interstellar environments.

9.8.3 Sensitivity to dipole moment orientation

It is not clear what is the correct assignment for the direction of the grain permanent dipole moment relative to the principal axes. Here we analyze the effect of the dipole moment orientation on the spinning dust spectrum; it appears to make only a minor difference in the WIM environment.

For the smallest grains where radiation-reaction damping is most important, we expect $\langle\Omega^2\rangle^{1/2} \propto \tau_{\rm ed}^{1/4}$ so

$$\langle\Omega^2\rangle^{1/2} \propto \begin{cases} \mu_{\rm ip}^{-1/2} & \text{(case 1)}, \\ \mu^{-1/2}\left(\frac{80}{39}-\frac{\mu_{\rm ip}^2}{\mu^2}\right)^{-1/4} & \text{(case 2)}. \end{cases} \tag{9.114}$$

In case 1 the rotation rate is very sensitive to the orientation of the dipole moment (only the in-plane component contributes to the power and the radiation reaction damping). Eventually, when the in-plane component becomes small enough, radiation-reaction damping becomes subdominant and the rms angular momentum will depend only on interactions with gas or infrared photons. In case 2 however the dependence on $\mu_{\rm ip}^2/\mu^2$ is quite weak, as the out-of-plane component contributes to the power and angular momentum loss. We show the normalized rms angular momenta in case 1

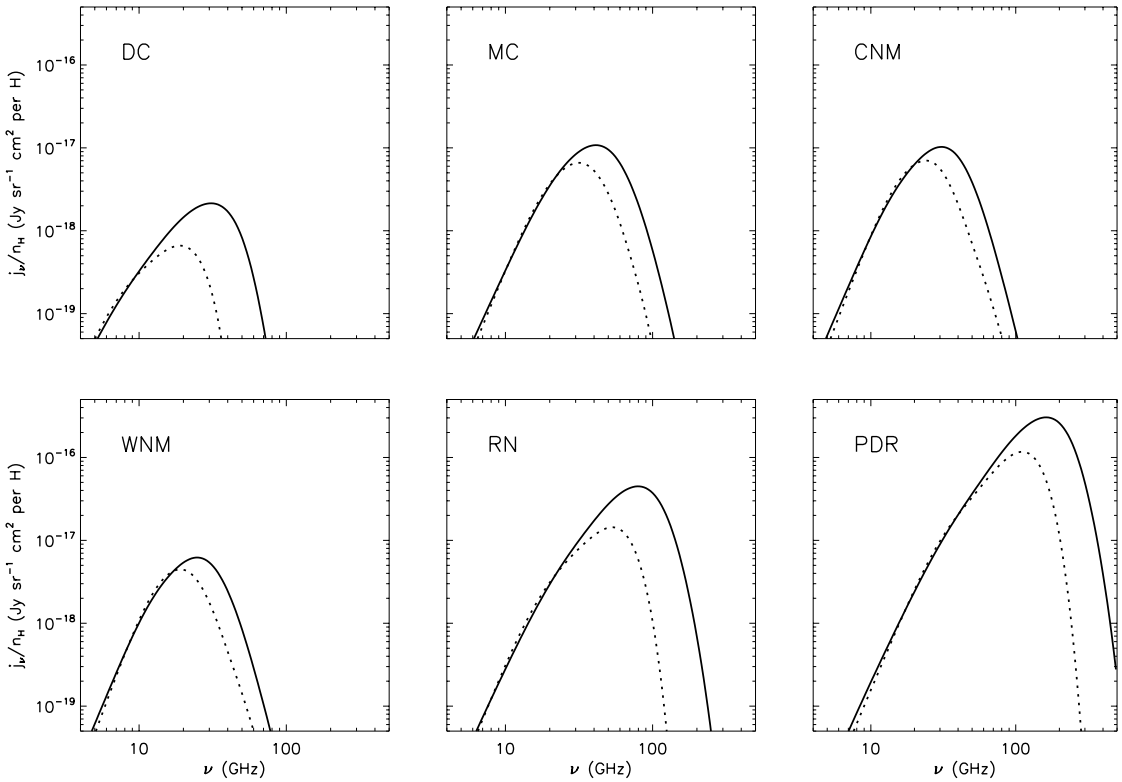

Figure 9.6: Spinning dust spectra for several environmental conditions: dark cloud (DC), molecular cloud (MC), cold neutral medium (CNM), warm neutral medium (WNM), reflection nebula (RN) and photodissociation region (PDR). The environments are defined in DL98b, table 1. The parameters for the grain size distribution are $R_V = 3.1, b_C = 6 \times 10^{-5}$ for the diffuse CNM and WNM phases, and $R_V = 5.5, b_C = 3 \times 10^{-5}$ for the dense DC, MC, RN and PDR. The dashed line is for a spectrum calculated assuming case 1 ($\theta = 0$), whereas the solid line is for case 2 (isotropic θ). The shift to higher frequencies and increase in emissivity in case 2 is systematic for all environments. We expect that case 2 should be a better approximation in the diffuse and high radiation intensity phases (WIM, CNM, WNM, RN, PDR).

and 2 in Fig. 9.7. Figure 9.7 also shows an estimate of the peak frequency of the emitted power in both cases.

The total power radiated by one grain, at a given angular momentum, was given in Eq. (9.55) for case 2. Taking $\Omega \sim \langle\Omega^2\rangle^{1/2}$, and using the above results, we obtain

$$P \propto \begin{cases} \text{constant} & \text{(case 1)} \\ \left(\frac{32}{17} - \frac{\mu_{\rm ip}^2}{\mu^2}\right) \Big/ \left(\frac{80}{39} - \frac{\mu_{\rm ip}^2}{\mu^2}\right) & \text{(case 2).} \end{cases} \tag{9.115}$$

Thus in both cases the total power is very nearly independent of $\mu_{\rm ip}^2/\mu^2$. In case 1, when $\mu_{\rm ip}^2/\mu^2 \to 0$, radiation-reaction damping becomes subdominant and the power becomes proportional to $\mu_{\rm ip}^2$. These features are shown in Fig. 9.8.

9.9 Discussion

The purpose of this chapter was to revisit the assumption of Refs. [8, 173] that PAHs rotate about their axis of main inertia. The motivation in doing so is that thermal spikes following the absorption of UV photons randomize the orientation of the grain with respect to the angular momentum axis. These absorption events happen frequently enough (i.e., on timescale shorter than the timescale for significant changes in the total angular momentum) that we expect such a randomization to be effective in most environments. Thus we expect the results from this work ("case 2") to be a better approximation to diffuse or high-radiation environments (CNM, WNM, WIM, PDR, and RN) than those from Chapter 8, which assumed rapid dissipation of the nutational energy ($\theta = 0$ or "case 1"). However, the new release of SpDust allows the user to choose either case; for example, one may wish to explore the range of cases in dark cloud environments where thermal spikes are infrequent, or what happens if an as-yet-unidentified dissipational process is active and restores $\theta = 0$.

In this chapter, we showed that, for a given angular momentum, the power radiated by a grain in case 2 is ~ 10 times higher than that radiated by a grain in case 1. This is because in case 2, the grain emits at higher frequencies, including above the one corresponding to the instantaneous angular velocity, as it is not rotating around the axis of greatest inertia.

We evaluated the rotational excitation and damping rates in case 2 as a function of grain size and environment conditions, and the resulting angular momentum distribution. We showed that in a given environment, grains in case 2 have a lower rms angular momentum than those in case 1, by a factor of ~ 0.7. This is due to larger damping rates, in particular radiation-reaction damping, in case 2.

The combination of these results leads to a spinning dust spectrum peaking at slightly higher frequencies in case 2, and a total power approximately twice as large as that emitted in case 1. Finally, we showed that the spectrum in case 2 is only weakly sensitive to the precise value of the

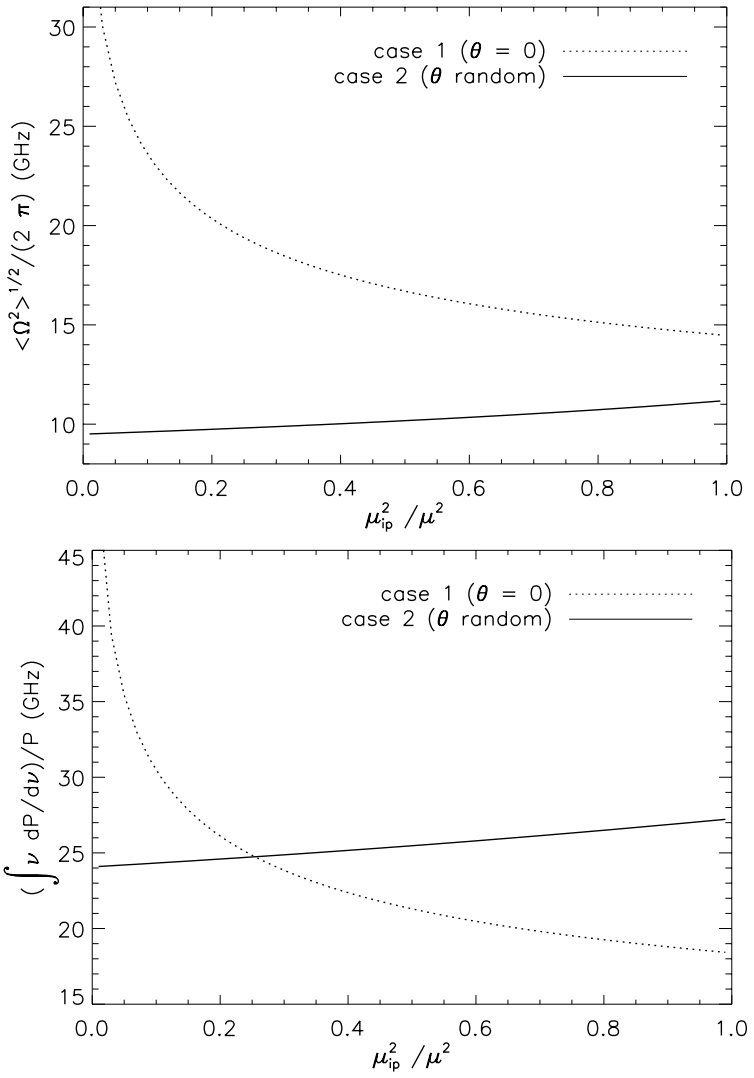

Figure 9.7: Top panel: normalized rms angular momentum $\langle\Omega^2\rangle^{1/2}$ as a function of the ratio of in-plane to total dipole moment. Bottom panel: estimate of the peak frequency $\int \nu(\mathrm{d}P/\mathrm{d}\nu)\mathrm{d}\nu/P$, as a function of this ratio. Both are for a dust grain of radius $a = 5\,\text{Å}$ and dipole moment per atom $\beta = 0.38$ Debye, in WIM conditions.

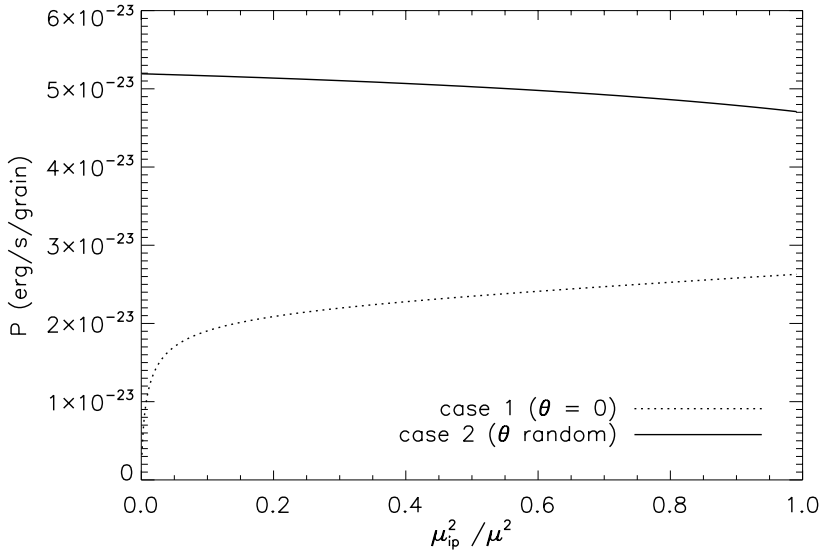

Figure 9.8: Total power emitted by a dust grain of radius $a = 5\,\text{Å}$ and dipole moment per atom $\beta = 0.38$ Debye, in WIM conditions, as a function of the ratio of in-plane to total dipole moment.

$\mu_{\rm ip}^2 : \mu_{\rm op}^2$ ratio.

Ref. [143] found a tension between theoretical results and microwave observations of the WIM: the theory was a factor of ~ 3 larger than the observations, and the peak frequency of the spinning dust and its amplitude could not be simultaneously reconciled by changing β (the normalization of the dipole moment). By increasing the theoretical emissivity and moving its peak to higher frequencies, our results may worsen this tension. This seems likely to strengthen the empirical case for depletion of the PAH population in the WIM phase, however there are other conceivable explanations for this discrepancy. The random walk model for the dipole moment may not apply well to the smallest grains (e.g. one could imagine that some of the small PAHs have symmetries that guarantee $\boldsymbol{\mu} = 0$ exactly), or one could imagine extra low-frequency internal degrees of freedom which allow the grain to relax to a state where it rotates around the axis of greatest moment of inertia. A detailed exploration of the parameter space (as was done in Ref. [143]) is beyond the scope of this work.

As a final note, we present some of the remaining issues in the treatment of the rotational physics of the smallest dust grains:

- *Triaxiality*: Many PAHs have triaxial moment of inertia tensors (e.g. ovalene $C_{32}H_{14}$, circumpyrene $C_{42}H_{16}$, and their derivatives). This case was not treated in the present work due to its much greater complexity.

- *Impulsive torques*: Some of the sources of torque, such as ion impacts, impart large but infrequent changes in angular momentum. This could in principle lead to "rotational spikes"

analogous to the well-known thermal spikes in the grains' internal energy, and would not be treated correctly by the Fokker-Planck equation (which is a diffusive approximation).[5]

- *Ancillary data*: We have not fully quantified the uncertainties in the ancillary data, such as evaporation temperatures, the emissivity in the lowest-frequency vibrational modes, and the grain charging model (photoelectric and electron/ion impact). However, our hope in making the SpDust code publicly available is to provide users the flexibility to explore deviations from default or fiducial parameters.

[5]This issue is treated in Ref. [172]; they find that the principal effect on the spinning dust spectrum is the existence of a "tail" to high frequencies resulting from transient spin-up of the grains.

9.A Appendix: Evaluation of the plasma excitation and drag coefficients

In this appendix we describe our implementation of the plasma drag coefficients $F_{\rm p}(\Omega)$ and $G_{\rm p}(\Omega)$, in SpDust. These are integrals over the function $G_{\rm p,AHD}(\omega)$, which is itself time-consuming to compute.

If we wish to calculate the integral $\int w(x)g(x)\mathrm{d}x$, where $w(x)$ is a known weighing function which properties will be discussed later, and the function $g(x)$ is smooth enough on the interval of integration that it can be approximated by a quadratic polynomial $g(x) \approx a + bx + cx^2$, then we may approximate

$$\int w(x)g(x)\mathrm{d}x \approx A\left[g(x_+) + g(x_-)\right], \tag{9.116}$$

where $A \equiv \frac{1}{2}\int w(x)\mathrm{d}x$, and $\{x_+, x_-\}$ are the solutions of the second-order system

$$\left\{\begin{array}{rcl} x_+ + x_- & = & A^{-1}\int x w(x)\mathrm{d}x, \\ x_+^2 + x_-^2 & = & A^{-1}\int x^2 w(x)\mathrm{d}x. \end{array}\right. \tag{9.117}$$

We now turn our attention to the specific cases of $G_{\rm p}(\Omega)$ and $F_{\rm p}(\Omega)$. With $x = \omega/\Omega$ and the weighing function $w(x) = (3-x)^2$, we get

$$G_{\rm p}(\Omega) \approx \frac{2\mu_{\rm op}^2}{3\mu_{\rm ip}^2} G_{\rm p,AHD}(2\Omega) + \frac{1}{3}\left[G_{\rm p,AHD}(\Omega_+) + G_{\rm p,AHD}(\Omega_-)\right], \tag{9.118}$$

where

$$\Omega_\pm = \frac{3 \pm \sqrt{3/5}}{2}\Omega \approx \{1.11\Omega, 1.89\Omega\}. \tag{9.119}$$

Similarly, with the weighing function $w(x) = x(3-x)^2$, we get

$$F_{\rm p}(\Omega) \approx \frac{4\mu_{\rm op}^2}{3\mu_{\rm ip}^2} G_{\rm p,AHD}(2\Omega) + \frac{1}{2}\left[G_{\rm p,AHD}(\tilde{\Omega}_+) + G_{\rm p,AHD}(\tilde{\Omega}_-)\right], \tag{9.120}$$

where

$$\tilde{\Omega}_\pm = \frac{8 \pm \sqrt{13/3}}{5}\Omega \approx \{1.18\Omega, 2.02\Omega\}. \tag{9.121}$$

We have tested the accuracy of the approximate integrator and found that the error was less than 1% in the regime where $F_{\rm p}, G_{\rm p}$ have significant values, i.e., for $\Omega \lesssim \Omega_{\rm th} = \sqrt{3kT/I_3}$. More precisely, we checked that

$$\frac{|\Delta F_{\rm p}(\Omega)|}{F_{\rm p}(\Omega)} \times \min\left(1, \frac{F_{\rm p}(\Omega)}{F_{\rm p}(\Omega_{\rm th})}\right) < 0.01 \tag{9.122}$$

for grain radii $a = 4, 5, 6$ Å, gas temperatures $T = 50, 500, 5000$ K and grain charge $Z = -1, 0, 1$, and similarly for $G_{\rm p}$.

Bibliography

[1] R. H. Dicke, P. J. E. Peebles, P. G. Roll, and D. T. Wilkinson, ApJ, **142**, 414 (1965).

[2] A. A. Penzias and R. W. Wilson, ApJ, **142**, 419 (1965).

[3] D. J. Fixsen, E. S. Cheng, J. M. Gales, J. C. Mather, R. A. Shafer, and E. L. Wright, ApJ, **473**, 576 (1996).

[4] E. Komatsu et al., ApJS, **192**, 18 (2011).

[5] W. Hu, D. Scott, N. Sugiyama, and M. White, Phys. Rev. D, **52**, 5498 (1995).

[6] The Planck Collaboration, arXiv:1101.2031 (2011).

[7] B. T. Draine and A. Lazarian, ApJL, **494**, L19 (1998).

[8] [DL98b], B. T. Draine, and A. Lazarian, ApJ, **508**, 157 (1998).

[9] J. C. Mather et al., ApJL, **354**, L37 (1990).

[10] G. F. Smoot et al., ApJL, **396**, L1 (1992).

[11] A. G. Riess et al., Astron. J., **116**, 1009 (1998).

[12] S. Perlmutter et al., ApJ, **517**, 565 (1999).

[13] C. B. Netterfield et al., ApJ, **571**, 604 (2002).

[14] T. J. Pearson et al., ApJ, **591**, 556 (2003).

[15] C. L. Kuo et al., ApJ, **600**, 32 (2004).

[16] P. Ade et al., ApJ, **674**, 22 (2008).

[17] E. Hawkins et al., MNRAS, **346**, 78 (2003).

[18] K. N. Abazajian et al., ApJS, **182**, 543 (2009).

[19] The Planck Collaboration, arXiv:astro-ph/0604069 (2006).

[20] J. A. Tauber et al., A&A, **520**, A1 (2010).

[21] The ACT Collaboration, ApJ, **722**, 1148 (2010).

[22] J. Ruhl et al., SPIE Conference Series, **5498**, 11 (2004).

[23] D. Baumann et al., AIP Conference Series, **1141**, 10 (2009).

[24] U. Seljak and M. Zaldarriaga, ApJ, **469**, 437 (1996).

[25] A. Lewis, A. Challinor, and A. Lasenby, ApJ, **538**, 473 (2000).

[26] M. Doran, JCAP, **10**, 11 (2005).

[27] U. Seljak, N. Sugiyama, M. White, and M. Zaldarriaga, Phys. Rev. D, **68**, 083507 (2003).

[28] W. Hu and M. White, ApJ, **479**, 568 (1997).

[29] S. Seager, D. D. Sasselov, and D. Scott, ApJS, **128**, 407 (2000).

[30] S. Seager, D. D. Sasselov, and D. Scott, ApJL, **523**, L1 (1999).

[31] P. J. E. Peebles, ApJ, **153**, 1 (1968).

[32] Y. B. Zeldovich, V. G. Kurt, and R. A. Syunyaev, Sov. Phys. JETP, **28**, 146 (1969).

[33] A. Lewis, J. Weller, and R. Battye, MNRAS, **373**, 561 (2006).

[34] J. A. Rubiño-Martín, J. Chluba, W. A. Fendt, and B. D. Wandelt, MNRAS, **403**, 439 (2010).

[35] J. A. Rubiño-Martín, J. Chluba, and R. A. Sunyaev, MNRAS, **371**, 1939 (2006).

[36] J. Chluba, J. A. Rubiño-Martín, and R. A. Sunyaev, MNRAS, **374**, 1310 (2007).

[37] D. Grin and C. M. Hirata, Phys. Rev. D, **81**, 083005 (2010).

[38] J. Chluba, G. M. Vasil, and L. J. Dursi, MNRAS, **407**, 599 (2010).

[39] Y. Ali-Haïmoud and C. M. Hirata, Phys. Rev. D, **82**, 063521 (2010).

[40] Y. Ali-Haïmoud, D. Grin, and C. M. Hirata, Phys. Rev. D, **82**, 123502 (2010).

[41] J. Chluba and R. A. Sunyaev, A&A, **475**, 109 (2007).

[42] E. E. Kholupenko, A. V. Ivanchik, and D. A. Varshalovich, Phys. Rev. D, **81**, 083004 (2010).

[43] J. Chluba and R. A. Sunyaev, A&A, **496**, 619 (2009).

[44] S. I. Grachev and V. K. Dubrovich, Astron. Lett., **34**, 439 (2008).

[45] C. M. Hirata and J. Forbes, Phys. Rev. D, **80**, 023001 (2009).

[46] J. Chluba and R. A. Sunyaev, A&A, **503**, 345 (2009).

[47] J. Chluba and R. A. Sunyaev, A&A, **446**, 39 (2006).

[48] E. E. Kholupenko and A. V. Ivanchik, Astron. Lett., **32**, 795 (2006).

[49] C. M. Hirata, Phys. Rev. D, **78**, 023001 (2008).

[50] V. K. Dubrovich and S. I. Grachev, Astron. Lett., **31**, 359 (2005).

[51] J. Chluba and R. A. Sunyaev, A&A, **480**, 629 (2008).

[52] J. Chluba and R. A. Sunyaev, A&A, **512**, A53 (2010).

[53] T. Matsuda, H. Satō, and H. Takeda, Progress of Theoretical Physics, **42**, 219 (1969).

[54] T. Matsuda, H. Sato, and H. Takeda, Progress of Theoretical Physics, **46**, 416 (1971).

[55] E. E. Kholupenko, A. V. Ivanchik, and D. A. Varshalovich, MNRAS, **378**, L39 (2007).

[56] E. R. Switzer and C. M. Hirata, Phys. Rev. D, **77**, 083006 (2008).

[57] C. M. Hirata and E. R. Switzer, Phys. Rev. D, **77**, 083007 (2008).

[58] E. R. Switzer and C. M. Hirata, Phys. Rev. D, **77**, 083008 (2008).

[59] J. A. Rubiño-Martín, J. Chluba, and R. A. Sunyaev, A&A, **485**, 377 (2008).

[60] E. E. Kholupenko, A. V. Ivanchik, and D. A. Varshalovich, Astron. Lett., **34**, 725 (2008).

[61] E. R. Switzer and C. M. Hirata, Phys. Rev. D, **72**, 083002 (2005).

[62] Y. Ali-Haïmoud and C. M. Hirata, Phys. Rev. D, **83**, 043513 (2011).

[63] S. Dodelson, *Modern Cosmology*, Academic Press (2003).

[64] I. D. Novikov and Y. B. Zeldovič, ARAA, **5**, 627 (1967).

[65] C. M. Hirata, Lecture notes on primordial recombination, unpublished (2008).

[66] G. Steigman, Annual Review of Nuclear and Particle Science, **57**, 463 (2007).

[67] D. E. Osterbrock and G. J. Ferland, *Astrophysics of gaseous nebulae and active galactic nuclei*, 2nd. ed., CA: University Science Books (2006).

[68] M. Göppert-Mayer, Annalen der Physik, **401**, 273 (1931).

[69] L. N. Labzowsky, A. V. Shonin, and D. A. Solovyev, Journal of Physics B Atomic Molecular Physics, **38**, 265 (2005).

[70] J. Chluba and R. A. Sunyaev, A&A, **458**, L29 (2006).

[71] B. J. T. Jones and R. F. G. Wyse, A&A, **149**, 144 (1985).

[72] D. Pequignot, P. Petitjean, and C. Boisson, A&A, **251**, 680 (1991).

[73] S. Sasaki and F. Takahara, PASJ, **45**, 655 (1993).

[74] Y. E. Lyubarsky and R. A. Sunyaev, A&A, **123**, 171 (1983).

[75] I. P. dell'Antonio and G. B. Rybicki, ASP Conference Series, **51**, 548 (1993).

[76] D. Larson et al., ApJS, **192**, 16 (2011).

[77] W. A. Fendt, J. Chluba, J. A. Rubiño-Martín, and B. D. Wandelt, ApJS, **181**, 627 (2009).

[78] W. Y. Wong, A. Moss, and D. Scott, MNRAS, **386**, 1023 (2008).

[79] M. S. Burgin, Bulletin of the Lebedev Physics Institute, **36**, 110 (2009).

[80] M. S. Burgin, Bulletin of the Lebedev Physics Institute, **37**, 280 (2010).

[81] A. Burgess, Mem. R. Astr. Soc. , **69**, 1 (1965).

[82] H. A. Bethe and E. E. Salpeter, *Quantum Mechanics of One- and Two-Electron Atoms*, New York: Academic Press (1957).

[83] S. P. Goldman, Phys. Rev. A, **40**, 1185 (1989).

[84] C. Hernández-Monteagudo, J. A. Rubiño-Martín, and R. A. Sunyaev, MNRAS, **380**, 1656 (2007).

[85] M. J. Seaton, MNRAS, **119**, 90 (1959).

[86] J. D. Hey, Journal of Physics B Atomic Molecular Physics, **39**, 2641 (2006).

[87] D. Grin, Ph.D. thesis, California Institute of Technology (2010).

[88] D. G. Hummer, Mem. R. Astr. Soc. , **70**, 1 (1965).

[89] D. G. Hummer, MNRAS, **125**, 21 (1962).

[90] G. B. Rybicki and I. P. dell'Antonio, ApJ, **427**, 603 (1994).

[91] C. M. Hirata, MNRAS, **367**, 259 (2006).

[92] G. B. Rybicki, ApJ, **647**, 709 (2006).

[93] J. H. Krolik, ApJ, **338**, 594 (1989).

[94] J. H. Krolik, ApJ, **353**, 21 (1990).

[95] S. Y. Sazonov and R. A. Sunyaev, ApJ, **543**, 28 (2000).

[96] D. G. Hummer and D. Mihalas, ApJL, **150**, L57 (1967).

[97] F. Iocco, G. Mangano, G. Miele, O. Pisanti, and P. D. Serpico, Phys. Rep., **472**, 1 (2009).

[98] P. C. Stancil, S. Lepp, and A. Dalgarno, ApJ, **509**, 1 (1998).

[99] R. N. Thomas, ApJ, **125**, 260 (1957).

[100] W. Unno, ApJ, **129**, 375 (1959).

[101] A. G. Nikogosian, Akademiia Nauk SSSR Doklady, **235** (1977).

[102] J. Chluba and R. M. Thomas, MNRAS, **412**, 748 (2011).

[103] W. Y. Wong and D. Scott, MNRAS, **375**, 1441 (2007).

[104] S. I. Grachev, Astrophysics, **30**, 211 (1989).

[105] S. I. Grachev and V. K. Dubrovich, Astrophysics, **34**, 124 (1991).

[106] J. A. Rubiño-Martín, J. Chluba, W. A. Fendt, and B. D. Wandelt, MNRAS, **403**, 439 (2010).

[107] F. Iocco et al., Phys. Rep., **472**, 1 (2009).

[108] F. Iocco, G. Mangano, G. Miele, O. Pisanti, and P. D. Serpico, Phys. Rev. D, **75**, 087304 (2007).

[109] K. Jedamzik, G. M. Fuller, G. J. Mathews, and T. Kajino, ApJ, **422**, 423 (1994).

[110] S. Matsuura, S. I. Fujimoto, S. Nishimura, et al., Phys. Rev. D, **72**, 123505 (2005).

[111] S. Matsuura, S. I. Fujimoto, M. A. Hashimoto, et al., Phys. Rev. D, **75**, 068302 (2007).

[112] R. Nakamura, M. A. Hashimoto, S. I. Fujimoto, et al., arXiv:1007.0466 (2010).

[113] A. Loeb, ApJ, **555**, L1 (2001).

[114] E. R. Switzer and C. M. Hirata, Phys. Rev. D, **72**, 083002 (2005).

[115] K. Basu, C. Hernández-Monteagudo, and R. A. Sunyaev, å, **416**, 447 (2004).

[116] M. Harwit and M. Spaans, ApJ, **589**, 53 (2003).

[117] A. M. Wolfe, E. Gawiser, and J. X. Prochaska, ARAA, **43**, 861 (2005).

[118] T. C. Beers and N. Christlieb, ARAA, **43**, 531 (2005).

[119] D. A. Verner, G. J. Ferland, K. T. Korista, and D. G. Yakovlev, ApJ, **465**, 487 (1996).

[120] K. P. Dere et al., Astron. Astrophys. Supp. Ser., 149 (1997).

[121] K. P. Dere et al., Astron. Astrophys. Supp. Ser., **498**, 915 (2009).

[122] M. Asplund, N. Grevesse, A. J. Sauval, and P. Scott, ARAA, **47**, 481 (2009).

[123] C. Dickinson et al., MNRAS, **353**, 732 (2004).

[124] A. C. S. Readhead et al., ApJ, **609**, 498 (2004).

[125] C. L. Kuo et al., ApJ, **664**, 687 (2007).

[126] G. Hinshaw et al., ApJS, **180**, 225 (2009).

[127] H. K. Eriksen, J. B. Jewell, C. Dickinson, et al., ApJ, **676**, 10 (2008).

[128] S. M. Leach et al., A&A, **491**, 597 (2008).

[129] E. M. Leitch, A. C. S. Readhead, T. J. Pearson, and S. T. Myers, ApJL, **486**, L23 (1997).

[130] B. T. Draine and A. Lazarian, ApJ, **512**, 740 (1999).

[131] W.C. Erickson, ApJ, **126**, 480 (1957).

[132] F. Hoyle and N. C. Wickramasinghe, Nature, **227**, 473 (1970).

[133] A. Ferrara and R.-J. Dettmar, ApJ, **427**, 155 (1994).

[134] D. Rouan, A. Léger, A. Omont, and M. Giard, A&A, **253**, 498 (1992).

[135] N. Anderson and W. D. Watson, A&A, **270**, 477 (1993).

[136] D. P. Finkbeiner, ApJ, **614**, 186 (2004).

[137] R. A. Watson, R. Rebolo, J. A. Rubiño-Martín, et al., ApJL, **624**, L89 (2005).

[138] S. Casassus, G. F. Cabrera, F. Förster, et al., ApJ, **639**, 951 (2006).

[139] S. Casassus, L.-Å. Nyman, C. Dickinson, and T. J. Pearson, MNRAS, **382**, 1607 (2007).

[140] S. Casassus et al., MNRAS, **391**, 1075 (2008).

[141] C. Dickinson, R. D. Davies, L. Bronfman, et al., MNRAS, **379**, 297 (2007).

[142] C. Dickinson et al., ApJ, **690**, 1585 (2009).

[143] G. Dobler, B. T. Draine, and D. P. Finkbeiner, ApJ, **699**, 1374 (2009).

[144] A. J. Banday, C. Dickinson, Davies, et al., MNRAS, **345**, 897 (2003).

[145] R. D. Davies et al., MNRAS, **370**, 1125 (2006).

[146] A. Bonaldi, S. Ricciardi, S. Leach, et al., MNRAS, **382**, 1791 (2007).

[147] S. R. Hildebrandt, R. Rebolo, J. A. Rubiño-Martín, et al., MNRAS, **382**, 594 (2007).

[148] B. Gold et al., ApJS, **180**, 265 (2009).

[149] G. B. Rybicki and A. P. Lightman, *Radiative processes in Astrophysics*, Wiley-VCH Verlag GmbH & Co. KGaA. Weinheim (2004).

[150] R. S. Sutherland, MNRAS, **300**, 321 (1998).

[151] E. L. Wright et al., ApJ, **381**, 200 (1991).

[152] The Planck Collaboration, arXiv:1101.2036 (2011).

[153] C. L. Bennett et al., ApJS, **148**, 97 (2003).

[154] [DL01], Draine B. T., and A. Li, ApJ, **551**, 807 (2001).

[155] E. M. Purcell, ApJ, **231**, 404 (1979).

[156] J. C. Weingartner and B. T. Draine, ApJ, **548**, 296 (2001).

[157] J. C. Weingartner and B. T. Draine, ApJ, **134**, 263 (2001).

[158] A. Li and B. T. Draine, ApJ, **550**, L213 (2001).

[159] B. T. Draine and B. Sutin, ApJ, **320**, 803 (1987).

[160] P. G. Mezger, J. S. Mathis, and N. Panagia, A&A, **105**, 372 (1982).

[161] J. S. Mathis, P. G. Mezger, and N. Panagia, A&A, **128**, 212 (1983).

[162] R. D. Blandford and K. S. Thorne, *Applications of Classical Physics*, unpublished (2008).

[163] A. Omont, A&A, **164**, 159 (1986).

[164] L. D. Landau and E. M. Lifshitz, *Quantum Mechanics*, Butterworth Heinemann (1997).

[165] M. A. Thomas and J. W. Humbertson, J. Phys. B, **5**, L229 (1972).

[166] J. H. Miller and H. P. Kelly, Phys. Rev. A, **5**, 516 (1972).

[167] W. C. Marlow, Proc. Phys. Soc., **86**, 731 (1965).

[168] F. T. Geyling and H. R. Westerman, *Introduction to orbital mechanics*, Addison-Wesley Aerospace Series (1971).

[169] Abramowitz M. and I. Stegun, *Handbook of Mathematical Functions*, New York: Dover (1972).

[170] K. Silsbee, Y. Ali-Haïmoud, and C. M. Hirata, MNRAS, **411**, 2750 (2011).

[171] A. Li and B. T. Draine, ApJ, **554**, 778 (2001).

[172] T. Hoang, B. T. Draine, and A. Lazarian, ApJ, **715**, 1462 (2010).

[173] Y. Ali-Haïmoud, C. M. Hirata, and C. Dickinson, MNRAS, **395**, 1055 (2009).

[174] D. P. Craig and T. Thirunamachandran, *Molecular Quantum Electrodynamics*, Dover Publications, INC, Mineola, NY (1998).

[175] A. R. Edmonds, *Angular Momentum in Quantum Mechanics*, Princeton University Press, Princeton, NJ (1996).

[176] H. B. Callen and T. A. Welton, Phys. Rev., **83**, 34 (1951).